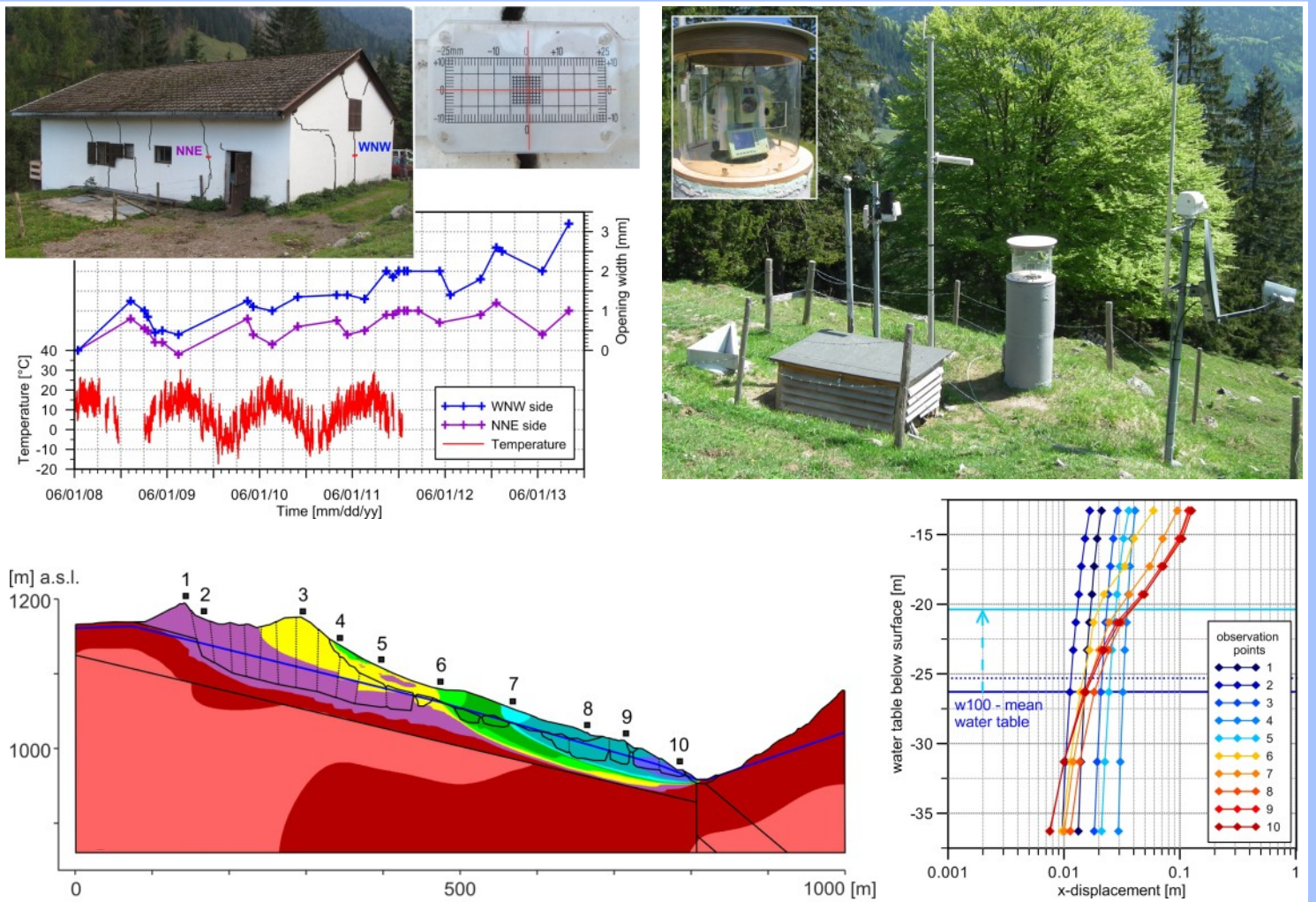




Analysis and Evaluation of the Geosensor Network's Data at the Aggenalm Landslide, Bayerischzell, Germany

Judith Susanna Festl

2014





TECHNISCHE UNIVERSITÄT MÜNCHEN

Ingenieur fakultät Bau Geo Umwelt

Lehrstuhl für Ingenieurgeologie

**Analysis and Evaluation of the Geosensor Network's Data at the
Aggenalm Landslide, Bayerischzell, Germany**

Judith Susanna Festl

Vollständiger Abdruck der von der Ingenieur fakultät Bau Geo Umwelt der
Technischen Universität München zur Erlangung des akademischen Grades eines

Doktor-Ingenieurs (Dr.-Ing.)

genehmigten Dissertation.

Vorsitzender: Univ.-Prof. Dr. rer. nat. Michael Krautblatter

Prüfer der Dissertation:

1. Univ.-Prof. Dr. rer. nat. Kurosch Thuro
2. Univ.-Prof. Dr.-Ing. habil. Thomas Wunderlich
3. Univ.-Prof. Dr. rer. nat. Christian Zangerl, Universität für Bodenkultur Wien,
Wien, Österreich

Die Dissertation wurde am 24.09.2014 bei der Technischen Universität München
eingereicht und durch die Ingenieur fakultät Bau Geo Umwelt am 10.12.2014
angenommen.

Abstract

Due to the feared increase in landslide activity in context of climate change and the continuous extension of settlement areas in the Alps, landslide monitoring gained more importance during the last years. It became necessary to monitor more mass movements not only in order to minimize the conflict between land use and natural hazard prevention but also to better understand the underlying mechanisms of the landslide as basis for a better prediction and prevention of catastrophic events.

Within the alpEWAS project (Development and testing of an integrative early warning system for alpine instable slopes) a monitoring system has been installed at the Aggenalm landslide, situated in the Bavarian Alps. The monitoring system consists of several innovative and accustomed measuring systems for the surveillance of surface (reflectorless VTPS, low-cost GNSS) and subsurface deformations (TDR, inclinometer), and also monitors possible trigger factors (precipitation, pore water pressure). Continuous data recordings of the various sensors exist since spring 2009.

In this study a holistic approach to evaluate the data of the alpEWAS geosensor network is taken in order to verify the geomechanical model of the landslide and to better understand and characterize the trigger factors; all aiming to derive threshold values for an early warning system. In a first step all data concerning the build-up and geology, the description of historic events, and site investigations are compiled and presented, whose findings led to the construction of new cross sections and a refinement of the geomechanical model. The mechanism of the Aggenalm landslide is thereafter classified according to CRUDEN & VARNES (1996) as a *complex, extremely slow rock spread–debris slide*, split into the top part – rock spread – where stiff limestone and dolomite (Upper Rhaetian formation) sink into the plastically deforming Kössen marl, and the lower half, where the material becomes more and more disintegrated and a shear zone developed within the Kössen marl, thus the mechanism merging to a debris slide.

Subsequently, an overview of the geosensor network, its components, and the sensors' individual results is given. All sensors included in the geosensor network show a reliable operation, especially since the start of the automated data retrieval and remote access via the alpEWAS Control software. The deformation measurement systems on surface are consistent with each other and reveal a displacement rate of approximately 1 cm/a at maximum, while the subsurface measurements detected no significant deformation. The one remaining piezometer displays the fluctuation of the groundwater level in regards to precipitation and snowmelt very detailed. Since it is fancied from analyzing prior landslides at the Aggenalm that one of the major influencing factors on the movement is precipitation and/or snowmelt, these data are characterized and analyzed more precisely by means of time series analysis.

Time series analysis methods are not only used to describe the relation between precipitation and fluctuation of the groundwater level, but also to analyze the data conjointly with deformation measurements, as the temporal discrepancy between precipitation and initiation of movements is of great relevance regarding the definition of thresholds. The temporal delay between rainfall and peak in water level is estimated to be 2.5–2.75 days, whereas it is not yet possible to prove its relation to deformation measurements with these models, even though a dependence of water masses on the Aggenalm landslide's displacements is nonambiguous.

As the current velocities of about 1cm/a and thus extremely slow movement rates only allow deriving threshold values for very small accelerations, thresholds for extreme events, possibly a catastrophic failure, are determined by numerical modeling. The numerical model is established based on the results of all the field surveys and the data analyses using the code FLAC (Fast Lagrangian Analysis of Continua) by Itasca. The results of the initial model reproduce the movement behavior as observed by the monitoring system very well and hence verify the landslide's mechanism as well. The simulations of heightened groundwater levels show that the water table needs to rise to an extreme level in order to reach an acceleration of the Aggenalm landslide that can result in failure. In addition, the results of the parameter variations present further possibilities that can cause the landslide to fail at a much lower water table, however, climatic conditions and/or the Kössen marls' properties would have to change in future for this.

In future, the continuing analyses of the time series recorded by the renewed version of the alpEWAS geosensor network will hopefully make it possible to also define the temporal delay between cause and effect, thus between precipitation and displacements, by means of time series analysis. Supplementary numerical simulations should also help to further improve and refine the understanding of the landslide's mechanism as well as the definition of threshold values for a catastrophic failure.

Zusammenfassung

Wegen der befürchteten Zunahme der Hangbewegungsaktivität im Kontext des globalen Klimawandels und der kontinuierlichen Ausdehnung von Siedlungsgebieten im Alpenraum, gewinnt die Überwachung von Hangbewegungen in den letzten Jahren immer mehr an Bedeutung. Die Überwachung von Hangbewegungen dient zum einen dazu, den zunehmenden Konflikt zwischen Landnutzung und Prävention von Naturgefahren zu minimieren, als auch dazu, die zu Grunde liegenden Hangbewegungsmechanismen als Basis für eine bessere Vorhersage und Prävention katastrophaler Ereignisse zu verstehen.

Im Rahmen des alpEWAS Projektes (Entwicklung und Erprobung eines integrativen Frühwarnsystems für instabile Hänge im alpinen Raum) wurde in den bayerischen Alpen an der Aggenalm Hangbewegung ein Monitoringsystem in einem Feldversuch aufgebaut, in dem sowohl innovative als auch etablierte Messsysteme Anwendung fanden. Neben Messeinrichtungen zur Überwachung der Deformationen an der Oberfläche (reflektorloses VTPS, kostengünstiges GNSS) kamen auch Systeme zur Aufzeichnung der Deformationen im Untergrund (TDR, Inclinometer) zum Einsatz. Des Weiteren wurden mögliche Triggerfaktoren wie Niederschlag und Porenwasserdruck überwacht. Von den verschiedenen Messsystemen liegen nun bereits seit dem Frühjahr 2009 Daten vor.

In dieser Arbeit wurde ein ganzheitlicher Ansatz für die Auswertung der Daten des alpEWAS Geosensornetzwerkes gewählt, um das geomechanische Modell zu verifizieren und ggf. zu verbessern, und um die Einflussfaktoren besser fassen und einschätzen zu können – mit der Absicht, Grenzwerte für ein Frühwarnsystem abzuleiten. Am Anfang stand die Recherche aller verfügbaren Informationen über den Aufbau und die Geologie, die Beschreibung historischer Hangbewegungsereignisse und weiterer Untersuchungen vor Ort im Fokus. Damit konnten neue Profilschnitte und ein detailliertes geomechanisches Modell entwickelt werden. Daraus abgeleitet kann die Aggenalm Hangbewegung nach CRUDEN & VARNES (1996) als „*complex, extremely slow rock spread-debris slide*“ bezeichnet werden, bei der sich anhand des Mechanismus zwei Bereiche differenzieren lassen. Im oberen Teil des Hanges, der durch Fels-Driften charakterisiert ist, sinken die steifen Oberrhätkalke und -dolomite in die darunterliegenden, sich plastisch deformierenden Mergel der Kössener Schichten ein. Weiter hangabwärts löst sich der Gefügeverband bedingt durch die fortschreitende Deformation mehr und mehr auf und es kommt zur Ausbildung einer Scherzone innerhalb der Kössener Schichten, so dass der Mechanismus in eine sehr langsame Schutt-Rutschung übergeht.

Im Anschluss wird ein Überblick über den Aufbau des Geosensornetzwerkes, seine Komponenten sowie deren individuelle Ergebnisse gegeben. Dabei konnten alle Messeinrichtungen verlässlich betrieben werden, vor allem nach der Installation der alpEWAS Control Software zur automatischen Datenerfassung, die auch die Möglichkeit der Fernabfrage bietet. Die Messungen der verschiedenen Sensoren an der Oberfläche ergaben sehr ähnliche Deformationsraten

von maximal 1 cm/a, während die Messungen der Deformationen im Untergrund keine signifikanten Ergebnisse erbrachten. Die Grundwasserspiegelschwankungen, gemessen mit dem verbleibenden Piezometer, konnten mit Niederschlagsereignissen sowie der Schneeschmelze parallelisiert werden. Da Schneeschmelze und Niederschlag als Hauptfaktoren für die Initialisierung von Hangbewegungen gesehen werden, werden diese Parameter und Zusammenhänge detailliert in Rahmen der Zeitreihenanalyse betrachtet.

Da die zeitliche Differenz zwischen Niederschlagsereignissen und dem Einsetzen von Bewegungen, gerade im Hinblick auf die Definition von Schwellenwerten für ein Frühwarnsystem von großer Relevanz ist, wurden mit Hilfe der Zeitreihenanalyse auch Niederschläge und Deformationsmessungen parallelisiert. Dabei konnte eine zeitliche Verzögerung zwischen Regenereignis und maximalem Grundwasserstand von 2,5 bis 2,75 Tagen ermittelt werden. Eine Beeinflussung der Bewegung konnte mit diesem Modell jedoch nicht nachgewiesen werden, wenngleich die Abhängigkeit der Bewegungsraten von Niederschlag respektive Grundwasserschwankungen an der Aggenalm Hangbewegung unbestritten ist.

Da es sich bei den gegenwärtigen Geschwindigkeiten von etwa 1 cm/a um sehr langsame Bewegungsraten handelt, lassen sich somit aus der Datenanalyse nur Schwellenwerte für sehr geringe Beschleunigungen ableiten. Daher werden Grenzwerte für Extremereignisse, möglicherweise für ein katastrophales Versagen, mittels einer numerischen Modellierung ermittelt. Das numerische Modell wurde unter Verwendung aller verfügbaren Daten aus der Detailkartierung, den Feldmessungen und der Datenanalyse im Code FLAC (Fast Lagrangian Analysis of Continua) von Itasca realisiert. Dabei konnte mit dem Anfangsmodell das Bewegungsverhalten, das durch das Monitoringsystem aufgezeichnet wurde, nachvollzogen werden und somit auch der Versagensmechanismus bestätigt werden. Durch die Simulation verschiedener Grundwasserspiegelhöhen kann gezeigt werden, dass das Grundwasser Extremwerte annehmen muss, ehe es zum Versagen kommt. Allerdings können auch andere Umstände zu einer erhöhten Bewegungsrate führen, wie die Ergebnisse der Parameterstudie zeigen. So kann es auch bei einem deutlich niedrigeren Grundwasserspiegel zum Versagen kommen, wenn sich die klimatischen Verhältnisse deutlich ändern und/oder sich die Eigenschaften der Kössener Mergel z.B. durch Verwitterung verschlechtern.

In Zukunft wird die weiterführende Analyse der Zeitreihen, die durch eine überarbeitete Version des alpEWAS Geosensornetzwerks bereitgestellt werden, es hoffentlich ermöglichen, die Zeitdifferenz zwischen Ursache und Wirkung – Niederschlag und Bewegungsrate – aufzuzeigen. Des Weiteren sollten zusätzliche numerische Simulationen helfen, das Verständnis des Hangbewegungsmechanismus noch weiter zu verbessern und zu verfeinern sowie den Schwellenwert für ein katastrophales Versagen noch exakter festzulegen.

Acknowledgement

This work was initiated already during my Master's studies, when the alpEWAS project started and I was asked by Prof. Kurosch Thuro and Dr. John Singer, if I wanted to write my Master's thesis about the evaluation of the geosensor network's data. However, due to several delays during installation, the topic was changed, nevertheless a strong connection to the alpEWAS project remained, especially because of the many hours attending the installation and helping dig, laying connection cables, and installing connectors, etc. Thus the initially planned topic was simply postponed and became the subject of this thesis.

I would like to thank Prof. Kurosch Thuro for giving me the opportunity to keep on working within the framework of the alpEWAS project and to write this thesis. His professional advice and support as well as the constructive discussions were strongly appreciated. I would also like to offer my special thanks to Prof. Michael Krautblatter for his valuable and constructive suggestions, especially during the final phase of this work.

My special thanks go to my colleagues in the alpEWAS team: Prof. Kurosch Thuro, Prof. Otto Heunecke, Prof. Thomas Wunderlich, Dr. John Singer, Stefan Schuhbäck, Dr. Peter Wasmeier, Jessica Glabsch, and Christoph Reith. Although the project officially ended in 2010, we have continued excellent cooperation in recent years, and have improved the monitoring system constantly, thus even leading to a refined version, alpEWAS 2.0. I am particularly grateful for the continuous discussions with John Singer and especially his tireless "tinkering" at the software's components, always with the aim to optimize the detection and evaluation processes. I also want to acknowledge the help by Christoph Reith, who not only introduced me to the methods of time series analysis but also helped finding a solution for all MATLAB-problems.

Furthermore, I would like to extend my thanks to my current and former colleagues at the Technische Universität München, Dr. Heiko Käsling, Dr. John Singer, Dr. Bernhard Lempe, Dr. Marion Nickmann, Silvia Beer, Florian Menschik, and Bettina Sellmeier. They always offered me help and advice, either while having lunch together or while actually working. A very special thank you goes to Silvia for all the discussions that encouraged me to keep on working on and finishing this thesis in the last months.

My sincere thanks also go to the families Zaglacher, Fürbeck, Bernthaler, and Keiss, the land owners and tenants of the Aggenalm, who not only let us install the alpEWAS monitoring system on their land but also helped proactively, especially Mr. Zaglacher, whenever we were in need of a tractor to haul heavy equipment or to save a stuck vehicle. Way too many students supported this work – either by helping during installation, maintenance, and with measurements and monitoring, or by writing their theses about certain aspects of the Aggenalm landslide – to be individually named in this place. However, special thanks go to Silvia Beer, Bettina Sellmeier, Thomas Brandhoff, Lisa Wilfing, Si-Yen Luu-Chucholowski, and Miriam Festl for carrying heavy equipment and conducting time-consuming inclinometer measurements.

None of this would have been possible without the strong support of my family and friends. Thank you for your support and encouragement, but also for the fun times in between long hours in front of my computer!

Thank You!

Table of contents

Acknowledgement	v
Table of contents	vii
List of figures	x
List of tables	xiii
List of acronyms and abbreviations	xiv
List of symbols	xvi
1. Introduction – motivation, project overview, and scope of study	1
1.1 Motivation.....	1
1.2 The alpEWAS project.....	2
1.3 Scope of study.....	4
2. Methodology	6
3. State of the art	8
3.1 Deep-seated gravitational movements	8
3.1.1 Overview of the research history of landslides.....	8
3.1.2 Classification and terminology of deep-seated landslides.....	10
3.2 Geosensor networks	14
3.3 Alarm/warning systems	15
3.4 Early warning systems	15
3.5 Methods of threshold derivation and landslide characterization	18
3.5.1 Time series analysis	18
3.5.2 Numerical modeling	20
4. The study site	23
4.1 Geographical setting	23
4.2 Climatic conditions at the study site	25
4.3 Tectonic overview and setting of the study site.....	27
4.4 Geological overview	30
4.5 Stratigraphy and lithological description.....	32
4.5.1 Triassic.....	32
4.5.1.1 Plattenkalk (bedded limestone)	32
4.5.1.2 Kössen formation (Kössener Schichten).....	32
4.5.1.3 Upper Rhaetian limestone and dolomite (Oberrhätalkalk & -dolomit)..	34
4.5.2 Jurassic.....	35
4.5.2.1 Allgäu formation (Allgäu Schichten, Fleckenkalk & -mergel).....	35
4.5.2.2 Siliceous Allgäu formation (Liaskieselkalk).....	35
4.5.3 Quaternary	35
4.5.3.1 Pleistocene.....	35
4.5.3.2 Holocene.....	36
4.6 The Aggenalm landslide	36
4.6.1 Historic events	37
4.6.1.1 The 1935 event – the Aggenalm landslide	38
4.6.1.2 The 1997 event – the Agggraben debris flow	41
4.6.1.3 Other landslide events	42

4.6.2 Morphologic features.....	43
4.6.2.1 The Aggenalm landslide.....	43
4.6.2.2 The Agggraben debris flow.....	47
4.6.2.3 Secondary mass movements.....	48
4.6.3 Field investigations.....	49
4.6.3.1 Extensometer and biannual geodetic survey (LfU).....	50
4.6.3.2 Reconnaissance borings.....	51
4.6.3.3 Geoelectric survey.....	52
4.6.4 Geological sections and landslide mechanism.....	54
4.6.4.1 Geological section by JUNG (2007).....	54
4.6.4.2 New geological sections and landslide mechanism.....	55
5. Monitoring system installed at the Aggenalm landslide.....	59
5.1 AlpEWAS measurement techniques.....	59
5.1.1 Surface measurements.....	60
5.1.1.1 Reflectorless video tacheometry (VTPS).....	60
5.1.1.2 Global navigation satellite system (GNSS).....	63
5.1.1.3 Additional deformation measurement systems on surface.....	65
5.1.1.4 Weather station.....	66
5.1.2 Subsurface measurements.....	67
5.1.2.1 Time domain reflectometry (TDR).....	67
5.1.2.2 Inclinator.....	70
5.1.2.3 Piezometer.....	72
5.2 Design of the alpEWAS geosensor network.....	73
5.3 Individual results of the different measurement systems.....	75
5.3.1 Reflectorless video tacheometry (VTPS).....	76
5.3.2 Global navigation satellite system (GNSS).....	77
5.3.3 Subsurface deformation measurements (TDR and inclinometer).....	79
5.3.4 Results of additional measurement systems.....	83
5.3.4.1 Crack meter.....	83
5.3.4.2 Weather station.....	84
5.3.4.3 Piezometer.....	85
5.4 Discussion of monitoring results.....	85
6. Time series analysis.....	87
6.1 Basic principle.....	87
6.2 Analysis approach.....	90
6.3 Data preparation.....	91
6.3.1 Filtering, smoothing, and sampling.....	91
6.3.1.1 GNSS data.....	91
6.3.1.2 Piezometer and rainfall data.....	92
6.3.2 Data gaps.....	93
6.4 Results.....	93
6.4.1 Visual examination and comparability of data sets.....	93
6.4.2 Correlation analyses.....	99
6.4.2.1 Correlation analyses of GNSS data.....	99
6.4.2.2 Correlation analyses of precipitation and piezometric data.....	101
6.5 TSA – threshold derivation and discussion of results.....	106

7. Numerical model of the Aggenalm landslide	109
7.1 Basic principles	109
7.1.1 Numerical modeling techniques	109
7.1.2 FLAC and the finite difference method (FDM).....	112
7.1.3 Mohr-Coulomb model	114
7.2 Modeling approach and strategy	117
7.3 Model setup.....	119
7.3.1 Geometry	119
7.3.1.1 Setup of grid	120
7.3.1.2 Implementation of material boundaries.....	121
7.3.1.3 Insertion of joints.....	121
7.3.1.4 Definition of boundary conditions	121
7.3.1.5 Implementation of water table.....	122
7.3.2 Material parameters	123
7.3.2.1 Properties of the Kössen marls – shear box testing.....	124
7.3.2.2 Joint properties	129
7.3.2.3 Seismicity	130
7.3.2.4 Properties of water tables	130
7.4 Results of parameter studies and sensitivity analyses	131
7.4.1 Parameter variations of Quaternary deposits and joints	131
7.4.2 Change of properties of marls and sensitivity analysis.....	134
7.5 Final model	137
7.6 Threshold derivation	140
7.7 Numerical modeling – discussion of results	144
8. Conclusion	146
9. Outlook and prerequisites for future projects	151
10. Bibliography	153
11. URL Resources	168

Appendices:

Appendix I: Geological map

Appendix II: Description of 1935 landslide

Appendix III: LfU geodetic survey, extensometers

Appendix IV: Boring logs and installation setup

Appendix V: Geoelectric survey – sections

Appendix VI: Results of inclinometer measurements – plots

Appendix VII: TSA – time series analysis, programming code

Appendix VIII: Time series plots and correlation diagrams

Appendix IX: Numerical modeling code

Appendix X: Direct shear test

List of figures

Figure 1: Schematic illustration of the alpEWAS integrative early warning system installed at the Aggenalm landslide. (...)	3
Figure 2: Four inter-related key elements, spanning hazard knowledge and vulnerabilities through to preparedness and response capability (...).	16
Figure 3: Simple scheme, illustrating the relation between physical, mathematical, and numerical systems. (...)	20
Figure 4: Location of the study site at the Aggenalm landslide.	23
Figure 5: Geographical overview of the eastern Mangfall mountain range. (...)	24
Figure 6: Geographical overview of the Aggenalm landslide and its closer vicinity. The hillshade of the area is overlain with the topographical map. (...)	24
Figure 7: Precipitation, snow height, and temperature over a time span of 3.5 years, starting January 1, 2009, for the Wendelstein observation station. (...)	26
Figure 8: Tectonic map of the Northern Calcareous Alps of the region between Lake Starnberg and Chiemsee. (...)	27
Figure 9: Tectonic map of the region between the Inn valley and the Lake Spitzing. (...)	29
Figure 10: Syncline and anticline structures as well as major faults surrounding the Aggenalm landslide. (...)	30
Figure 11: Geological map of the area surrounding the Aggenalm landslide uncovered of the Pleistocene and Holocene deposits. (...)	31
Figure 12: The outcrop of the Kössen formation at the toe of the landslide (...).	33
Figure 13: a) This photo shows the typical development of a well-bedded, light-gray colored Upper Rhaetian limestone (...).	34
Figure 14: 3d-model of the Aggenalm area, looking southwest. (...)	37
Figure 15: Hillshade model of the Aggenalm landslide (...).	38
Figure 16: The lower graph shows the daily rainfall (light blue) and the monthly summation curve (blue) at the Tatzelwurm observation station in 1935. (...)	41
Figure 17: The amount of precipitation at the Sudelfeld (Polizeiheim) weather station for the year 1997 is depicted in light blue. (...)	42
Figure 18: Morphological features in the area of the main scarp. (...)	44
Figure 19: a) Due to the light snow cover and shadowing the hummocky topography becomes visible. (...)	45
Figure 20: Tension crack within an Upper Rhaetian limestone block at the back of the landslide's over-steepened front. (...)	46
Figure 21: Exemplary damages at structure works inflicted by the movements (...).	47
Figure 22: View into the Agggraben debris flow from the connection road to Grafenherberg, looking west. (...)	48
Figure 23: a) Small debris flow at the southern edge of the Aggenalm landslide, looking at it from the Aggenalm hut (No. 1). (...)	49
Figure 24: This figure displays the location of the different measuring sites (...).	50

Figure 25: Displacement vectors of the geodetic survey with 21 measurement points along one central section across the Aggenalm landslide (...).	51
Figure 26: Exemplary boring log of borehole B3, located at the Lampl Alm.	52
Figure 27: Interpreted geoelectric profiles (location see Figure 24) (...).	53
Figure 28: Longitudinal cross section through the Aggenalm landslide, the exact location of the section is denoted in Figure 11 and Figure 24 (JUNG 2007).	55
Figure 29: Geological sections across the Aggenalm landslide based on the data and new information acquired (...).	57
Figure 30: Orthophoto of the complex, deep-seated Aggenalm landslide (...).	59
Figure 31: a) Photograph of the alpEWAS main sensor node (...).	62
Figure 32: GNSS sensor nodes installed at the Aggenalm landslide. (...)	64
Figure 33: Schematic depiction of the setup of a TDR measurement system for monitoring subsurface deformations. (...)	69
Figure 34: Top of the inclinometric measurement site at KB1. (...)	71
Figure 35: Structure of the alpEWAS Control software. (...)	74
Figure 36: The two main frames of the alpEWAS Live Viewer are pictured. (...)	75
Figure 37: Results of the VTPS measurements depicted as movement vectors of the detected target rocks. (...)	76
Figure 38: Results of the GNSS sensor nodes 1–3 for the time period February 2009 through December 2011 (...).	77
Figure 39: Movements at sensor GNSS 2 from mid-March to mid-August 2009. (...)	78
Figure 40: Exemplarily, the results from the TDR measurements in borehole B2 are displayed. (...)	80
Figure 41: Results of the inclinometer measurements from borehole B5. (...)	81
Figure 42: The photo on the left shows the Aggenalm hut. Major fissures in the walls of the building have been traced black for better visibility (...).	83
Figure 43: Graph of the precipitation, temperature and piezometer data recorded at the Aggenalm landslide from 2009 through 2011. (...)	84
Figure 44: Time series of the data from the GNSS stations 1–3 (Easting only), piezometer (B4, B6) and weather station (1-hour rainfall sums, rainfall summation curve, and outside temperature) for the years 2009, 2010, and 2011. (...)	95
Figure 45: Interpreted time series of the data from the GNSS sensors 1–3 (Easting only, filtered data and trend), piezometer (B4), and weather station (1-hour rainfall sums, rainfall summation curve, and outside temperature) for the time February 2009 through December 2011. (...)	96
Figure 46: Filtered and sampled (6-hour intervals) rainfall, pore water pressure, and displacement (Δ Easting in [mm]) of all three GNSS sensors (...).	98
Figure 47: Auto- and crosscorrelation diagrams of the GNSS data for 2010. (...)	100
Figure 48: Examples of auto- and crosscorrelations calculated from precipitation and piezometric data over two intervals of different length. (...)	102
Figure 49: Comparison of absolute pore water pressure and the calculated differenced pore water pressure (...).	103

Figure 50: Two sample crosscorrelations calculated from precipitation and pore water pressure data (...).	106
Figure 51: Basic calculation cycle in explicit solution schemes (...).	113
Figure 52: Mohr-Coulomb failure criterion represented in the σ_1 - σ_3 -plane (...).	115
Figure 53: Typical solution procedure in numerical modeling (...).	118
Figure 54: Setup of geometry and geology used as a basis for the simulation. (...)	120
Figure 55: Applied water tables, with w100 (light blue) representing the mean water table measured in B4. (...)	122
Figure 56: Results of the direct shear tests performed with the apparatus by Wille Geotechnik incorporating the results of eight tests (...).	127
Figure 57: Range of cohesion and friction angle of the Kössen marls considered in the sensitivity analyses depicted in a σ_n - σ_s -diagram.	129
Figure 58: X-displacement contour plot of the Aggenalm landslide after 100,000 steps before adjusting the properties of the Quaternary deposits. (...)	132
Figure 59: X-displacement contour plot of the Aggenalm landslide after adjusting the Quaternary deposits' properties (calculation over 100,000 steps). (...)	132
Figure 60: Y-displacement contour plot and displacement vectors (insert) for the slope's upper third after 100,000 cycles. (...)	133
Figure 61: Influence of Kössen marls' cohesion and angle of friction on the x-displacements, observed at 10 different observation points scattered across the slope after 100,000 calculation cycles.	134
Figure 62: Contour plots of the x-displacements applying a cohesion of 0 kPa for the Kössen marls (top), respectively 40 kPa (bottom) after 100,000 cycles. (...)	135
Figure 63: Contour plots of the x-displacements while applying a friction angle of 16° (top), respectively 31° (bottom) after 100,000 steps. (...)	136
Figure 64: X- and y-displacement contour plots of the verified numerical model. (...)	138
Figure 65: Displacement vectors of the Aggenalm landslide at selected areas. (...)	139
Figure 66: Plasticity indicators, displaying zones where yield in shear or tension occurs (after 100,000 cycles). (...)	140
Figure 67: Results of the numerical analysis applying a high water table, w14 (+9 m), while keeping all other parameters constant. (...)	141
Figure 68: X-displacements at the 10 observation points at different water tables. (...)	142
Figure 69: Total displacement (xy) plotted against water table height applying various friction angles of the Kössen marls (...).	143
Figure 70: Geological section across the Aggenalm landslide incorporating the new information acquired during the field investigations and also updated by the results of the numerical model. (...)	146
Figure 71: Enhanced hillshade model of the Aggenalm landslide (...).	147

List of tables

Table 1: The five main types of movement and their according velocities as classified by CRUDEN & VARNES (1996: 38, 50) (...).	12
Table 2: Activity of a landslide in accordance with WP/WLI (1993a, b).	13
Table 3: Mean annual precipitation (1931–1960 and 1961–1990) at different observation stations (...).	25
Table 4: Mean monthly precipitation (1931–1960 and 1961–1990) for the Brunnsteinhaus and the Sudelfeld (Polizeiheim) observation stations (...).	26
Table 5: Results from the crosscorrelation of precipitation and absolute and differenced pore water pressure. (...)	104
Table 6: Results of the crosscorrelation analysis of short data intervals (10–28 days) with no or negligible gaps. (...)	105
Table 7: Comparison of explicit and implicit solution methods. (...)	111
Table 8: Material parameters used in the numerical simulation (...).	123
Table 9: Collection of geotechnical parameters of Kössen marl and comparable soil and rock material as published by different authors.	125
Table 10: Joint parameters and parameter variations applied to the numerical model. (...)	130
Table 11: Material properties used in the verified and final model of the Aggenalm landslide. (...)	137

List of acronyms and abbreviations

This list defines acronyms and abbreviations used not only in the text but also in references and in the bibliography.

a.s.l.	above sea level
alpEWAS	Early Warning System for Alpine Instable Slopes
AVO	Almwirtschaftlicher Verein Oberbayern
BEM	boundary element method
BMBF	Bundesministerium für Bildung und Forschung (Ministry of Education and Research)
BMU	Bundesministerium für Umwelt, Naturschutz und Reaktorsicherheit (Federal Ministry for the Environment, Nature Conservation and Nuclear Safety)
BUWAL	Bundesamt für Umwelt, Wald und Landschaft (Swiss Agency for the Environment, Forests and Landscape)
CCD	charge-coupled device
CMOS	complementary metal-oxide-semiconductor
CNR IRPI	Consiglio Nazionale delle Ricerche, Istituto di Ricerca per la Protezione Idrogeologica (National Research Council, Research Institute for Hydrogeological Protection)
CP	carrier phase
CR	corner reflector
CSV	comma-separated value
DDA	discontinuous deformation analysis
DEM	discrete element method
DFG	Deutsche Forschungsgesellschaft (German Research Foundation)
DGM	Digitales Geländemodell (Digital Elevation Model)
DGSD	deep-seated gravitational slope deformation
DIN	Deutsches Institut für Normung (German Institute for Standardization)
D-InSAR	differential interferometric synthetic aperture radar
DKKV	Deutsches Komitee Katastrophenvorsorge e.V. (German Disaster Platform)
DSGSD	deep-seated gravitational slope deformation
DWD	Deutscher Wetterdienst (Germany's National Meteorological Service)
EWS	early warning system
FD	finite difference
FDM	finite difference method
FE	finite element
FEM	finite element method
FISH	FLACish
FLAC	Fast Lagrangian Analysis of Continua

GNSS	global navigation satellite system
GPS	global positioning system
GSN	geosensor network
GUI	graphical user interface
HDN	Humanitarian & Development Network
IAEG	International Association of Engineering Geology
IATS	image-assisted total station
IDNDR	International Decade for Natural Disaster Reduction
ILEWS	Integrative Landslide Early Warning Systems
ISRM	International Society for Rock Mechanics
LAN	local area network
LfU	Bayerisches Landesamt für Umwelt (Bavarian Environment Agency)
MC	Mohr-Coulomb
MEMS	micro-electro-mechanical systems
NRTP	near-real-time processing
OcCC	Organe consultatif sur les Changements Climatiques (The Advisory Body on Climate Change)
PDGNSS	precise differential GNSS
PFC	Particle Flow Code
PLANALP	Platform on Natural Hazards of the Alpine Convention
PS	persistent scatterer
RS-232	recommended standard
SLEWS	Sensor-based Landslide Early Warning System
SMS	short message service
SQL	Structured Query Language
TDR	time domain reflectometry
TSA	time series analysis
TUM	Technische Universität München (Technical University Munich)
UDEC	Universal Distinct Element Code
UN	United Nations
UNEP	United Nations Environmental Programme
UNESCO	United Nations Educational, Scientific, and Cultural Organization
UniBw Munich	Universität der Bundeswehr München (University of the Federal Armed Forces Munich)
UNISDR	United Nations International Strategy for Disaster Risk Reduction
USGS	U.S. Geological Survey
VTPS	reflectorless video tacheometer
WLAN	wireless local area network
WP/WLI	Working Party on the World Landslide Inventory (International Geotechnical Societies and UNESCO)
WSN	wireless sensor network
WWA	Wasserwirtschaftsamt (Water Management Office)

List of symbols

A	area of shear plane	Δ	difference/increment
A_{red}	reduced area of shear plane	α	inclination of probe
C_{XX}	autocovariance	α_1, α_2	factors
C_{XY}	crosscovariance	α^P, σ^P	constants
E	Young's modulus/expected value	μ	mean
G	shear modulus	ν	Poisson's ratio
K	bulk modulus	ρ	density
L	liter/basis length of probe	σ	stress/standard deviation
N	normal load	$\sigma_1, \sigma_2, \sigma_3$	principal stresses
N_{ϕ}, N_{ψ}	factors	σ_{zz}	out-of-plane stress
S	shear force	τ	lag
T	number, integer values $\in \mathbb{N}_0$	ϕ, φ	friction angle
X, Y	random variables	φ'	effective friction angle
XS	cyclic part of variable	φ_{res}	residual friction angle
XT	trend of variable	ψ	dilatancy, dilation angle
XR	random part of variable	\emptyset	diameter
Super- and subscripts			
a_g	ground acceleration	e	elastic
c	cohesion	max	maximum
c'	effective cohesion	min	minimum
c_{res}	residual cohesion	n	normal
d	displacement	p	plastic
e₁, e₂, e₃	principal strain elements	res	residual
f	yield function	s	shear
g	potential function	t	tensile
h	height	tot	total
i	integer values, $\in \mathbb{N}_0$		
k	stiffness		
l	length/displacement		
m_w	wet mass		
n	number, integer values $\in \mathbb{N}_0$		
r	radius		
t	time /timestep/point in time		
w	water content		
z	width		

1. Introduction – motivation, project overview, and scope of study

1.1 Motivation

Only a decade into the twenty-first century, several natural disasters have already been declared once-in-a-hundred-years events. The year 2003 was characterized by heatwave and drought, known as the century's summer. Only two years later, in 2005, extreme rainfall and flooding – the so-called hundred year flood – led to landslides¹ as documented in the Alps (GORE 2006: 75, KEUSEN 2006: 58, 60). Almost every year somewhere in Europe, sometimes only local, sometimes at a regional or national scale, heavy precipitation leads to flooding and often initiates mass movements. Within Germany and the neighboring Alpine countries, not just the two above-mentioned events were categorized as once-in-a-hundred-years events. The Danube and Elbe catchment floods in 2002, the Elbe catchment flood in 2006, the flooding in Switzerland in 1999 as well as in 2007 and 2009 in Central Europe, especially Austria, fell into this category (LATELIN et al. 2001: 159, ALCAMO et al. 2007, PLANALP 2012: 5f.). Most recently, heavy rainfall in the beginning of June 2013 caused extreme flooding in Germany, Austria, and the Czech Republic, also initiating numerous landslides, mostly earth and debris flows.

Do such phenomena still occur within normal limits, or is it intensifying because of climate change? In the context of climate change, the increase of the mean annual temperature is accompanied by permafrost degradation, thus leading to a destabilization of rock mass and therefore to a higher susceptibility for the initiation of landslides such as rock falls, debris flows, slides, etc. (HAEBERLI & MAISCH 2007: 104f., HUGGEL et al. 2012: 87ff., GRUBER & HAEBERLI 2007). In their studies regarding the influence of climate change on landslides, BMU (2008), PARRY et al. (2007), OCCC (2008: 17ff.), and SCHÖNWIESE (2007: 63f.) point out that the expected shift in rainfall/snowfall distribution patterns may enhance landslide activity. These patterns are characterized by less rain during summer and more precipitation during fall through spring, and also more severe precipitation events.

Expanding settlement and increasing development in landslide-prone areas enforce the conflict between land use and hazard prevention, leading to high social and economic damages (PETLEY 2012). Though the awareness of landslide hazards has risen and many hazardous areas are detected early, particularly by national and regional hazard mapping programs,² and can be monitored, in reality few active mass movements are monitored. Fewer still are instrumented with a

¹ In this thesis the term *landslide* is used to denote “the movement of a mass of rock, debris or earth down a slope” (CRUDEN 1991: 27) regardless its type of mass or type of movement.

² The Alpine countries, Austria, France, Germany, Italy, Liechtenstein, Monaco, Slovenia, and Switzerland, obligated themselves in an international treaty – *The Alpine Convention* aiming to promote sustainable development and protect the natural environment in the Alps – to create hazard maps of Alpine areas and to designate danger zones when necessary (www-01: cue “soil conservation”). For instance, in Bavaria, the Bavarian Environment Agency (LfU) is responsible for the realization of this directive (LfU 2009a, b).

permanent continuous monitoring system. High costs and time-consuming measurements may contribute to the low use of monitoring systems at this time. The increasing conflict due to sprawling settlement areas requires an even better understanding of climatic influences, mass movement mechanisms and monitoring systems and their further development. Thresholds for the development of an early warning system (DKKV 2010) can be derived and determined only with an accurate grasp of processes and sufficient monitoring data on a local and/or regional scale.

1.2 The alpEWAS project

The Chair of Engineering Geology and the Chair of Geodesy of the Technische Universität München (Technical University Munich, TUM) as well as the Institute of Geodesy of the Universität der Bundeswehr München (University of the Federal Armed Forces Munich, UniBw Munich) successfully applied for a joint research project for the development and testing of an integrative 3D early warning system for alpine instable slopes (THURO et al. 2006). The project's funding (2007–2010) was provided by the special geoscientific research and development program 'Geotechnologien' of the Federal Ministry of Education and Research (Bundesministerium für Bildung und Forschung, BMBF) conjointly with the German Research Foundation (Deutsche Forschungsgesellschaft, DFG). The alpEWAS research project (Early Warning System for Alpine Instable Slopes) aimed to "... integrate innovative, efficient and cost-effective measurement techniques for landslide monitoring [and early warning] into a geo sensor network" (FESTL et al. 2012: 907).

The main foci of the alpEWAS project are three different innovative deformation measurement techniques; each primarily performed and worked on under the auspices of one of the three project's partners. As one main part of the geosensor network (Figure 1), a low-cost global navigation satellite system (GNSS) determines the movements on surface at selected points with high accuracy. A reflectorless video tacheometer (VTPS) observes on-surface movements over a major area and subsurface deformations are monitored by a newly developed time domain reflectometry (TDR) system installed in boreholes. Rainfall, snowfall, and temperature data sets are also gathered by a weather station. The pore water pressure – or rather, the water table – is detected using piezometers (www-02).

The Aggenalm landslide, located at the edge of the Sudelfeld skiing area near Bayrischzell, was chosen as an appropriate site to install and test the functionality of the geosensor network and its components. According to THURO et al. (2007: 101f.) yearly displacements of about 2 cm and a depth of the sliding surface of approximately 25 m, should allow researchers to detect deformations after short time span and detecting first thresholds to issue a warning.

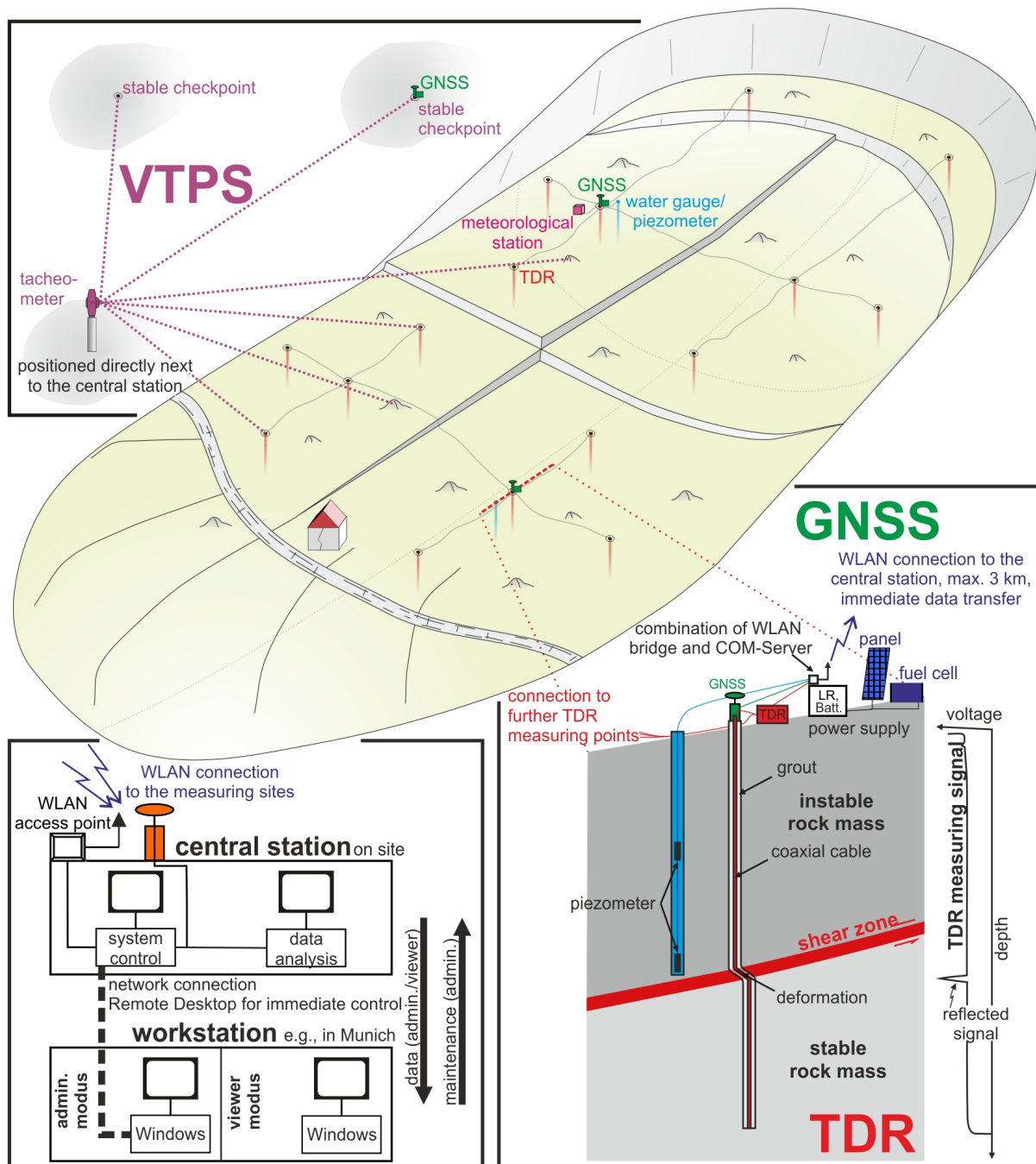


Figure 1: Schematic illustration of the alpEWAS integrative early warning system installed at the Aggenalm landslide. GNSS (global navigation satellite system; e.g., GPS and GALILEO) and TDR (time domain reflectometry) continuously gather punctiform information about movements on and below surface, respectively. The VTPS (reflectorless video tacheometer) also gains information about on-surface displacements, covering great parts of the landslide. Triggering factors, such as precipitation and pore water pressure are measured by a weather station and piezometers. With the combination of all the gathered data, quantitative causal and temporal relations between triggers and displacements can be deduced. The measured data are transmitted to the central station via WLAN and stored in a central database. The data can easily be accessed and downloaded remotely (for instance, from a workstation in the office) for further analysis and interpretation. (Adapted from SINGER et al. 2006: 22, Fig. 5)

The alpEWAS project (THURO et al. 2011a) was consecutively followed by an add-on project called alpEWAS-Markt (THURO et al. 2011b), during which certain components of the geosensor network were further developed to marketability. Since the end of the funding phases of these projects at the end of 2010, the alpEWAS test site – the Aggenalm landslide – continues to be monitored and up until now has worked as a field test site.

1.3 Scope of study

For an early warning system to be able to issue a reliable warning, it is necessary to have an accurate geological model and, preferably, to fully understand the underlying processes of the landslide. Whether at a regional or local scale, data concerning the triggering factors, such as rainfall, snowfall/snowmelt, and/or pore water pressure, as well as data of movement rates, are essential to identify thresholds for early warning. Therefore the aim and scope of this thesis is a holistic interpretation and analysis of the data collected throughout the alpEWAS project and within its framework so as to derive appropriate thresholds for an early warning system.

In their guideline on process-oriented analyses on landslides, ZANGERL et al. (2008) suggest a working scheme for a holistic analysis approach that consists of six modules, which are largely based on each other. All parts of this guideline are included in this thesis, though the focus is laid on modules 4 (triggers, stabilizing and accelerating factors), 5 (numerical modeling), and especially module 6 (data analysis and interpretation).

In order to achieve a holistic interpretation and proper thresholds, the following main steps were taken and had to be accomplished:

- Evaluating existing investigations of the Aggenalm landslide and presenting the geological inventory of the study site.
- Researching historic events to improve the understanding of the landslide's mechanism and trigger, as well as to help interpret results of the data analysis and numerical model.
- Attending the build-up of the alpEWAS monitoring system, logging and sampling drill cores, documenting the installation procedures, etc.
- Verifying, respectively implementing all attained data into a geological model.
- Conducting periodic measurements of inclinometers and crack meters, etc.; analyzing and putting them into context.
- Interpreting data retrieved by the automatic monitoring system individually and combined by means of time series analysis, e.g., autocorrelations and crosscorrelations, with the aim to derive thresholds.
- Performing laboratory tests and researching material properties in order to set up a numerical model of the landslide.

- Adjusting the numerical model by means of parameter studies to represent the currently observed movement rates realistically.
- Deriving thresholds for extreme events using the verified numerical model.

2. Methodology

Prior to the installation of the geosensor network at the Aggenalm landslide, several studies examined the geology as well as the landslide's mechanism and deformation rate (SCHORMAIR 2003, JUNG 2007, GALLEMANN 2012). The results of these studies led to a first model of the Aggenalm landslide (Chapter 4.6.4.1 on page 54f.). Accordingly, the layout for the installation of the geosensor network was made. First, as a basis for all the following considerations, this dissertation describes the Aggenalm landslide, especially its morphological and structural features (Chapter 4.6.2 on page 43ff.). New, additional information concerning the substratum was gathered by evaluating the drill cores at seven sites scattered across the slope, as well as through a geoelectric survey along several profiles (two cross sections and one longitudinal section) (Chapter 4.6.3.2 and 4.6.3.3 on page 51ff.). Documents describing historic mass movement events at the Aggenalm landslide (Chapter 4.6.1 on page 37ff.) and the survey data from the LfU (Bavarian Environment Agency) as well as the newly attained data from the monitoring system are interpreted. All this newly acquired geological knowledge and monitoring data led to an advancement of the geological model and a better characterization of the landslide's processes (motion model), graphically presented by several geological sections of the landslide body and discussed in Chapter 4.6.4 on page 54ff.

Since the testing and advancement of each of the three main systems has been the major aim of an individual doctoral thesis, which has already been conducted or is currently underway, the measurement techniques themselves will only be summarized shortly after a brief description of the sensor network's layout (Chapter 5.1 & 5.2 on page 59ff.). Thereby WASMEIER (2009) mainly focused on the development of the VTPS, while SINGER (2010) worked on the improvement of the TDR system (both TUM) and Schuhbäck's thesis on the GNSS component is still in progress (UniBw Munich). The present thesis focuses on evaluating the individual results of all the geosensor network's components with respect to the landslide's processes as well as to the geological model (Chapter 5.3 on page 75ff.) but also on combined analyses. An illustration of the results of time series analysis follows an explanation of the basics of time series analysis and data preparation methods (filtering, sampling, etc.) (Chapter 6 on page 87ff.). Analyses of the various GNSS data and comparing them among one another contribute to the understanding of the landslide's model and its movement characteristics. By evaluating rainfall, pore water pressure, and GNSS displacement measurements, especially calculating crosscorrelations between these data sets, first thresholds for the onset/increase of movement rates are derived (Chapter 6.4 on page 93ff.).

As it is essential for an early warning system to define thresholds also for the onset of greater movement rates (as they are currently observed), a numerical model was set up to analyze extreme events. Chapter 7 (on page 97ff.) outlines the methodology of the numerical code FLAC 2D and describes the model setup and the attainment of material properties. Before calculating an extreme event, the model is verified by conducting parameter studies so as to best

represent the currently observed movement rates and patterns. The affirmed model is then used to simulate extreme water tables and evaluate movement rates for the derivation of thresholds (Chapter 7.5 and 7.6 on page 137ff.).

Chapter 8 (on page 146ff.) summarizes the full results attained by the different analysis techniques pertaining to the landslide's mechanisms and the early warning system and contains a concluding discussion. Finally, perspectives for further research and possible advancement of the developed models as well as a short list of prerequisites for the setup of such systems at a local scale, is given (Chapter 9 on page 151f.). The Appendix contains additional information on the data, analyses and modeling codes described and used within this thesis.

3. State of the art

Since landslides, their mechanisms and monitoring and also hazard prevention, are such a wide research field, an abundance of literature and research projects concerning these topics exists (GOKCEOGLU & SEZER 2009: 345). As this thesis is about a holistic analysis of the gathered monitoring data in respect to deriving thresholds for an early warning system, the following will mostly concentrate on similar exemplary projects concerned with deep-seated gravitational movements, rainfall-induced landslides, their monitoring systems, and/or similar analysis methods.

3.1 Deep-seated gravitational movements

The term *landslide* has been defined quite concisely by CRUDEN (1991: 27) as “the movement of a mass of rock, debris or earth down a slope” regardless its type of mass or movement. Even though the word *landslide* can be confusing, when considering the individual parts of the word (*land* might suggest ‘granular soil’, *slide* a ‘sliding movement process’ as noted by CRUDEN (1991: 27) and CRUDEN & VARNES (1996: 36)), it became well established in the research community as an overarching term referring to all movement and material types. In the present work, therefore, the term *landslide* and interchangeably *mass movement* is used in the sense of Cruden’s definition.

3.1.1 Overview of the research history of landslides

The systematic scientific investigation of landslides within the field of geosciences has been launched quite late, at the turn of the nineteenth to the twentieth century (RIEDMÜLLER 2003: 13). Only very few useful reports and descriptions predate this time, e.g., the report by ZAY (1807) on the Rossberg landslide (Goldau, Switzerland), the description of the Bindon landslide of 1839 in England (TURNER & JAYAPRAKASH 1996: 6f.), the book by BALTZER (1875) on several large landslides in the Alps, and the very detailed documentation by BUSS & HEIM (1881) and HEIM (1882a) of the catastrophe at Elm, Switzerland, in 1881. This seems really late, considering that also during earlier times, mass movements endangered and affected agriculturally used and populated areas (even though not as densely populated as today), oftentimes entailing fatalities (e.g. HEIM 1882b). The Industrial Revolution, especially from the middle of the nineteenth century onwards, seems to be one of the major reasons for the change (TURNER & JAYAPRAKASH 1996: 4f.). A concomitant rapidly advancing development of sensitive and vulnerable infrastructure (canals, railways, skiing infrastructure, etc.) and the increasing settlement in endangered areas (e.g., mountain slopes and valleys) placed new importance on slope instabilities and thus increased the general awareness of the public to possible dangers arising as well as established the systematic scientific research of landslide types and processes.

Among the first authors who targeted the topics of geological problems of natural hazards, in particular mass movements, was Albert Heim at the onset of the twentieth century, best known for his work *Bergsturz und Menschenleben* (HEIM 1932). He was already engaged in his research on mass movements since the late 1800s and was by then a respected expert in the field of landslide interpretation and analysis, for example through his contributions on the catastrophes in Elm, in 1881 (BUSS & HEIM 1881, HEIM 1882a), and in 1887 in Zug, Switzerland (known as the *Vorstadtkatastrophe* of Zug, N.N. & HEIM 1887), as well as on the Campo Vallemaggia landslide, Switzerland, in 1897 (HEIM 1932: 49ff., EBERHARDT et al. 2007). Another early contributor to the research on natural hazards was Josef Stini³, whose monograph about debris flows (in the sense of CRUDEN & VARNES's (1996: 64ff.) classification) was published in 1910 (STINÝ 1910) and who continuously conducted research in the field of slope instabilities. In the following decades landslides continued to be investigated more and more in detail as were their underlying processes and mechanics. Important publications about mass movements and their underlying mechanics – from the perspective of an engineer – were published, for instance, by TERZAGHI (1925, 1947, 1950), STINÝ (1938a), and STINI (1952a).

Deep-seated⁴, large-area landslides, often moving slowly and rather continuously over long time spans, without catastrophic failure that could not be referred to known landslide mechanisms, have been described in literature only since the late 1930s in detail. Although such mass movements have already been mentioned earlier, e.g., in HEIM (1919: 685ff., 1921/1922: 806ff.) and STINÝ (1929), the first detailed descriptions of the phenomena and initial considerations concerning the processes of such mass movements were published by AMPFERER (1939, 1940, 1941) and STINI (1941, 1942, 1952b), who introduce the terms *Bergzerreißung*, respectively *Talzus Schub* for such large-scale movements (see Chapter 3.1.2). In the following years, the number of publications in the broad field of mass movements – its various forms and processes – increased rapidly, so that only a few works will be mentioned in the following as well as in the subsequent subchapter, exemplarily. Several authors, such as JAHN (1964) and ZISCHINSKY (1968, 1969), focus on the understanding of the causes and the processes of such deep-seated landslides. A good overview of the development of research in this field is given, for example, by DRAMIS & SORRISO-VALVO (1994) and IMRE et al. (2009). CROSTA et al. (2013) have compiled an inventory of deep-seated gravitational mass movements, containing more than a 1,000 case histories in the European Alps (Austria, France, Italy, and Switzerland). Aim of compilation has been to analyze their occurrence in respect to a variety of geological, geomorphological, and morphometric variables, and to find the most important controlling and predisposing factors of such deep-seated slope deformations. Many individual case studies, concerned with the processes and/or the monitoring or risk assessment of individual deep-seated

³ Josef Stiný (Stiny) changed the spelling of his last name to Stini, but never had it officially changed by the authorities. In this text the spelling Stini will be used unless referencing publications with the previous old spelling (KIESLINGER 1957: 389).

⁴ Nowadays a sliding or flowing (creeping) mass movement (in accordance with the classification by CRUDEN & VARNES 1996) is referred to as deep-seated if the landslide's surface of rupture is at a depth greater 10 m, or if its body's thickness is greater 10 m, respectively (HEINIMANN et al. 1998: 38).

mass movements, exist today (e.g., VARNES et al. 1989, WEIDNER (2000), BRÜCKL & BRÜCKL 2006, WILLERICH 2013, GRANA & TOMMASI 2014).

Regardless of the type of landslide, a variety of causes and triggers must be considered as possibly preparatory or triggering factors. Preparatory effects and causes of landslides can be quite diverse. They can be of geological, morphological, physical, and human nature or of any combination of these (WIECZOREK 1996: 76ff., CRUDEN & VARNES 1996: 70). Whereas only one of several external stimuli – such as earthquake shaking, volcanic eruption, storm waves, and intensive rainfall and/or rapid snowmelt – can be the trigger of the mass movement (VARNES 1978: 26). In their book *Destructive Mass Movements in High Mountains*, EISBACHER & CLAGUE (1984) summarize more than a hundred case histories concerning mass movements in the European Alps with different causes and triggers. VITA et al. (1998) compiled a reference list of rainfall-triggered landslides worldwide containing more than 450 entries, most of them discussing shallow landslides rather than deep-seated mass movements. In the last 15 years, a vast number of published journal articles, books, proceedings, etc., have introduced case studies of mass movements in which often rainfall and snowmelt seemed to be of importance and thought to be the trigger (VAN ASCH et al. 1999, AGLIARDI et al. 2009, PROKEŠOVÁ et al. 2013).

3.1.2 Classification and terminology of deep-seated landslides

In early years of landslide research, no consensus existed concerning the terminology used to describe the landslide's phenomena and mechanisms. Therefore a correct translation to modern terminology and classes is not always easy nor even possible. Up to the 1930s, only the discrimination between the basic modes of motion *fall*, *slide*, and *flow* existed. These types are still part of all modern classification systems, however, supplemented by the modes *topple* and *spread* (Table 1). Additionally, several authors, for instance HEIM (1882b: 4, 1932: 14ff.) and STINÝ (1910: 1) distinguished the material, dividing it into two categories: earth/debris and rock. This left several mass movements uncategorized or they were put into the category of mixed or special movements (HEIM 1882b: 22).

AMPFERER (1939) introduced the term *Bergzerreißung* (translated as 'mountain splitting') to describe large-scale, deep-seated and slowly moving landslides, which didn't fit into any of the known categories at the time. He realized that such movements – characterized by structures such as double ridges, tension cracks, multiple scarps, counter slopes and uphill facing scarps, gradation, bulging, and a generally strongly dissected morphology over the complete slope – are not special, but a common and widely spread phenomenon in the Alps (AMPFERER 1940: 51). They often affect entire mountain flanks, especially at valley flanks steepened by glacial activity (IMRE et al. 2009: 277). Ampferer also points out that over large areas the original structures remain and are moved more or less en block, thus no or only slight changes in their orientation might occur. Even though Ampferer's definition of mountain splitting referred to the complete process from top to bottom, it is nowadays rather used to only describe the

initiation of such deep-seated landslides with the progressive opening (splitting) of cracks, particularly at the top.

In STINI (1929), he has already described sliding processes of greatest extent that occur in mountainous areas and lead to a coalescing of valleys. Stini attributed the movements to an unbalanced gradient of mountain slopes. Later, in STINI (1941, 1942), he takes up on this topic again, coining the term *Talzus Schub* (translated as ‘closing-up of the valleys’), which basically amounts to the original description of mountain splitting by AMPFERER (1939), but better describes the most concise phenomenon – the bulging at the toe – as Stini puts it (STINI 1941: 72). Just as Ampferer, Stini was mostly concerned with the description of the morphological phenomena of such deep-seated landslides, which he had observed mainly at steep mountain slopes, oftentimes predisposed by unfavorable discontinuities (STINI 1952a). Several times he emphasized their vague as well as disguised morphological features (STINI 1941: 71f., STINI 1942: 80f.), as a result of the small movement rates.

While Ampferer and Stini described the morphological features of *Bergzerreißung* or *Talzus Schub* quite detailed, they hardly weren’t concerned with the underlying processes and mechanisms of such mass movements, on which ZISCHINSKY’S (1968, 1969) publications later focused. Zischinsky included considerations on mechanical and kinematic processes (e.g., variable movement patterns, deformation rates and processes in context of creep of solids under load) and again introduced the new term *Sackung* (translated as ‘sagging’) to describe such movements that STINI (1941) called *Talzus Schub*. Both these terms continue to be used to date, despite the new terminologies and classification systems established more recently. In the 1980s, yet again a new, more neutral term *deep-seated gravitational slope deformation*, abbreviated as *DSGSD* (e.g., in AGLIARDI et al. 2009, CROSTA et al. 2013) or *DGSD* (e.g., in DRAMIS & SORRISO-VALVO 1994, IMRE et al. 2009), became established in international literature to describe mass movements in the sense of STINI’S (1941) and ZISCHINSKY’S (1969) definition of *Talzus Schub* and *Sackung*.

The ever increasing literature not only on deep-seated mass movements, but on landslides in general, showed the need for a unified classification system, one of which was first introduced by VARNES (1978), with a few changes and revisions in the years following. Due to the also confusing, complex and variable terminology used up to this point, a standardized, internationally acknowledged nomenclature, based on VARNES (1978) and HUTCHINSON (1988) was agreed on and published in IAEG (1990) in English as well as in French. Only three years later the International Geotechnical Societies’ UNESCO Working Party for World Landslide Inventory (WP/WLI 1993a) added translations of this standard terminology into Spanish, German, Russian, and Chinese. Additionally, they authored recommendations on how to report a landslide and its causes (WP/WLI 1990, 1991, IAEG 1994), but also on how to describe its activity and rate of movement (WP/WLI 1993b, IAEG 1995).

Table 1: The five main types of movement and their according velocities as classified by CRUDEN & VARNES (1996: 38, 50) (adapted from ZANGERL et al. 2008: 18, Fig. 14).

Class	Description of velocity	Velocity limit [mm/s] (typical velocities)	Type of movement					
			Fall	Topple	Slide	Flow	Spread	
1	Extremely slow	5×10^{-7} (16 mm/a)				Soil flow	Rock flow	
2	Very slow	5×10^{-5} (1.6 m/a)						
3	Slow	5×10^{-3} (13 m/month)						
4	Moderate	5×10^{-1} (1.8 m/h)						
5	Rapid	5×10^1 (3 m/min)						
6	Very rapid	5×10^3 (5 m/s)						
7	Extremely rapid							

Complex*

*If a landslide is composed of two or more of the 5 movement types (for instance, *rock fall* at the top evolving into a *debris flow* downslope), the descriptor *complex* can be added to indicate the sequence of movement in the landslide and to discern it from the *composite* types.

CRUDEN & VARNES (1996: 37ff.) based their classification on VARNES (1978), while keeping a consistency with the terminology and methods suggested by the UNESCO WP/WLI. This process-oriented classification takes into account the type of movement (discerning five types: fall, topple, slide, flow and spread) and material (rock and soil, soil subdivided in earth and debris), which together make up the name (classification) of the landslide (Table 1). In addition, descriptors, such as velocity (rate of movement), activity (Table 2), and relevant water content, can be added to get a more elaborate name of a landslide. The sixth name *complex* that was part of the VARNES's (1978) classification, has been removed from the name forming types of movement, but has been retained as an additional description, to indicate a sequence of movements.

Talzus Schub and Sackung can now, using the classification by CRUDEN & VARNES (1996), be described more detailed solely by its name. According to this classification, large, deep-seated gravitational mass deformations often fall into the category of complex, thus sequential movements. For instance, evolving from an extremely to very slow flow (creep) to a slide earning the name *complex, very slow rock flow-rock slide*, to which additional descriptors can be added,

if applicable. Usually, slides, spreads, or flows, or any combination of these describe the processes of a sagging best, with the modes often depending on the lithology as well orientation and strength of discontinuities in the displaced rock mass. Spreads are often found when massive, strong rocks are underlain by weak rocks, such as marls. In metamorphosed rocks, with pronounced foliation, schistosity, or cleavage, or hard, but fractured, crystalline igneous rocks, flows and slides dominate. (VARNES et al. 1989: 1f.)

Table 2: Activity of a landslide in accordance with WP/WLI (1993a, b).

Activity class	State of activity	Description of activity
1	Active	Landslide is currently moving
2	Suspended	Landslide has moved within the last 12 months but is not active (1) at present
3	Reactivated	Landslide, which has been inactive (4), is currently active (1)
4	Inactive	Landslide has not moved within the last 12 months and can be subdivided into states 5–8
5	Dormant	Landslide is inactive (4), but can be reactivated (3) by its original or by other causes
6	Abandoned	Landslide is inactive (4) and is no longer affected by its original causes
7	Stabilized	Landslide, which has been protected from its original causes by artificial remedial measures, is inactive (4)
8	Relict	Landslide, which developed under climatic or geomorphological conditions considerably different from those at present, is inactive (4)

Even though this classification is nowadays widely used and accepted, the older terms *Talzus Schub* and *Sackung* are still being used, particularly in German literature. Internationally, the describing terms *DSGSD* and *DGSD* are still common. Additionally, since 1996, several authors (e.g., CRUDEN & COUTURE 2010 and HUNGR et al. 2014) suggested minor changes, most of them additions and more precise subdivisions to the classification by CRUDEN & VARNES (1996). It has been proposed to subdivide the materials involved in greater detail and to add ice and additional states of activity to the descriptions (CRUDEN & COUTURE 2010: 1034ff.). HUNGR et al. (2014) describes the different classes very detailed and also adds three new ones (compared to the ones used by CRUDEN & VARNES (1996) that result from combining material and type of movement in all possible ways). Hungr et al. add the group ‘slope deformation’ which, by their scale/size, can be sub-classified into the two categories ‘mountain slope deformation’ and ‘rock slope deformation’ to describe large-scale gravitational deformations with extremely slow movement rates (HUNGR et al. 2014: 189f.). At the same time, he notes

that such slope deformations may sometimes be better described by their old names (e.g., *rock spread-debris flow*) in accordance with the classification by CRUDEN & VARNES (1996).

This overview of the development of description and terminology for landslides, in particular for deep-seated mass movements, shows its complexity and the diverse problems finding a classification that meets all requirements. Although a few changes and additions have been added to CRUDEN & VARNES's (1996) classification, ambiguities still remain where different types evolve from one to another without a well-defined boundary, which most often applies to deep-seated landslides. Therefore, within this thesis, the terminology and classification following WP/WLI (1993a) as well as CRUDEN & VARNES (1996) will be used, as it is still the most-widely spread and internationally accepted classification.

3.2 Geosensor networks

For mitigation and hazard prevention purposes, or in order to better understand the underlying processes of a landslide, individual mass movements or whole landslide-prone areas are often instrumented with miscellaneous measurement sensors. Most commonly, measurement techniques survey movements of a landslide above or below surface, as well as other geotechnical, hydrological and meteorological sensors, with the aim to monitor movement rates or patterns and triggering factors, such as rainfall. If more than one sensor is being used, they are often interlinked to a geosensor network (GSN) or wireless sensor network (WSN) if the node's connection is wireless based. SOHRABY et al. (2007: 1) define such a WSN as

“... an infrastructure of sensing (measuring), computing, and communication elements that gives an administrator the ability to instrument, observe, and react to events and phenomena in a specified environment⁵ [and which should be comprised of these] four basic components:

1. an assembly of distributed or localized sensors;
2. an interconnecting network (usually, but not always, wireless-based);
3. a central point of information clustering; and
4. a set of computing resources at the central point (or beyond) to handle data correlation, event trending, status querying, and data mining.” (SOHRABY et al. 2007: 1)

Many modern GSNs not only allow a data flow through the network to a main computing station, but work bi-directionally, enabling an administrator to control sensor activity, such as altering data acquisition frequencies.

⁵ In case of a geosensor network (GSN) the *specific environment* refers to a *geographic space*, which can be a ‘confined environment, such as an individual landslide or an entire ecosystem region’ (NITTEL et al. 2008).

All the techniques used and installed during the alpEWAS project were integrated in such a bi-directional GSN, which itself was developed in the course of the project (SINGER 2010: 137ff.). Even though many different components or systems are available on the market, they still almost always have to be adapted to or even purposely designed for the individual monitoring tasks at the specific landslide (INTRIERI et al. 2012: 125). The Illgraben debris flow in Switzerland utilized geophones (GRAF et al. 2007, BADOUX et al. 2009), while at the Dollenhofner Hardt landslide in Germany GARCÍA et al. (2010) integrated high resolution tiltmeters amongst many other detection systems into such a sensor network. However, the alpEWAS GSN was the first monitoring system to include the time domain reflectometry (TDR) deformation measurement technique while meeting all of the four above-mentioned basic requirements for GSNs (SINGER 2010: 28).

3.3 Alarm/warning systems

Monitoring systems provide the basis for alarm, warning, or early warning systems. Warning or alarm systems may issue an alert to notify the authorities and/or might be linked to traffic lights to automatically block the hazard area. For example, rock fall nets can be equipped with sensors to generate an alarm when hit by rock fall in order to avoid major damage and possibly take further measures (for instance, such a system, including other sensors as well, has been installed at the quarry Spitz in Austria (www-04)).

Debris flows, which often are suddenly initiated and correspondingly hard to predict, are instrumented with warning systems, sometimes early warning systems (depending on the distance and travel time between release area of the debris and the nearest endangered infrastructure or populated area). These usually aim to prevent fatalities at minimum, since the advance warning is generally only minutes (BADOUX et al. 2009: 517f.). Another sample warning system, concerned with mass movements, mostly rock fall or debris flow, is the one installed at the track system of the railroad running from Mals to Meran in South Tyrol, Italy. If the tracks become blocked by material, such as rocks or debris, the track system closes instantly. Despite the warning system, a tragedy occurred on March 12, 2010, when a train was directly hit by a debris flow and nine persons were killed and many injured (www-06). The unlucky coincidence of the train passing this spot at the exact same time as the debris flow hit the track system led to this tragic accident (had the train arrived several seconds early or late, the warning system would have kicked in and prevented the accident) and rendered the warning system powerless (www-05, www-06).

3.4 Early warning systems

While alarm or warning systems usually only give an alarm upon the occurrence of the event itself, an early warning system (EWS) should alert beforehand (before the causative phenome-

non will happen) with sufficient lead-time to be able to take mitigating measures, such as preparing effective emergency and response plans. The United Nations International Strategy for Risk Reduction (UNISDR) defines the term early warning system (EWS) as

“... the set of capacities needed to generate and disseminate timely and meaningful warning information to enable individuals, communities and organizations threatened by a hazard to prepare and to act appropriately and in sufficient time to reduce the possibility of harm or loss.” (UNISDR 2009: 12)

To achieve effective responses to warnings, four key elements must be embedded into an EWS – also known as people-centered or end-to-end EWS. Such systems need to include all steps from hazard detection through to community response with guidance on how to act upon warnings. These four major steps are: “knowledge of the risks; monitoring, analysis and forecasting of the hazards; communication or dissemination of alerts and warnings; and local capabilities to respond to the warnings received” (UNISDR 2006: 3, UNISDR 2009: 12). Figure 2 depicts these inter-related key elements and gives short definitions of each. Many reports (for example, IDNDR 1997, UNEP 2012, and SASSA 2013) not only point out the importance of early warning systems needing a scientific and technical basis, but also strongly focus on social aspects such as points three and four in Figure 2 (*dissemination and communication, response capability*), the alpEWAS system mainly brings the second key element *monitoring and warning service* into focus.

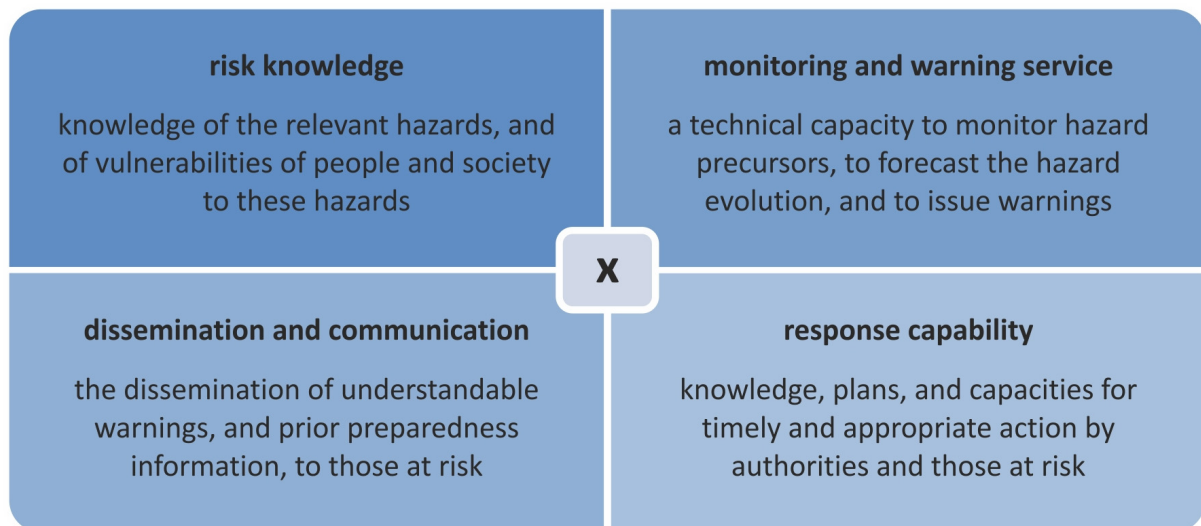


Figure 2: Four inter-related key elements, spanning hazard knowledge and vulnerabilities through to preparedness and response capability (adapted from Basher 2006: 2170, Fig. 2).

Regardless their principal task – if just aiming at one or all of the major elements – different types of landslide early warning systems and approaches to them exist and will be briefly described in the next few passages, highlighting select case studies. The models underpinning EWSs vary greatly depending on several factors, such as the geology of the area of interest, the

processes of hydrological influences (rainfall, groundwater flow, etc.) involved on the slope's stability, the accuracy of information on geotechnical and hydrological processes, the data's quality, and the spatial scale of the investigated area, ranging from single landslides (local) to regions as big as thousands of square kilometers (regional) (CAPPARELLI & VERSACE 2011: 67).

Depending on the size of the area under investigation and on the model being used, the operational systems can be distinguished into empirical or physically based models (ALFIERI et al. 2012: 38). Empirical models often predict the probability of landslide occurrence within a certain region (e.g., in a climatic region or of a specific type of landslide). These often use historical data and put it into relation with antecedent rainfall, which does not require hydrological or geotechnical in situ monitoring (GLADE et al. 2000: 1060f.). On a local scale – mostly a single landslide – physically based models find more use. Hazards at deep-seated, slow-moving landslides most often cannot be analyzed in terms of probability analysis because of the usually very small number of recorded past events and thus rather aim at reproducing and understanding the physical behavior of the processes at an individual landslide. They therefore require more detailed, site-specific information regarding geology, deformation measurements, measurement of triggers, etc. (ALFIERI et al. 2012, CAPPARELLI & VERSACE 2011, FERRARI et al. 2014).

By analyzing the data gained from the post-storm reconnaissance of landslips and debris flows initiated by exceptional rainfall in 1969 in the greater Santa Monica area of Southern California, CAMPBELL (1975: 1f., 31f.) was able to derive empirically based thresholds (total rainfall/rainfall intensity) for when a high probability of slope failure in the area will apply, outlining the basis of one of the first (early) warning systems. Since then several similar studies (e.g., by CAINE 1980, WIECZOREK et al. 1983) in different regions have been conducted. In 1986 one of the earliest landslide EWSs issued its first warnings in California, in the San Francisco Bay area (KEEFER et al. 1987: 921). In recent decades, research into regional and sometimes local antecedent rainfall thresholds initiating landslides was continued by, e.g., AU (1993), COROMINAS & MOYA (1999), ALEOTTI (2004), BRUNETTI et al. (2010), and LAGOMARSINO et al. (2013).

Local investigations of a single landslide frequently employ a more holistic approach using physically based models, often incorporating some kind of continuous monitoring system or GSN as a basis for an early warning system (IDNDR 1997: 21ff.). One such system is the EWS based on a versatile and sophisticated GSN, which has been installed at the Åknes rockslide in Norway. While the rockslide itself doesn't endanger a populated area or infrastructure, its location on a rock slope above a fjord involves the risk of triggering a tsunami if it fails, which then may endanger people along the fjord (KRISTENSEN et al. 2010). Several other local EWSs are described, e.g., by HUSAINI & RATNASAMY (2001), LACASSE & NADIM (2009), YIN et al. (2010), and MAYER et al. (2010). The alpEWAS project, which laid its emphasis mainly on the second key element *monitoring and warning service*, was not the only one to develop a local-scale landslide EWS within the framework of the funding program 'Geotechnologien' (Chapter 1.2). Two other projects did the same, although with different main objectives. The SLEWS

project (Sensor-based Landslide Early Warning System) brought micro-electro-mechanical systems (MEMS) sensors into focus and integrated them into a low-cost, self-organizing, multi-hop ad-hoc wireless GSN (www-07). In contrast, the ILEWS project (Integrative Landslide Early Warning System) doesn't limit its focus on the development of a GSN and its measurement systems, but takes a more holistic approach including *dissemination and communication* as well as *response capability* (Figure 2) (BELL et al. 2010).

Recent decades have seen significant advancement in monitoring techniques, geosensor networks, and real-time data acquisition, all of which has helped to further develop EWSs and especially landslide EWSs. So, for instance, at the Second World Landslide Forum held in Rome in 2011 many papers concerned with instrumentation, monitoring, and early warning of landslides have been presented (MARGOTTINI et al. 2013).

3.5 Methods of threshold derivation and landslide characterization

In order to avoid false alarms, a lot of effort has not just to be put into the development of such an EWS with its monitoring but also into the evaluation and determination of alarming thresholds. Many different methods of deriving thresholds for early warning exist; however, the exact determination of resilient and reliable alarming values remains a challenge and needs to be adapted consistently to new information regarding the landslide, its model, or the analysis method. Oftentimes analysis methods, such as time series analyses and/or numerical models and simulations (NADIM et al. 2009), will be consulted to better understand the landslide's mechanics and triggers and to deduce alarming values.

3.5.1 Time series analysis

Time series and *time series analysis* are both quite generic terms, the former being defined as 'a collection of quantitative observations that are typically measured at successive points in time while spaced at uniform time intervals'. The latter 'comprising many differentiable analysis methods to extract meaningful statistics or characteristics from the time series' (SCHLITTGEN 2001: 1ff.). Time series analysis (TSA) not only includes the actual data analysis but also all the data acquisition, processing, data cleansing, and filtering methods.

Comparing data series visually or applying stochastic procedures as methods to gather information has been applied for many hundreds of years in history especially in financial mathematics or when analyzing meteorological data sets. Alone in the field of geosciences lots of papers, books, and conference proceedings, all concerned with retrieving additional information from data sequences, exist (ANDERSON et al. 1985, GILGEN 2006). For example, STINY (1938b) attempted to analyze the regularity of recurrence of damages caused by floods, landslides and sturzstroms in Austria, based on records starting in the eleventh century. Mostly in regional EWSs methods of TSAs have been used to identify alarming thresholds as early as the 1970s, when the first landslide EWSs were developed (Chapter 3.4 on page 15ff., CAMPBELL 1975).

Especially in models at a regional scale rainfall thresholds are often derived using empirical approaches based on statistical analyses of historical data of landslides and related antecedent rainfall, whose duration differs highly from only hours to several weeks and even months, depending on geomorphology, geology, area, depth, and type of the landslides under investigation (CAPPARELLI & VERSACE 2011: 67f., ALEOTTI 2004: 247f.). Even though quite some simplifying assumptions are usually adopted, these empirical models can provide good threshold values for the occurrence of landslides within a whole region without needing any further site investigation or incorporating monitoring techniques. In one of the first models used to predict landslides in regards to rainfall CAMPBELL (1975) defined the triggering threshold by critical cumulative rainfall. Other methods involve the occurrence of landslides related to antecedent rainfall, duration, and intensity, or any combinations of these (POLEMIO & PETRUCCI 2000: 1221, WIECZOREK & GUZZETTI 2000: 408). For instance, COROMINAS & MOYA (1999) and GLADE et al. (2000) examined antecedent rainfall; DAI & LEE (2001) analyzed the duration's influence; and CAINE (1980), ALEOTTI (2004), CHLEBORAD et al. (2006), as well as BRUNETTI et al. (2010) applied intensity-duration models. The Istituto di Ricerca per la Protezione Idrogeologica at the Consiglio Nazionale delle Ricerche (CNR IRPI) compiled all different kinds of empirical thresholds in a worldwide database on their web page (www-08).

The approaches described above are not applied exclusively to whole regions, but also to the threshold evaluation of single landslides. In this case usually site-specific data such as piezometric pressure, surface/subsurface movements, etc., are included into the analysis, altering the model in a more physical-based one. FLORIS & BOZZANO (2008) calculated the antecedent rainfall threshold for two complex landslides in Italy and combined it with numerical models (to perform stability analyses of different water tables) to estimate the probability of rainfall-induced landslide reactivation. In the study area of the Terres Noires of Barcelonnette (France) a combined model relating precipitation with a groundwater model and stability analyses showed that short-term, heavy rainfall are not effective but high precipitations over 6 months during colder seasons with constant snowmelt over a longer time are most likely to result in failure (VAN ASCH & BUMA 1997). The relationship between rainfall, pore water pressure/water table(s), and displacements is often investigated by means of correlation and/or spectral analysis. Aim of these techniques is to quantify influences of triggers, to calculate possible time lags between triggering event and activation of the landslide, and to derive threshold values as well as to gain a better understanding of the landslide's mechanisms (WEIDNER 2000, CROSTA & AGLIARDI 2002, OKAMOTO et al. 2004, HONG et al. 2005, CAPPARELLI & VERSACE 2011).

In several case studies the time lag between rainfall – maximum in pore water pressure – and displacements has been determined using crosscorrelations, since it also gives an estimate of how much time between triggering event and onset of movements is available to take mitigative measures, such as evacuation and protection of structures and infrastructure (LEE & LEE 2000, SIMONI et al. 2004, ARATTANO & MARCHI 2005, LEBOURG et al. 2010). For instance in Cabelle Ligure in the northwestern Italian Apennine Mountains, a complex, deep-seated landslide has

been monitored by LOLLINO et al. (2002) using piezometers and an automatic inclinometer system. Crosscorrelations revealed only a very short delay (hours) between rainfall peak and according peak in the recorded water table, while the time lag to the onset of movements produced by these rainfall events was found to be 8-9 days (LOLLINO et al. 2002, 2006). Next to rainfall MATSUURA et al. (2003, 2008) included snowmelt into their analyses and researched its effects on displacement behavior, showing time lags of only hours between peak in the water table and according displacements, while the delay between rainfall/snowfall and displacements differs strongly depending on the season and weather conditions prior to the event (snow melting period vs. snow cover period). Even though the time lag may vary strongly depending on the landslide's geometry (shallow versus deep-seated), its geology, and climatic conditions, cross-correlation analysis is a helpful tool to investigate the influencing factors and their relationship to movement characteristics of (usually) an individual landslide.

3.5.2 Numerical modeling

Over the last few decades numerical models have made great progress in their development and are now routinely used not only in technical sciences but also in fields such as economics, sociology, or psychology. A *numerical model* can be generally defined as 'a system, in which the relationships and dependencies between its elements are described and approximated by variables and mathematical equations' (Figure 3).

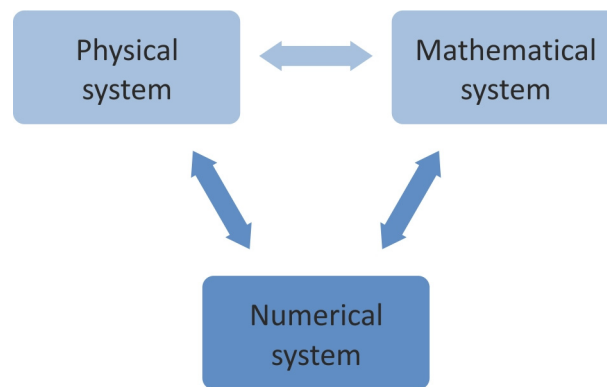


Figure 3: Simple scheme, illustrating the relation between physical, mathematical, and numerical systems. Processes of a real-world object (conceptual model) are translated into mathematical terms, while the numerical model assists with applying the appropriate mathematical abstraction. (Adapted from BARBOUR & KRAHN 2004: 45, Fig. 2)

In the field of landslide modeling the relations between predisposing and triggering factors, as model inputs and as the outputs, the according responses of the slopes are specified by mathematical equations (VAN ASCH et al. 2007). BARBOUR & KRAHN (2004: 46) differentiate the aim of such a numerical analysis into the three major categories:

- Interpretation: The model helps with the interpretation of field and/or laboratory data. It can also be used to conduct back-analyses to better comprehend the model's evolution.
- Design: The performances of design alternatives are compared, e.g., for mitigation measures.
- Prediction: Validated and calibrated models, oftentimes based on back-analyses help to provide a quantifiable prediction of future landslide evolution.

A great variety of commercial programs and codes are offered on the market, which can be categorized into three different levels of sophistication. STEAD et al. (2006: 217) discriminate between kinematic & limit-equilibrium analysis (Level I), continuum & discontinuum numerical methods (Level II), which are sometimes subdivided into two separate categories (e.g., JING & HUDSON 2002, EBERHARDT 2006), as well as hybrid finite/discrete element with fracture approaches (Level III) for use in landslide analyses.

Level I analyses are primarily suited to simple translational failures or focus on assessing critical key blocks (kinematic analysis). The stability then can be further calculated using limit-equilibrium methods issuing a factor of safety (ratio of resistant forces to disturbing forces) as a result, but stress and strain conditions within the slope cannot be evaluated with these methods. If more complex problems, such as geometry and material anisotropy, stress state within the rock mass, influence of complex deformation, etc., need to be addressed, level II and III models should be considered. If the slope's rock mass is comprised of massive, intact rock, weak rock, heavily fractured material, or soil/debris without joint- and fault-systems of influence, a continuum-based approach (finite element/finite difference method) is suitable. A discontinuum model (distinct element/discontinuous deformation analysis method) should be used when joint sets control the failure mechanism or blocky mediums are analyzed. Hybrid models, level III, combine the advantages of the above-mentioned limit-equilibrium-, continuum- and, discontinuum-methods and codes (for example, a particle method coupled with finite differences in a particle flow code (PFC)). (JING & HUDSON 2002, STEAD et al. 2006, VAN ASCH et al. 2007)

In order to deduce the landslide's evolution and especially threshold values, usually level II and level III models are used, since the underlying processes are hardly ever simple enough to be reproduced by very simple models. While PICARELLI & VINALE (2009) and THORNES & ALCÁNTARA-AYALA (1998) combined finite element models (continuum approach) to calculate the water movement throughout the slope, directly with limit-equilibrium stability analyses, to investigate the slope's kinematics and evolution, a discontinuum approach was chosen at rock-slope case-studies, e.g., at the Ruffi and Goldau mass movements (both Switzerland), and at the Åknes rockslide in Norway (EBERHARDT et al. 2005, HATEM & THURO 2008, KVELDSVIK et al. 2009). At the Åknes rockslide (Chapter 3.4 on page 15ff.) a discontinuous deformation analysis using the numerical code UDEC was conducted, altering fracture geometry, fracture friction,

and groundwater conditions within reasonable limits based on observations by the GSN. The evaluation of the modeling results has helped to better understand the rockslide's kinematics, but has also been beneficial for the planning and interpretation of future measurements as well as the further development of the EWS and the tsunami modeling (KVELDSVIK et al. 2009: 689ff.).

The continuum code FLAC by Itasca was first released in 1986 (www-09) and since then has been applied in multiple case studies to perform back-analyses (BARON et al. 2005, SEGALINI et al. 2009), as a validation tool (FLORIS & BOZZANO 2008), to simulate the performance of mitigative measures (MARCATO et al. 2012), and to derive thresholds and predict the slope's evolution (SEGALINI et al. 2009). For instance, FLORIS & BOZZANO (2008) applied a modified rainfall-threshold model to two complex landslides in the Apennine foredeep in Italy and tested the reliability of their results inter alia by simulating variable water tables and interpreting the resulting changes in the stress-strain behavior but also to estimate the landslides' development following extreme events (very high water tables). This powerful software has been applied in many different case studies and is not limited to landslide modeling but is also for instance applied in the field of mining and tunneling. Several symposia on FLAC have been held, starting 1999, that were concerned with basic and underlying problems as well as specific cases studies (www-09, DETOURNAY & HART 1999).

This code (FLAC 2D) has been chosen to analyze the Aggenalm landslide, to perform back-analyses, and to evaluate the model's evolution as well as for the definition of alert threshold values. A more detailed description of the underlying basics of the finite differences code and its application to the Aggenalm landslide will be given in Chapter 7.1.

4. The study site

A slowly moving slide (cm/a) with discrete shear zones not too far away from Munich was looked for, for the installation and testing of the alpEWAS geosensor network. Hence, meeting the mentioned major prerequisites, the mass movement at the Aggenalm was chosen on the recommendation of the Bavarian Environment Agency (LfU) that had already conducted a periodical survey over the last few years at this site. The following passages will shortly introduce the geographical layout, climatic conditions and the tectonic and geologic setting at the study area. Subsequently, a detailed description of the mass movement itself, including geomorphologic features and historic events is given, followed by a presentation and discussion of the geotechnical model and the landslide's mechanism.

4.1 Geographical setting

The field test site at the Aggenalm, further on referred to as Aggenalm landslide, is located in the south of Bavaria, about 80 km southeast of Munich and 30 km south of Rosenheim at the northern edge of the Alps within the Mangfall mountain range (Figure 4).

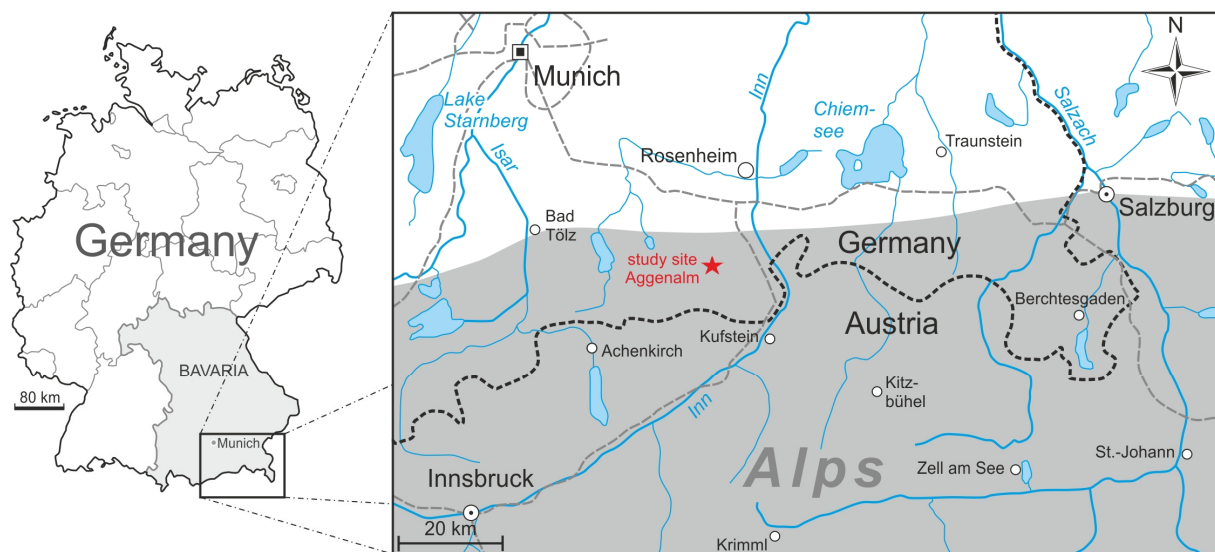


Figure 4: Location of the study site at the Aggenalm landslide.

The study site is part of the hilly Sudelfeld region between the towns of Bayrischzell and Oberaudorf and the two major valleys the Ursprung valley in the west and the Auerbach valley in the east. The undulating Sudelfeld area is framed by the Brunnstein-Traithen ridge in the south and the Wildbarren-Wendelstein ridge in the north, shown and highlighted in Figure 5.



Figure 5: Geographical overview of the eastern Mangfall mountain range. The Aggenalm landslide is marked red. (BayernAtlas © Bayerische Vermessungsverwaltung 2013, www-10)

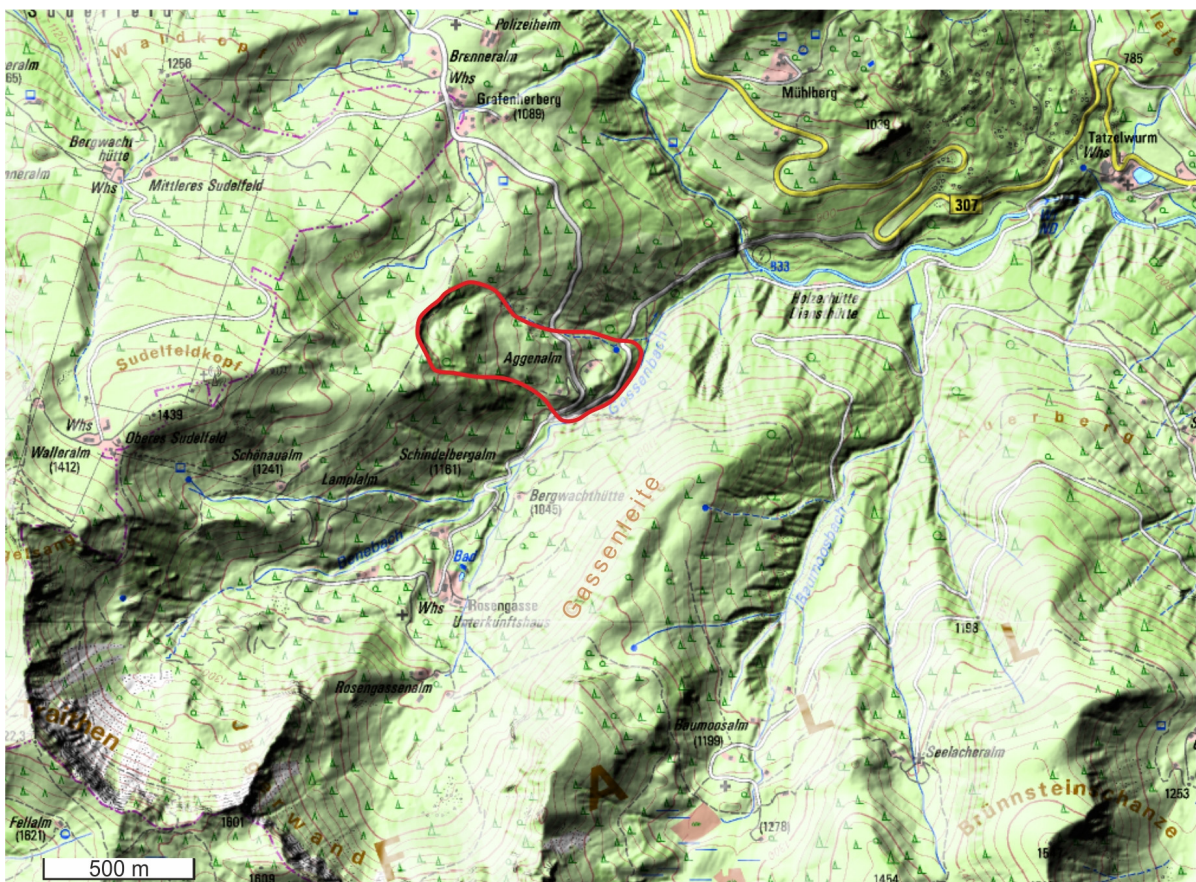


Figure 6: Geographical overview of the Aggenalm landslide and its closer vicinity. The hillshade of the area is overlain with the topographical map. The landslide is outlined red. (BayernAtlas © Bayerische Vermessungsverwaltung 2013, www-10)

The Aggenalm landslide is located at the eastern slope at the edge of the Sudelfeld skiing resort in the Gassenbach valley across the Gassenleite at the road connecting the Rosengasse and Grafenherberg. The location of the landslide is depicted in the two figures (Figure 5, Figure 6). The maximal length of the Aggenalm landslide is about 780 m and the maximum width is 340 m. The elevation at the main scarp of the landslide is about 1200 m a.s.l. and at its toe about 920 m a.s.l.

4.2 Climatic conditions at the study site

The study site, located at the northern edge of the Alps, is controlled by a continental climate which may be locally influenced by its position within the mountains. According to WOLFF (1985: 156) and Germany's National Meteorological Service (DWD) the mean annual precipitation (1931–1960 and 1961–1990) for several observation stations in the area varies between 1346 mm/a and 1814 mm/a (Table 3). 15–40 % of the mean annual precipitation comes from snow depending on the elevation, valley or high on mountains, respectively.

Table 3: Mean annual precipitation (1931–1960 and 1961–1990) at different observation stations (WOLFF 1985: 155f., Table 3, Germany's National Meteorological Service (DWD)).

Observation station	Mean annual precipitation [mm/a]
Degerndorf-Brannenburg	1346
Oberaudorf	1398
Bayrischzell	1403
Brünnsteinhaus	1594
Sudelfeld (Polizeiheim)	1523
Tatzelwurm	1660
Wendelstein	1814

The data sets from the Brünnsteinhaus station (1594 mm/a) as well as the Sudelfeld (Polizeiheim) station (1523 mm/a) and Tatzelwurm station (1660 mm/a) can be compared best to the conditions at the Aggenalm landslide. All three observation stations are at a similar elevation and at similarly oriented slopes, the Brünnsteinhaus station just south, the Tatzelwurm station east, and the Sudelfeld (Polizeiheim) station in Grafenherberg north of the Aggenalm landslide (Figure 6, Table 4). Table 4 shows the monthly distribution of the precipitation (rain-fall/snowfall) for the above-mentioned stations. The observation points show a similar distribution with a maximum in surface runoff during the rain-laden and relatively warm spring and summer months including the period of snowmelt.

Table 4: Mean monthly precipitation (1931–1960 and 1961–1990) for the Brunnsteinhaus and the Sudelfeld (Polizeiheim) observation stations (data from Germany's National Meteorological Service (DWD)).

	Precipitation	Oct.	Nov.	Dec.	Jan.	Feb.	Mar.	Winter
Brunnsteinhaus (1345 m a.s.l.)	[mm]	89.6	109.2	115.7	102.9	100.5	103.2	621.1
	[%]	5.6	6.9	7.3	6.5	6.3	6.5	39.0
Sudelfeld (Polizeiheim) (1070 m a.s.l.)	[mm]	84.7	98.3	113.1	82.7	82.2	95.5	556.5
	[%]	5.6	6.5	7.4	5.4	5.4	6.3	36.5
Tatzelwurm (795 m a.s.l.)	[mm]	109.9	106.1	99.1	123.2	118.7	110.9	667.9
	[%]	6.6	6.4	6.0	7.4	7.1	6.7	40.2

	Precipitation	Apr.	May	June	July	Aug.	Sep.	Summer
Brunnsteinhaus (1345 m a.s.l.)	[mm]	121.9	138.4	194.3	208.6	193.0	116.8	973.0
	[%]	7.6	8.7	12.2	13.1	12.1	7.3	61.0
Sudelfeld (Polizeiheim) (1070 m a.s.l.)	[mm]	103.7	152.3	204.2	195.1	199.2	112.0	966.5
	[%]	6.8	10.0	13.4	12.8	13.1	7.4	63.5
Tatzelwurm (795 m a.s.l.)	[mm]	115.8	149.4	194.8	224.9	185.6	121.9	992.4
	[%]	7.0	9.0	11.7	13.5	11.2	7.3	59.8

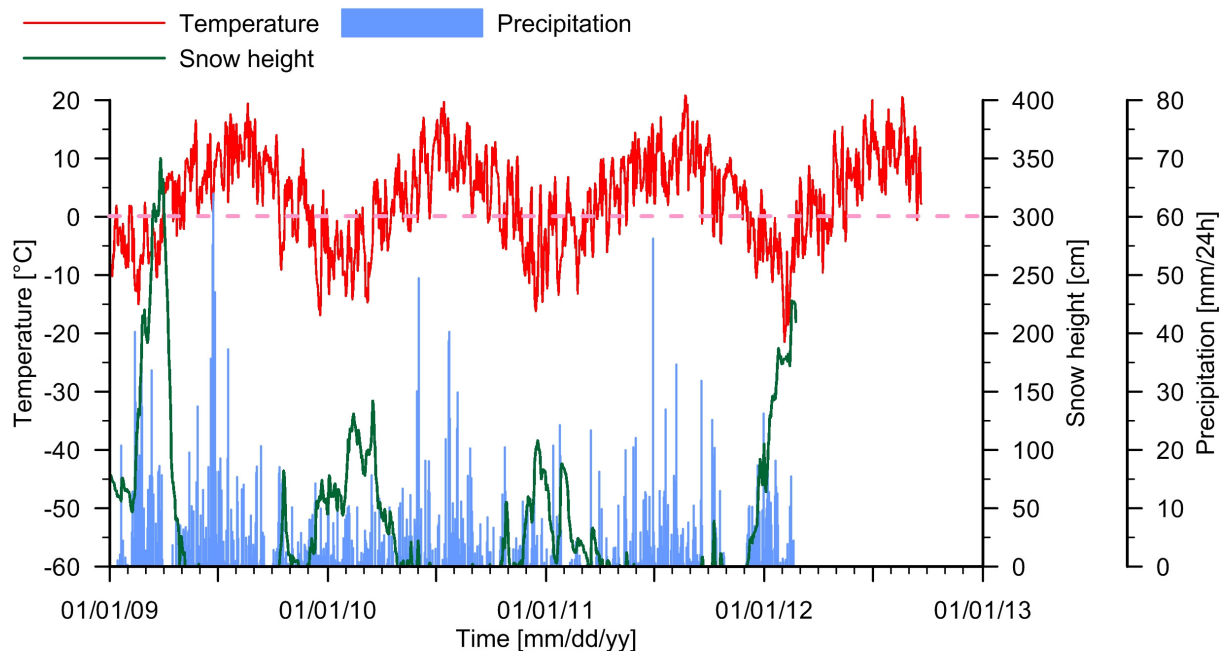


Figure 7: Precipitation (blue), snow height (green), and temperature (red) over a time span of 3.5 years, starting January 1, 2009, for the Wendelstein observation station. Precipitation and snow height data were only acquired through February 2012, the recording of temperature stopped in September 2012. (Data from Germany's National Meteorological Service (DWD))

For the years 1935, 1997, and 2009–2012 data sets of precipitation and snow height were acquired from different observation stations (Wendelstein and Brunnsteinhaus (Figure 5), Sudelfeld (Polzeiheim) and Tatzelwurm (Figure 6)) for comparative reasons. The yearly data sets, especially from the stations Tatzelwurm and Sudelfeld (Polzeiheim) help to interpret the historic events at the Aggenalm landslide (Chapter 4.6.1 on page 37ff.) but also the current data sets acquired by the geosensor network.

Figure 7 shows a plot of the data from the Wendelstein observation station exemplarily for the last three and a half years. Further plots of the other stations are displayed in the following chapters when interpreting and analyzing the historic events or the current data sets from the geosensor network.

4.3 Tectonic overview and setting of the study site

The project's study site is situated within the Lechtal nappe of the Northern Calcareous Alps, which can be subdivided into three main parts. These are from North to South the Allgäu nappe, Lechtal nappe, and Inntal nappe (Figure 8), which were stacked by north-directed thrust forces during the Alpidic orogenesis.

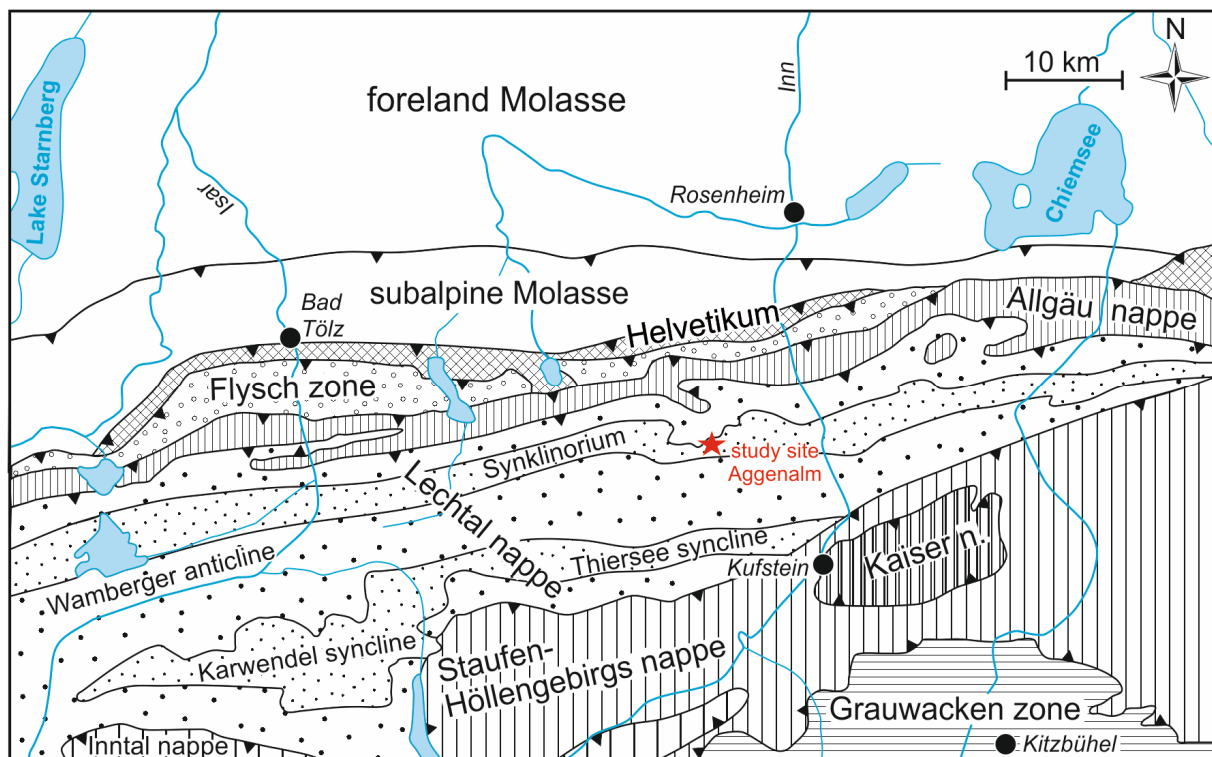


Figure 8: Tectonic map of the Northern Calcareous Alps of the region between Lake Starnberg and Chiemsee. The study site (red star) is part of the Lechtal nappe, located within the complex Synklinorium (a syncline–anticline–syncline structure), approximately 14 km northwest of Kufstein (adapted from SCHMIDT-THOMÉ 1964: 289, Fig. 39, GWINNER 1971: 244, Fig. 244).

The Lechtal nappe in turn is built up by a series of W–E oriented syncline- and anticline-structures that themselves may be of a complex internal build-up (HASEMANN 1929: 34f.). The northernmost part of the Lechtal nappe is the *Nördliche Hauptdolomitzone* (‘northern main dolomite zone’), subsequently to the south follows the *Synklinorium* (‘synclinorium’, a double syncline with an anticline in between) that extends over 150 km, stretching from a bit west of Lake Starnberg (Garmisch-Partenkirchen) to the Chiemsee. South of the Synklinorium succeeds the *Südliche Hauptdolomitzone* (‘southern main dolomite zone’), to which the Wamberger anticline belongs, while the southernmost structure of the Lechtal nappe is the Thiersee syncline (Figure 8, Figure 9) (HAHN 1912, 1914, HASEMANN 1929: 31ff., THURNER 1961, WOLFF 1985: 10).

As the Aggenalm landslide is situated within the Synklinorium, its structures and tectonics will be specified in the following, as they probably were one reason for the location of the mass movement at this point. They are also of importance for the construction of the geologic model, the interpretation of the movement’s mechanism, as well as the interpretation of survey data. In this area the Synklinorium has several synonyms, e.g., HAHN (1912: 337) named it *Audorfer Synklinorium* or *Synklinorium des Brunnstein*, while HASEMANN (1929: 34) refers to it as *Audorfer Großmulde*. According to HASEMANN (1929: 34ff.) and GANSS (1950: 204f.) its tectonics are quite differentiated and can be broken down into three W–E oriented synclines, with more or less well-developed anticlines in between. The synclines themselves again can be subdivided into several parts, which appear independently and are mostly confined or cut off by faults.

From north to south, the Synklinorium consists of the northern, middle and southern synclines, which HASEMANN (1929) divided respectively from west to east into the structures listed below (Figure 9):

- Northern synclines:
 - Larchgraben syncline
 - Mühlberg syncline
 - Klamm-Alpe syncline
- Middle synclines:
 - Sudelfeld syncline
 - Auerberg syncline
 - Fahrenberg syncline
- Southern synclines:
 - Traithen syncline
 - Brunnstein syncline
 - Oberaudorfer syncline

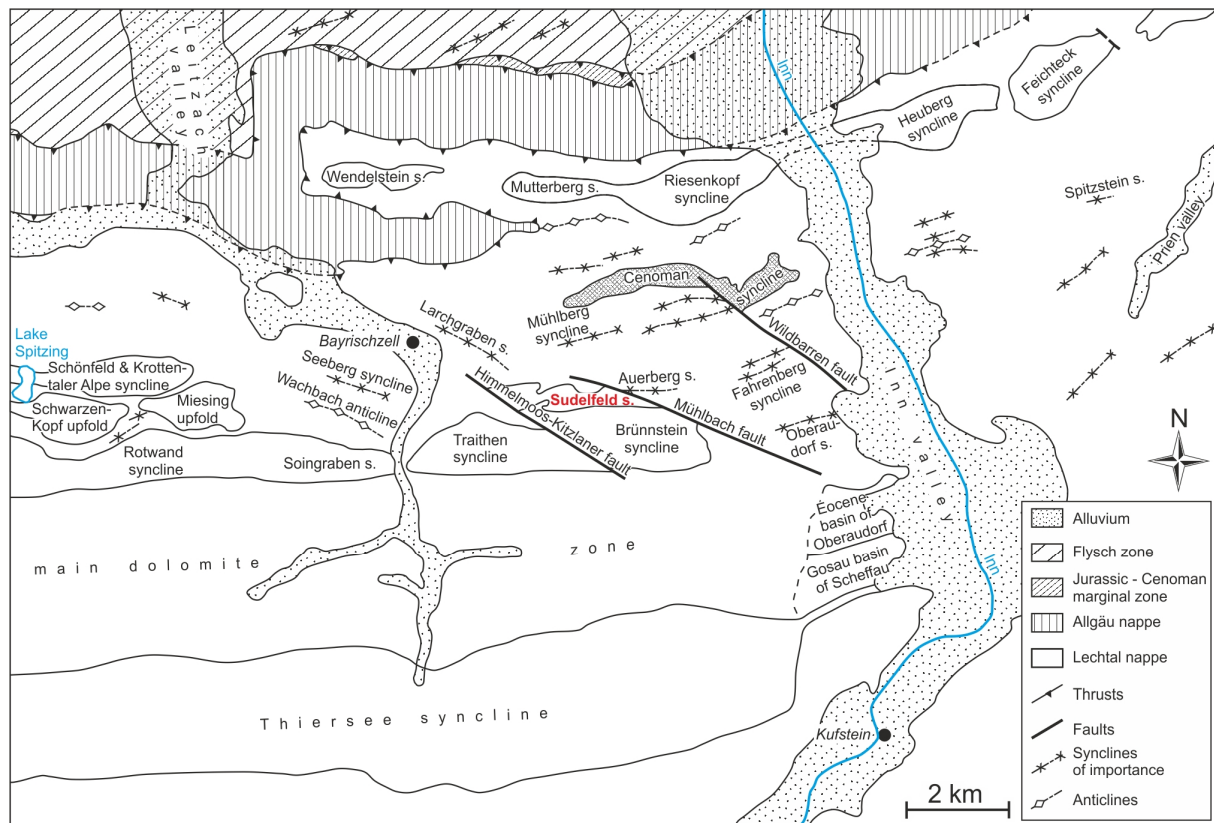


Figure 9: Tectonic map of the region between the Inn valley and the Lake Spitzing. Especially within the Synklinorium major synclines and anticlines are depicted either by outlining the structure or by showing its axes. The study site is part of the Sudelfeld syncline, highlighted red. (Adapted from GANSS 1950: 205, Fig. 1)

In Figure 9 all these synclines are depicted while Figure 10 shows a detail of the surroundings of the Sudelfeld and Larchgraben synclines. The mass movement at the Aggenalm is situated between the northern Sudelfeld syncline and the Larchgraben syncline at the Zellerrain-Auerberg anticline. The axis of this anticline has a mean eastward dip of about 8° (WOLFF 1985: 135), which can be greater at selective points, e.g., at the Aggenalm landslide, where JUNG (2007: 20) determined dip values varying between $15\text{--}30^\circ$. The anticline's dip is therefore responsible for the nearly slope parallel orientation of the rock mass at the landslide. The area is not only heavily folded but also characterized by many faults that confine or cut off the different synclines and anticlines.

To the north, the Zellerrain-Auerberg anticline is abruptly cut off by the Mühlbach-Larchgraben fault, a main fault, next to the Himmelhoos-Kitzlaner fault, which both are oriented NW–SE and cut through the folding structures further complicating them (Figure 10). At the toe of the landslide the Gassenbach fault with an NE–SW orientation, located mostly within the correspondent Gassenbach creek, defines the eastern edge of the landslide (Figure 11). Further smaller and local faults, especially along the landslide's scarp and southern edge were mapped and/or described by WOLFF (1985) as well as JUNG (2007: 21). This heavy faulting together

with the folding of the area surrounding the Aggenalm landslide leads to an extremely tectonically weakened and degraded rock mass that next to its geology and external stimuli also encourages the onset of mass movements.

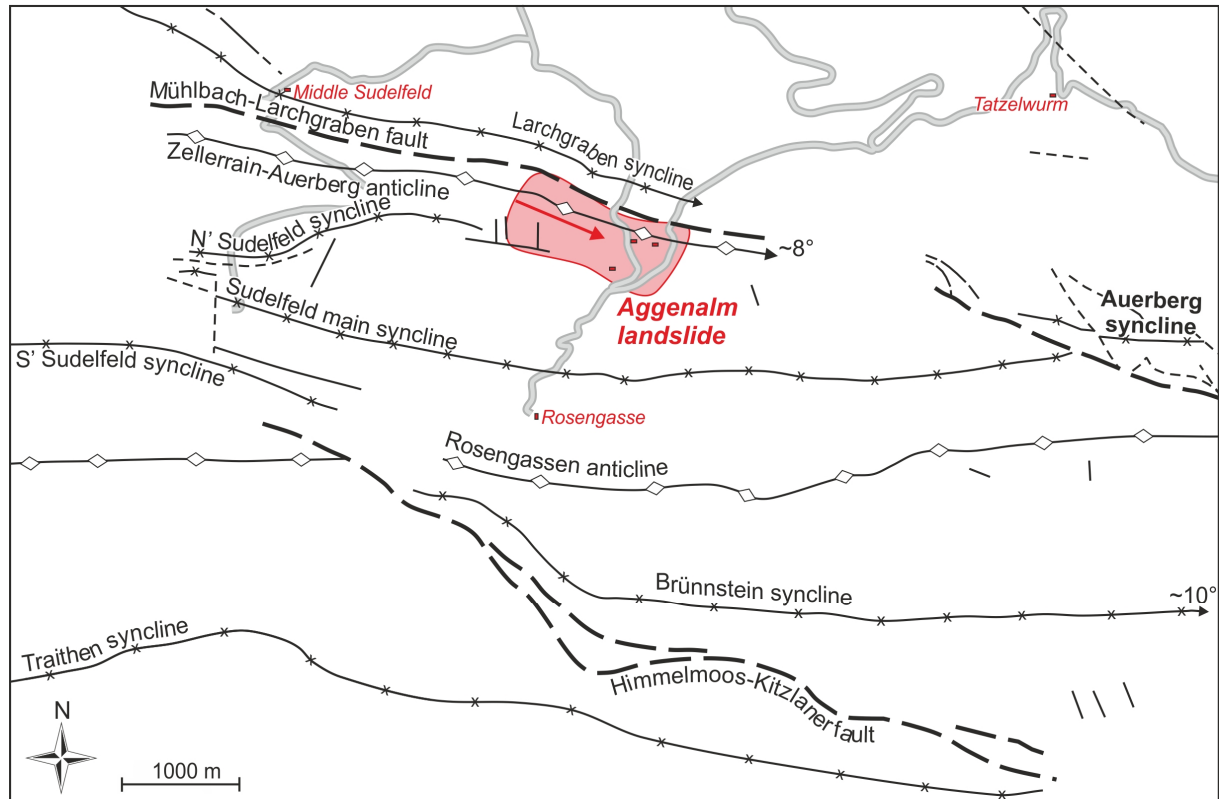


Figure 10: Syncline and anticline structures as well as major faults surrounding the Aggenalm landslide. The axis of the Zellerrain-Auerberg anticline dips with a mean of 8° toward east and is therefore the reason for the almost slope parallel orientation of the rock mass. The tectonic systems were constructed based on the geological map 1:25000, No. 8338 Bayrischzell (WOLFF 1985).

4.4 Geological overview

The area of the Aggenalm landslide, situated within the Synklinorium of the Lechtal nappe, is mainly built up of various Triassic and Jurassic limestones, dolomites, and marls. The oldest rock unit surfacing in the closer vicinity of the mass movement, mapped in detail by JUNG (2007) (Figure 11, Appendix I), is the Norian *Plattenkalk*, a ‘well-bedded limestone’, which doesn’t really outcrop but should be located, covered by Pleistocene and Holocene material, west of the Gassenbach (Figure 11). It is superposed by the *Kössener Schichten* (‘Kössen formation’), an alternating sequence of limestones and marls of Upper Triassic – Rhaetian – age. The marls underlying major parts of the slope due to weathering effects are thought to be of main responsibility for the slope’s instability. Above the Kössen formation follows the *Oberrhätalkalk* (‘Upper Rhaetian limestone’) of Upper Rhaetian times, a rather light colored limestone. In this area the Upper Rhaetian limestone is often developed dolomitic and is

therefore referred to as *Oberrhätdolomit* ('Upper Rhaetian dolomite'). The youngest stratigraphic member (hard rock) surfacing in the described area is the Lower Jurassic *Allgäu Schichten* ('Allgäu formation'), built up of limestones and marls that are sometimes developed siliceous. The Allgäu formation surfaces in the Larchgraben syncline's core as well as in parts of the Sudelfeld syncline south of the Aggenalm landslide.

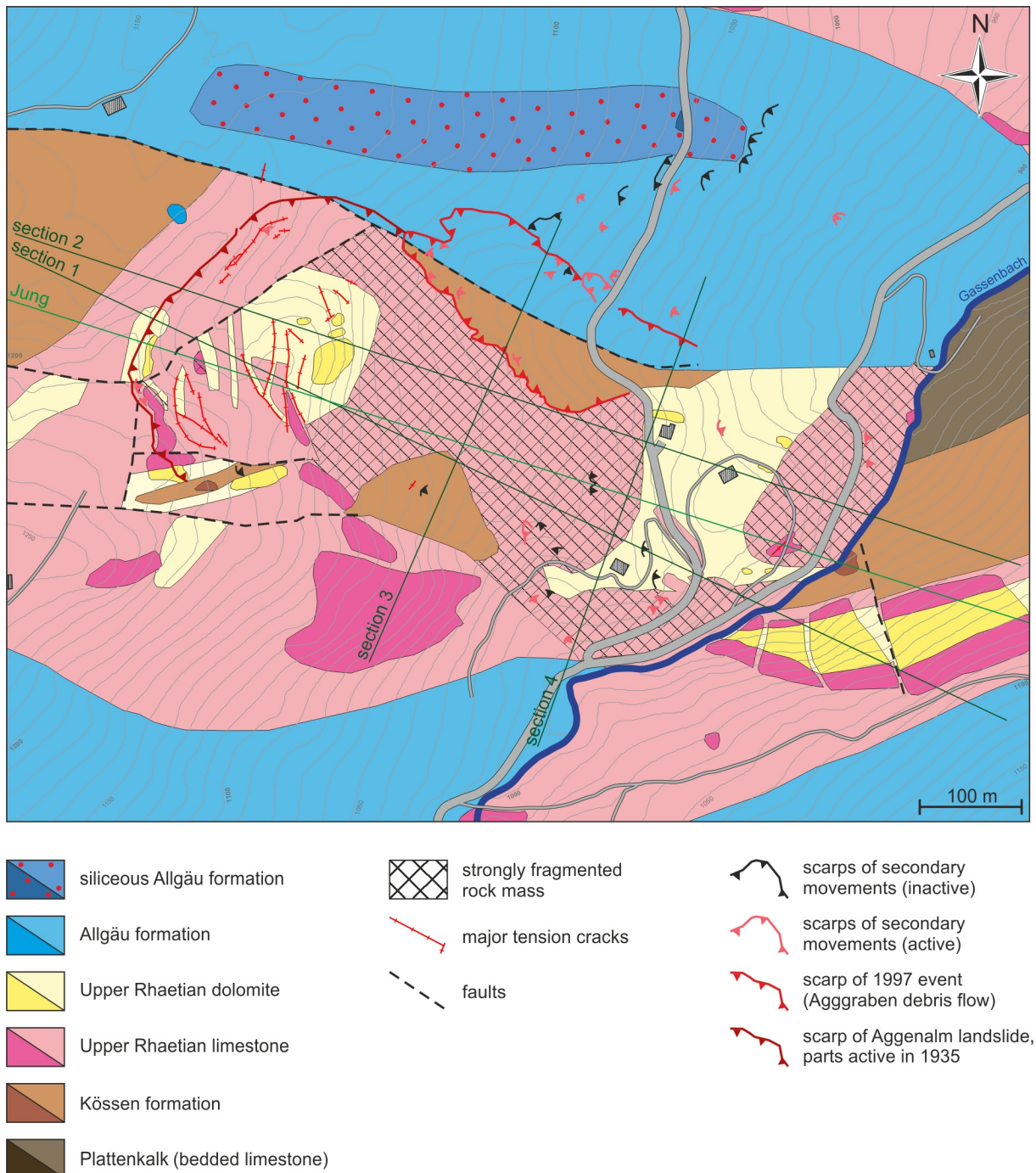


Figure 11: Geological map of the area surrounding the Aggenalm landslide uncovered of the Pleistocene and Holocene deposits. For a clearer view, only the main scarps of the different landslide bodies are pictured. The green lines represent the different locations of cross sections. (Adapted and simplified from JUNG 2007)

Glaciers covering the area during the last ice age are responsible for the typical glacial morphology and have left behind a variety of glacial deposits, such as tills, which are often covered by a veneer of talus material. The most recent formations in this area are an abundance of shallow and deep-seated mass movement masses of different generation, of which the Aggenalm landslide is the most dominant one. For clarity, these most recent Pleistocene and Holocene formations that cover the bedrock throughout the illustrated detail are not depicted in Figure 11 but are further differentiated and shown in additional maps in Appendix I.

4.5 Stratigraphy and lithological description

In this section only a very short summary of the rock's development and characterization will be given, particularly with regards to the following construction of sections (e.g., thickness, special structures, etc.) but also the deduction of rock properties for the numerical modeling. More detailed lithological descriptions can be found in, for instance, WOLFF (1985: 29ff., 113ff.), SCHORMAIR (2003: 10ff.), and JUNG (2007: 8ff.).

4.5.1 Triassic

4.5.1.1 Plattenkalk (bedded limestone)

The Norian *Plattenkalk* ('well-bedded limestone') doesn't outcrop at the Aggenalm landslide or its surroundings at the surface but appears because of stratigraphic and geometric considerations in the cross sections and also in the west of the uncovered geological map (Figure 11, JUNG 2007: 8). It can be described as a close- to medium-spaced limestone, with bedding thicknesses ranging from 5–50 cm, colored light- to dark-gray. Individual beds of the fine-grained, dense limestone can be dolomitic, especially in the lower part of the Plattenkalk unit, at the transition to the *Hauptdolomit* ('main dolomite formation'), whereas closer to the top intercalations of marly beds and fossil-rich limestone layers display the transition to the above following Kössen formation.

The strong internal folding exacerbates the specification of the unit's thickness. While SCHORMAIR (2003: 11) assumed a maximum thickness of 100 m for the Aggenalm area, a thickness of up to 500 m is reached in the Traithen and Brunnstein area, which reduces to 200 m toward south in the Thiersee syncline (WOLFF 1985: 32).

4.5.1.2 Kössen formation (Kössener Schichten)

The Rhaetian *Kössen formation* ('Kössener Schichten') can also hardly be found in outcrops and is mostly covered by a veneer of glacial and/or talus material. Only at the hillside cut of the Gassenbach at the toe of the landslide a small outcrop can be found. The Kössen formation is an alternating sequence of dark gray to black marls and limestones, and it seems likely that the marls dominate since outcrops are very rare.



Figure 12: The outcrop of the Kössen formation at the toe of the landslide is pictured. Photo a) shows the few visible limestone beds the center, with a maximum thickness of about 20–25 cm. Picture b) on the right shows a detail of the almost black marls of the Kössen formation, which are extremely stressed tectonically and disintegrated into cm-sized chips, with specular slickenside surfaces.

The intermediary banks of limestone or marly limestone are usually fine-grained and dense and their dark, almost black color, can change to a lighter gray or beige when weathered. The bedding thickness ranges from only a few centimeters to maximum 25 cm (SCHORMAIR 2003: 12). The dominating marls of the Kössen formation also become beige to brown due to weathering, and due to increasing decalcification processes they turn into a grayish-brown homogeneous mass. If fresh, the marls are usually finely laminated (mm range), causing a foliated fabric (REIBMÜLLER 1997: 14).

A strong tectonic strain yields a very close joint system with an abundance of bright slickenside surfaces. The marly beds can be several meters thick with hardly any limestone beds in between.

The primary low rock strength of these marls, together with heavy jointing, makes them prone to weathering, coinciding with a further reduction of the rock mass strength, probably being the main cause for the slope's instability (JUNG 2007: 9).

The total thickness of the Kössen formation in the area is hard to define owing to the small and rare outcrops, but also due to the strong internal minor folding especially within the marls. WOLFF (1985: 35) accounts for a thickness ranging from only a few meters to 50 m maximum for the area of Bayrischzell depicted in the geological map.

4.5.1.3 Upper Rhaetian limestone and dolomite (Oberrhätkalk & -dolomit)

The *Upper Rhaetian limestone* and *dolomite* ('Oberrhätkalk and -dolomit') surface frequently and are also responsible for most of the steep rock walls in the Aggenalm area, e.g., building up the crown and main scarp of the landslide.

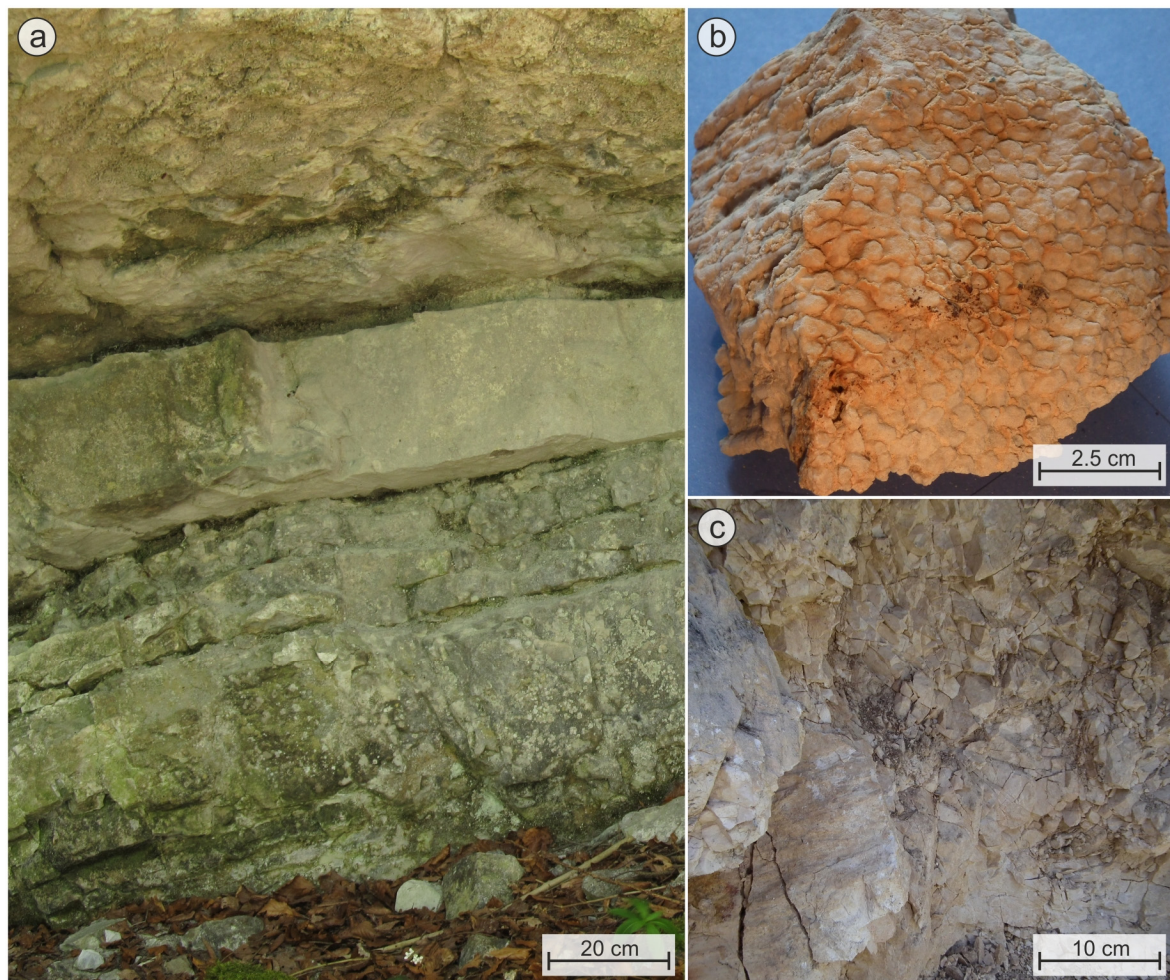


Figure 13: a) This photo shows the typical development of a well-bedded, light-gray colored Upper Rhaetian limestone with bedding thicknesses varying from 0.1 m to 2 m. b) Especially within the limestone often fossilized corals (*Thecosmilia*) can be found. c) Pictured is the dolomitic variety of the Upper Rhaetian formation, which is strongly fragmented due to its brittleness and jointing. (Photo a) by courtesy of Bettina Sellmeier)

The limestone is light-gray to almost white when weathered. The beds' thickness varies from 0.1 m to about 2 m (medium- to wide-spaced). This competent rock mass couldn't compensate the tectonic stresses by folding but responded by jointing and faulting, at which the strata is displaced. The dolomitic variety originated during early to late diagenesis and is interlaminated in the limestone. The dolomite is beige to white, not as competent and more brittle and jointed as the limestone and therefore easily erodible and can thus often be found as fragmented debris.

The total thickness of the limestone and dolomite derived from the outcrop findings and geometric constrains sums up to about 100 m (JUNG 2007: 12ff.). Whereas SCHORMAIR (2003) and WOLFF (1985) quote thicknesses ranging from 150–200 m in the area.

4.5.2 Jurassic

4.5.2.1 *Allgäu formation (Allgäu Schichten, Fleckenkalk & -mergel)*

The Lower Jurassic (Lias) *Allgäu formation* ('Allgäu Schichten') is mostly composed of so-called *Fleckenkalk* and *Fleckenmergel* ('spotted limestones and marls'), which, for example, build up the core of the main Sudelfeld syncline and Larchgraben syncline, but hardly outcrop. The limestone is characterized by a grayish color with dark-gray to bluish-black spots and schlieren that are accountable for their name. It shows distinct bedding with thicknesses of a few centimeters up to 20 cm (JUNG 2007: 19f.). Between the limestone beds, layers of dark marls are intercalated. The total thickness of the limestones and marls of the Allgäu formation can be up to 200 m.

4.5.2.2 *Siliceous Allgäu formation (Liaskieselkalk)*

Above the spotted limestones and marls follows the Early Jurassic *Liaskieselkalk*, a 'siliceous limestone' that surfaces within the Larchgraben syncline. Just as the spotted limestones it is well bedded and gray, sometimes also with darker spots or schlieren. The chert is well distributed within the sedimentary rock and chert nodules were formed only rarely. The thickness ranges from a few meters to 150 m (SCHORMAIR 2003: 23).

4.5.3 Quaternary

Pleistocene deposits of the Würm glacial are the most common and characterize the landscape's morphology. Older glacial deposits were either removed or at least covered by the youngest glacial advance and are therefore only rarely found. Holocene formations aren't as characteristic as Pleistocene deposits, consisting of talus material or landslide material.

4.5.3.1 *Pleistocene*

The area was shaped by the Inn glacier, which during the Würm glacial reached up to at least 1280 m above sea level, covering all of the Aggenalm area (SCHORMAIR 2003: 26, WOLFF 1985: 114ff.). Except for rock walls, almost the whole area is covered by glacial tills, which

may also contain rocks different to those surfacing in its direct surroundings (e.g., *Adneter Kalk*, a ‘red Jurassic limestone’ was found during the drilling campaign).

4.5.3.2 Holocene

Talus material covers the steep slopes, e.g., below the main scarp or at the hillside across the landslide at the Gassenleite. It consists of mainly hard rocks from the surrounding outcrops, primarily of Upper Rhaetian limestone and dolomite. Bigger blocks and boulders are usually limestone rather than dolomite, which is strongly fragmented. The mass movements in this area, depending on their depth, are made up by several of the above-described rocks and sediments (Appendix IV – photos of KB1 coring). Their individual composition, especially of the two major mass movements in the area will be closer specified in the following passages.

4.6 The Aggenalm landslide

As mentioned before several mass movements are located in the area under investigation, whereupon the subsequent description will focus on the most prominent mass movement, the Aggenalm landslide. Other landslides as, for instance, the Agggraben debris flow, or small secondary mass movements associated with or located on the Aggenalm landslide will only be characterized briefly.

Major parts of the Aggenalm landslide (red boundary in Figure 14) were last active in 1935. According to the Bavarian Environment Agency (LfU) only at the main scarp of the mass movement an ongoing activity was documented during a site inspection in 1988 (GALLEMANN 2012: 1). At the following site survey in 2000 activity across the whole landslide was recorded. New fissures and cracks in the three huts on the mass movement as well as new cracks in the tarmac of the connection roads from Grafenherberg, respectively Tatzelwurm to the Rosengasse were documented. The new activity at the Aggenalm landslide itself as well as the occurrence of the Agggraben debris flow (blue outline in Figure 14) at the northern edge of the Aggenalm landslide initiated the first periodical survey of the movement rates conducted by the LfU. Both major events from 1935 and 1997 have been entered into the GEORISK-program (www-11) as objects (No. 8338013 and No. 8338012).

In the hillshade, based on a 1 m digital elevation model, but also in the aerial photograph (orthophoto), the Aggenalm landslide stands out most notably, especially the area of its crown and main scarp (Figure 14, Figure 15).

In the subsequent passages, historic events at the site as well as the landslide’s morphologic features will be described. Together with the geological information from Chapters 4.3 and 4.4 as well as findings from the field investigation program (boring logs and geoelectric sounding – Chapter 4.6.3) a geological model has been developed and the landslide’s mechanism will be discussed.



Figure 14: 3d-model of the Aggenalm area, looking southwest. The Aggenalm landslide is outlined red while the Aggraben debris flow is marked blue. (Geobasisdaten © Bayerische Vermessungsverwaltung 2010)

4.6.1 Historic events

Only two events of greater magnitude have been described in the past, 1935 and 1997, each reactivating parts of the mass movement referred to as Aggenalm landslide (Figure 15). No exact information about prior movements in this, at the time quite remote area, exists. BERNRIEDER (1991: 393) mentions damages in 1899 to the paths and bridges just completed in the area, while MARKLSEDER (1935: 2) only refers to recurrent movements at different time intervals. Next to field observations, old tree trunks, cleared during the 1935 event, also indicate antecedent incidents (www-11).

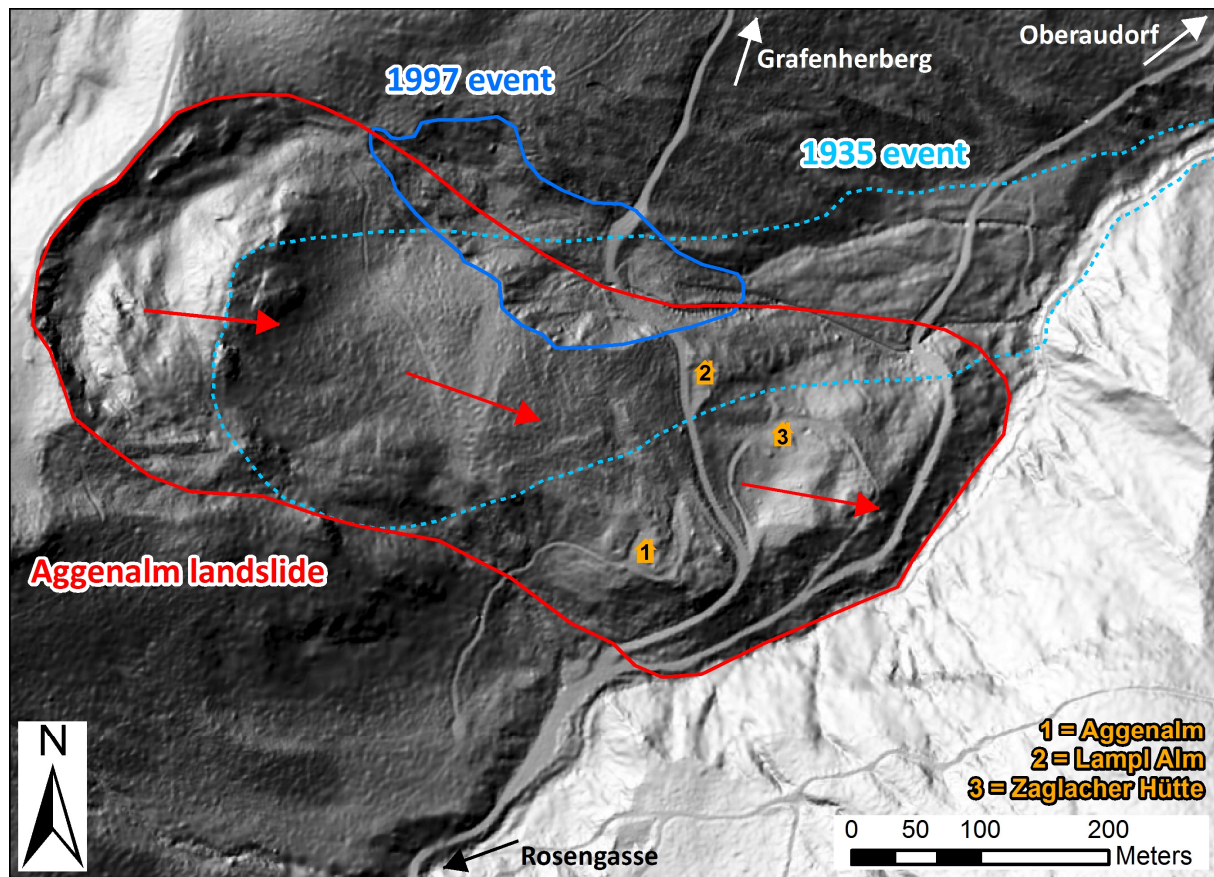


Figure 15: Hillshade model of the Aggenalm landslide based on a digital elevation model (DEM, 1 m laser scan). The deep-seated mass movement (red line) is monitored by the alpEWAS system and shows only very slow movement rates of 1–2 cm per year, expressed by the red arrows. The dimensions of the two documented events from 1935 and 1997 are sketched in blue colors. The location of the three alpine huts⁶ is shown as well. (Geobasisdaten © Bayerische Vermessungsverwaltung 2010; schematic movement vectors adapted from GALLEMANN (2012: 5, Fig. 6); outline of 1935 event adapted from WALLER (n.d.))

4.6.1.1 The 1935 event – the Aggenalm landslide

The greatest documented event happened on April 22, 1935, during Easter at the Aggenalm area. Major parts of the Aggenalm landslide were active and accelerated, starting at the main scarp which today can still be seen, but mostly in areas further downslope in the debris/soil dominated parts (see Chapter 4.6.4). WALLER (n.d.), a contemporary witness, describes the catastrophe quite adventurously in his account *Die Brücke*. The following passage taken from this adventurous story has been freely translated by the author.

‘... At the last landslide in Bavaria, 1.5 Mio. m³ of debris moved as the Tatzelwurm crawled. During this time at the Tatzelwurm over 1.5 Mio. m³ soil with rocks, boulders

⁶ The names of the three huts vary and seem to be jumbled depending to which document one refers to. In most of the maps only hut No. 2 is plotted, sometimes called Aggenalm, though this name also applies for this specific region incorporating all three huts. Since hut No. 2 displays a sign calling itself Lampl Alm, this name was chosen when referring to this hut. As JUNG (2007) gives the most detailed description and therefore will be referenced the most, the names he has used (Figure 15), will be applied when referring to one of the three huts in the following.

and tree trunks were pushed down to the Gassenbach valley over a length of more than 1.5 km, which in turn was filled up to 8 m in depth. Even today, a quarter of a century after the catastrophe, the last remains of this huge landslide can still be seen, when hiking from the Tatzelwurm to the Rosengasse. As the landslide finally came to rest after 4 days, on Sunday, April 28, 1935, it accelerated again shortly, the soil masses had moved up to 1.5 km from the scarp, more than 20 days' work of pasture were strewn with debris originating from debris flows, as well as 3 bridges, 7 days' work of forest and a trout breeding destroyed, etc., ...

When we came down, the debris flow had already a width of 20 meters, the whole mountain was moving, and trees were moving standing crooked back and forth toward us. ...' (WALLER n.d.)

In his account of the 1935 events, WALLER (n.d.) also included a graphic depicting the approximate dimensions of the mass movement at the time, which is incorporated into Figure 15 as a light blue dotted line. In the chronicles of the town of Audorf by BERNRIEDER (1991), the mass movement from 1935 is characterized very shortly but also more objectively:

“Am 22. April 1935 rutschte infolge von Regengüssen bestes Weideland (3 Tagwerk) des Aggeraipl⁷ (Bauer von Agg, Lampl von Agg) ab. 3 Tage lang war die Aggeralm [Aggenalm] höchst gefährdet. 20 Tagwerk Almboden waren völlig vermurt. 1 Million Kubikmeter Erdmassen waren in Bewegung.“ (BERNRIEDER 1991: 393)

‘On April 22, 1935, in consequence of rainfall best pasture (3 days' work) at the Aggeraipl⁷ (Bauer of Agg, Lampl of Agg) slid down. For 3 days the Aggeralm [Aggenalm area] was highly at risk. 20 days' work of alpine pasture has been affected by debris flows. 1 million cubic meters of soil masses were moving.’

Probably the most accurate and detailed description of the events can be found in the issue from May 4, 1935, of the weekly newspaper *Anzeiger für Oberaudorf und Kiefersfelden*. An excerpt from this account is quoted and translated below, while the complete article and its translation are attached in Appendix II.

„(Bergrutsch am Tatzelwurm). Am Morgen des Ostermontags [22. April 1935] machte sich am Aggeralpl [Aggenalm] oberhalb des Tatzelwurms zwischen den dort liegenden Hütten der Beginn eines Erdrutsches bemerkbar. Kurze Zeit darauf begannen bereits größere Strecken Weideland in den Gassenbach abzurutschen und sich dort zu stauen. ... Der Gassenbach wurde bis zu einer Tiefe von 5 Metern mit Gestein, Felsblöcken und Bäumen aufgefüllt. Die beiden Brücken zum Aggeraipl⁷ und zur Gassenalm waren ebenso wie die oberen Teile der Straße spurlos verschwunden.

... Die Bewegung der gewaltigen Erdmassen kam auch am Dienstag nicht zum Stillstand. Die Erdmassen bewegten sich vielmehr mit einer Geschwindigkeit von etwa 4 Metern in der Stunde abwärts und hatten in den Nachmittagsstunden den Gassenbach in einer Länge von 1 ½ km vollkommen ausgefüllt. ...

Bis Dienstag Nachmittag sind schätzungsweise eine Million Kubikmeter Erdmassen in Bewegung geraten. ... Über die Ursachen des riesigen Bergrutsches können nur Mutmaßungen geäußert werden. Man nimmt an, daß durch die starken Regenfälle der letzten Zeit unter dem Hang liegende Erdschichten ins Rutschen geraten sind. ...

⁷ Lampl Alm according to the nomenclature used in this thesis – hut No. 2 in Figure 15.

Meldung vom Donnerstag: Die im Gebiete des Tatzelwurms abgerutschten Erdmassen sind nunmehr durch das Aufhören der Niederschläge nahe zum Stillstand gekommen. Die Hauptmure hatte sich bis Donnerstag früh noch ganz langsam fortbewegt. Durch die Beendigung der Schneeschmelze hat sich die Wasserbildung vermindert und übt nicht mehr Druck aus wie bei Beginn des Erdbebens. ...” (MARKLSEDER 1935: 2)

‘**(Landslide at the Tatzelwurm)**. On Easter Monday morning [April 22, 1935] the start of a landslide became noticeable between the alpine cabins at the Aggeralpl [Aggenalm area] above the Tatzelwurm. Shortly after, major parts of pasture started to slide into the Gassenbach and accumulated thereabout. ... The Gassenbach was filled to a depth of five meters with rocks, boulders, and trees. The two bridges leading to the Aggeralpl⁷ and Gassenalm as well as the upper parts of the road disappeared.

... Neither on Tuesday the movement of these huge masses did come to a stand. Rather, the debris masses moved with a velocity of 4 meters per hour downhill and completely filled the Gassenbach over a length of 1 ½ km until the afternoon. ...

By Tuesday afternoon, an estimated one million cubic meters of earth masses were set in motion. ... About the causes of the huge landslide only conjectures can be expressed. It is believed that due to the heavy preceding rains the strata below the slope started to slip. ...

Message from Thursday: The slid, instable masses came to a halt almost completely because of the cessation of rainfall. The main debris flow was still moving very slowly on Thursday morning. Due to the end of the snowmelt the formation of water decreases and therefore doesn't exert as much pressure as at the onset of the landslide. ...’

The event from 1935 has also been described by MALAISÉ (1951: 85) and AVO (n.d.: 44) as well as www-12. Here it is mentioned that the event's main scarp was located about 90 m above the Aggenalpe (it is not clear which of the huts is meant, probably No. 1 or 2) in an area of moraine-covered Kössen formation as well as Lower Jurassic marls (Liasfleckenmergel). These sources also best describe the landslide's dimensions. In AVO (n.d.: 44f.) it is stated that almost two million cubic meters, weighing five metric tons with a maximum depth of 30 m, were moved along an approximately 250 m long sliding surface toward the Gassenbach, while parts of the masses were carried along by the creek (Gassenbach) up to 700 m to the confluence with the Auerbach. Figure 15 shows the extent of this event as it has been documented by WALLER (n.d.)⁸, while photographs of the event can be found in www-11.

The landslide seemed to be triggered by snowmelt (AVO n.d.: 44f., www-12) or a combination of snowmelt and heavy rainfall (MARKLSEDER 1935: 2, MALAISÉ 1951: 85, BERNRIEDER 1991: 393). This can be supported by the data tables from Germany's National Meteorological Service (DWD) (JUNG 2007: 26, Table 2) and from the rainfall data collected at the Tatzelwurm observation station, just 1.5–2.0 km to the northeast. These show that on the day/days prior to the first signs of the mass movement (April 22, 1935) no rainfall was recorded for Bayrischzell,

⁸ The outline of the 1935 event has been adapted without changes from WALLER (n.d.). Compared to the other above-mentioned descriptions and photographs the affected area seems to be on the big side. Nonetheless it gives one a good idea of the landslide's dimensions and affected area. Taking the descriptions by MALAISÉ (1951: 85) and AVO (n.d.: 44) into consideration, a somewhat smaller area, reaching not as far above the Lampl Alm and not as far to the south but rather a bit more to the north (closer to the 1997 event, debris flow) seems most likely.

Tatzelwurm, nor any other station within the Mangfall/Inn area, but the weeks before have been dominated by partly heavy rainfall. In total, 192 % of the 30-year average of rainfall (see Table 4) was recorded at the Tatzelwurm station in April (Figure 16), in other areas even up to 270 %. This above-average rainfall combined with the ongoing snowmelt (precipitation, mostly snowfall, in the months prior was above average, too, e.g., in February 207 %) is assumed to be causative for the 1935 landslide event.

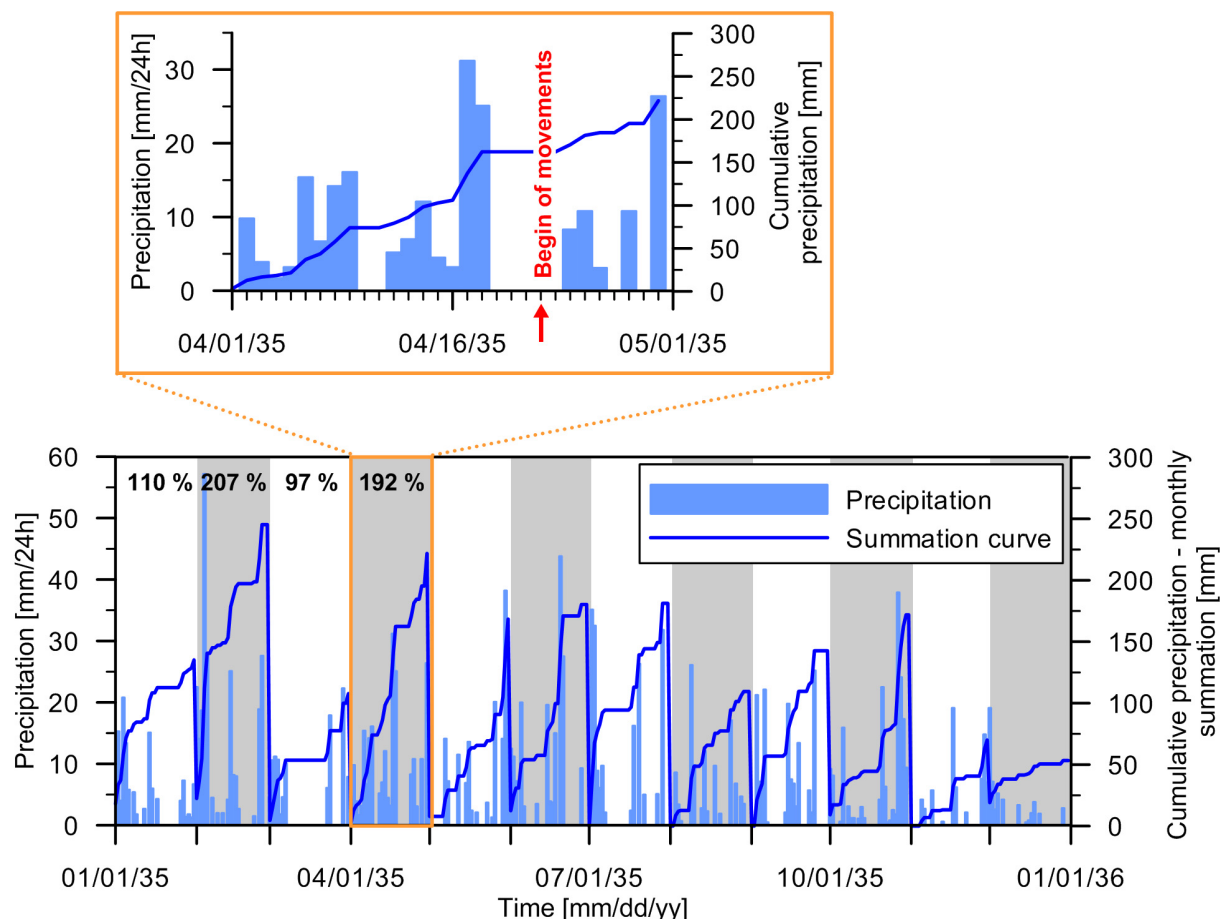


Figure 16: The lower graph shows the daily rainfall (light blue) and the monthly summation curve (blue) at the Tatzelwurm observation station in 1935. The percentages printed across the first four months of the year represent the amount of rainfall in comparison to the 30-year average from 1931–1960. The detail above pictures the heavy rainfalls that have been recorded over the days prior to the first recognized movements at the Aggenalm landslide on April 22, 1935.

4.6.1.2 The 1997 event – the Aggraben debris flow

The second, considerably smaller event happened in 1997. A precise time couldn't be determined. The Water Management office (WWA) of Rosenheim states that during fall of 1997, after a period of heavy rainfall, about 30.000 m³ soil/debris as well as marls originating from the northern edge of the Aggenalm overwhelmed the road leading to Grafenherberg and the

drainage system of the Agggraben (WWA ROSENHEIM n.d.), which was reconstructed and expanded right after the event by the WWA Rosenheim. The approximate extent of this debris flow is depicted by a blue line in Figure 14 and Figure 15.

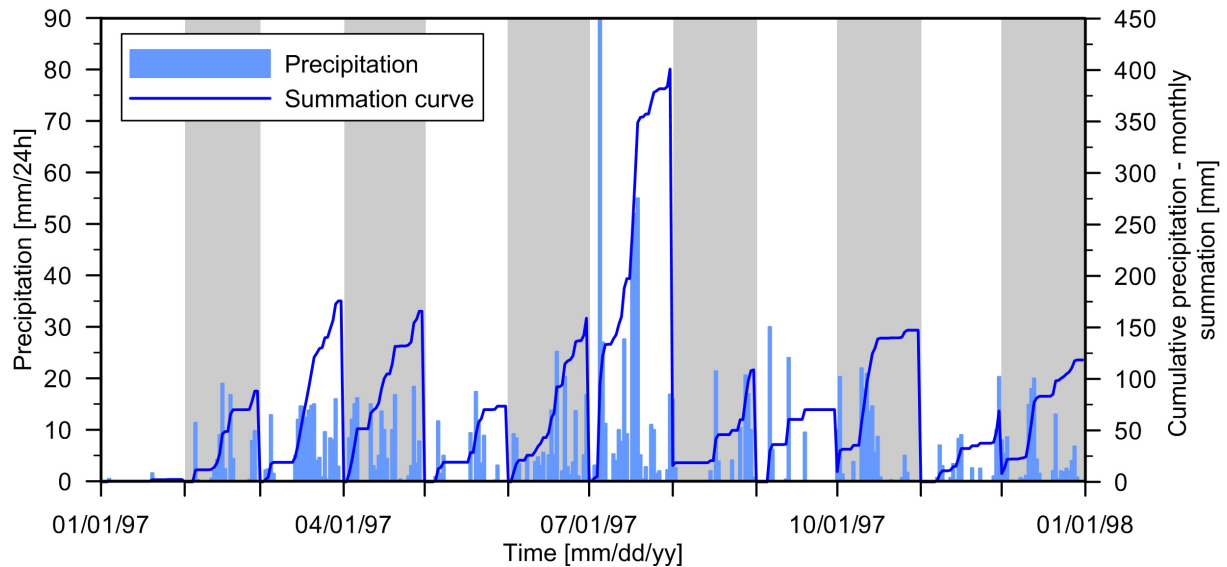


Figure 17: The amount of precipitation at the Sudelfeld (Polizeiheim) weather station for the year 1997 is depicted in light blue. The dark-blue lines show the monthly summation curves of rainfall. The annual rainfall (1579 mm) is only slightly above the 30-year mean (Table 3), while the monthly distribution deviates strongly from the mean. Most months have been dryer than on average, but in July about twice as much and in October 1.75 times as much rainfall than usual for these months has been documented.

The yearly amount of rainfall (1579 mm) that has been documented at the Sudelfeld (Polizeiheim) weather station in 1997 does not differ ostentatiously from the 30-year mean (1523 mm, Table 3). A comparison of the individual months (Figure 17) shows that in general the months are dryer than average (Table 4) except for the months of July (205 %) and October (175 %). Since the exact date of the event is not known it can only be assumed that the cause of the debris flow was a precedent high water table with a subsequent strong rainfall event (in July, August, or October), triggering the debris flow.

4.6.1.3 Other landslide events

JUNG (2007: 47) has mapped and described several scarps of shallow movements that seem to be of older date at the slope north of the Agggraben debris flow. Due to erosion over time and natural cover, an exact evaluation of the mass movements' depths is problematic, but a maximum depth of 5 m seems most likely. He assumes that the landslide masses are made up from debris and glacial deposits, while their basis lies presumably within the Allgäu formation located just below the surface.

In the last few years while monitoring the Aggenalm landslide several small debris flows and slides could be observed. After periods of heavy rainfall, usually during the wet summer

months, smaller mass movements occurred across the slope (Aggenalm landslide). At the connection road to the Rosengasse parts of the tarmac were destroyed due to small rotational slides, several times during the last years. Small debris flows originating from the Aggenalm landslide mass or the Agggraben debris flow could be observed, the latter just very recently in June 2013 after intense rainfall (320 mm within 3 days) as pictured in Figure 23.

4.6.2 Morphologic features

This chapter will give a short overview about the different morphological features of the landslides in the Aggenalm area, with a special focus on the Aggenalm landslide itself by shortly describing the area of the main scarp, the transportation zone (zone of depletion), as well as the features at the landslide's toe. A much more detailed description of the morphological features of the Aggenalm landslide and Agggraben debris flow can be found in SCHORMAIR (2003: 40ff.) and particularly in JUNG (2007: 25ff.).

4.6.2.1 *The Aggenalm landslide*

Crown and main scarp

The southern half of the main scarp is characterized by rock walls made up of Upper Rhaetian limestone and dolomite while the latter dominates in the northern half of the rock walls, with heights up to 25 m (Figure 18). The formation is displaced along several faults (Figure 11), often by many meters (10–55 m). The northern half of the scarp is dominated by soil and debris, mostly glacial deposits of up to 15 m thickness. Here, the scarp reaches a height of 15 m maximum.⁹

Below the main scarp a distinctive depression succeeds. Within this depression, particularly in the faulted zones, debris cones, composed of the material outcropping above in the rock walls, can be found. Downhill of the debris cones several transverse cracks – tension cracks – mostly within the Upper Rhaetian formation and transverse ridges, each with small depressions on their upslope side due to back-tilting, are noticeable. These can be found in all of the upper third of the slope, to which the distinctive ridge (Upper Rhaetian formation) about 100 m east of the main scarp belongs, too. On its downslope side en-echelon tension cracks are separating huge slabs of hard rock, while on its western face mostly blocky material and debris are found. Since most of this area is covered by forest several curved tree trunks and occasionally roots under tension can be observed (Figure 18).

⁹ See WOYTOWITZ (2010) for an inventory and detailed description of the joint systems and faults in the area of the scarp.

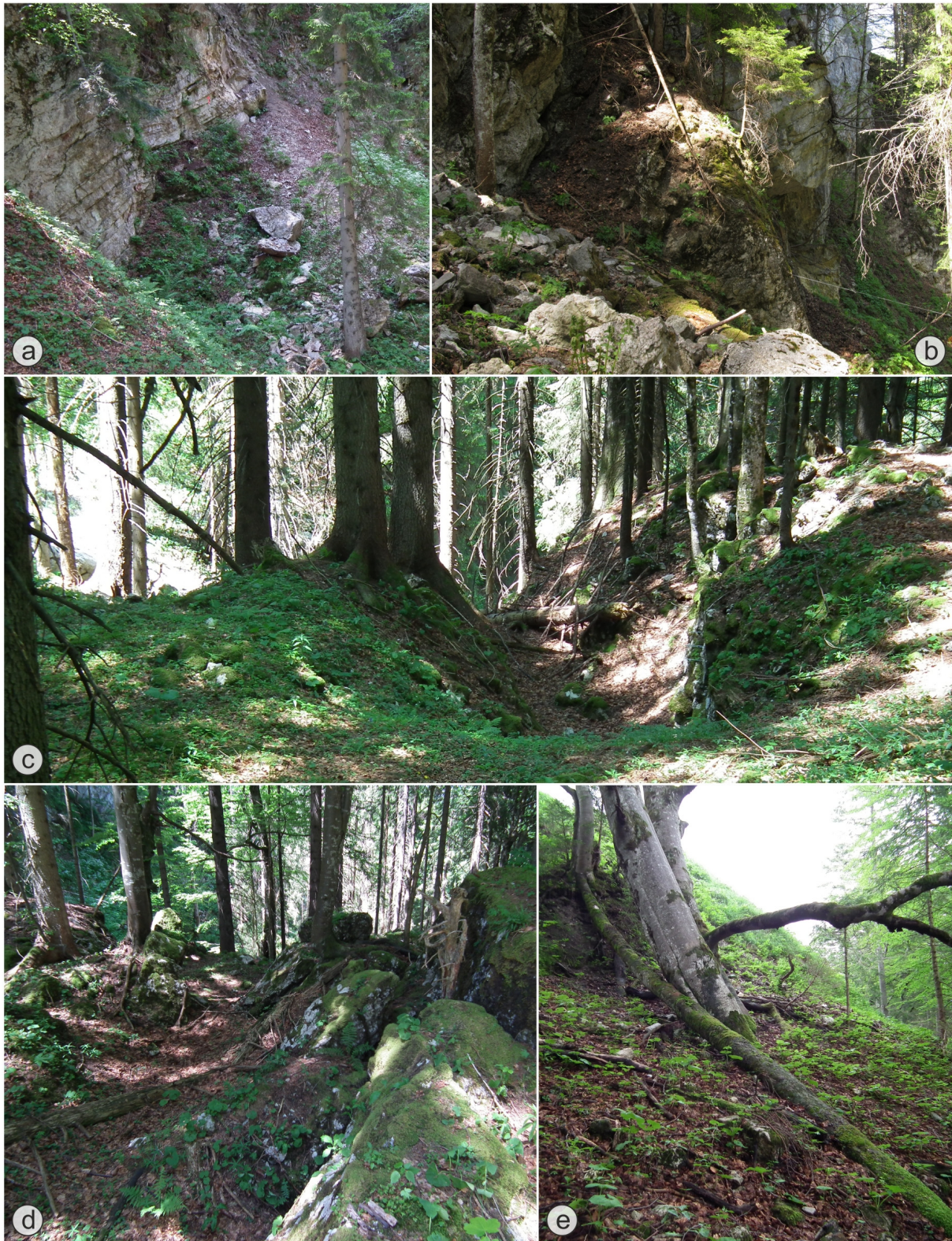


Figure 18: Morphological features in the area of the main scarp. Photo a) shows the well-bedded Upper Rhaetian limestone (partly dolomitic) at the southern edge of the main scarp while b) depicts the middle portion of the scarp, looking along the rock wall toward north. In both pictures blocky material below the rock wall, dominating in faulted areas can be seen building up debris cones. In c) and d) the tension cracks, transverse depressions and ridges following below the main scarp and debris cones are pictured. Photo e) depicts a root under tension, with a length of several meters and a diameter of roughly 10 cm, located at the northern part of the scarp. (Photo b) by courtesy of Bettina Sellmeier)

Zone of depletion – transportation zone

The zone of depletion stretches across the pastures from the eastern side of the massive Upper Rhaetian formation ridge (afforested) downslope to the southernmost hut (Aggenalm) and the easternmost hut (Zaglacher Hütte) (Figure 15). All of this area is used as pasture during summer. This zone can be roughly divided into three parts due to its steepness. After the first, still very steep part a distinctive gradation succeeds before the slope steepens again toward the connection road crossing the landslide.

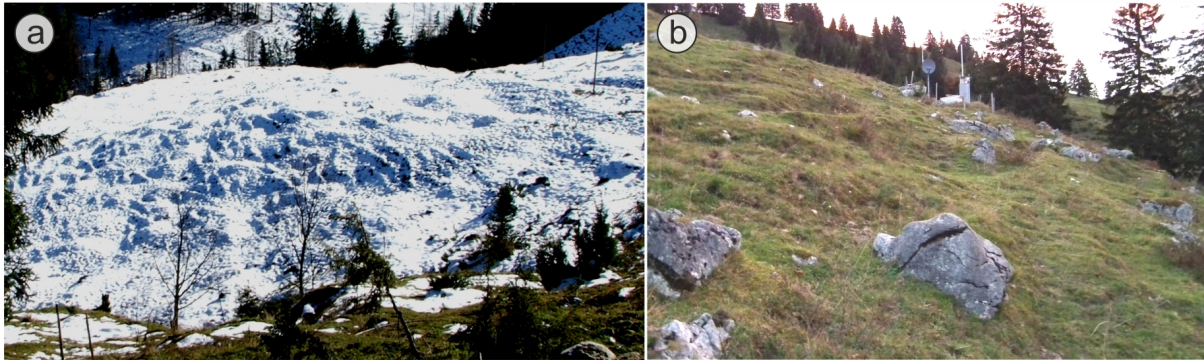


Figure 19: a) Due to the light snow cover and shadowing the hummocky topography becomes visible. Here, the relatively leveled area above the main sensor node is depicted. Photo b) shows a detail of the hummocky surface below the main sensor node (pictured in the upper middle of this photo).

The whole area is built up by a block-in-matrix mass strewn with blocks and boulders, while the leveled section in particular is characterized by its hummocky topography (Figure 19). This hummocky topography results from minor slips when blocks below surface move, piling up material in front of them and causing depressions on their rear side, entailing soil wetness or even sag ponds (especially around the collar of B5, see Figure 24). Particularly at the edges of the landslide secondary instabilities, such as rotational slides or small debris flows, occur. The northern edge has been superimposed by the Agggraben debris flow.

Zone of accumulation – toe of landslide

The zone of accumulation succeeds at the above-mentioned huts with another gradation, where the accumulated material is battered by the landslide's movements and therefore already strongly disintegrated. This is especially the case at the outward-bulging, steep toe of the landslide. At the extremely steep toe, curved trees are characteristic as well as slightly higher movement rates and secondary movements are more likely. The Upper Rhaetian limestone surfacing in this area can only be found in blocks, sometimes disrupted by tension cracks, due to its strong disintegration. To hinder erosion at the toe by the Gassenbach, several weirs and a small barrage have been installed, which is also used for power generation.



Figure 20: Tension crack within an Upper Rhaetian limestone block at the back of the landslide's over-steepened front. The crack's opening width is about 4 m, accentuated by the red arrow.

Structural damages

On both roads crossing the Aggenalm landslide, on retaining walls, but also on all of the three huts damages have been inflicted by the movements (Figure 21). The roads exhibit numerous cracks in their roadbed. In particular in the area of the steep toe, the downhill side of the road subsides but also the retaining stone-wall displays sagging structures. At parts, the connection road to Grafenherberg is secured by a retaining concrete-wall. Mostly at the joints of individual elements of the concrete wall, displacements of up to 15 cm are the result.

The Aggenalm is the hut, showing the most damages, which are also favored by its construction technique. Especially in its northern and western walls, cracks running through the complete wall with opening widths of up to 2.5 cm are clearly visible (Figure 21). The other huts show cracks, too, although not as prominently or continuously. At all three huts the cracks are plastered and painted over in more or less regular intervals, so that the entire opening width and length is covered or at least not as obvious. A complete inventory of all the structural damages in the manner of a preservation of evidence has been conducted and documented by JUNG (2007: 35ff.).

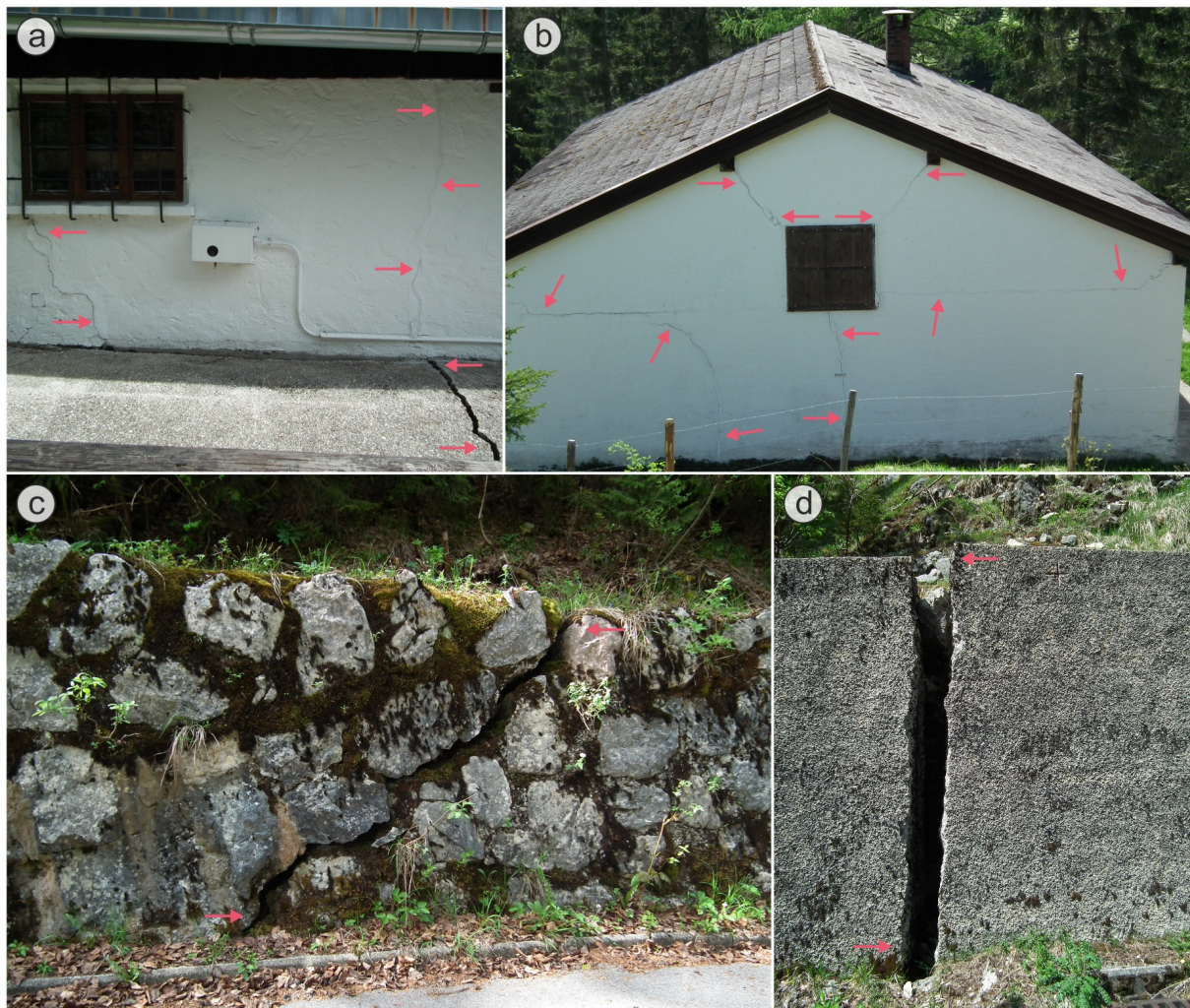


Figure 21: Exemplary damages at structure works inflicted by the movements of the landslide. The pink arrows point toward cracks and fissures within the structures. a) Detail of the southern wall of the Lampl Alm (hut No. 2). Some of the cracks have been recently painted over. b) Western wall of the Aggenalm hut (No. 1). Only the major cracks, opened up to 2.5 cm, have been marked. c) The crack in the natural-stone wall at the connection road to Oberaudorf has an opening width of 5–10 cm. d) Crack in the retaining wall at the road leading to Grafenherberg. It is about 16 cm wide.

4.6.2.2 The Agggraben debris flow

The crown and main scarp of this debris flow (Figure 22) is situated within soil/debris masses consisting of moraine and talus material. At its crown tension cracks within these masses can be observed. The transportation zone becomes quite narrow especially around the crossing of the road to Grafenherberg, while the zone just below the road is comparably leveled and marked by soil wetness. Below this relatively narrow channel the masses fan out to the accumulation zone characterized by a sizeable debris cone, which coincides with the lower parts of the accumulation zone of the 1935 landslide event (Figure 15). As mentioned before, in the description of the historic events, the Agggraben debris flow was presumably caused by a high water table and triggered by heavy rainfall.



Figure 22: View into the Agggraben debris flow from the connection road to Grafenherberg, looking west. The main scarp (red line) can only be partially seen, since the whole landslide mass became overgrown over the years. On the photo's left side minor scarps or rather the material below, originating from the Aggenalm landslide mass, are visible.

Since the volume of 30,000 m³ for the debris flow, cited by the WWA ROSENHEIM (n.d.), doesn't even conform roughly to the missing volume of roundabout 135,000 m³, estimated by JUNG (2007: 44f.), it can be presumed that mass movements must have occurred prior to this event within the Agggraben or affected it, as the 1935 event did, for instance.

4.6.2.3 Secondary mass movements

The secondary mass movements that have been observed during the last five years were all small volume-wise and rather shallow (<2 m). Especially at the edges of the Aggenalm landslide and/or within the Agggraben debris flow small mass movements happened in succession to heavy rainfall. Just in June 2013 rainfall (170 mm within 24 hours, 320 mm over three days) initiated a small debris flow from the Agggraben main scarp, while at the steep toe of the Aggenalm landslide a translational slide covered the connection road (Figure 23). As mentioned before, the roadbed subsided on its downhill side at several occasions following spells of bad weather.

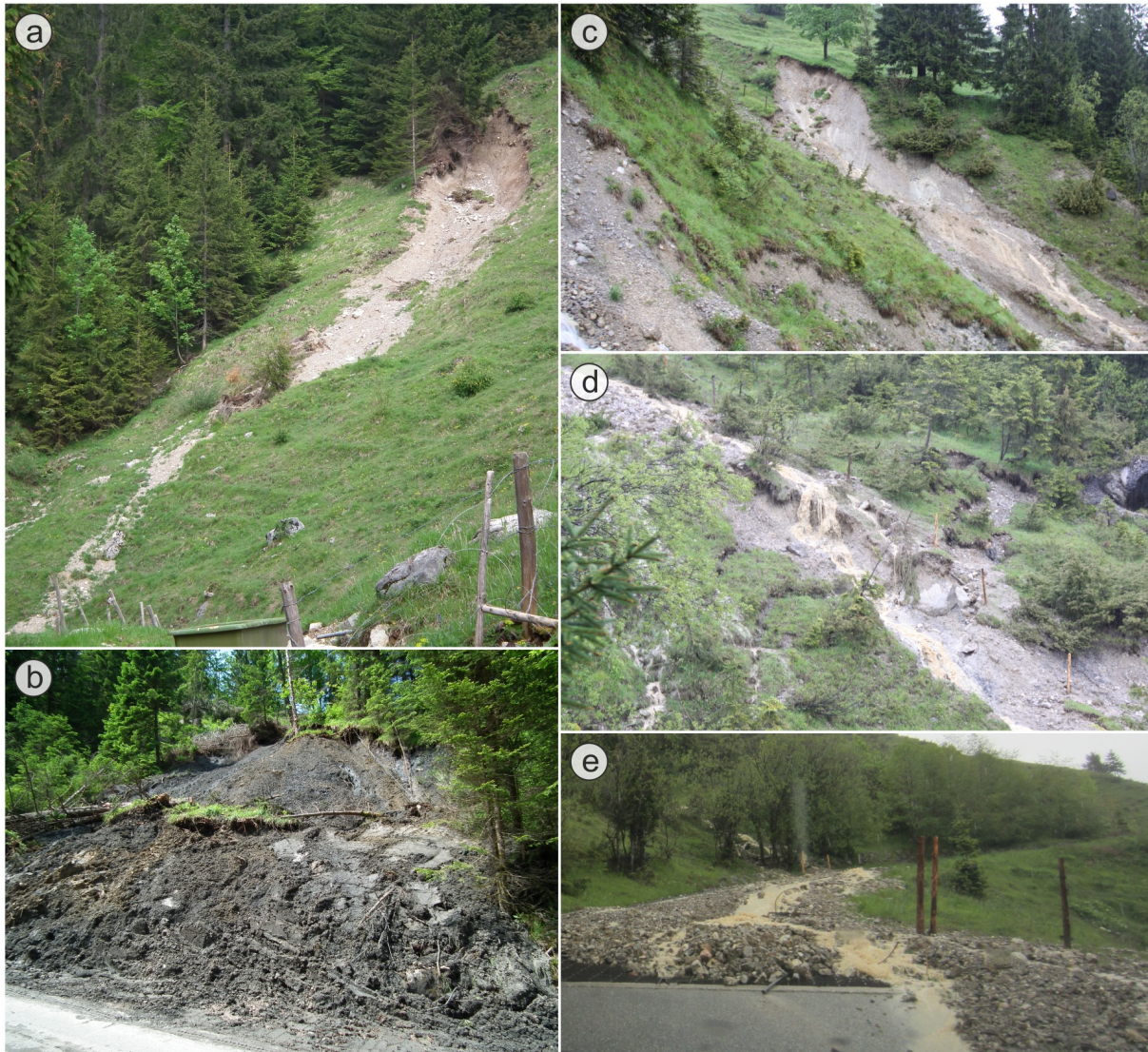


Figure 23: a) Small debris flow at the southern edge of the Aggenalm landslide, looking at it from the Aggenalm hut (No. 1). The debris flow has a width of approx. 3–4 m and occurred between late fall 2010 and spring 2011. b) Translational slide at the connection road to Oberaudorf in consequence of the heavy rainfall at the beginning of June 2013. Width: approx. 20 m, length: 15–20 m, depth: max. 2 m. c) –e) Debris flow occurring on June 2, 2013, in the Agggraben at the northern edge of the Aggenalm landslide. Its scarp is located within the main scarp from 1997 (c). The material was transported in the space of the bed of the old Agggraben debris flow (d) and ran over and accumulated on the connection road to Grafenherberg (e). (Photos c)–e) by courtesy of Stefan Schuhbäck)

4.6.3 Field investigations

While the Bavarian Environment Agency (LfU) conducted biannual measurements of the surface movements starting already in 2001, the drilling operations in 2007 and 2008 as well as the geoelectric survey in 2009 provided an insight into subsurface build-up of the landslide. Figure 24 shows the location of these investigative measures in relation to the run of the geological sections constructed also based on their results.

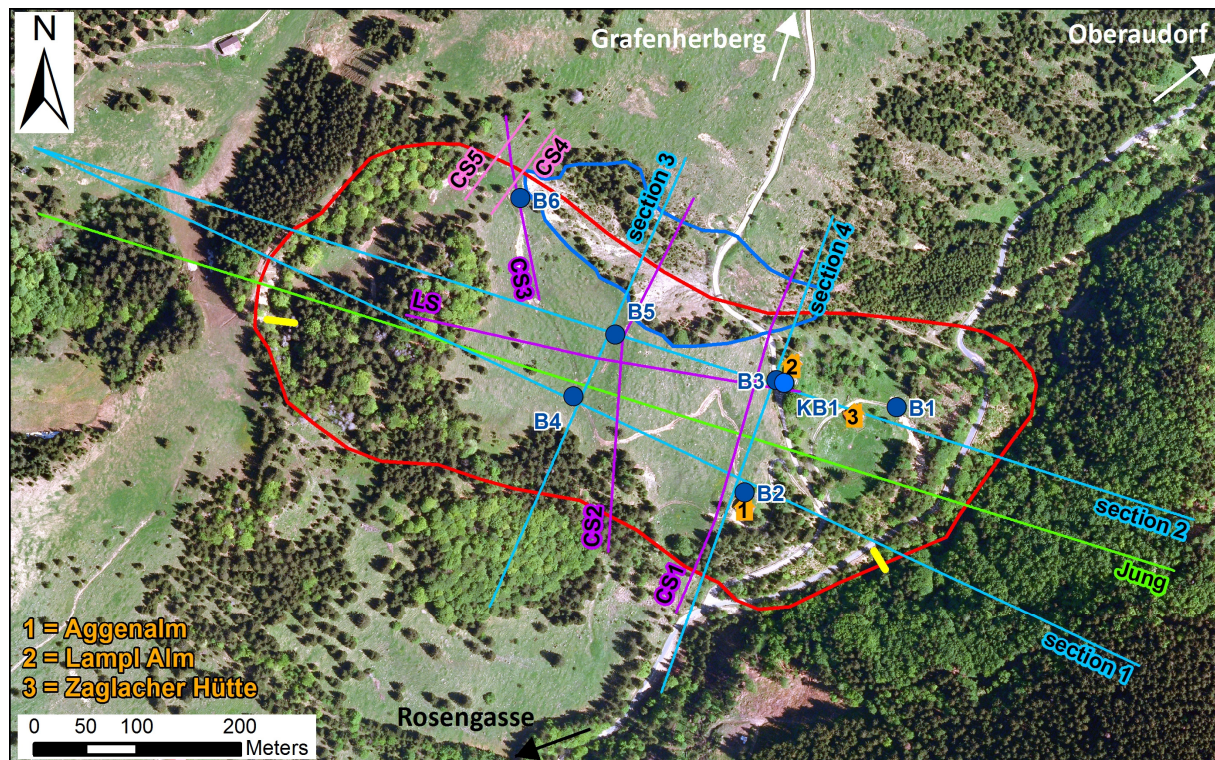


Figure 24: This figure displays the location of the different measuring sites as well as the run of the geological sections that have been constructed based on results of field investigation available at the individual time. The two yellow lines indicate the extensometers at the scarp and toe of the landslide that were installed in 2001 by the LfU. The boring campaign in 2007 and 2008 resulted in 7 bore holes, KB1 and B1–B6. While in 2009 the main geoelectric survey was conducted along four profiles, LS and CS1–CS3, a second survey was undertaken in 2010 along two short profiles, CS4 and CS5. (Geobasisdaten © Bayerische Vermessungsverwaltung 2010)

4.6.3.1 Extensometer and biannual geodetic survey (LfU)

After the 1997 landslide event within the Agggraben, the LfU acted by annual inspections and started a biannual geodetic survey as well as installed three wire extensometers (at the scarp and toe of the Aggenalm landslide) in summer 2001. The geodetic survey has been conducted along a line running across the landslide from top to toe as well as at points of special interest such as the three huts using a total of 21 measuring points. As a reference two additional points were chosen on stable ground, one at the counter slope and the other at the access road Oberaudorf-Rosengasse just east of the bridge across the Auerbach. During the eleven-year period (June 2001 through May 2012) quite homogeneous movement rates of 1.0–1.35 cm on average per year could be observed. Only one measuring point (point 40) showed a slightly deviant behavior with a mean movement rate of 1.9 cm annually (GALLEMANN 2012: 3ff.). As it is located east of the Aggenalm hut at the over-steepened toe of the landslide, it may point out according to GALLEMANN (2012: 6) that small secondary mass movements may happen more likely at this location (only about 10–15 m below this point a secondary movement occurred in June 2013 (Figure 23b)).

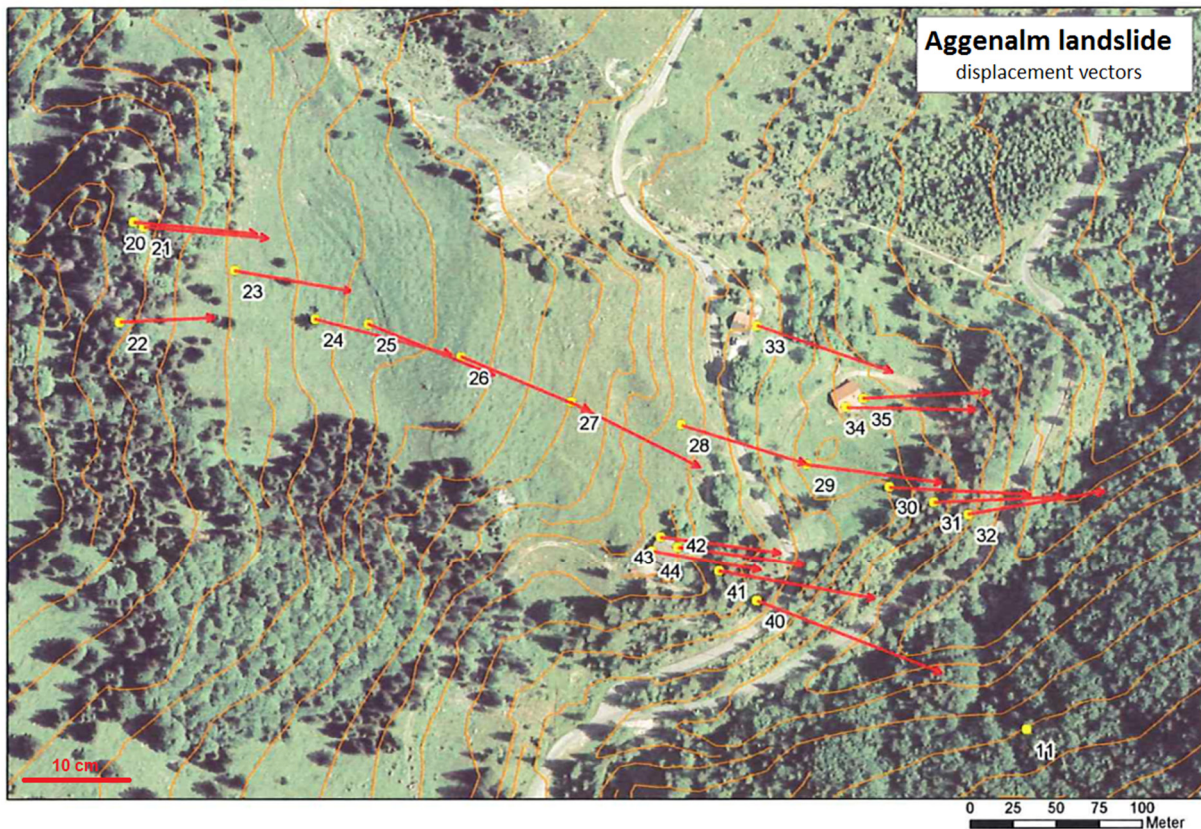


Figure 25: Displacement vectors of the geodetic survey with 21 measurement points along one central section across the Aggenalm landslide and at the three huts. The displacements accumulated over a period of 11 years (June 2001 through May 2012) are on average 1.0–1.35 cm/a, with an exception at point 40 reaching an average of 1.9 cm/a. (Geobasisdaten © Bayerische Vermessungsverwaltung 2010, GALLEMANN 2012: 5, Fig. 6)

The wire extensometers installed at the scarp and toe (for exact location see Figure 24) in general show a similar movement behavior of about 1 cm/a, but also display displacements of up to 25 cm that can be attributed to individual, small-sized secondary events. The results of the extensometer measurements as well as additional diagrams of the LfU geodetic survey are depicted in Appendix III.

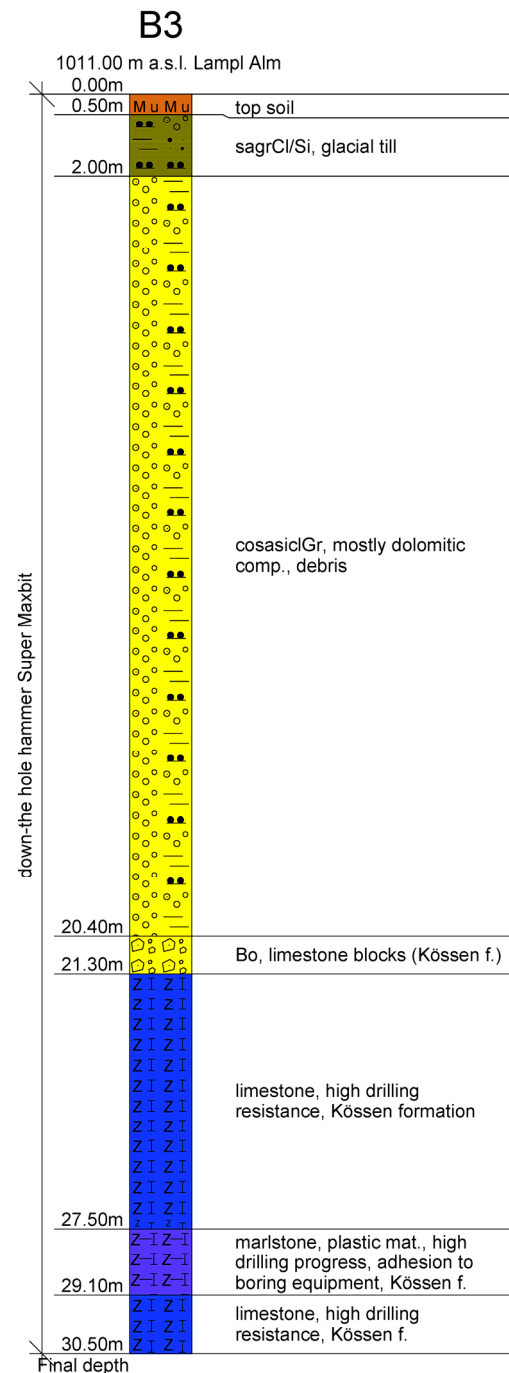
4.6.3.2 Reconnaissance borings

As part of the alpEWAS project drillings were carried into execution in order to gain additional information about the geological build-up of the Aggenalm landslide and to install subsurface measurement equipment in boreholes. The seven boreholes (Figure 24) were executed during fall 2007 and summer 2008. Based on the geological model by JUNG (2007) an approximate depth to reach the shear surface of the Aggenalm landslide was estimated. The final depth of the boreholes was adjusted again during the drilling operation, to reach the marls of the Kössen formation, as the required depth was relying on the assumption of the shear surface being within the marls of the Kössen formation. Due to problems arising during the first borehole (stability,

high loss of drilling fluid, jamming/wedging of casing, etc.) the method for the following was changed from coring (at KB1) to using a down-the-hole hammer and compressed-air flushing. This alleviated the boring process but downgraded the geologic information and complicated their interpretation as only the cuttings and dirt, blown out by the compressed-air flushing, could be evaluated in regards to lithology while structures were completely destroyed by the boring process.

As it can be seen in the boring logs (Figure 26, Appendix IV), material interpreted as glacial till and especially debris was logged to a depth of up to 25 m (B5), often with sections of particular blocky material in between, resembling the strongly disintegrating limestone and dolomite (Upper Rhaetian formation). At depths of around 20 m a dark-colored limestone (Kössen formation) was logged in the boreholes, B1, B3–B5, and KB1 with marls or marly limestones interlayering. In B6, which is located at the edge of the Aggenalm landslide, just west of the scarp of the Agggraben debris flow, the Kössen formation was already found at a depth of about 10 m. In contrary, in B2, located at the Aggenalm hut, Upper Rhaetian dolomite was logged starting at a depth of 9 m to the final depth of 32 m, where the borehole was abandoned due to mechanical problems.

Figure 26: Exemplary boring log of borehole B3, located at the Lampl Alm.



4.6.3.3 Geoelectric survey

In 2009 a geoelectric survey along four profiles (location see Figure 24) was conducted within the framework of STÖRZBACH's (2009) Master's thesis, in order to gain additional information about the subsurface structures and build-up.¹⁰ For the geoelectric sounding (resistivity) a multi-

¹⁰ An additional two profiles (CS4 and CS5 in Figure 24) were measured in 2010 within the scope of the bachelor's theses of HEPP (2010) and BAUR (2010). These theses aimed to investigate the influence of rainfall on the

electrode system with electrodes at a 4-meter interval (max. length of a section: 400 m) based on the Schlumberger array was used. Even though the resistivity of limestone and dolomite is not always sufficiently variable and overlaps, the marls' resistivity (e.g., marls of Kössen formation) should clearly be discernible lower due to higher conductivity (REYNOLDS 1997: 422, Tab. 7.1, KEAREY et al. 2002: 184). As a reference, the logs of the borings were incorporated into the interpretation of the geoelectric data. Additionally, due to the distinct topography and steepness of major parts of the Aggenalm landslide a topographic correction was introduced to the data analysis, as well.

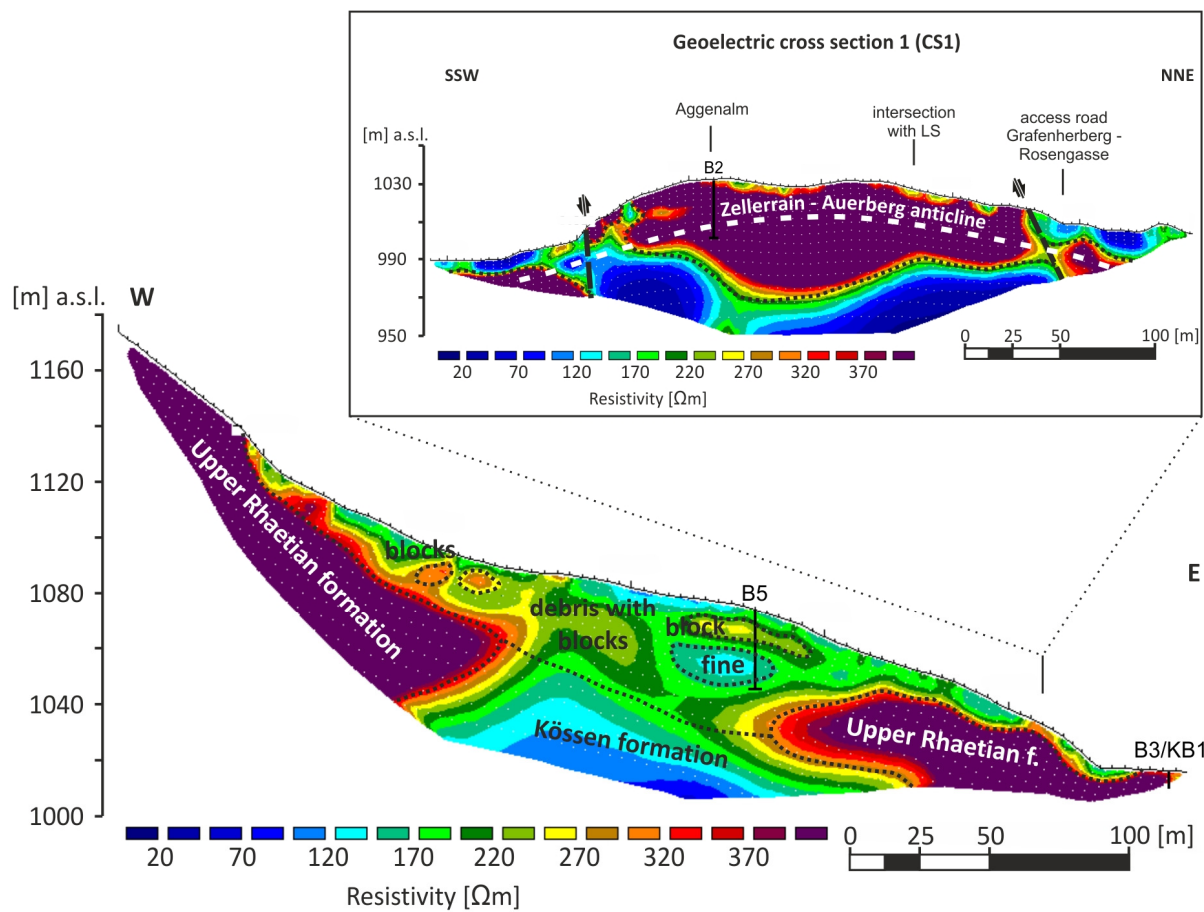


Figure 27: Interpreted geoelectric profiles (location see Figure 24) of the Aggenalm landslide (adapted from STÖRZBACH 2009, SINGER 2010: 154, Fig. 74).

The longitudinal section in Figure 27 displays a tripartite build-up of the Aggenalm landslide mass. The superior part, below the main scarp, is characterized by massive limestones and dolomites of the Upper Rhaetian formation, reaching a thickness of up to 100 m (not completely

groundwater table in the area above the scarp of the Agggraben debris flow by measuring the same profile repeatedly. Due to their task, only a short profile length was surveyed, resulting in a low survey depth. Geologically, their results show the heterogeneous build-up of debris, with different sized blocks, on top of fine-grained material (Kössen formation) as it can also be seen in Appendix V, Figure IV-4, but were rather inconclusive in regard to their main scope.

visible in Figure 27), overlain by a petering layer of Quaternary sediments and debris. The middle section is mainly built up by an inhomogeneous mass of debris, probably containing huge blocks of limestone but also areas of finer-grained material as it is also found in boring log B5 (Appendix IV). The lower third of the profile is again characterized by the Upper Rhaetian formation with a thickness of 50 m maximum.

In the cross sections (inlet in Figure 27, Appendix V), especially CS1, it becomes clear that the Aggenalm landslide is part of Zellerrain-Auerberg anticline (Figure 10), which is cut off at both flanks by faults (Mühlbach-Larchgraben fault in the north). The missing of a continuous Upper Rhaetian limestone layer throughout all three sections can be attributed to its tectonic history, like the folding, leading to a rupturing of the original layer, which remnants are nowadays rather individual, small to big slabs of Upper Rhaetian formation overlaying the Kössen formation.

In all geoelectric profiles with exception of the upper part of the longitudinal section it can be seen that the Kössen formation follows below the Upper Rhaetian formation. This can be attributed to the insufficient penetration depth of the geoelectric measurement, due to geometric causes, especially at the start and end of each profile. Also, no differentiation between marl and limestone banks of the Kössen formation can be made, because of geometric causes, as the banks' thickness (limestone) is clearly below the achievable resolution, which in addition decreases with increasing surveying depth.

4.6.4 Geological sections and landslide mechanism

4.6.4.1 Geological section by JUNG (2007)

Based on his detailed geological mapping JUNG (2007) constructed several geological cross sections (longitudinal and transverse) cutting through the Aggenalm landslide, one of which is shown in Figure 28.

From his findings of the various geological formations outcropping at the surface (Figure 11, Appendix I) as well as literature studies concerning typical thicknesses in the area for the different layers, as well as considering other restraints (such as geometry, tectonics, etc.), JUNG (2007) developed the cross section pictured in Figure 28 and a first hypothesis of the landslide's mechanism.

He suggested that at the upper slope the Upper Rhaetian limestone and dolomite with an approximately thickness of max. 40–50 m slowly sink into the plastically deforming underlying marls of the Kössen formation and thus the according mechanism is classified in accordance with CRUDEN & VARNES (1996: 38, Table 3-1) as a *rock spread*. The lower two thirds of the landslide mass with increasing deformation become more and more disintegrated changing their mechanism into a *very slow debris flow* of maximum 25 m of thickness, again overlaying the Kössen formation. The cavernous debris-flow mass mainly consists of disintegrated Upper Rhaetian limestone and dolomite, varying greatly in size, from gravel to rock slabs of several meters, mixed with Pleistocene deposits, especially at the surface. (JUNG 2007: 41)

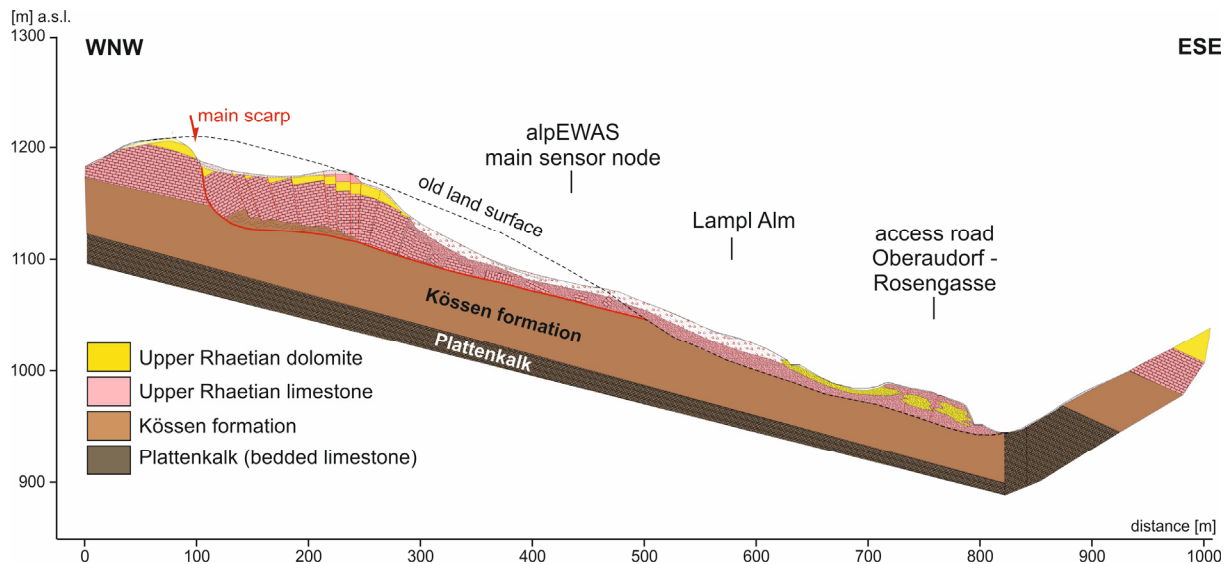


Figure 28: Longitudinal cross section through the Aggenalm landslide, the exact location of the section is denoted in Figure 11 and Figure 24 (JUNG 2007).

4.6.4.2 New geological sections and landslide mechanism

The results of the field investigations (drillings, geoelectric survey) show large deviations from the original model and thereby reinforce the need to incorporate the new findings and adapt the geological sections and perception of the landslide's mechanism.

Therefore, the new results from the boring campaign and geoelectric survey, led to the construction of several new cross sections, two longitudinal (section 1 & 2) and two transverse (section 3 & 4) to the landslide (Figure 11, Figure 29). In the upper part of the Aggenalm landslide (section 1 & 2) mainly the thickness of the Upper Rhaetian formation had to be adjusted from only 40–50 m to over 100 m at parts due to the geoelectric surveys results (Chapter 4.6.3.3, Figure 27). This is also in accordance with the findings of SCHORMAIR (2003: 17) who indicated a thickness of 150 to 200 m in the Sudelfeld area. Meanwhile the mechanism can still be classified as spreading or *rock spread* according to CRUDEN & VARNES (1996: 38, Table 3-1) and Table 1 on page 12, whereupon huge slabs of Upper Rhaetian formation sink into the underlying plastically deforming and decaying marls of the Kössen formation and slowly spread/move downhill.

Downhill, the thickness of the Upper Rhaetian formation decreases and generally becomes more and more disintegrated into individual blocks and slabs before it is then totally interrupted in the middle of the landslide, supposedly also due to its tectonic history as well as glacial and landslide evolution. Here, the subsidence and spreading of the downward moving limestone blocks cause the underlying Kössen formation to bulge toward the surface. In this part the Kössen formation is directly overlain by debris and Quaternary deposits, reaching a maximum thickness of approximately 40–50 m, and including different sized blocks of Upper Rhaetian formation (Appendix IV and V). Further downhill, the Upper Rhaetian formation is again found

at the surface (maximum thickness: approx. 40 m), displaying wide open crevices and a strong disintegration, which is likewise related to the subsidence into the underlying marls of the Kössen formation.

It can be assumed that the forces introduced by the downhill movement of the Upper Rhaetian formation not only led to an upward bulging of the Kössen formation in the middle section of the slope but subsequently resulted in the development of a shear zone within the Kössen formation and therefore a detachment of the whole rock mass from its base. Accordingly, the mechanism for the bottom two-thirds rather would be a *debris slide* than a *debris flow* (CRUDEN & VARNES 1996: 38, Table 3-1) as proposed by JUNG (2007: 41). This new interpretation and hypothesis is also supported by the results of the geodetic survey by the LfU (GALLEMANN 2012, Figure 25) as well as various alpEWAS measurement results, which show a quite homogeneous movement pattern throughout the Aggenalm landslide area. However, just as the description of the 1935 event suggested, a transition from sliding to flowing may happen, if the masses accelerate strongly and become saturated when reaching the Gassenbach.

The Agggraben mass movement originated from Quaternary deposits bulged upwards in the middle section of the Aggenalm in the ditch at northern flank of the Aggenalm landslide, where the material is additionally stressed by the Mühlbach-Larchgraben fault. Last in 1997, a *fast debris flow* was documented. Since then only small secondary flows were observed but further movements are probable following strong rainfall events, as this ditch also seems to serve as a major drainage for the area uphill as well as for the area of the scarp of the Aggenalm landslide.

The description and interpretation given above combines all the information gathered during the field investigations, drilling campaign, and geoelectric survey. These new geological sections and the according landslide mechanics presented, also explain why the different alpEWAS subsurface deformation measurements (inclinometer, TDR) failed to detect any movements due to an insufficient depth of the installations. On the contrary the results of the surface deformation measurements (Chapters 5.3.1, 5.3.2 and 6) and of the numerical model (Chapter 7) support the hypothesis of the landslide's mechanism.

Multiple terms and classification systems to describe large, deep-seated landslides have been presented in Chapter 3.1, several of which have been applied to the Aggenalm landslide (e.g., *Talzus Schub* by WWA ROSENHEIM (n.d.), *debris slide* by LfU (2010: 2)) or are applicable, only the nomenclature and classification by WP/WLI (1993a) and CRUDEN & VARNES (1996) has been used in this thesis. Summarizing, the Aggenalm landslide can be described as an active, complex, homogeneously moving, extremely slow, deep-seated mass movement, with a rock spread at the top third of the slope transitioning to an extremely to very slow debris slide downhill, which would be named a *complex, extremely slow rock spread-debris slide* (Table 1, CRUDEN & VARNES (1996: 38, Table 3-1).

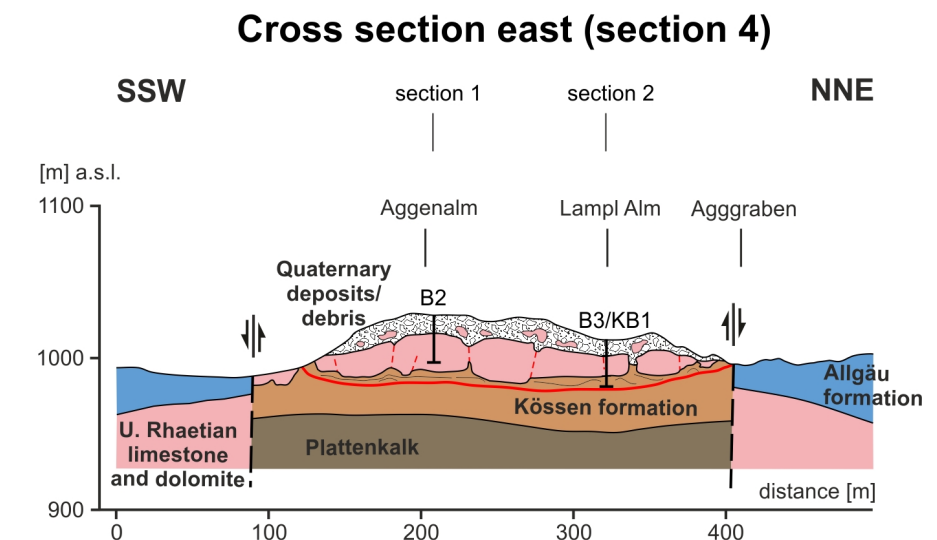
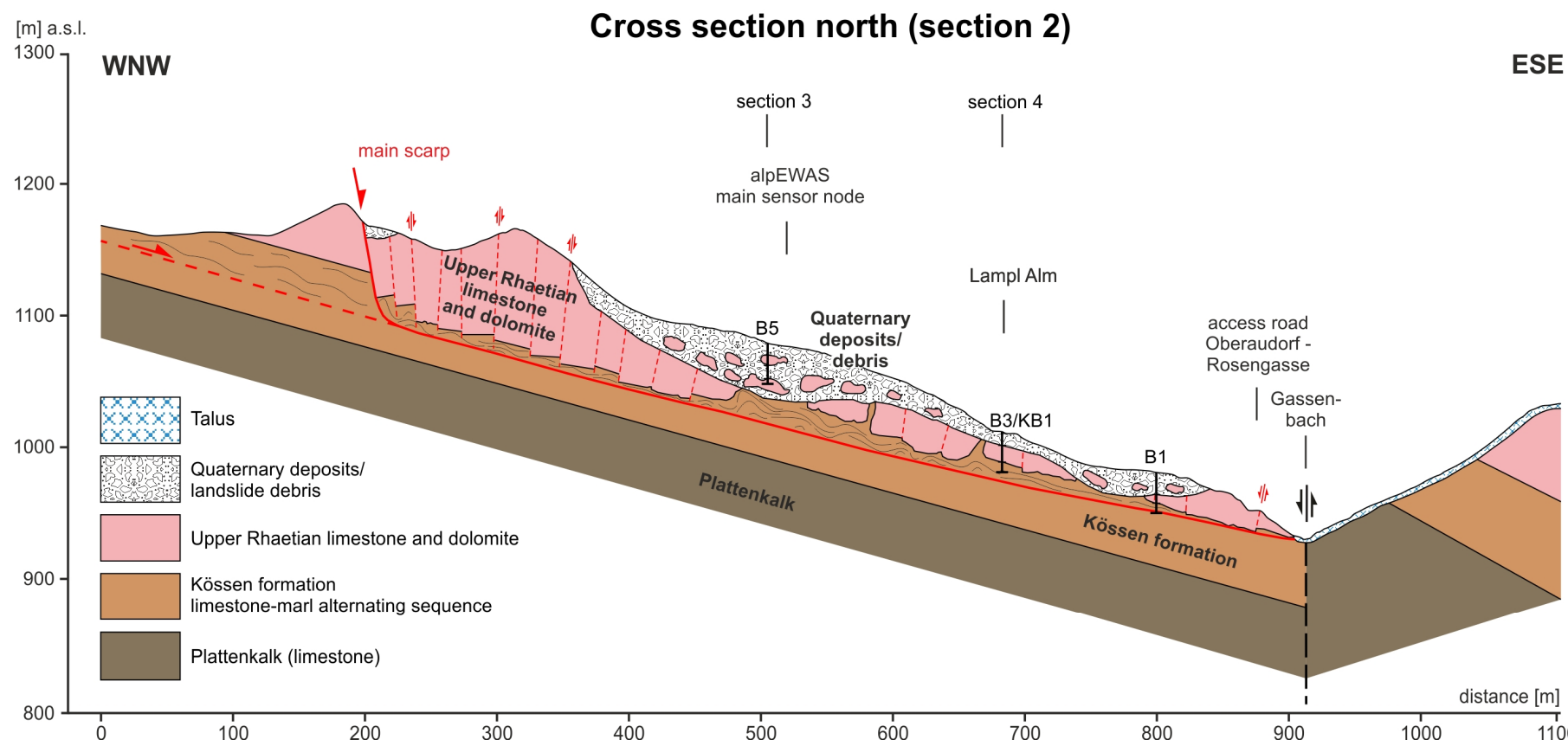
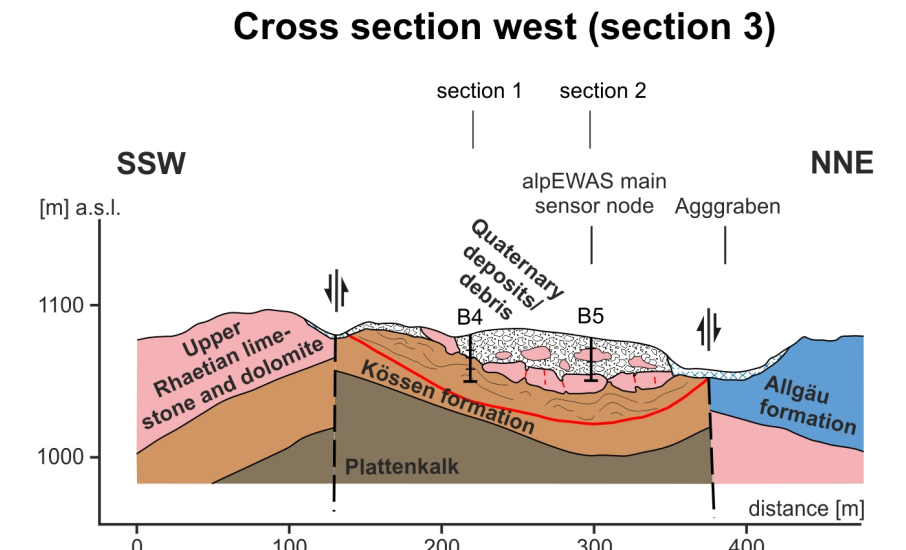
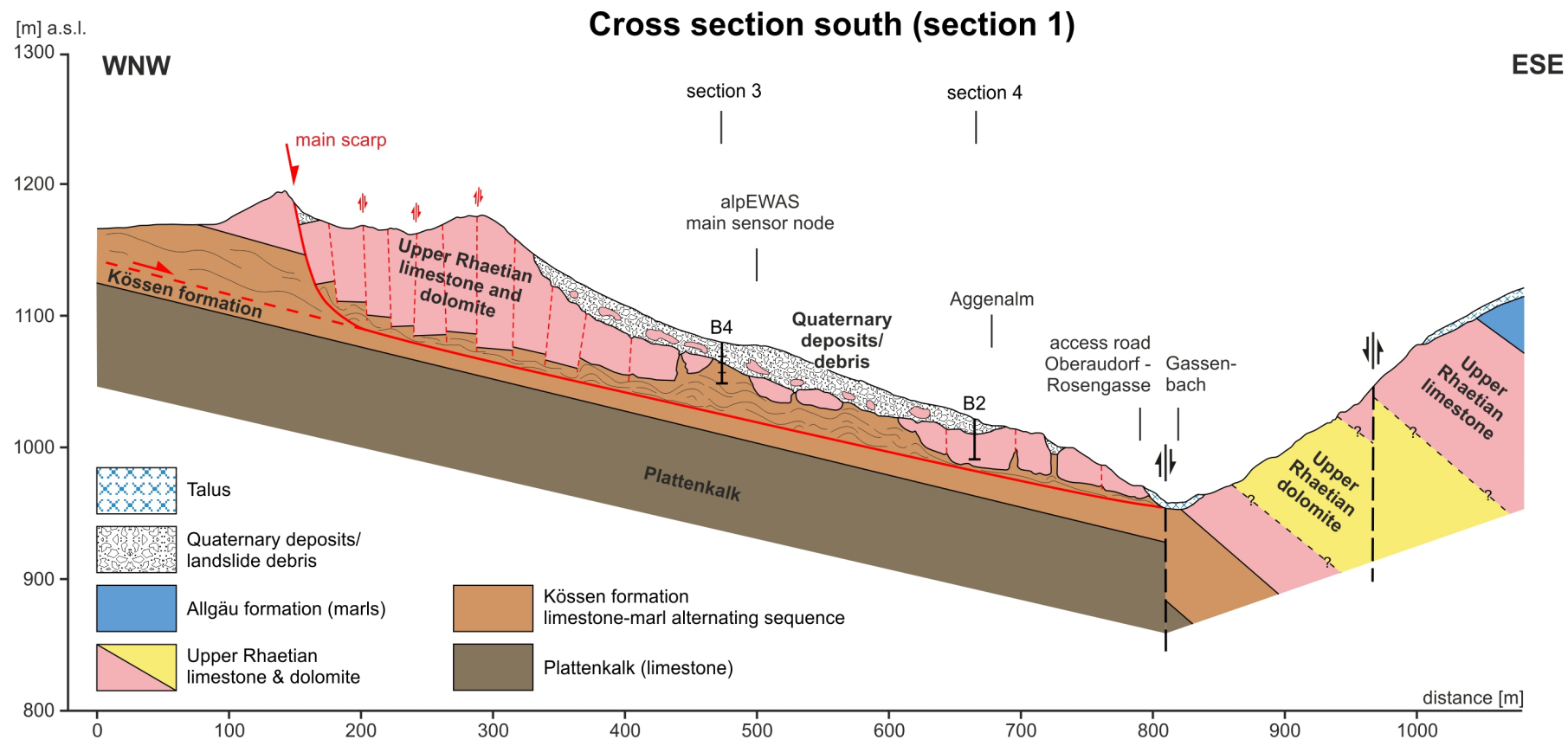


Figure 29: Geological sections across the Aggenalm landslide based on the data and new information acquired, e.g., by the drilling campaign and geoelectric survey. The location of the sections is depicted in Figure 11 and Figure 24.

5. Monitoring system installed at the Aggenalm landslide

In this chapter the monitoring system installed in course of the alpEWAS project at the Aggenalm landslide will be outlined. Its design and the different measurement techniques, on and below surface, are presented as are the individual results of each of the measurement systems.

5.1 AlpEWAS measurement techniques

As mentioned before three innovative deformation measurement systems were used and installed at the Aggenalm landslide, each overseen and advanced by one of the participating institutions.

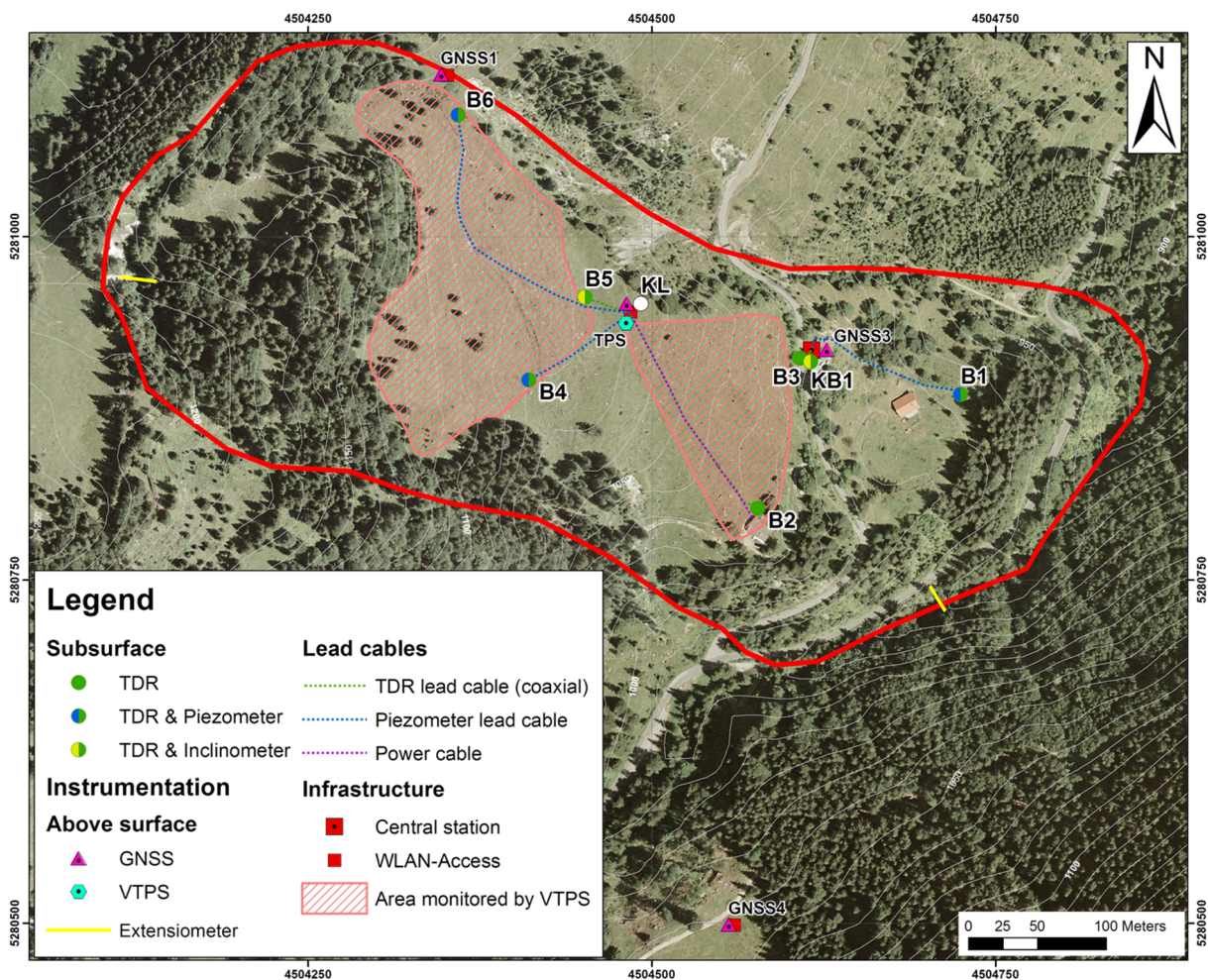


Figure 30: Orthophoto of the complex, deep-seated Aggenalm landslide, outlined red. The various measuring devices, and the geosensor network's infrastructure elements, and the area in the viewshed of the VTPS are marked on the image (FESTL et al. 2011: 3, Figure 2, Geobasisdaten © Bayerische Vermessungsverwaltung 2010).

The main three systems are time domain reflectometry (TDR) to monitor shear displacements subsurface, reflectorless video tacheometry (VTPS) and a low-cost global navigation satellite system (GNSS) to detect displacements on surface extensively over major parts of the landslide or punctiform, respectively. Even though these systems have been used before, aim of the alpEWAS project has been to enhance these techniques and to embed them into the geosensor network (THURO et al. 2013: 79ff.). Further already well-established techniques – such as inclinometers, crack meters, and extensometers for deformation measurements as well as several piezometers and a weather station, including a rain gauge to monitor potential causative and triggering factors – were installed at the Aggenalm landslide (THURO et al. 2011a: 18). For purposes of clarity, Figure 30 only pictures the location of the main measuring devices installed on surface and in boreholes at the Aggenalm landslide as well as the most important infrastructure elements of the alpEWAS geosensor network. Additional information regarding locations of measurement systems, reference points, and sections is displayed in Figure 11, Figure 24, and Figure 25.

5.1.1 Surface measurements

In this subchapter the different techniques to measure displacements on surface as well as potential triggering factors (precipitation measured by the weather station) are presented at which a special focus is laid on the two innovative main alpEWAS systems, GNSS and VTPS.

5.1.1.1 Reflectorless video tacheometry (VTPS)

The reflectorless video tacheometry system (VTPS) that has been installed on the Aggenalm slope (Figure 30, Figure 31) is overseen by the Chair of Geodesy of the Technische Universität München (TUM). Mainly WASMEIER (2009) has worked on the advancement of this technique and describes it in detail in his doctoral thesis, while the following description will only shortly outline this measurement technique.

Geodetic surveying methods to detect and measure deformation rates are often used and already well-established in, e.g., landslide monitoring. At slow-moving landslides with a low risk exposure, periodic measurements are sufficient, resulting in spatial displacement vectors at selected points on the slope. When using a traditional tacheometer, it is necessary to have long-lasting, permanent benchmarks or targets in the moving area that are unlikely to be damaged throughout time. At a high risk site with impending slope failure and a corresponding risk for men and goods, permanent measurements are necessary and are usually achieved by setting up the tacheometer on stable ground at a fixed observation point and by installing retro-reflecting target prisms on the fast moving landslide (THURO et al. 2009: 9f., 2011a: 32f.). Nowadays these modern tacheometers are usually motorized, computer-controlled and can automatically detect retro-reflecting target prisms using ordinary implemented CMOS or CCD sensors to assess the

reflected infrared radiation. With this technique, the execution of predefined periodical measurement cycles without human interference is possible just as the automatic forwarding of the results to the office via internet. (THURO et al. 2010a: 79)

These permanent tacheometric systems are quite cost-intensive (equipment, power supply, data connection, and software) and in need of regular maintenance but are suitable to serve as EWSs due to their continuous observation of surface displacements. Therefore, the tacheometric sensor is often the most expensive element of such monitoring systems, as it is the case in the alpEWAS project, too. As one of the aims of the alpEWAS project has been to find economic and cost-effective solutions for landslide monitoring, additional costs concerning installation and target prisms were minimized by using a special reflectorless video tacheometer (VTPS). (THURO et al. 2010a: 79ff.)

In theory, reflectorless tacheometry allows one to forgo permanent, retro-reflecting target prisms in the affected area, while still performing high precision measurements. At the moment, this technique is still in its infancy and prototypical in deformation measurements, while the long-term aim for this reflectorless tacheometer technique is to only use natural target objects such as rock surfaces, and observe them repeatedly (SINGER 2010: 162f.). This minimizes not only the installation costs (targets) and decreases the time of stay of the personnel in the hazardous and/or difficult to access area but also adds the possibility to monitor areas where a reflector installation isn't realizable (e.g., debris flows). Additionally, reflectorless tacheometry raises the targeting flexibility, allowing easy adjustment to the observation range of the tacheometer to the respective situation (THURO et al. 2009: 11f.).

Next to the use of reflectorless tacheometers the other technical innovation is to use video tacheometry by replacing the eyepiece of the tacheometer with a high resolution camera and thereby displaying the field of view. By radiometric and segmentation operators the images are normalized before intensity/edge-based-matching detection-algorithms are used to automatically select target points from the image for tacheometric deformation measurements. (THURO et al. 2011a: 34f.)

An off-the-shelf prototype (IATS – Image Assisted Total Station) of such a VTPS by Leica Geosystems (www-14) has been used in the alpEWAS project. The eyepiece of this tacheometer has been replaced by a 5 megapixel CMOS colored camera. Additionally, it has been altered so that all controls and data can be accessed remotely, while still all functions of a generic tacheometer are maintained. Due to a suitable calibration, which incorporates a changing imaging geometry when refocusing, and temperature variances as well as device errors, a spatial direction can be assigned to each pixel value at any telescope position. On the basis of the high resolution camera, of the 30x telescope magnification, and of detection algorithms working on a sub-pixel basis, relative resolutions of <0.1 mgon within the image can be attained. In absolute terms, thus the accuracy of the overall system is determined not by the camera but by the pitch resolution of the tachymeter. In an uncontrollable measurement environment significant restrictions may result, e.g., due to different refraction effects (scintillation, air flickering), so that the

resolution decreases to about <2 mgon. Adapted to these conditions, evaluation strategies such as the integration over multiple frames enhance the results ultimately to about 1 mgon. (WASMEIER 2009, THURO et al. 2010b: 6f.).



Figure 31: a) Photograph of the alpEWAS main sensor node located on the middle part of the landslide. On the far left pole the GNSS receiver is mounted, on the poles to the right follow the weather station and on the next one the directional antennas ensuring the connection to other GNSS sensor nodes. The VTPS (inset b)) is installed on the pillar and a webcam and a satellite dish for the internet access are fixed to the right pole. In the measuring box, the TDR devices are installed amongst others. (Photo b) by courtesy of John Singer)

The VTPS has been installed on a pillar at the main sensor node (Figure 31) at the middle of the Aggenalm landslide overlooking major parts of the upper/middle slope (area of visibility is hatched in Figure 30). In this case mostly rock blocks surfacing at the landslide were used as natural targets. As the tacheometer is only in a prototypical stage, it was not set up permanently at the alpEWAS test site, but rather installed for periodic measurements, since also a lot of testing was performed under laboratory conditions.

5.1.1.2 Global navigation satellite system (GNSS)

The other main deformation monitoring system on surface that has been installed in course of the alpEWAS project is an all-weather-proof, low-cost global navigation satellite system (GNSS) which has been developed and is overseen by the staff of the Institute for Geodesy at the Universität der Bundeswehr München (UniBw Munich). A more detailed description of the measuring system, its components as well as its assets and drawbacks can, amongst others, be found in (GLABSCH et al. 2009: 181f., THURO et al. 2010a: 84ff., THURO et al. 2011a: 36ff.).

For such a monitoring task, solely a carrier phase (CP) based GNSS method, specifically precise differential GNSS (PDGNSS) comes into question, as it can achieve accuracies within the range of a few millimeters only. With this technique CP measurements are recorded over an arbitrary and freely selectable period of time at the different sensor nodes in the investigated area. Usually, a 15-minute interval with a recording frequency of 1 Hz is chosen for the CP-raw-data acquisition, which, however, depends on various factors, such as the chosen receivers themselves, the expected velocity¹¹ at the individual measurement points and the satellite visibility. (THURO et al. 2010a: 84f.)

During each acquisition period independent position solutions are obtained which then are automatically forwarded to a central computing station. Here, the baseline processing of the raw data starts immediately. This complete process, acquisition of position solutions over a certain time span, automatic transfer of raw data, and prompt baseline processing is usually referred to as near-real-time processing (NRTP). This near-real-time approach does not stand in any contradiction to the use and implementation in an early warning system, as long as the time needed for acquisition, transfer, and processing has been adapted to the expected movement rates of the investigated process and necessary advance warning times. GLABSCH et al. (2009: 182) gives a more detailed description of the NRTP PDGNSS approach and its technical realization.

The NRTP method is not only restricted to high-end receivers but can also be conducted using low-cost of-the-shelf receivers as long as the receivers have the possibility to read out the CP raw data. Unfortunately, only few of these simple navigation receivers have the ability of an independent phase-based positioning solution like customary rovers, but solely use the CP data for internal smoothing operations. The few sensors that do allow the output of raw data can usually easily be linked to a geosensor network (GSN) via a serial RS232 interface. (THURO et al. 2010a: 85)

Under the low-cost approach within the alpEWAS project, antennas (Novatel Smart Antenna and Novatel Smart V1G Antenna) in the price range of about 800–1200 € each were chosen (THURO et al. 2011a: 39, Table 5), that allow phase tracking of the American GPS and the

¹¹ The velocity of the investigated process should be low compared to the chosen time interval, as it is assumed that during a single acquisition period the measuring point isn't moving and thus the process' dynamics do not interfere with such a time interval (GLABSCH et al. 2009: 181f.)

Russian Glonass satellites. At the Aggenalm landslide, four of these GNSS receivers have been installed, of which one has been positioned as a reference station (GNSS 4) on stable ground across the valley on the Gassenleite. The other three sensors/rovers are distributed over the landslide. Rover one (GNSS 1) is positioned in the top third of the landslide, right at the northern edge just a few meters above the main scarp of the 1997 debris flow event. Rover two (GNSS 2) is located at the main sensor node and the third rover (GNSS 3) is mounted on the roof of the Lampl Alm. GNSS #1 and #4 were designed as autarkic nodes and consist of the GNSS receiver, a WLAN antenna for transmitting the data to the central computing station, and a solar panel for power supply, all installed on poles about 2 m above ground (Figure 32 a)–c)). The corresponding modules, such as backup battery, charge controller, and wireless device server are located in a metal box. Figure 30 pictures the position of GNSS nodes on an orthophoto and Figure 31 as well as Figure 32 show pictures of the individual sensor nodes.

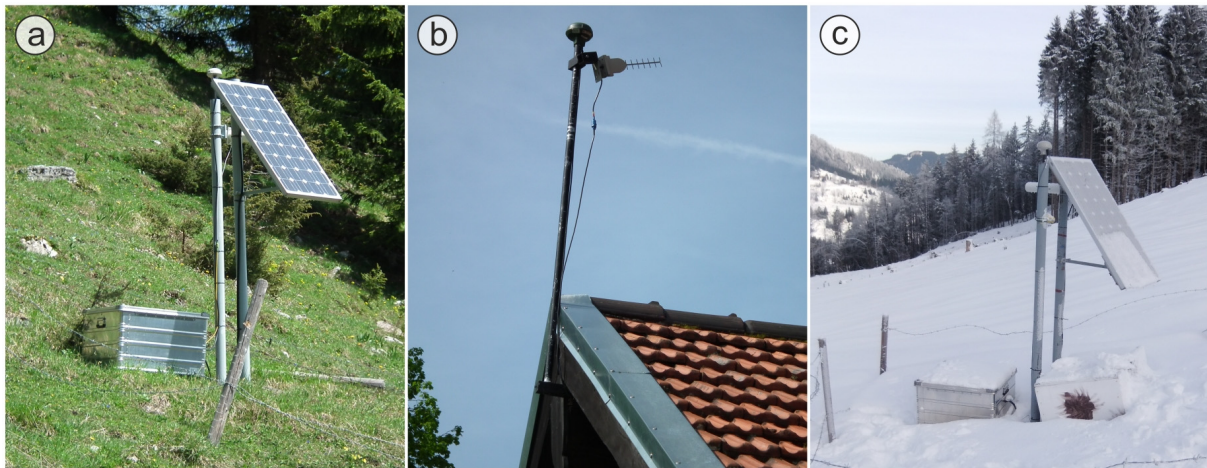


Figure 32: GNSS sensor nodes installed at the Aggenalm landslide. Two of the three rover stations, a) autarkic node GNSS 1 and b) rover GNSS 3, as well as the equally autarkic reference station, c), are pictured. (Photo c) by courtesy of Christoph Körner)

The geographic situation of the Aggenalm landslide at an elevation of 920–1200 m a.s.l. entails some unfavorable effects. Due to its position within the mountains, especially because of the high mountain chain in the south, and the area's general topography, negative impact on the GNSS capability as a consequence of shadowing effects has to be accounted for. Thus, during such a phase with only a few satellites in view, an inaccurate position solution or even no reasonable solution for a 15-minute interval can result.

Other adversary effects may occur due to weather conditions even though the system has been explicitly designed for harsh outdoor conditions. Heavy snowfall can lead to an increased possibility of either small signal disturbances or even failure of an entire sensor node. However, the most problematic situation in such a mountainous environment is that a sensor node – including solar panel, GNSS receiver, and WLAN antenna – becomes completely snow covered

for a period of time (this actually already occurred, although the solar panel and the antennas are installed on poles at about 2 m above ground for exactly this reason). Though the autarkic GNSS nodes (#1 and #4) can operate without any recharge for a couple of days, they are taken out of service before a deep discharging of the battery occurs until the solar panel picks up charging again. Since these types of weather conditions are usually apparent a few days in advance, there is time to consider and take remedial action, such as connecting a fuel cell for additional/alternative power supply. One of these fuel cells is installed permanently during the winter months at GNSS 4 due to the minimal solar radiation (less than two hours of sunshine per day) to stabilize its power supply (even though it is not completely covered by snow at all times). (THURO et al. 2010a: 85f.)

5.1.1.3 Additional deformation measurement systems on surface

Several additional deformation measurement systems on surface have been installed and/or conducted at the Aggenalm landslide. These systems are a periodic geodetic survey and wire extensometers (overseen by the LfU), as well as simple crack monitors and several corner reflectors. None of these systems is incorporated into the alpEWAS geosensor network and data management but monitored and evaluated manually.

Geodetic survey and wire extensometers

Already prior to the initiation of the alpEWAS project the Bavarian Environmental Agency (LfU) conducted a biannual geodetic survey on the Aggenalm landslide and installed a total of three wire extensometers, one at the scarp and the other two at the toe of the landslide. After the start of the alpEWAS project these measurements were continued but partly on a larger interval (once a year to every other year for the geodetic survey) (GALLEMANN 2012). The course of the measurement profiles, the location of the extensometers and the respective results have already been described in Chapter 4.6.3.1 of this thesis and are depicted both in Figure 25 and Appendix III. In summer 2013 two additional extensometers have been affixed at the landslide's scarp and will hopefully add new information to the landslide's dynamics at the scarp.

Crack meters/monitors

Two very simple crack meters/monitors have been installed at the onset of the alpEWAS project in June 2008 on the outer walls of the Aggenalm hut (hut No. 1, NNE and WNW side of building) to monitor the movement along two major cracks (see picture b) in Figure 21). These crack monitors consist of two mutually displaceable plastic plates, which can be fixed at zero by pegs during installation. A grid (−25 mm to +25 mm horizontally and −10 mm to +10 mm vertically) is applied on the rear monitoring plate, while a cross-hair is painted on the front plate, so that both a horizontal (either opening or closing of the crack) and vertical displacement can be read off (www-15). Additional spigots on the monitors allow using a caliper to get an even more accurate reading (± 0.1 mm) than using the cross-hair, which on the other hand is

more practicable as it can easily be documented by photo to be able to confirm the reading at a later time (Figure 42).

Corner reflectors

Several low-cost corner reflectors (CR) of different makes have been installed at the project site in 2011 in course of an add-on project using the infrastructure already in existence as well as the results of the other measurement systems for comparative reasons. The CRs (one can be seen in Figure 31 in the lower left corner) serve as persistent scatterers (PS) to measure movement rates of landslides by means of the D-InSAR method (differential interferometric synthetic aperture radar). Only for the sake of completeness, this measuring system is mentioned here, but no further details will be given in the following, since a short outline of this project can be found in SINGER et al. (2012) while PLANK (2012) describes the techniques used as well as first results in detail in his dissertation about exactly this subject.

5.1.1.4 Weather station

As weather station a semi-professional Davis Vantage Pro2 (www-13) weather station by Davis Instruments Corp. has been used. While it is not quite as accurate as professional systems, it is a very good choice with regard to the cost-effective approach of the alpEWAS project. All sensors (temperature, humidity, barometric pressure, wind speed and direction, rain collector) of this weather station are combined into one easy-to-install package. The Vantage Pro2 console provides the user interface, data display and calculations, but also contains a RS-232 (or USB) interface that has been used to integrate the system (by developing a sensor plug-in) into the alpEWAS geosensor network instead of using the standard accessory user interface. Due to the system's large data storage capacity and backup batteries to overcome power shortages as well as errors during communication, there has been no data loss since the beginning of the automatic data recording, making it an extremely reliable system (SINGER 2010: 163). Figure 31 pictures the sensors (rain collector and the anemometer can be seen) installed on one of the poles at the main sensor node, while the console is located within the measuring box.

The rain collector of the Davis Vantage Pro2 weather station uses a tipping bucket to measure 0.2 mm of rain with each tip, thereby also indicating the resolution range/accuracy. To ensure the continued use in winter, heating is installed within the rain collector during the winter months, which melts¹² the snow, so that precipitation measurements can be continued by the rain collector. The Vantage Pro2 weather station measures the atmospheric pressure at the station's location and then consistently translates it into barometric pressure with the help of the location's altitude that has been entered during setup. The barometric pressure measurements have a nominal accuracy of ± 1.0 hPa and are needed to correct the readings of the piezometers, for instance. Two temperature sensors are included in the weather station, one for inside (console) and another one for outside (outside station) temperature measurements, both with a resolution of 0.1 °C and reaching an accuracy of ± 0.5 °C (DAVIS 2012: 49f.). The

¹² During heavy continuous snowfall, the melting process can lead to a short temporal delay in the recording.

outside temperature is used in all graphs in this thesis, as the inside temperature is measured within the measuring box (Figure 31), which includes a heating and ventilation system.

5.1.2 Subsurface measurements

Subsurface, in the boreholes scattered across the landslide, measurement systems to both detect deformation and interstitial water pressure were installed, of which the time domain reflectometry (TDR) system is the third innovative technique focused on in the alpEWAS project. Subsequently, the TDR technique, as well as the other subsurface measurement systems will be outlined.

5.1.2.1 Time domain reflectometry (TDR)

The third one of the three innovative techniques of the alpEWAS project is time domain reflectometry (TDR) which has been developed and is overseen by the Chair of Engineering Geology, TUM. A circumstantial description of the TDR technique, its basic principles, advancements, pros and cons, and application spectrum, especially to landslides is given by SINGER (2010) in his doctoral thesis in great detail as well as in SINGER et al. (2006) and THURO et al. (2011a, 2014).

So far, time domain reflectometry has been known primarily from soil moisture measurements; however, with only small modifications it can also be used for monitoring locally discrete shear deformations, such as for monitoring landslides or displacements between structure elements. This ambit was limited mainly to America up to now, where the technique was used in slope monitoring (DOWDING et al. 1989, KANE & BECK 1994, 1996) and advanced at the Northwestern University (Evanston/Chicago, Illinois) under the auspices of Ch. Dowding and K. O'Connor, certainly demonstrating the usefulness of TDR as a landslide monitoring technique (O'CONNOR & DOWDING 1999).

The TDR measurement method, which was originally developed and used in the cable and telecommunication industry for the detection of faults and cable breaks, is based on the principle of radar and is therefore also referred to as cable-based radar. Basic principle of all TDR applications is the analysis of reflection characteristics of electromagnetic waves in the cable (O'CONNOR & DOWDING 1999: 15ff.). Time domain reflectometry essentially consists of two components: a TDR device that emits electromagnetic pulses and a transmission line, for which mostly coaxial cables are used. By the known propagation velocity (almost speed of light) and the time difference between transmitting and receiving the signal after reflection from an impurity (or end of cable, which is an impurity, too), the removal (usually depth in landslide monitoring) of this impurity can be calculated at the encoder (TDR device) (FELLNER-FELDEGG 1969: 616). An analysis of the received signal (amplitude, width, shape) then allows one to estimate amount and type of deformation.

TDR has indeed many favorable characteristics – such as cost-effective installation, continuous measurements, remote data transmission, and, with minor adjustments, variable measurement

applications (shear deformation, soil moisture, water level, and snow height and density). Thereby it offers an interesting alternative to inclinometers which are usually used. However, up to now TDR can only determine the depth of the shear zone and just make a semi-quantitative statement regarding the amount of deformation. This is due to the interaction between rock mass and built-in materials (cable type, grouts, etc.), which may attenuate the transmission of the movements onto the cable causing ambiguous signals (identical signals that represent different types and amounts of deformation). To establish TDR as a deformation monitoring technique and to resolve these problems/disadvantages, a system for calibrating the TDR deformation measurements was developed at the TUM. This allows making statements about the deformation mechanism and interpreting the up to now ambiguous signals on the basis of laboratory calibration tests (SINGER et al. 2006, FESTL 2008, SINGER 2010).

Mode and dimension of deformation, type and length of cable, as well as type of grout greatly influence the received signals and can be ambiguous, if not considered in the analyses. Therefore, extensive laboratory testing was performed in course of several theses (FESTL 2008, WOYTOWITZ 2008, FÜBL 2009, MEHNERT 2009, RÖHRL 2010, SINGER 2010) in order to overcome these ambiguities. For this purpose, artificial specimen (semi-rigid coaxial cable CommScope P3-500 JCAT encased in grout) were prepared and once hardened sheared under known, constant conditions in a specially designed shear apparatus. By testing different types of lead cable as well as variable lengths (different damping features), umpteen grout compositions (variable mixture between water, cement, bentonite, cement additives), variable diameters of specimen, and different deformation modes, especially variable shear widths, it was possible to analyze the individual influences and create an abundance of calibration curves for use in the signal analyses. With the help of these results, installation standards for different types of movement and velocities were defined (Table 13 in SINGER 2010: 98).

Specifically for the task of signal analysis, SINGER (2010) has developed a program (TUMTDR Analysis) by means of the graphical development environment LabView by National Instruments (www-16) to firstly manage the large amounts of data and secondly accomplish the complete processing automatically – from data readout up to display and storage of results. Prior to the automated signal analysis, the installation parameters must be defined and according calibration curves, if not already existing, have to be generated by laboratory tests. The signal analysis itself consists of several steps: Zero reading and following readings, signal recognition, parameterization, signal correction, validation, and analyses of deformation mode as well as deformation amount, for which the relationship between signal strength and deformation amount in the polynomial calibration curves is needed. This installation procedure now allows a quantitative determination of the amount of deformation. More details concerning the variable influencing factors, the steps of the laboratory tests as well as the signal analysis can be found in SINGER (2010) and THURO et al. (2011a).

When using TDR for landslide monitoring, the measurement cable is installed in a borehole, and force-fit connected to the surrounding rock mass by grout (Figure 33). Based on the installation suggestions mentioned above, a compliant grout–cable combination has to be chosen, taking into consideration the expected mode and rate of deformation in context with the surrounding rock mass. Additionally to an independent installation (TDR in a borehole of its own), it is an option to install the TDR cable parallel to an inclinometer in a borehole or into an inclinometer casing, which became unusable due to shearing, to prolong the measurement period. With these other two installation options it is yet not possible to quantify deformation due to the interaction between coaxial cable and inclinometer casing, since it hasn't been considered in the calibration tests (SINGER 2010: 105ff.).

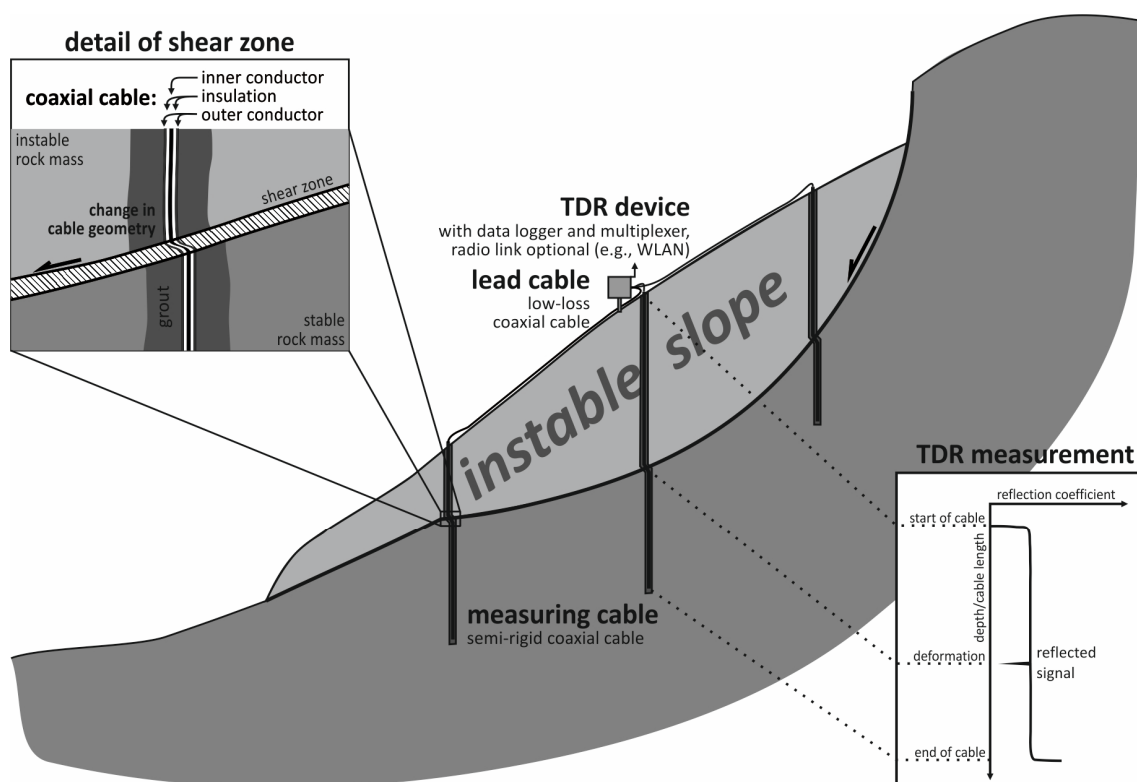


Figure 33: Schematic depiction of the setup of a TDR measurement system for monitoring subsurface deformations. The coaxial measurement cable in the borehole, which penetrates the landslide's basal shear zone, is coupled force-fit to the surrounding rock mass by grout. On surface it is connected to a TDR device via a low-loss coaxial lead cable. (SINGER 2010: 21, Fig. 7)

At the Aggenalm landslide eight TDR cables were installed in the seven boreholes (Figure 30), described in Chapter 4.6.3.2 and in Appendix IV, where also the individual interior work of each borehole is pictured. In KB1 and B5 instrumentation parallel to the inclinometer casings was carried out, while in B1, B4, and B6 TDR has been installed parallel to piezometers¹³,

¹³ Aim of piezometers in landslide monitoring often is to measure the pore water pressure within the deformation zone and they are therefore installed as close as possible to it. But the typical piezometer installation setup isn't

which don't influence the measurements as much, as long as the piezometer isn't installed within the assumed deformation zone but rather above or below, as it is the case at the Aggenalm setup. In the other boreholes TDR has been installed independently, e.g., in B3 only a few meters apart from KB1, which helps to better interpret the results of an installation parallel to an inclinometer casing. In order to keep the cable more or less centered within the borehole, spacers were attached to the cable in a one-meter interval prior to installation (except for installation parallel to inclinometers, where the TDR cable was bound to the outside of the casing at intervals). The high permeability of the strata made it necessary to adjust the grout composition by adding more solids at the first borehole setup, therefore altering the preselected grout composition. Further on, to be able to use the preselected grout, a thick plastic hose was added around the cable (and spacers) to decrease the draining.

On surface a flexible coaxial cable (Ecoflex 15) was used as lead cable¹⁴, connecting the measurement cables in the borehole with the TDR device (Figure 33) at one of the two main stations (middle of slope and at Lampl Alm). Due to the pasturing in the summer months, the lead cable had to be laid underground, in trenches about 20 cm deep, in order to protect it from damage (for approximate running of lead cables see Figure 30). The lead cables are connected to the TDR device via a multiplexer, which makes it possible to monitor several measurement cables simultaneously at a preset frequency. The device itself is controlled by the Campbell Scientific CR1000 data logger, which also functions as preliminary data storage until the data is collected via WLAN by the alpEWAS Control Software (Chapter 5.2). Thus the intermediate data caching increases the reliability of the system considerably, for example, during a temporary disturbance of the wireless connection. The integration into the alpEWAS GSN is achieved by the just mentioned alpEWAS Control Software and the according sensor plug-in for the CR1000 data logger and thus allows for a direct automatic analysis of the data received by the TUMTDR Analysis program and a remote access as well as control of the measurement program. (THURO et al. 2011a)

5.1.2.2 Inclinometer

For reasons of comparability two inclinometers were installed (in KB1 and B5, Figure 30) in addition to the TDR measurement system, with TDR measurement cables on the outside of the inclinometer casings, in spite of the disadvantages for TDR evaluation in this installation setup (Chapter 5.1.2.1).

favorable for TDR measurements, as the piezometric sensor is embedded into a loose gravel layer, which is sealed by water-impermeable bentonite (compressed pellets) above and below. This setup opposes a reliable transfer of the deformation of rock mass to the TDR cable and should therefore be avoided by an installation above or below (including gravel and bentonite layer).

¹⁴ Some of the lead cables are considerably longer than the 100 m suggested by SINGER (2010: 63ff., 157f.) mostly due to economic constraints of the alpEWAS project. Even though this hinders a quantification of deformation from the signals, they can still be used for event notifications (B6) and can be measured manually without the lead cable for deformation quantification, if necessary.

For the measurements a system by SISGEO S.r.l. (www-17) has been used. The inclinometric probe works with a servo acceleration sensor which is able to measure the angle of inclination in two orthogonal planes in unison (biaxial), so that only two measurements (first set of readings and second set in opposite groove) have to be conducted at a time. The probe, which is connected to the data logger via a measurement cable, is lowered to the base of the inclinometer casing running in two opposite grooves (of four) and is then slowly pulled toward the top in 50 cm increments with the help of a pulley wheel assembly (Figure 34), taking readings manually at every stop. The sensor gauges the inclination (α) of the probe to the normal and displays the reading as $\sin \alpha$ multiplied by a probe-specific constant (20,000) on the readout unit for better visualization. With (L), the basis length between the pairs of wheels (L = 0.5 m for the probes used), the relative lateral difference (Δd) can be obtained by Eq. 5-1:

$$\Delta d = \sin \alpha * L \quad (5-1)$$

Δd = relative lateral difference [mm]
 α = inclination of probe to the normal [°]
 L = basis length of probe [mm]



Since the base is defined as stable when measuring from bottom to top, as it is usually done in landslide monitoring, the relative lateral displacements are summed up from base to top to display the distribution of deformation over the length of the inclinometric site, assuming an installation of the inclinometer's base below the shear surface in stable ground.

Figure 34: Top of the inclinometric measurement site at KB1. The yellow measurement cable is connected to the probe (in the casing – not pictured) and can be pulled up and be clamped in the jaws of the pulley at the 0.5 m intervals. On the left, outside of the casing, the connectors of the TDR system installed parallel to the inclinometer are visible.

For each subsequent measurement, the deviance from the initial reading is taken to calculate (according to Eq. 5-1) and properly display the deformation over time. As a result the deformation in one of the orthogonal planes is mostly displayed, but can also be shown in a polar plot, as to ascertain a direction of movement. Several correction methods exist, such as bias

correction, in order to overcome negative effects from installation or errors during measurement (Mikkelsen 2003, Cornforth 2005: 78ff.).

A very detailed description of the inclinometric system used at the Aggenalm landslide is given by BRANDHOFF (2010). He also addressed the accuracy (0.01 % v.E.) of such a system by extensive laboratory testing, and showed that, despite the high accuracies achieved, the resolution of the measurements at the Aggenalm landslide is considerably affected by noise, having a much higher influence on the results. According to the calibration specifications from the factory, the inclinometric probe (TU) together with the portable data logger has a system accuracy of ± 4 mm per 30 m.

From October 2008 onwards, the two sites were gauged periodically about every other month until 2011 when measurements took place only three to four times a year. The inclinometer casing in B5 was shortened by half a meter in June 2009, when changing the site to a complete subsurface installation. This required using a new baseline reading (1. measurement after shortening) as reference for all subsequent measurements at B5. Additionally, from the same time onwards a different probe (probe TU) was used for all further readings (Appendix VI).

5.1.2.3 Piezometer

At the Aggenalm landslide, a total of four piezometers by the company SISGEO S.r.l. (www-17) were installed in boreholes (B1, B4, B5, and B6 (Figure 30)). According to the installation setup parallel to TDR, mentioned in Chapter 5.1.2.1, the piezometric sensors (in a sand filled geotextile bag) were installed shortly above the assumed deformation zone, in order to not influence the TDR measurements, and were embedded into a loose gravel layer, which is sealed at the top and bottom by a watertight layer of compressed bentonite pellets. The exact position of the piezometers is pictured in the borehole's interior work in the boring logs in Appendix IV. Unfortunately, during the installation process the lead cable of one piezometer (B5) was accidentally severed in the borehole, rendering the sensor unusable. The other three piezometers have been connected by long lead cables (parallel to TDR lead cables in trenches) to the CR1000 data loggers (same as for TDR), by which measurements of the pore water pressure are taken every 5 minutes (SINGER 2010: 163). This setup allows a complete integration into the alpEWAS GSN with all its advantages.

Following the data acquisition, the pore water pressure readings are corrected for barometric pressure, due to the different barometric conditions at the Aggenalm landslide (mean barometric pressure at the main sensor node is 892 mbar) and at the factory during calibration of the probe (zero reading calibrated at 1007 mbar). Hence the corrected pore pressure is obtained by adding (due to higher elevation on-site than at factory) the change in barometric pressure between factory and on-site to the pore water pressure with respect to the conditions during calibration. The corrected pore water pressure can then be easily converted to a corresponding water table height, and can be used in further analyses.

For unknown reasons, after a few weeks of operation only, the piezometer in borehole B1 went out of service and the piezometer in B6 was destroyed after nine months of operation by a short-circuit in May 2009. Therefore solely the piezometer installed in B4 remained working.

5.2 Design of the alpEWAS geosensor network

As it has already been mentioned in the descriptions of the measurement systems, most of them (TDR, GNSS, piezometer, weather station) have been integrated into the alpEWAS geosensor network (alpEWAS GSN). The GSN consists of a total of four sensor nodes, namely the central station, the main sensor node, and two GNSS sensor nodes (#1 and #4) as pictured in Figure 1 and Figure 30. The data collected at the individual sensors is forwarded to the central station by wireless LAN and stored in a central database (MySQL), which allows worldwide access to the data via internet. At the Aggenalm landslide a DSL connection via satellite (upstream and downstream via satellite) is used for remote access. A more detailed description of the GSN's layout and its characteristics is given by THURO et al. (2010b, 2011a, 2013).

The software package "alpEWAS Control" (Figure 35) forms the core of the alpEWAS GSN and is responsible for all data management. It has been developed by SINGER (2010: 137ff.) in course of his thesis using the graphical development environment LabView. It is flexible and easily extendible control, management, and data analysis software package. Its modular setup allows using only the necessary program components or adding additional sensors, no matter the type of module.

This is achieved by using a certain program structure, with so-called sensor plug-ins, which each communicate (control and data acquisition) with one major program element (sensor I/O, database management, data viewers, data analyzer, etc.). Each plug-in integrates a graphical user interface (GUI) into the main application and thereby provides complete access and control to the sensors incorporated. Next to the data control and acquisition, the plug-ins provide additional information, such as sensor status information or first data analyses (GNSS baseline processing or TDR deformation analysis). All this data is stored in the central part of the software – a MySQL database – that all subprograms of the alpEWAS Control software access (THURO et al. 2011a: 42ff.).

Two components of the alpEWAS Control software monitor the sensor status and thresholds respectively. If an error in one of the sensors or sensor plug-ins is encountered or individual programs or sensors fail, the system administrator is notified automatically via e-mail. A part of it is an alarm function, which monitors any data from the database by means of logical operators (thresholds), and issues and alarm e-mail when a threshold (e.g., amount of precipitation, deformation rate) is exceeded (THURO et al. 2011a: 44). In addition to the e-mail service, a SMS notification service can be easily added, if a more flexible and rapid alerting becomes necessary.

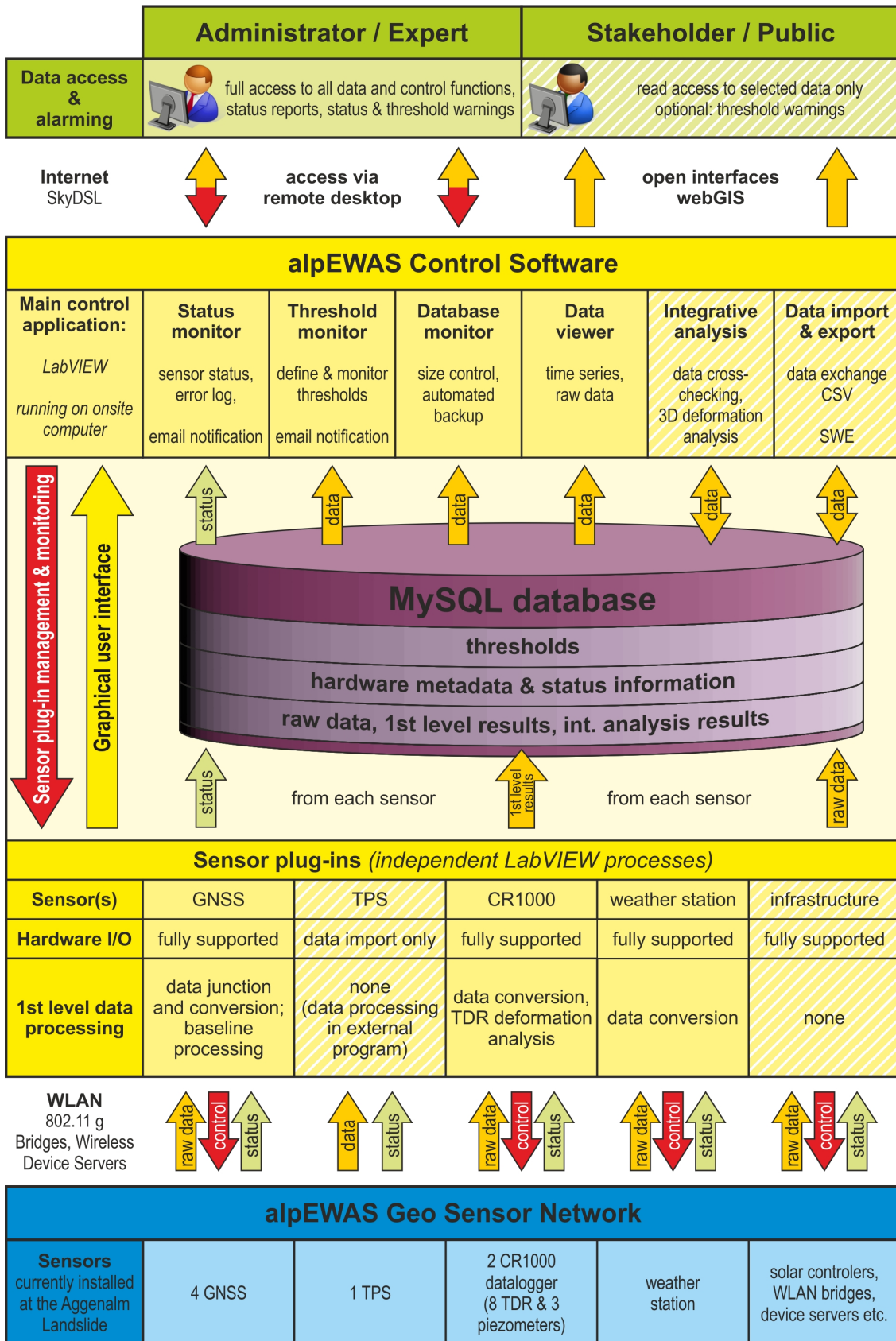


Figure 35: Structure of the alpEWAS Control software. All sensors of the alpEWAS GSN (blue) are controlled by sensor plug-ins that write all collected data in the central MySQL database. Additionally, a status-, threshold-, and database-monitor as well as a data viewer, providing easy access to the data, is included. The hatched elements are still in development. (SINGER 2010: 138, Fig. 64)

Another important component is the alpEWAS data viewer, which informs the end user – e.g., administrators/experts and stakeholder/public – about the current system state (sensor, database- and threshold-status, webcam picture) and at the same time offers several data visualization and manipulation techniques. All data in the database can be plotted as time series for chosen periods, and a variety of filter options (smoothing, interpolation, and synchronization) is provided (Figure 36). Additionally it offers the possibility to graphically display the TDR raw data and to export the currently displayed data as CSV files. (SINGER 2010: 140)

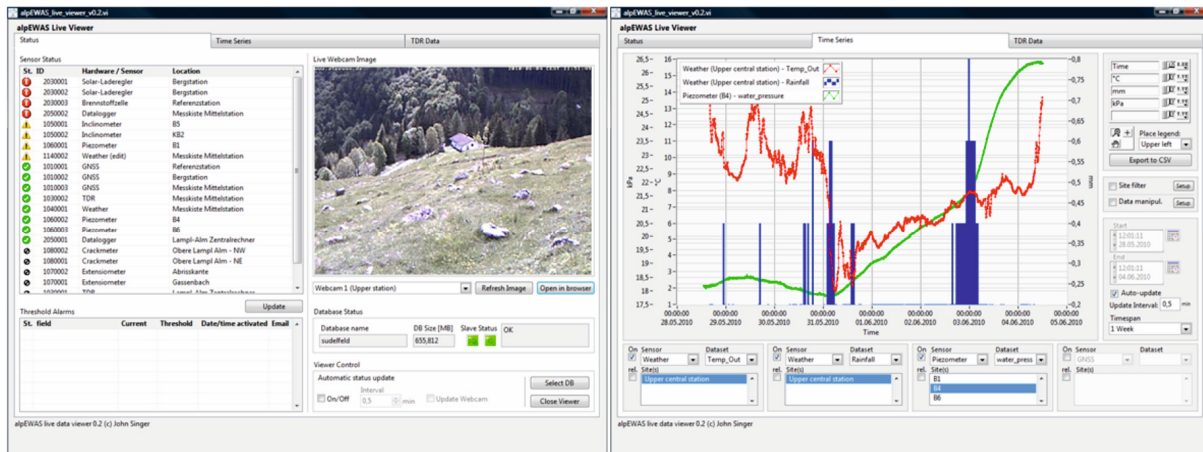


Figure 36: The two main frames of the alpEWAS Live Viewer (data viewer) are pictured. The left side shows the current system status and on the right, the interface to graphically display the acquired data is pictured. (THURO et al. 2011a: 46, Fig. 27)

5.3 Individual results of the different measurement systems

The measurement systems at the Aggenalm landslide have now been in operation for about five years. Due to several problems in the starting phase in late 2008 (power outages, full data storage, manual readout, etc.) many gaps in the data occurred before the automatic data acquisition was started in February 2009. After several major incidents due to power outages, difficulties with the WLAN connection and broken equipment in early 2012 the alpEWAS GSN has been disabled in order to set up a renewed version of the GSN (alpEWAS GSN 2.0). In this new setup, the central station (computing station, Figure 30) has been combined with the main sensor node to overcome initial communication problems. Therefore only the data from 2009 through 2011/beginning of 2012 is reviewed in the following (Chapters 5.3 and 6.4), except for data not incorporated in the GSN, such as inclinometer, crack meter, etc., whose results over the complete monitoring period is presented.

5.3.1 Reflectorless video tacheometry (VTPS)

Due to the prototypical state of the video tacheometer used, only periodic measurements were performed about once a year. Figure 37 displays the results of the VTPS measurement campaign. It shows the displacement at certain targets (mostly rocks) as displacement vectors, each depicting a time span of about one year. The time from November 2008 through August 2009 is depicted by red arrows and the orange ones stand for the time from August 2009 through June 2010. At the tacheometer itself (installed on a pillar at the main sensor node) a displacement of 1.2 cm was detected in each of the yearly epochs. In the first year the displacements measured at the targets rocks varied between 0.3–0.8 cm and in the following year between 0.7–2.5 cm (THURO et al. 2011a: 60f.). At target points without displacement vectors it wasn't possible to acquire data for all epochs because of single measurement failure or false range measurements.

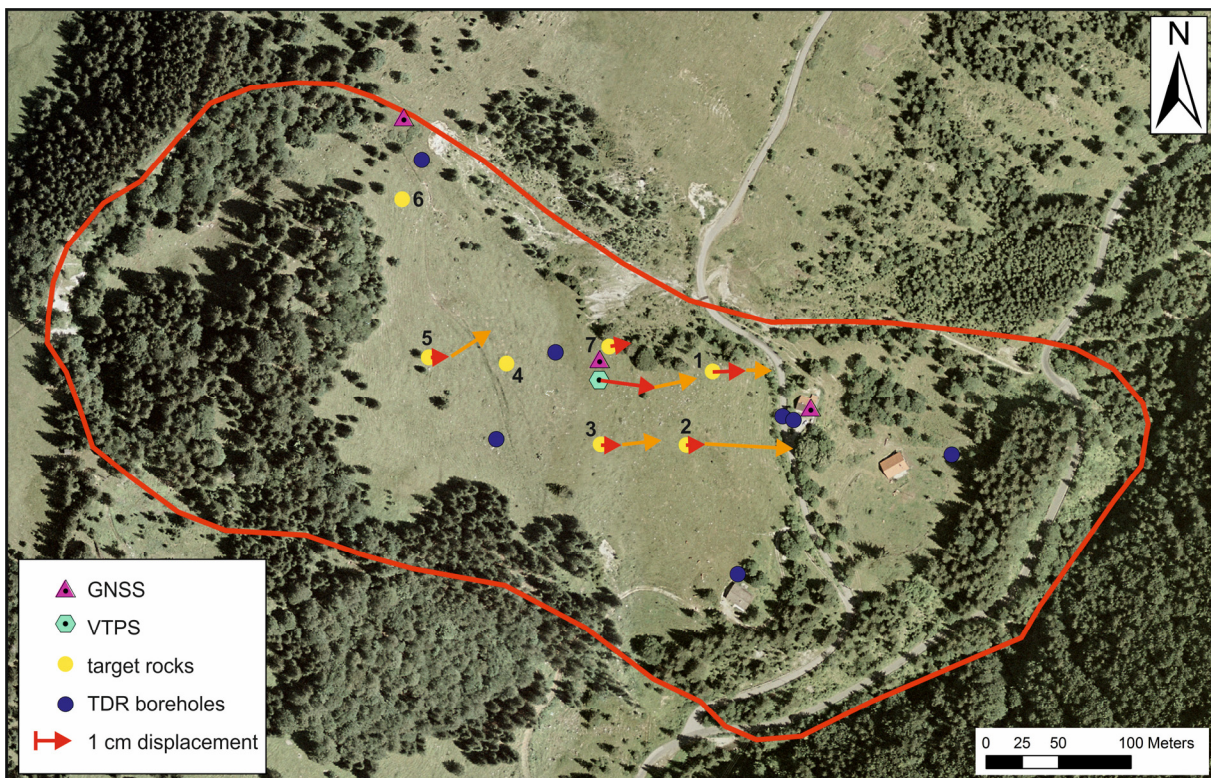


Figure 37: Results of the VTPS measurements depicted as movement vectors of the detected target rocks. Vectors are red for 2008–2009 and orange for 2009–2010. (Adapted with minor changes from THURO et al. 2011a: 60, Fig. 41, Geobasisdaten © Bayerische Vermessungsverwaltung 2010)

Since the distance between pillar (tacheometer) and reference points on stable ground are quite long, uncertainties in the exact positioning arise, rendering the acquired displacements as statistically insignificant, particularly as the displacements at the Aggenalm landslide seemed to have slightly decreased compared to the measuring results of the LfU in previous years (Chapter 4.6.3.1). However, both the absolute value as well as the orientation appear as highly plausible

and correspond well with movement rates detected by the independent GNSS system (Figure 38).

5.3.2 Global navigation satellite system (GNSS)

Some of the results of the GNSS monitoring component at the Aggenalm are presented in this section and are depicted in Figure 38 as well as Figure 39 at a glance. A more detailed evaluation and description of the attained data as well as correlations with other GSN data is given in Chapter 6.4.

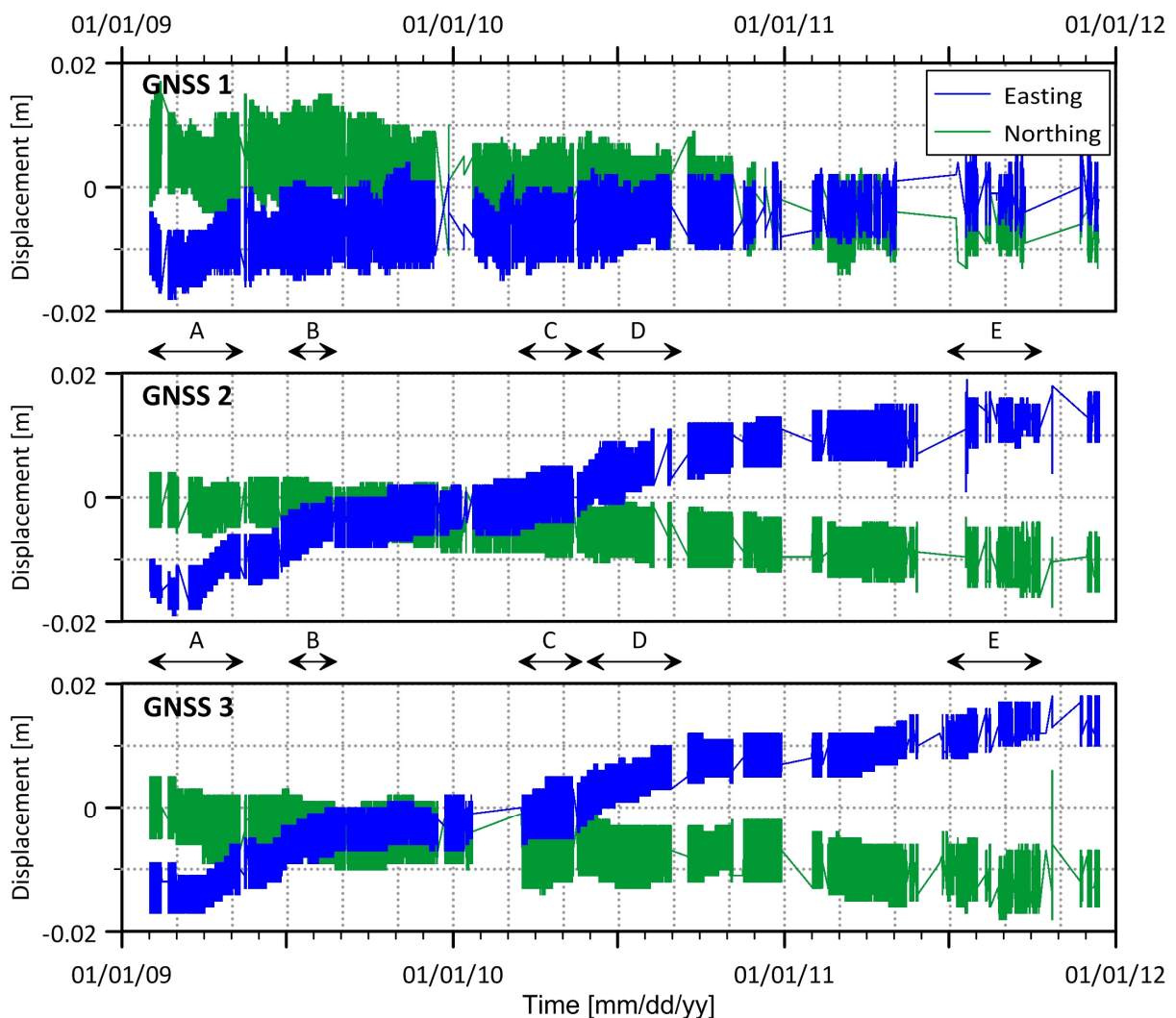


Figure 38: Results of the GNSS sensor nodes 1–3 for the time period February 2009 through December 2011 filtered by a moving average (filter length: 12 hours for GNSS 1 and 6 hours for GNSS 1 and 2) based on a robust estimator (edited and amended, basis adapted from THURO et al. 2014: 299, Fig. 2.5). Greater shadowing at GNSS 1 leads to a stronger noise than at GNSS 2 and 3, which thus show a considerably better empirical standard deviation of the solution epochs in the data processing.

In Figure 38 the two position components – Easting and Northing, whereupon Easting is about parallel to the slope’s orientation – are pictured for all three GNSS nodes on the Aggenalm landslide for the period from February 2009 through December 2011. Due to the surrounding mountain ridges and trees and thus the partially bad obstruction and shadowing (sometimes only four or less satellites are visible at a time), leading to temporary incorrect processing results, a moving average filter has been applied to the data to overcome these negative impacts. The moving average filter extends over 24 (GNSS 2 and 3) and 48 (GNSS 1) epochs, which corresponds, in regards to the 15-minute interval for the carrier phase acquisition, to a filter length of 6 and 12 hours, respectively. Despite some technical problems and the resulting data gaps – partially because no solution at all could be computed for an epoch – long term trends of the movement can be detected satisfactorily, nevertheless.

In the plotted time series a displacement of about 1 cm for GNSS 1 and about 3 cm for nodes GNSS 2 and 3 over a 3-year period (2009 through 2011) can be observed in the downhill components (Easting – blue graphs), with several acceleration phases in between (marked and labeled A–E in Figure 38). While node 2 and 3 show about the same total displacement with an apparently similar acceleration pattern, node GNSS 1 differs in overall displacement and also the movement pattern isn’t as clearly visible (due to small displacement and greater noise of data). These results, especially the ones of node 2 and node 3 correspond well with the displacement vectors attained by the VTPS measurements, which shows approximately 2 cm displacement in total over the 2-year period.

Phase (A) and (C) mark the period of snowmelt during spring 2009 and 2010 respectively. While in spring 2009 (A) an acceleration phase in slope direction (Easting) is clearly visible, even slightly in the graph of GNSS 1, it is hardly apparent during the snowmelt period of 2010 (C) and 2011 (not marked), two consecutive years with considerably less snow coverage (see Figure 7: In 2009 the snow reached a height of approximately 3.5 m and in 2010 and 2011 only about 1.0–1.5 m at the Wendelstein observation station). (B), (D), and (E) each mark periods of heavy rainfall during summer and fall. Following these rainfall-rich periods slight acceleration phases can again be observed, especially in GNSS 2 and 3.

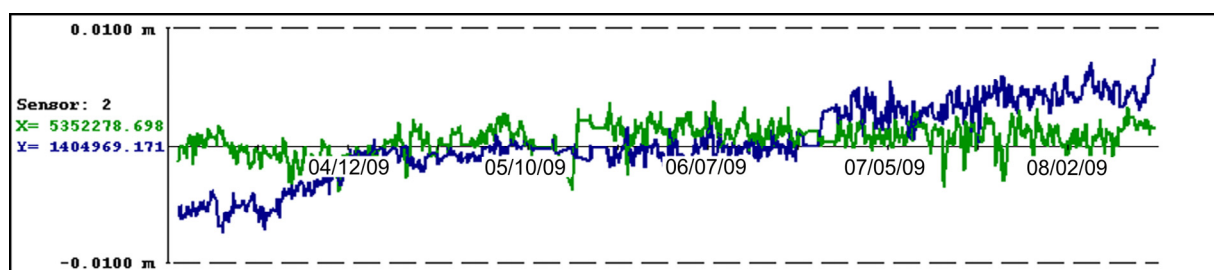


Figure 39: Movements at sensor GNSS 2 from mid-March to mid-August 2009. A moving average filter (length: 12 hours) has been applied. (Adapted from THURO et al. 2014: 300, Fig. 2.6)

Figure 39 pictures an enlarged view of the period (A) and (B) of Figure 38 from March 15 through August 15, 2009. From mid-March through the end of April the Easting component (Y – blue chart) shows an acceleration phase during the snowmelt and then stays leveled through the end of June where a second acceleration phase following intense rainfall can be observed (THURO et al. 2011a: 61). For additional detailed plots of sections of the GNSS measurements in relation to the climatic conditions on site see Chapter 6.4.

During the measuring epoch from 2009 through 2011 only a few malfunctions occurred, mainly caused by energy shortages. The big data gaps in 2011 were caused by failed elements due to short-circuit and an according delay until replacement. All in all, at the field installation at the Aggenalm landslide the system – sensor nodes and current software, control application – has proven a robust operation under the environmental conditions. The results also show that low-cost receivers can achieve high accuracies, too, which normally can only be obtained by geodetic high-end receivers.

5.3.3 Subsurface deformation measurements (TDR and inclinometer)

The results of the TDR and inclinometer measurements will be described and interpreted together in this section, since both systems have been installed parallel in boreholes, thus leading to very similar, partly mutually influencing results and interpretations.

Figure 40 displays the results of the TDR measurements at the Aggenalm landslide, exemplarily. Not a single deformation caused by the Aggenalm landslide could be detected in any one of the TDR measuring sites. The reflected signal stayed constant throughout time over the complete length of the coaxial measuring cable as the results at site B2 show. Except for data gaps caused by infrastructure issues and some maintenance adjournments only a small deformity caused during installation is visible at a depth of about 10 m in B2, depicted in Figure 40.

The results at both inclinometer sites, at KB1 and B5, are very similar to the TDR findings and up to date no significant deformation has been detected. In Figure 41 the data collected at the inclinometer site B5 is plotted exemplarily, while the results of KB1 as well as the results differentiating between the two probes used can be found in Appendix VI. In all these plots it can be observed that the data is very noisy and fluctuates about ± 3 –5 mm over the complete length of the borehole, with the highest fluctuation at the top (measurements are summed up from bottom to top). Within this noise the results at KB1 (Figure VI-1 and VI-2 in Appendix VI) seem to show a tendency of the borehole to slightly tilt toward ENE, which corresponds well with the orientation of the general movement at the slope, but can't yet trustworthy be determined.

A similar trend can be observed at B5 (Figure 41, Figure VI-3 and VI-4 in Appendix VI), even though not as clearly. Here, a small tendency in the tilting toward south can be seen up until spring 2011, when its orientation seems to shift to SE, and a kink at a depth of –4.5 m becomes visible. In contrast to the results in KB1, in B5 the amount of deformation along the B axis is about the same as along the A axis, which can be explained by the proximity of the borehole to

the Agggraben just 20 m to the north. Movements toward the Agggraben cause the higher amounts of deformation along the B axis and thus also explain orientation of the overall movements, which don't correspond as well with the results gathered by GNSS or VTPS.

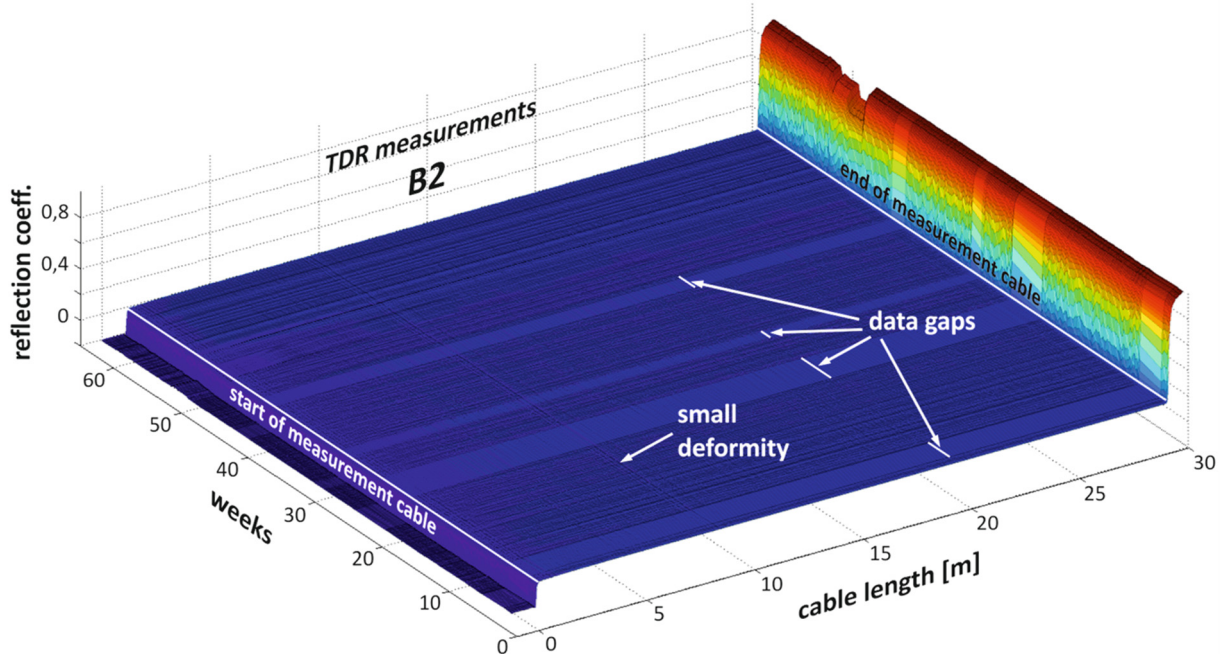


Figure 40: Exemplarily, the results from the TDR measurements in borehole B2 are displayed. Pictured are the daily measurements (daily averages) along the cable (from start at the top to the end at the bottom of the borehole) over approximately 60 weeks, starting on January 1, 2009. At a depth of about 10 m a small deformity can be seen, which has been caused during installation, and thus is visible from the start over the complete measurement period. (Adapted from SINGER 2010: 164, Fig. 80)

Since the results of the GNSS and VTPS measurements show approximately 1 cm deformation per year, two different explanations for the disappointing results from the TDR and inclinometer measurement systems come into consideration, which are:

1. Incorrectly embedded coaxial cables and inclinometer casings.
2. Boreholes are not deep enough to penetrate the basal shear zone, thus the complete landslide body.

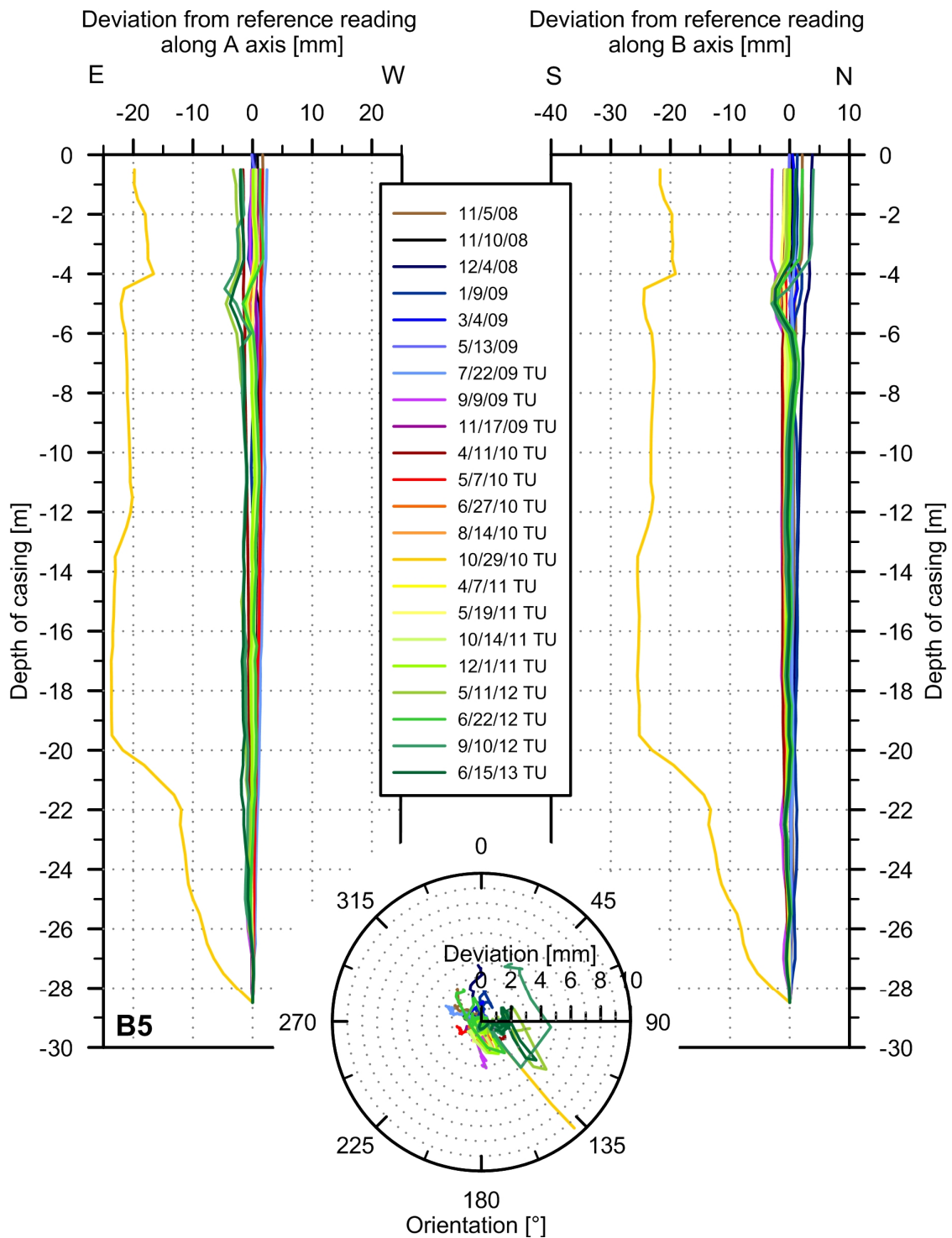


Figure 41: Results of the inclinometer measurements from borehole B5. The measurements up until May 13, 2009, were taken using the inclinometer probe (GeoMessTec) and are referenced to the reading from October 14, 2008. After reconstructing the site (shortening of casing by approx. 0.5 m) a new reference measurement was taken with the TU probe on July 16, 2009, to which all further measurements are referenced (marked "TU"). At the bottom, a polar plot shows the overall orientation of deformation for each of the measurements.

The first possibility could explain parts of the disappointing measurement results. Because of the debris and heavily jointed rock mass at the Aggenalm, the rock mass's permeability is very

high, which entailed problems during the installation of these systems. The grout drained into the surrounding rock mass, especially in the beginning before countermeasures had been taken, such as adding a plastic hose for sealing and increasing the solids content of the grout. Although the countermeasures decreased the loss of grout (through draining) considerably, it didn't guarantee for an entirely intact backfill. Voids within the grout surrounding the inclinometer casings but especially the TDR coaxial cables, affect or even prohibit a correct transfer of the deformation of the rock mass to the measuring device. Such an inaccurate grout column could be the reason for the noisy inclinometer results, but doesn't explain it completely, as according to the measuring systems on surface more than 3 cm of deformation have occurred so far. Since this amount is a multiple of the noise seen in the inclinometric data, at least some trustworthy deformation should have been detected by now.

The second possibility that the boreholes are not deep enough to penetrate the basal shear zone, is another explanation for the extremely little deformation detected with these two systems. The newly constructed geological model (Figure 29), incorporating all findings from the different field investigations, shows that most likely most of the boreholes didn't reach the basis of the Aggenalm landslide. The approximate target depth of the boreholes was determined on the basis of the old geological model by JUNG (2007) (Figure 28) by which it was also assumed that the main basal shear zone was located close to the boundary between Kössen formation and overlying strata (Upper Rhaetian formation and debris) within the marls of the Kössen formation. Therefore, during the drilling campaign it was aimed to ultimately drill a few meters into the Kössen formation. The results of TDR and inclinometer measurements support the interpretation in the new geological model, in which the basal shear zone of the Aggenalm landslide is located at much greater depth as originally assumed. Even though B1 and B6 are the only ones that possibly penetrated the whole landslide body, at least scantily, neither in these boreholes deformation has been detected so far.

The slightly higher deformations observed in the inclinometer data at B5 compared to the data at KB1 can probably be attributed to the influence of the Agggraben, thus to movements toward the Agggraben along a possible shear zone that is not quite as deep as the basal shear zone of the Aggenalm landslide; even though the heavy noise hinders a nonambiguous interpretation. To reduce the noise of the data (e.g., remove a possible "windshield wiper effect" from the tilting (CORNFORTH 2005: 78f.)) a bias correction would be helpful, but this is hindered by the insufficient depth of the boreholes. For a correction (bias shift error) of the inclinometer data as it has been mentioned in Chapter 5.1.2.2, it is necessary that the basal shear zone is penetrated and that the casing is fixed in stable ground over a minimum length of 3–6 m (MIKKELSEN 2003: 558) for calibration purposes, which hasn't been fulfilled, rendering this correction method useless. Therefore, the measurement systems on surface have to be considered for reliable deformation measurements and inclinometer B5 may only be helpful in interpreting influences on the Aggenalm landslide by the escarpment toward the Agggraben debris flow if stronger deformations become detectable in future measurements.

5.3.4 Results of additional measurement systems

5.3.4.1 Crack meter

The results of the crack meters installed at the NNE and WNW side of the Aggenalm hut are pictured in Figure 42. Readings were taken starting a couple of months after the installation in June 2008 at almost every visit on Aggenalm landslide and documented by a photograph, thus leading to irregular intervals, with fewer readings during the winter months. However, it can be observed that both crack monitors show an opening of the cracks (3.4 mm on WNW side and 1.0 mm on NNE side at the last reading in October 2013). In addition, it is not a constant increase in opening width but rather only an increase during fall and winter months and even a decrease/closure during spring and summer with an increasing trend over the years.

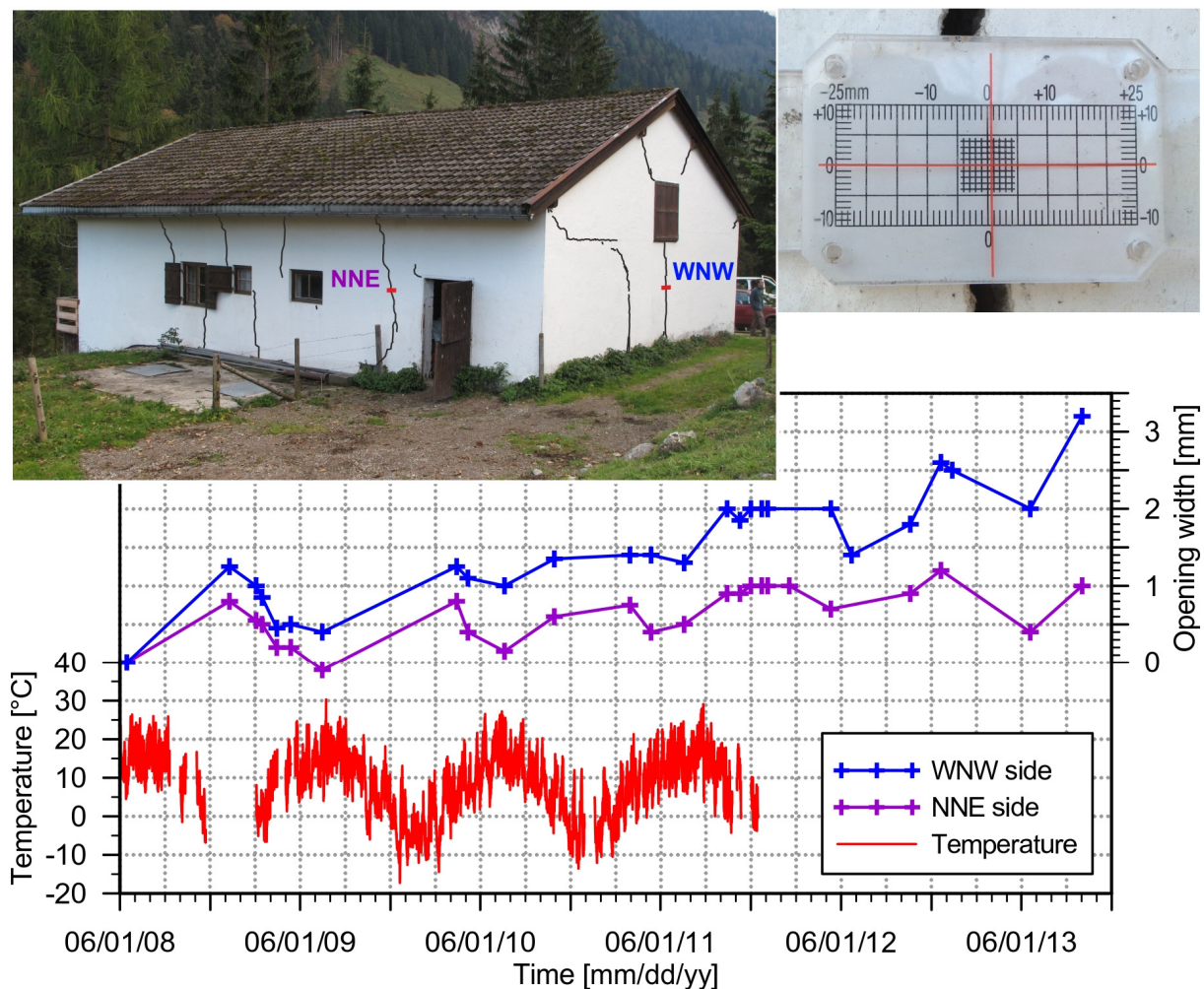


Figure 42: The photo on the left shows the Aggenalm hut. Major fissures in the walls of the building have been traced black for better visibility and the position of the two crack meters that have been installed in the beginning of June 2008 is marked. Exemplarily the photo on the right depicts one of these crack meters. At the bottom, the graph shows the results of the crack meter readings for the period June 2008 through October 2013.

This phenomenon – opening during cold periods and partial closure during warm periods – can be explained by the properties of the building material (bricks/brickwork), which slightly expand with heat and contract with cold, thus the up- and downturns. Furthermore, the cracks in the hut's outer walls allow conclusions on the ground movements. Hence, it can be assumed that the hut is located on at least two blocks that show a different movement behavior that is then called to the surface and becomes visible in the hut's walls.

5.3.4.2 Weather station

The weather station has recorded data since summer 2008 and only a few times data losses occurred (mainly before the start of the automatic data acquisition). Mostly temperature, barometric pressure, and precipitation data has been used to help with the interpretation of other data sets and for time series analysis (precipitation).

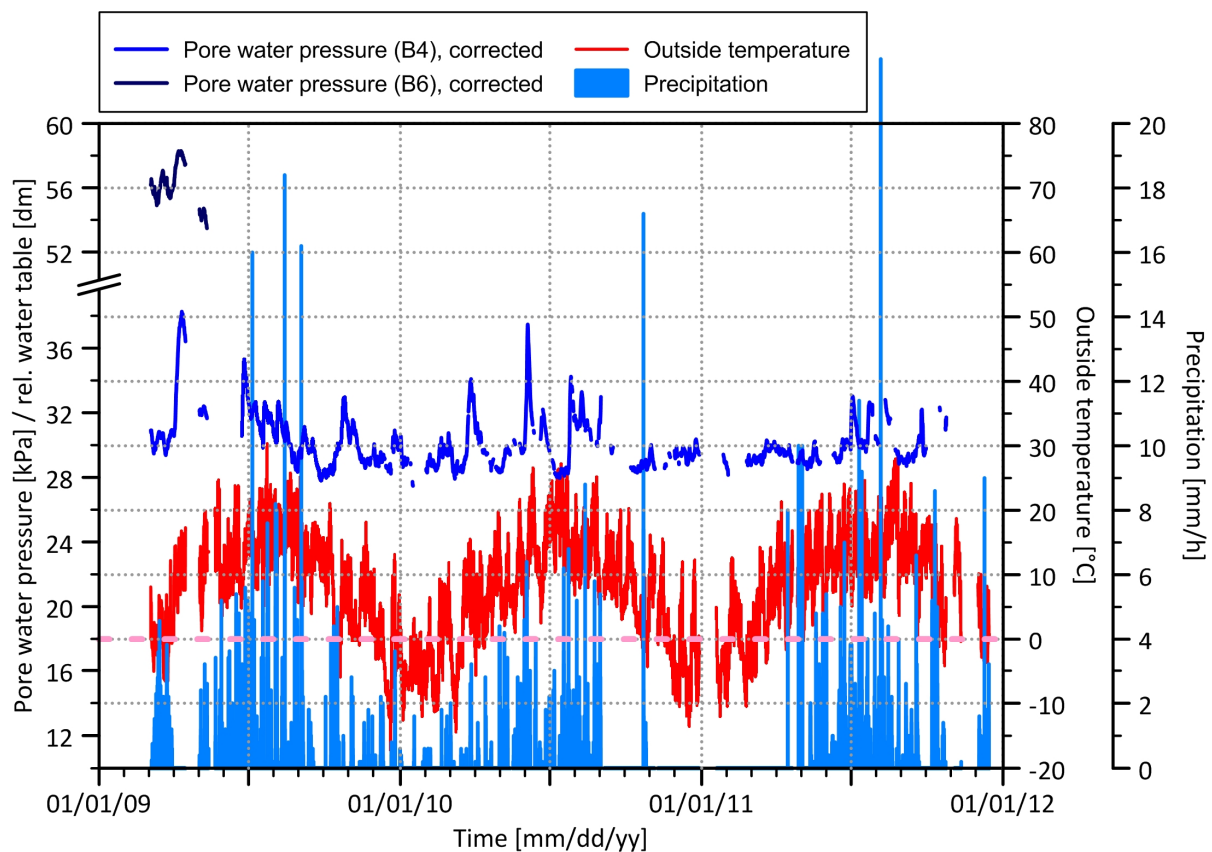


Figure 43: Graph of the precipitation, temperature, and piezometer data recorded at the Aggenalm landslide from 2009 through 2011. The pink dashed line marks 0 °C for easier interpretation. All precipitation is considered as snowfall if the temperature is below 0 °C. The data of both piezometers has been corrected to the atmospheric pressure on site.

The temperature data has been useful for instance to interpret the crack meter data, but has also been used to approximately discern between snowfall and rainfall (Figure 43), as both were

measured using the rain gauge (with a heater to melt the snow). The barometric pressure measurements have been necessary to adjust the piezometer readings to the barometric pressure on site and thus to calculate correct water table heights. Figure 43 depicts the precipitation data over the period 2009 through 2011. In 2011 the heater for the rain gauge, to eventually measure snowfall hadn't been installed, thus leading to a major data gap (for an estimation of the amount of snowfall in 2011 the data from the Wendelstein station has to be used – Figure 7). Several times during the period hourly amounts of up to 22 mm have been recorded. A detailed presentation and discussion of the rainfall data follows in Chapter 6 on time series analysis.

5.3.4.3 Piezometer

Here, the results of the piezometer will be presented only shortly, as all piezometer data have been part of the time series analysis as well, thus a detailed description and interpretation can be found in Chapter 6. In Figure 43 the results of the piezometric measurements, corrected by the barometric pressure, are shown. As mentioned before, only one piezometer (B4) is still working properly, while the others broke during installation or shortly after, after only a few months in use (B6). Since the piezometer at B4 has been installed at an approximate depth of -29.6 m below surface (1051.4 m a.s.l.) and now shows a mean pressure of about 30 kPa (pressure head 3 m above piezometer), the water head is assumed to be at an elevation of approximately 1054.4 m a.s.l. The water pressure fluctuates between 28 kPa and 38 kPa, corresponding to a water table change of 1 m, while the biggest single rise/drop occurred in June 2010 with a relative water table change of about 0.8 m (30–38 kPa). A closer look at these single events and their correlation with other data – rainfall and deformations – has been taken and will be presented in Chapter 6.

5.4 Discussion of monitoring results

The three main measuring systems as well as additional sensors – piezometer, weather station, etc. – installed in course of the alpEWAS project at the Aggenalm landslide have shown a very reliable operation, especially since the start of the automated data retrieval and remote access using the alpEWAS Control software. After overcoming initial problems and according maintenance interruptions, hardly any maintenance and interventions were necessary in the following years (which then were mostly due to power outages).

The deformation measurement systems on surface – namely VTPS and GNSS – showed reliable deformation measurements, which were consistent with the results of the geodetic survey. Even though, due to the long distance between tacheometer and reference points, the acquired displacements by the VTPS are not statistically significant, they seem to be highly plausible and correspond well with the movement rates detected by the other independent surface deformation measurement systems. The GNSS, which was included into the alpEWAS Control software, proved to be very reliable, detecting deformation with sub-centimeter accuracy, which was previously reserved for high-end receivers. Several periods of acceleration following precipitation-

rich periods/snowmelt periods could be detected, which will be analyzed in detail in the following chapter on time series analysis (Chapter 6).

The very disappointing results of the subsurface deformation measurement systems, TDR and inclinometer, were most likely not caused by the insufficiencies of the systems, but by an at the time (2007) plausible geological model (Figure 28). This suggested the landslide's shear zone at a much lower depth than it is assumed today, after including the new information of the geoelectric survey. Even though the results from the TDR and inclinometer measurement sites are not very conclusive in light of interpreting and describing the movement characteristics at the Aggenalm landslide, both systems have proven to attain valuable and accurate information at other sites, whether used independently or together to prolong the time span of measurements (e.g., at the Gschlifgraben landslide (SINGER 2010: 144ff.)).

The results of all systems together, including data concerning the piezometric water table and precipitation, allow describing the movement characteristics and its dependencies more precisely. On this basis, statistically significant correlations between precipitation, groundwater level, and deformation can be identified by means of time series analysis, which then help to better understand the landslide's mechanisms and triggering factors and to determine threshold values (Chapter 6). Additionally, all of the information attained by different surveys and by the alpEWAS monitoring system has been used to alter the geological model of the Aggenalm landslide and to set up a new numerical model, with the aim to substantiate the influence of extreme triggering events exceeding the observed values and to further improve the understanding of the landslide's mechanism (Chapter 7).

6. Time series analysis

The collected data of the alpEWAS monitoring system has not only been evaluated individually – separated into the various measurement systems – but also as a whole. Subsequently, the precipitation combined with the piezometric data and the results of the deformation measurements (GNSS), were analyzed using time series analysis (TSA) techniques. With the help of TSA, dependencies – statistically significant correlations – between precipitation, groundwater level, and deformation could often be identified, improving the understanding of the landslide’s mechanism and triggering factors. Furthermore, it was possible to deduce threshold values for the onset of movements and/or acceleration phases of the Aggenalm landslide.

In the beginning of this chapter, the basic principles of the TSA techniques applied in this thesis as well as the analysis approach are outlined. This is followed by a description of the data preparation, such as filtering and sampling. Then, the results of the various analyses amongst triggering factors and deformation as well as between different sensors (e.g., GNSS 1–3) are presented. Finally, the derived threshold values as well as the entire results of the TSA are summarized and discussed as a whole.

6.1 Basic principle

The terms *time series* and *time series analysis* are both very general and cover a wide range of applications. A *time series* is defined as a ‘sequence of observations that are arranged at successive points in time’. Thereby, the measurements are spaced at uniform time intervals, which, however, can vary greatly in length, e.g., recording data points in intervals of seconds, minutes, or hours, or at monthly or even yearly intervals (SCHLITTEGEN 2001: 1ff., KREISS & NEUHAUS 2006: 4ff.). Many different time series analysis methods exist – ranging from basic to highly sophisticated – all aiming to analyze the time series characteristics (patterns), their generating mechanism, and/or their dependencies from external parameters, often with the intention of short-term forecasting of the future development of the data series (HIPEL & MCLEOD 1994: 65).

However, TSA does not only comprise methods of data analyses but also summarizes procedures involved with, e.g., the preparation, processing, cleansing, and filtering of time series data. This is due to the nature of a time series – given by x_1, x_2, \dots, x_n – whose data are realizations of random variables $X(t)$, which themselves are built by the sum of three components as illustrated in Eq. 6-1:

$$X(t) = X_T(t) + X_S(t) + X_R(t) \quad t = 1, \dots, n \quad (6-1)$$

In Eq. 6-1, $X_T(t)$ is a function of time, t , describing the trend of the data series, while $X_S(t)$ represents some nonrandom cyclic influence, which itself can be composed of several long- and/or short-term cyclic parts, such as seasonal influences. The third part, $X_R(t)$, is the random

variable that makes up a time series. Since $XR(t)$ represents the true characteristics of a time series, it is usually necessary to extract this random part before applying further TSA models, to describe dependencies, for instance. In Chapter 6.3, the models used for the trend and seasonal adjustment will be briefly mentioned, but without detailed explanation of the underlying stochastic processes as this is beyond the scope of this work. However, some annotations concerning the data preparation and filtering methods can be found in the according programming code in Appendix VII, while a detailed description of these is given, e.g., by SCHLITGEN (2001), KREISS & NEUHAUS (2006), GILGEN (2006), FOPPE et al. (2009), and FALK (2012).

A typical and common analysis method for time series is the correlation analysis. In landslide investigations, the analyses often aim to characterize the relationship between rainfall, pore water pressure, and displacements, thus between trigger and event (e.g., LOLLINO et al. 2002, 2006, MATSUURA et al. 2003), while in hydrogeology, hydrological data sets are often analyzed to better understand the characteristics of karstic or aquiferous systems (e.g., LAROCQUE et al. 1998, LEE & LEE 2000). Two different correlation functions – autocorrelation and crosscorrelation – are used to describe dependencies within a single or between two different data series.

The former, the autocorrelation function, quantifies the linear dependency of equidistantly spaced values over a time period, thus revealing information about the data series' memory effect. According to NEUNER & FOPPE (2009: 31ff.), the autocorrelation function, R_{XX} , (Eq. 6-3) can be calculated by normalizing Eq. 6-2, the autocovariance function, C_{XY} .

$$C_{XX}(t, \tau) = E \{ [X(t) - \mu_X(t)] \cdot [X(t + \tau) - \mu_X(t + \tau)] \}$$

$$= \lim_{n \rightarrow \infty} \frac{1}{n} \cdot \sum_{j=1}^n \{ [x_j(t) - \mu_X(t)] \cdot [x_j(t + \tau) - \mu_X(t + \tau)] \} \quad (6-2)$$

C_{XX} = autocovariance function
 E = expected value
 X = random variable
 t = point in time
 τ = lag, time difference
 μ = mean
 n = number of data points in series

The two arguments in Eq. 6-2 illustrate the two-dimensional state of the autocovariance function, which depends on the point in time, t , as well as on the lag, the time difference, τ , between the random variables $X(t)$. For an easier interpretation of the results, the autocovariance function is then normalized by the standard deviation of the random variables according to Eq. 6-3, so that the results are restricted to $[-1, 1]$ (KREISS & NEUHAUS 2006: 47ff.).

$$R_{XX}(t, \tau) = \frac{C_{XX}(t, \tau)}{\sigma_X(t)\sigma_X(t + \tau)} \quad (6-3)$$

R_{XX} = autocorrelation function

C_{XX} = autocovariance function

X = random variable

t = point in time

τ = lag, time difference

σ = standard deviation

An autocorrelation value of 1 (–1) shows that the analyzed variables have identical (opposite) variation properties, while an autocorrelation value of 0 suggests statistical independence (THE MATHWORKS 2008: 4-63f.). If the time lag is set to zero, $\tau = 0$, the result of autocorrelation function is always 1, which is due to the fact that a random variable completely correlates with itself. Shifted by a lag, τ , the autocorrelation function reveals information about the series' memory effect, thus how a value at $t + \tau$ is influenced by its preceding value at time t (NEUNER & FOPPE 2009: 32). An uncorrelated time series is thus characterized by a very quickly decreasing autocorrelation function, which reaches a value of zero in a very short time (short lag), as it is exemplarily the case for (most) rainfall time series. If, however, the autocorrelation function decreases only slowly with nonzero values over a long time lag, this shows the interdependence of the time series' values, thus its memory effect (LEE & LEE 2000: 191). The length of such a memory effect is given by the lag until a value of zero (sometimes a level of significance is applied instead, e.g., 0.05 as applied by WEIDNER (2000: 79)) is reached in the autocorrelation function.

While the autocovariance function and thus the autocorrelation function describe the interdependence of the random variables of a single stochastic process in relation to its temporal shift, the crosscovariance function (C_{XY}) and its normalized crosscorrelation function (R_{XY}) represent the interdependency in relation to a time shift but of two different stochastic processes (NEUNER & FOPPE 2009: 36f.).

$$\begin{aligned} C_{XY}(t, \tau) &= E \{ [X(t) - \mu_X(t)] \cdot [Y(t + \tau) - \mu_Y(t + \tau)] \} \\ &= \lim_{n \rightarrow \infty} \frac{1}{n} \cdot \sum_{j=1}^n \{ [x_j(t) - \mu_X(t)] \cdot [y_j(t + \tau) - \mu_Y(t + \tau)] \} \end{aligned} \quad (6-4)$$

C_{XY} = crosscovariance function

E = expected value

X, Y = random variable

t = point in time

τ = lag, time difference

μ = mean

n = number of data points in series

Eq. 6-4 and Eq. 6-5 show the crosscovariance and crosscorrelation function, adjusted to two different input time series – x_1, x_2, \dots, x_n and y_1, y_2, \dots, y_n – which both must be equidistantly spaced and be clipped to the identical sample interval and length (ZEIMETZ et al. 2009: 196f.).

$$R_{XY}(t, \tau) = \frac{C_{XY}(t, \tau)}{\sigma_X(t)\sigma_Y(t + \tau)} \quad (6-5)$$

R_{XY} = crosscorrelation function

C_{XY} = crosscovariance function

X, Y = random variable

t = point in time

τ = lag, time difference

σ = standard deviation

Contrarily to the autocorrelation function, the result of the crosscorrelation function for $\tau = 0$ must not be 1, nor must the function reach its maximum value at $\tau = 0$. Rather can the highest correlation of the two analyzed processes be at any point τ (NEUNER & FOPPE 2009: 37). The crosscorrelation is thus a measure of the time lag or phase shift between causally related processes, e.g., between trigger (rainfall) and landslide event (displacement), while the value of the highest correlation determines the magnitude of correlation between the two events.

6.2 Analysis approach

The data of interest for the TSA – namely precipitation, pore water pressure, and GNSS deformation measurements – have all been stored in the central MySQL database of the alpEWAS geosensor network as described in Chapter 5.2. Even though the long-term aim of the alpEWAS system is to incorporate the complete analysis into the alpEWAS Control software to allow easy access for administrators and/or stakeholder, the data sets were read out and analyzed independently. However, it is planned to add selected, suitable analysis functions to the renewed version of the GSN (alpEWAS GSN 2.0) additionally to the functions that are already embedded in the Live Viewer (data viewer), such as sample manipulation, simple interpolation, etc., after completion of the external analyses.

In a first step the data series are simply plotted below each other, which allows one to visually recognize prominent characteristics within the time series. Trend, seasonality, outliers, and data gaps, but also distinct causal relations between the time series can be identified and help to choose the appropriate further analysis procedures. The data can mostly be plotted as they have been extracted from the database, with the exception of the GNSS data. Due to the low-cost approach and thus a great variance of the unfiltered data, the GNSS data has to be prepared and filtered, so that trends and dependencies become visible. For these basic plots (Figure 44) the GNSS data has been prepared and filtered according to the description in Chapter 5.3.2 using a moving average (6 respectively 12-hour filter length).

The raw data (output of database) is then inputted into the program MATLAB 2009b by The MathWorks, Inc. – “a high-level language and interactive environment for numerical computation, visualization, and programming” (www-20) – for filtering, sampling, and correlation analyses. The GNSS data is also imported in their raw data state and prepared and filtered in MATLAB. In this program, outliers in the data series are removed and all data is detrended. Additionally, several manipulations are performed, such as the calculation of a summation curve of the rainfall data, computing the differenced pore water pressure (change between two consecutive measurements), and applying moving average filters. Afterwards, the data is tailored to the time interval to be analyzed and loaded into the *tstool*-toolbox incorporated in MATLAB (THE MATHWORKS 2008: 4-1ff.), where the now manipulated time series data can again be plotted and correlation analyses are performed.

6.3 Data preparation

As above-mentioned most of the data preparation takes place in the programming language MATLAB. All data is imported to MATLAB as raw data, or rather as readout from the database. In the case of the *alpEWAS* monitoring system, a position solution over a 15-minute interval – calculated by the baseline processing (Chapter 5.1.1.2 on page 62f.) – for the GNSS is stored in the database and imported to MATLAB without any further changes. However, the piezometric data and the data acquired by the weather station, which all are recorded in 5-minute intervals, are sampled in 1-hour intervals (1-hour sums for rainfall data) in the Live Viewer upon readout. Additionally, data gaps within the data series are preserved, while data dangles are removed. Other than that everything else, such as filtering, detrending, etc., is performed after the import to MATLAB, of which the programming file is attached in Appendix VII.

Prior to processing the time series data, the corresponding date and time of each of the data points has to be converted to a so-called MATLAB-time, which allows easier handling of the time series data. Thereby, the data vector is assigned a MATLAB-time vector, which, by default, has an interval of one second and ranges from 0 to $N-1$, where N is the number of samples. For the MATLAB-time 0, a user-defined date and time can be entered, which in case of this analysis was set to January 1, 2009, at 00:00:00. After the processing of the data has been completed, the data series are cut to intervals of various lengths by giving the begin- and end-date in MATLAB-time, before loading the time series into the *tstool*-toolbox for correlation analyses.

6.3.1 Filtering, smoothing, and sampling

6.3.1.1 GNSS data

After loading the GNSS raw data (15-minute solutions) into the program for the complete analysis period, February 2009 through December 2011, blanks incorporated in the data series are

deleted before performing the date/time conversion to MATLAB-time as described in the previous section. Due to the low-cost approach of the GNSS measurement system, the data series are very noisy and also contain many erroneous measurements (outliers). Extreme outliers are removed by applying a filter, which finds and deletes values exceeding the global mean of the data by 1.0, 0.5, and 0.1 m, respectively (see function `gM_Schwellenfilter` in Appendix VII, page 12). Additionally, this function also finds outliers/values exceeding a moving average (length: 5) by more than one time the threshold (0.2) and deletes them as well. To further reduce the noisiness of the data a moving average smoothing is performed on the time series, applying a filter length of 100, which corresponds to approximately one day (25 hours to be exact). Additionally, any short-term periodical components are removed by this moving average smoothing as well.

In the next step, the filtered GNSS time series are detrended by means of the built-in detrending function (*detrend*) in MATLAB. The function removes the best straight-line fit linear trend (long-term trend) from the GNSS time series and returns the residual (THE MATHWORKS 2008: 1-17ff., 4-32). The aim of detrending is to gain stationarity, thus to attain a data series without trend and a constant variance and constant autocorrelation structure¹⁵ over time. Thereafter, time doublets contained in the data are deleted and the data series are transformed into time-series-objects. In a final step, the GNSS data is each sampled in 1-, 6-, 12-, 24-, and 48-hour intervals and cut to the interval to be analyzed in the `tstool`-toolbox.

6.3.1.2 Piezometer and rainfall data

The data series from the piezometer and the weather station are imported to MATLAB in the state of a readout from the `alpEWAS Live Viewer` as outlined in Chapter 6.3 with the exception of the piezometric data, which is corrected by the on-site barometric pressure prior to import. The first step in the analysis, again, is to convert the timestamps to MATLAB-time. Afterwards, several calculations are performed on the data series, which are:

- A summation curve of the rainfall data over the complete sampling period (2009–2011);
- 6-, 12-, 24-, and 48-hour sums of the rainfall data;
- and the differenced pore water pressure (pressure change between two consecutive measurements)¹⁶.

Similarly to the GNSS data handling, the various data sets (original and calculated) are subsequently reprocessed by linear detrending, filtering, and smoothing, even though, e.g., a moving average smoothing isn't applied to all data sets. Finally, the data sets are sampled with identical

¹⁵ If the trend remains in the data series, it would induce a temporal correlation between the random variables leading to a slow decrease of the autocorrelation function, thus feigning a strong autocorrelation and possibly superimpose a cyclic component/seasonality contained in the data (NEUNER & FOPPE 2009: 39). However, due to the 25-hour moving average filter that has already been applied to the data, short-term cyclical components have already been eliminated.

¹⁶ By calculation of the differenced water pressure any periodical components are removed.

sampling frequencies¹⁷, transformed into time-series-objects, and cut to the respective analysis intervals, as well, before performing correlation analyses.

6.3.2 Data gaps

Several minor and major data gaps appear in the various data sets acquired over a 3-year period (2009–2011) as depicted in Figure 44 and Figure 45. The partially bad obstruction and shadowing of the GNSS sensors, which, at times, prevented the computation of a solution for an epoch (one epoch equals a 15-minute interval), led to many of the short-term gaps, oftentimes of only one to a few epochs in length. Maintenance disruptions, power outages, and short-circuits destroying components caused most of the longer data gaps, not just in the GNSS data but also in the piezometer and weather station data.

All data gaps were preserved during the analyses performed with MATLAB so as to not alter the spacing of the time series. However, most of the short-term gaps (especially in the GNSS data) are compensated by smoothing and sampling of the data, with the exception of the precipitation data. Although it isn't possible to discern between data gap and precipitation-free interval by simply looking at the data, longer data gaps can be detected with the help of, e.g., the temperature data, which is likewise recorded by the weather station and thus contains gaps at the identical time. Exception to that is the winter 2010/2011, in which the heater to melt the snow wasn't installed, resulting in a gap of approximately 5 months. It was refrained from analyzing data series containing long data gaps, rather than trying to replace the missing data by estimations, especially because ample significant results quantifying the causal relations between the various data series were attained from intervals with no or only a few short data gaps. These results will be characterized and pictured in the succeeding subchapter, with additional illustrations in Appendix VIII.

6.4 Results

As described above, several analysis methods were applied to the time series data collected by the alpEWAS monitoring system over a period of three years (2009–2011). In the following, the results of these are introduced and discussed, starting with the most basic method – the visual examination. Succeeding, the results of the correlation analyses are presented.

6.4.1 Visual examination and comparability of data sets

Even though most of the time series have already been displayed and discussed individually in the preceding chapter on the alpEWAS monitoring system, Figure 44 and Figure 45 display the data of the GNSS sensors 1–3, the piezometers (B4, B6), and the rainfall gauge, combined in

¹⁷ The sampling frequency for the various data sets has to be identical, so that one gets time series data of identical length and time interval, which is a prerequisite for the subsequent crosscorrelation analysis.

single plots. This facilitates easy comparability between the individual sensors of a measurement system and also between data of different systems and processes (e.g., trigger and displacement). In a first step, the data series of different sensors of a single measurement system are compared with each other before comparing the data of different systems.

Only over a short period of time, data from two piezometers (installed in B4 and B6) exist. However, during this time from March through mid-May 2009 (when the piezometer in B6 was destroyed by short-circuit), a similar behavior of the two time series can be seen in Figure 44, even though they have been installed at quite different depths. The piezometer in B4 (in the middle of the Aggenalm slope) was installed at a depth of -29.6 m, while the piezometer in B6, at the edge of the movement, is only 14.2 m below surface. However, both piezometers were installed within the Kössen formation (Appendix IV). Especially during snowmelt (April 2009) a significant rise in pore water pressure and thus water head (0.4–0.5 m in B6 and 0.8 m in B4) can be observed. Besides, hardly any time shift between the piezometric data series is visible, meaning that both show a similar responding time and behavior following rainfall or onset of snowmelt.

The results of the three GNSS sensors monitoring the displacements at the upper slope (# 1), at the main sensor node (# 2), and at the Lampl Alm (# 3), are plotted in yearly intervals in Figure 44 and over the complete period in Figure 45, supplemented by the trend of each of the GNSS data series. For the GNSS, only the Easting component of the measurements is plotted, as this complies with the overall downslope direction of the Aggenalm landslide (a positive change corresponds to a downslope movement). The results of the visual examination have already been described in Chapter 5.3.2 (on page 77ff.), so that they are only briefly summarized subsequently. GNSS 1 detected displacements of only 1 cm over the 3-year period, whereas the other two sensors showed 3 cm each over the same period. Besides, the latter bear obvious resemblance to each other in regards to their response (acceleration of movement) to an elevated water table, thus to aforegoing precipitation-rich periods. A more thorough analysis with the aim to verify and quantify these observed dependencies follows in the chapter describing the correlation analysis.

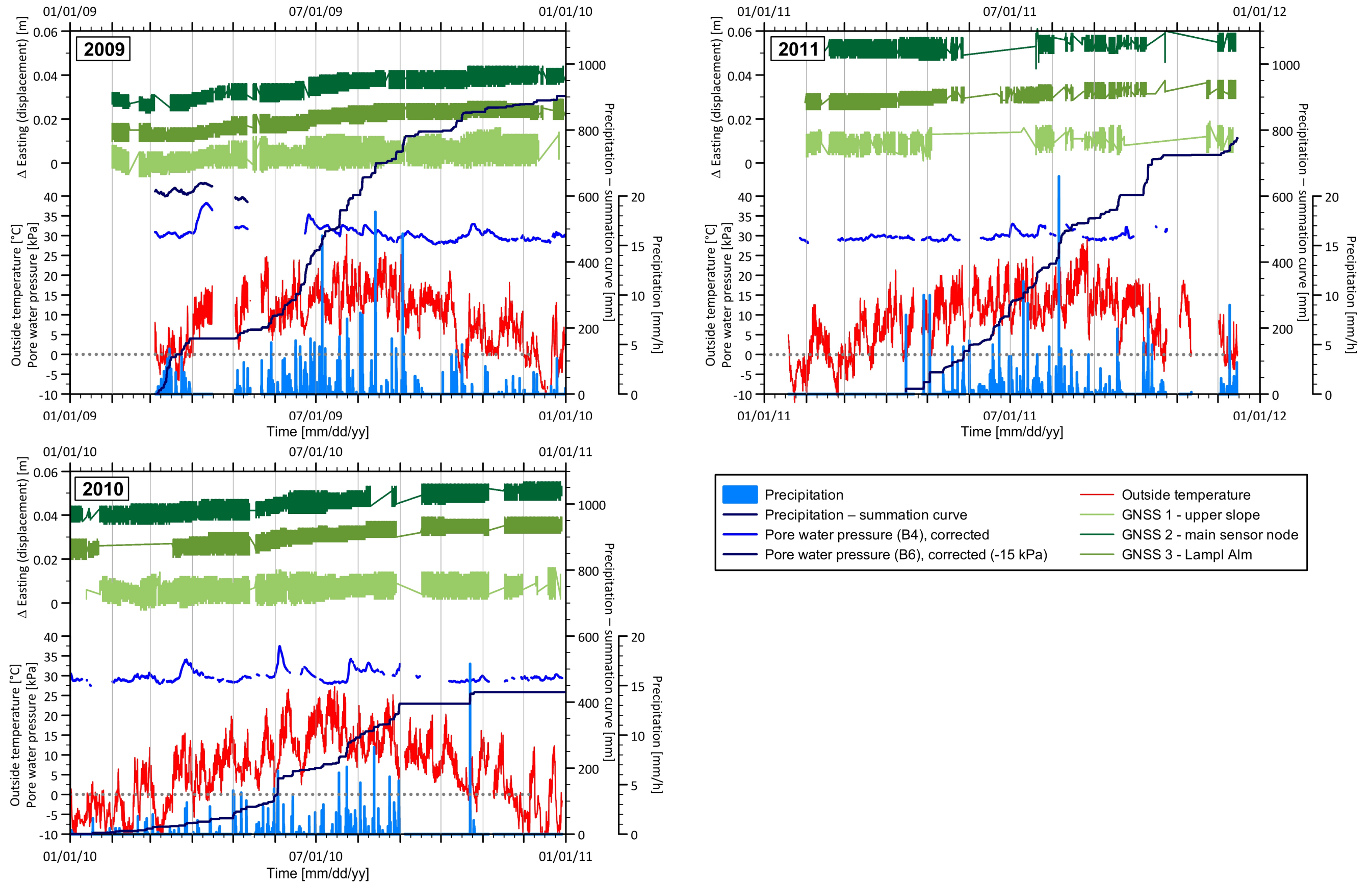


Figure 44: Time series of the data from the GNSS stations 1–3 (Easting only), piezometer (B4, B6) and weather station (1-hour rainfall sums, rainfall summation curve, and outside temperature) for the years 2009, 2010, and 2011. The pore water pressure in B6 has been decreased by a constant of 15 kPa due to displaying reasons and to allow better comparability.

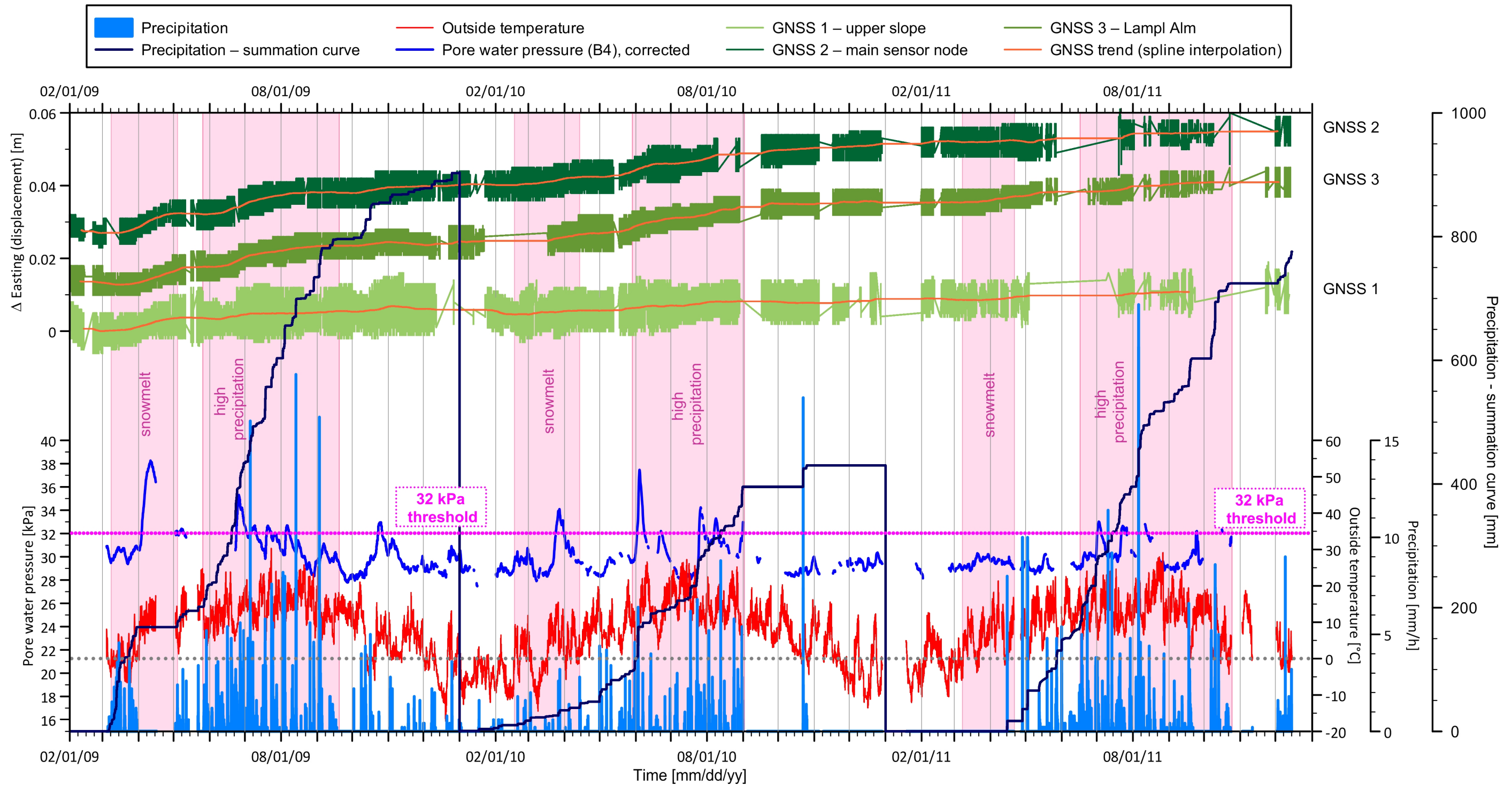


Figure 45: Interpreted time series of the data from the GNSS sensors 1–3 (Easting only, filtered data and trend), piezometer (B4), and weather station (1-hour rainfall sums, rainfall summation curve, and outside temperature) for the time February 2009 through December 2011. Precipitation-rich periods, which resulted in visible movements in the GNSS data (trend), are highlighted pink. From this plot, a very conservative and simple threshold value for the onset of deformation can be derived (pink dotted line): If the water pressure in B4 rises above 32 kPa and remains at an elevated level for several days, small movements/accelerations can be expected.

As above-mentioned simple dependencies between rainfall, pore water pressure, and GNSS deformation measurements can already be derived visually from the plots in Figure 44 and Figure 45, even though the analysis is limited by the relatively small deformation rates of about 1 cm/a at the maximum. However, it was possible to detect several very small increases in the displacement rates (mainly in GNSS sensors 2 and 3) after periods of heavy rainfall and/or snowmelt during the observation period (pink highlights in Figure 45). These can be seen best in the GNSS trend (spline interpolation), since the filtered data is still noise-afflicted, thus do not reveal such small accelerations either.

In spring 2009 and 2010, after the onset of the snowmelt, the pore water pressure surpassed a value of 32 kPa (pink highlights in Figure 45), whereas in spring 2011, hardly any influence of the snowmelt on the pore water pressure can be observed. In spring 2009, the snowmelt caused a rise of 8 kPa (30–38 kPa), which equals a water level rise of 0.8 m. In the following year a maximum rise of 0.6 m (28–34 kPa) was initiated by the snowmelt and in 2011 the pore water pressure fluctuated only slightly (29–30 kPa) during snowmelt (FESTL et al. 2013: 182). These significant variations of the water pressure response to snowmelt over these three years can be attributed to the very different amount of snow in the respective years. This high variation in the amount of snow is also strongly supported by the data of the Wendelstein observation station (Figure 7 on page 26), where a snow height of over 3.5 m in 2009, barely 1.5 m in 2010, and only 1.0 m in 2011 was recorded (due to the lower elevation at the Aggenalm landslide, the amount of snow was considerably lower; even so, the relation between the years seemed to be very similar). In the first two years, 2009 and 2010, an according increase of the movement rate can be attributed to the snowmelt, which, however, is not very prominent in 2010 and only visible in GNSS 2 and GNSS 3, whereas in 2009 a response to snowmelt is also visible in GNSS 1, even though not significant when compared to the noise.

Not only during springtime, after the onset of snowmelt, but also after rainfall-laden periods and extreme rainfall events, such dependencies can be observed, e.g., in July and August 2009, in June, July, and August 2010, as well as in July 2011 (pink highlights in Figure 45). During these periods the water pressure exceeded 32 kPa several times following heavy rainfall, while the displacement rate increased as well (mostly in GNSS 2 and GNSS 3). Based on these above-mentioned observations it is possible to deduce a first, still very simple threshold, which can be expressed by the water pressure: If the water pressure in piezometer B4 exceeds a value of 32 kPa over several days, small movements can be expected (the threshold is marked by the pink dotted line in Figure 45).

The visual examination of shorter and thus more detailed periods of these data sets reveals additional information. Exemplarily, a section of 60 days from June 22 to August 20, 2009, is pictured in Figure 46. The involved data was prepared (filtered, smoothed, etc.) as described in Chapter 6.3. To reduce gaps due to minor data losses a 6-hour resampling was applied to all data sets. Additional plots of comparable 60-day intervals are depicted in Appendix VIII. In these detailed figures, one can clearly see that a few days after a major rainfall (>20 mm in

2 days), the pore water pressure and thus the water level begins to rise (e.g., from 30 to 35 kPa between June 23–26, and from 30 to 33 kPa in mid-July and beginning of August). A similar relation can also be identified following smaller rainfall events, which result in water level rises of only 10–20 cm (1–2 kPa); however, also with a responding time of a couple of days.

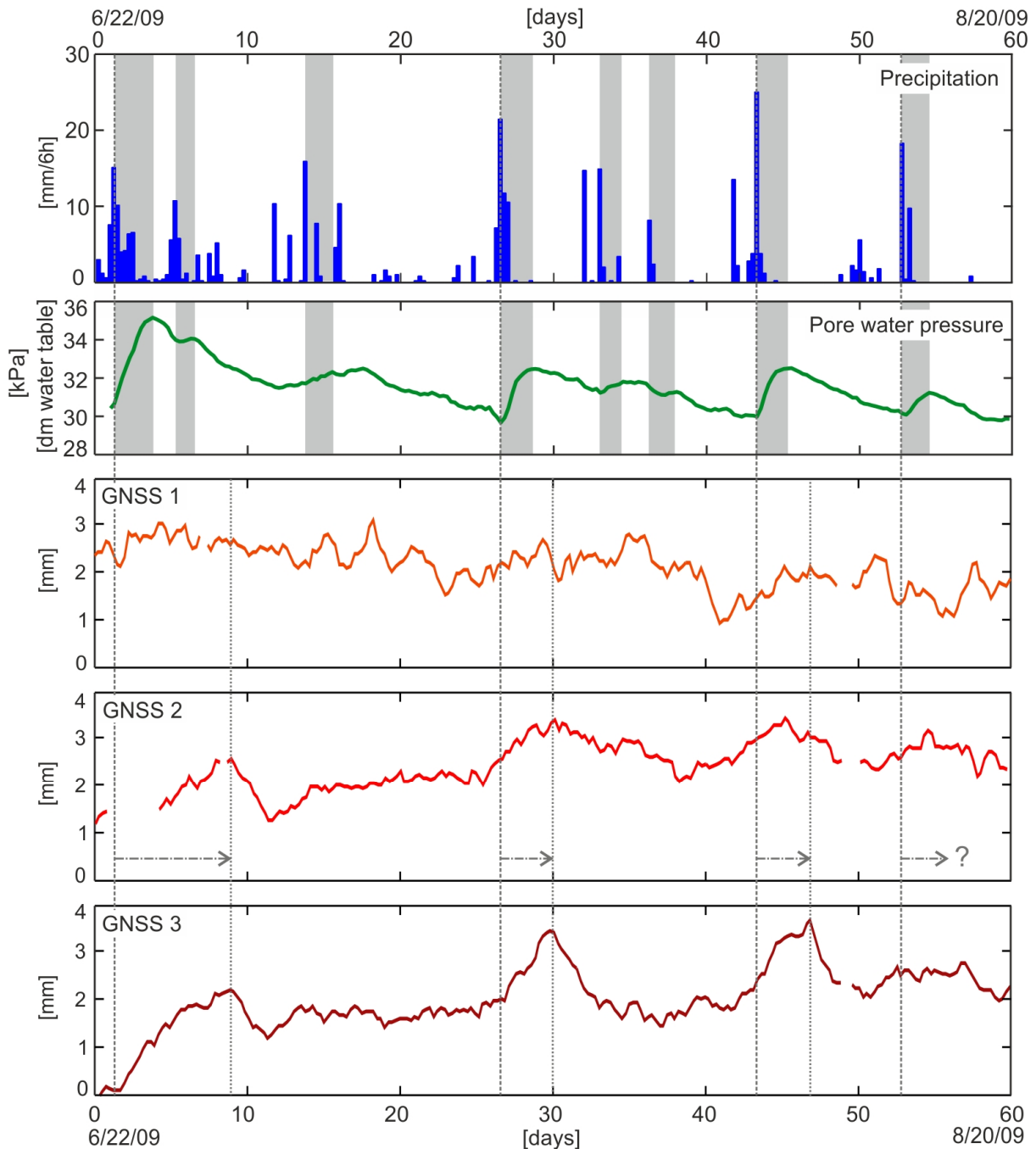


Figure 46: Filtered and sampled (6-hour intervals) rainfall, pore water pressure, and displacement (Δ Easting in [mm]) of all three GNSS sensors over a 60-day period (June 22 to August 20, 2009). The response time between precipitation and rise of water level is shaded gray. However, significant responses of the GNSS sensors to rainfall and thus to an elevated water level can't be derived properly, even though some slight dependencies can be visually drawn, especially with GNSS 3.

Since it is the aim of TSA to find not only dependencies between rainfall and pore water pressure, but particularly between trigger (rainfall/pore water pressure) and movement rate, it was tried to transfer and expand the analysis to the movement rate, thus including the GNSS displacement measurements. As pointed out in Figure 45, a displacement of approx. 5 mm was visually identified during summer 2009. However, after filtering these data and looking at said section in detail (Figure 46, Appendix VIII), it isn't possible to pinpoint dependencies. Indeed, some correlations seem to be visible – especially with GNSS 3. However, most changes (increasing movement rate) aren't attributable to a certain rainfall event, and at times the displacements even seem to increase prior to a rainfall event. This is due to the very little deformation rate of 1 cm/a – in the mm-range for single events – thus still within the noise of the GNSS, which superposes the results despite the filters applied, making it difficult to derive significant dependencies.

6.4.2 Correlation analyses

The results of the correlation analyses, auto- and crosscorrelation analyses, are illustrated and discussed in this subchapter, thematically divided into GNSS data and precipitation/piezometer data.

6.4.2.1 Correlation analyses of GNSS data

In a first assessment, autocorrelations of GNSS time series of various lengths have been calculated, for further characterization of the data and in order to be able to better interpret and classify the results of the crosscorrelations. Exemplarily, in the left column of Figure 47 the results of the autocorrelation for each of the three GNSS sensors on the Aggenalm landslide over the year 2010 are illustrated. Prior to the correlation analyses, the data series have been filtered, smoothed, and sampled in a 24-hour interval.

The autocorrelation of GNSS 1 decreases rather quickly compared to GNSS 2 and GNSS 3 and falls below a level of significance – set at 0.05 – after 12 days, while $R_{XX} = 0$ is reached after approximately 25 days. GNSS 2 and GNSS 3 display similar autocorrelation characteristics, falling below the level of significance after 94, respectively 87 days (100, respectively 95 days for $R_{XX} = 0$), showing a strong influence of preceding values over a long time and thus a strong memory effect. While the length of the time lag, thus the length of the memory effect, varies depending on the analyzed data interval (yearly data, monthly data, etc.), the main aspects remain the same: The autocorrelation of GNSS 1 differs visibly from GNSS 2 and GNSS 3, while the latter show similar characteristics. Additional correlation diagrams of the GNSS data are pictured in Appendix VIII.

The crosscorrelation analyses confirm the results and interpretations of the autocorrelation of the three GNSS sensors. A comparison of the data from GNSS 1 with the data from sensor 2 or 3 shows a rather low crosscorrelation, with a correlation coefficient, R_{XY} , of 0.36 for GNSS 1 vs. GNSS 2 (Figure 47, right column), and even less, 0.26, for GNSS 1 vs. GNSS 3 (not pictured

in Figure 47). In contrast, GNSS 2 vs. GNSS 3 display a very strong correlation with a coefficient of 0.82 (Figure 47), which varies only slightly for different data intervals, of which some are attached in Appendix VIII.

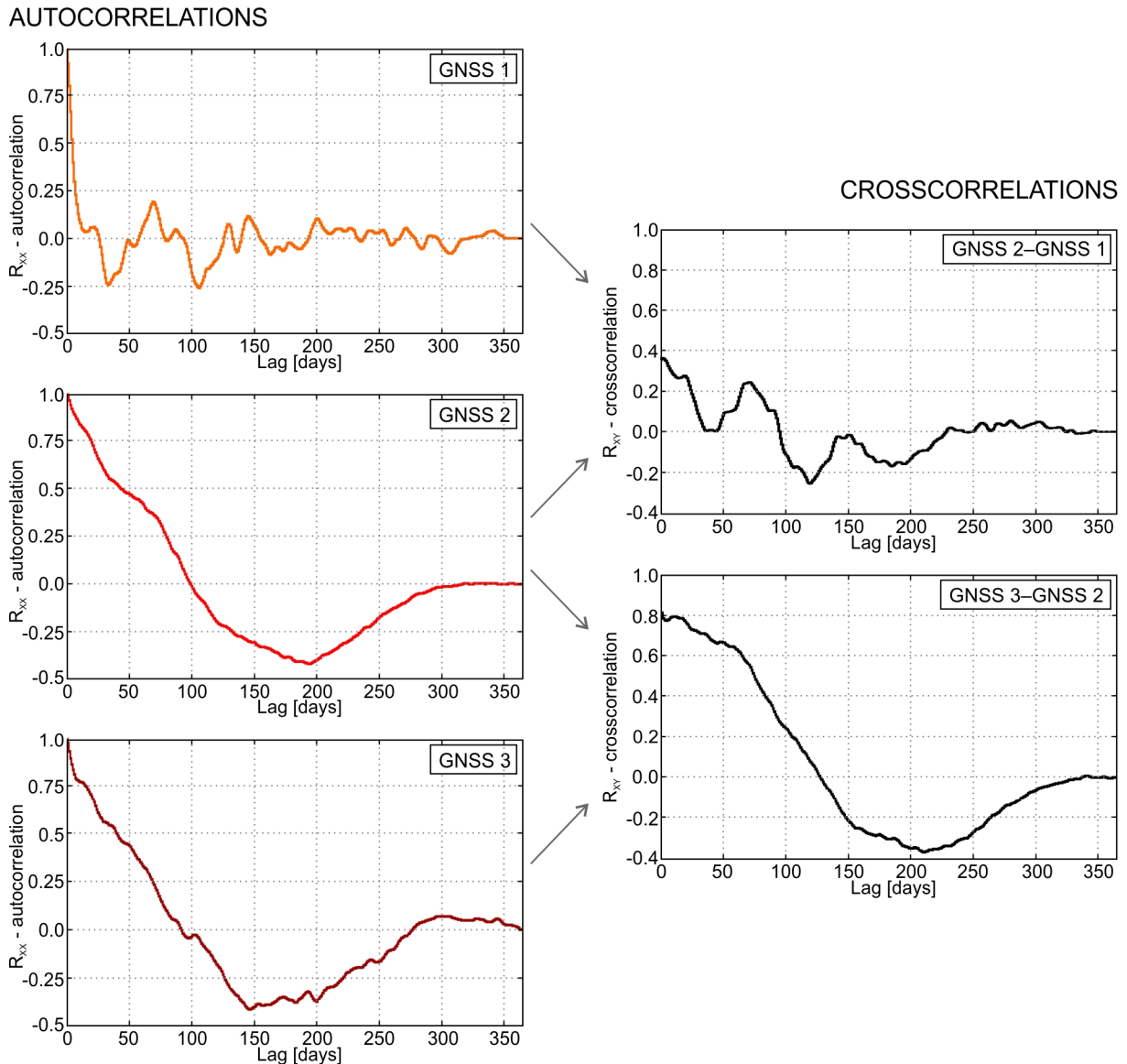


Figure 47: Auto- and crosscorrelation diagrams of the GNSS data for 2010. The filtered and smoothed data sets of the three GNSS sensors have been sampled in a 24-hour interval.

Putting these results in context with the complete results from the field observations and the alpEWAS monitoring system, the different behavior of the three GNSS sensors can be explained: The location of GNSS 1, at the very edge of the Aggenalm landslide, above the scarp of the Agggraben debris flow as pictured in Figure 30, is responsible for the comparably small displacements of approximately 1 cm over a 3-year period. The other two sensors are situated more centrally on the Aggenalm landslide, at the main sensor node and at the Lampl Alm: Both

show a yearly displacement rate of 1 cm, thus three times as much as sensor GNSS 1. Additionally, the very similar displacement patterns of GNSS 2 and GNSS 3 are reflected in the crosscorrelation results, which also show no temporal delay between the data series. Therefore, these results confirm a rather homogeneous movement of the Aggenalm landslide, especially of the landslide's lower two-thirds, where a sliding mechanism has been proposed.

6.4.2.2 Correlation analyses of precipitation and piezometric data

Just as with the GNSS data, autocorrelations of the data series have been calculated in a first assessment, before the precipitation and piezometric data have been compared with one another by means of crosscorrelation. Figure 48 pictures auto- and crosscorrelations for two different intervals, exemplarily. The data of 2010 was sampled using a 24-hour interval, thus allowing comparisons with the results of the GNSS in Figure 47, while for the 60-day interval (June 22 through August 20, 2009, same interval as pictured in Figure 46) a 6-hour sampling was applied.

For both intervals, the autocorrelation of the precipitation shows that the data isn't hardly correlated, thus the coefficient decreases to 0 rapidly after a single or a few lags at the most. This, however, is not the case for the piezometric data, which has a significant memory effect of about 20 days (20 days for the 1-year interval and 18 days for the 60-day period in Figure 48). This memory effect of the piezometer data decreases to only a few days (2–3 days) when analyzing not the absolute data but the differenced piezometric data. The resulting autocorrelation function of the differenced piezometer resembles the function of the precipitation data a lot more than does the one of the absolute piezometer data, which is also affirmed by the results of the crosscorrelations.

The crosscorrelation coefficient, R_{XY} , of the precipitation data versus the absolute piezometer data reaches 0.39 for the data of 2010 and 0.31 for the 60-day period in 2009 at its maximum. Thereby, the maximum is shifted by a lag of 2–3 days¹⁸ from zero, thus revealing the time that needs to pass for the water pressure/water table to reach its peak following precipitation. The relatively low coefficient and therefore low correlation can be attributed to mainly two factors: the length of the time series and the type of data. The former, the length of the time series, has only minor influences on the results, even though the data still contains some gaps that haven't been eliminated by the filtering and smoothing processes. The major influence comes from the type of data, in this case from correlating uncorrelated data (precipitation) with the correlated pore water pressure.

¹⁸ Note that the resulting lag is always an integer multiple of the chosen sampling interval of the data. Thus, the lag can only be determined with a resolution of ± 24 hours for the data from 2010 and ± 6 hours for the data of the 60-day period.

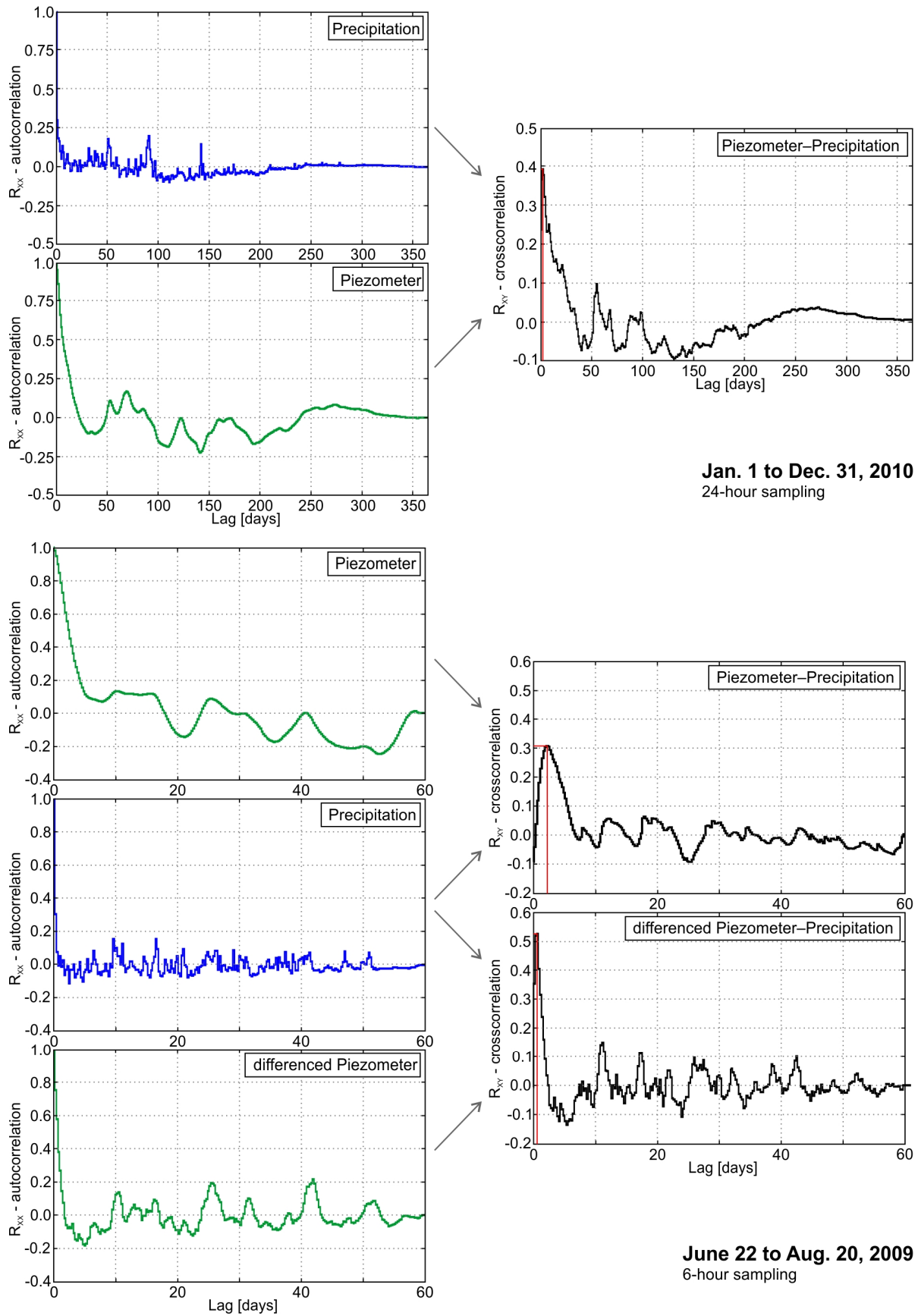


Figure 48: Examples of auto- and crosscorrelations calculated from precipitation and piezometric data over two intervals of different length. The data of the 1-year interval (2010) has been sampled every 24 hours, while a 6-hour sampling was chosen for the 60-day period (June 22 through August 20, 2009).

This rather low correlation coefficient can be compensated for by not using the absolute water pressure but rather the differenced data, which, as above-mentioned, already shows a higher visual resemblance to the precipitation data in its autocorrelation diagram. The crosscorrelation coefficient for the identical 60-day period between precipitation and differenced pore water pressure is, with a value of 0.53, significantly higher. However, due to the calculation process of the differenced pore water pressure, essential information in the piezometric data is smoothed, shifted or sometimes even eliminated, depending on the data series combined with the sampling interval. Exemplarily, Figure 49 depicts the smoothing, shifting, and elimination of data that occurs during the calculation process, for an artificially generated data series. Such a shift of the time lag toward 0 happened in the example in Figure 48, showing a shift from 3 days to only 1 day.

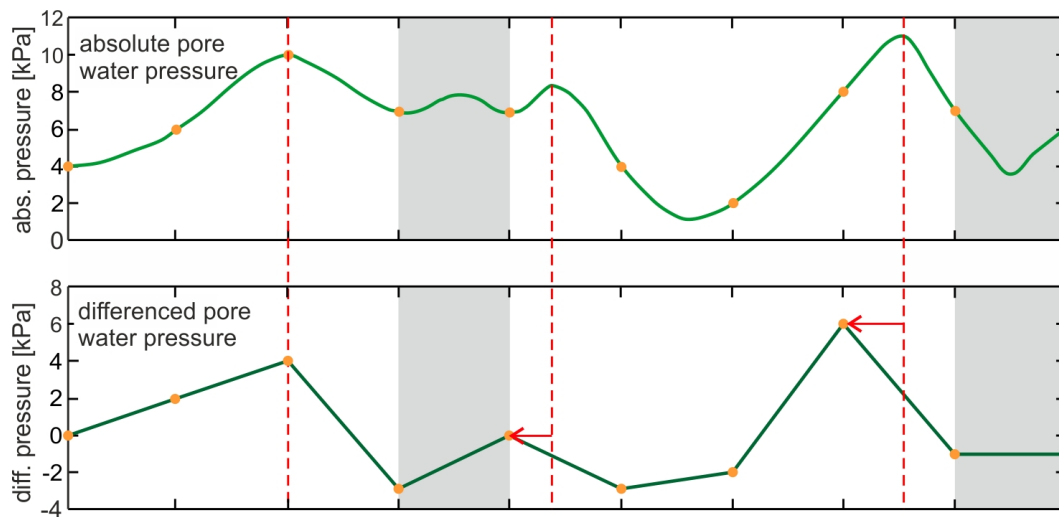


Figure 49: Comparison of absolute pore water pressure and the calculated differenced pore water pressure (the pore water pressure was artificially generated for this example). The orange dots mark the points at which the data series is being sampled. Smoothing occurs over the complete data series. A peak in pore water pressure, sometimes remains at its position in time in the differenced pore water pressure (first red line) or gets shifted to an earlier point in time (second and third red line). Sometimes information also gets eliminated due to the smoothing effect of the calculation (gray highlights).

Even though the correlation coefficient between precipitation and absolute pore water pressure is relatively low, the considerably higher crosscorrelation with the differenced pore water pressure proves clearly that the variation of the water table in B4 is directly linked to precipitation. Since, however, the time lag between rainfall event and peak in pore water pressure can only be properly derived from the crosscorrelation with the absolute water pressure, this combination has been chosen for all further analyses despite the comparably low crosscorrelation coefficient.

Table 5: Results from the crosscorrelation of precipitation and absolute and differenced pore water pressure. Results of months, in which the temperature dropped below 0 °C for a period of time at minimum, thus influenced by snowfall and possibly snowmelt, are in brackets and italicized. In August 2011 too many data gaps remained in the series for a trustworthy outcome. The lag of all other months (bold) varies between 1.25 and 6 days, with an average of 2.75 days.

		Mar.	Apr.	May	June	July	Aug.	Sep.	Oct.	Nov.
2009	Precipitation [mm/month]	168.3	0.0	68.8	196.8	169.6	130.6	61.8	59.0	22.8
	R_{xy} (Rain–PWP)	(0.25)	–	0.32	0.25	0.28	0.24	0.33	(0.24)	0.19
	R_{xy} (Rain– Δ PWP)	–	–	0.42	0.53	0.55	0.48	0.36	(0.24)	0.19
	Lag* [days]	(2.75)	–	3.25	2.25	2.0	2.75	3.0	(12.5)	2.75
		Mar.	Apr.	May	June	July	Aug.	Sep.	Oct.	Nov.
2010	Precipitation [mm/month]	17.4	14.0	64.2	84.0	92.4	102.6	0.0	34.8	0.0
	R_{xy} (Rain–PWP)	(0.22)	(0.08)	–	0.39	0.34	–	–	(0.33)	–
	R_{xy} (Rain– Δ PWP)	(0.26)	(0.25)	–	0.6	0.45	–	–	–	–
	Lag* [days]	(1.0)	(2.5)	–	1.25	2.5	–	–	(8.75)	–
		Mar.	Apr.	May	June	July	Aug.	Sep.	Oct.	Nov.
2011	Precipitation [mm/month]	0.0	36.0	108.2	126.0	125.2	136.8	70.6	121.2	0.2
	R_{xy} (Rain–PWP)	–	0.14	–	0.17	0.2	(0.33)	0.48	–	–
	R_{xy} (Rain– Δ PWP)	–	0.42	–	0.62	0.34	(0.25)	0.45	–	–
	Lag* [days]	–	1.75	–	2.5	2.75	(5.0)	6.0	–	–

PWP = absolute pore water pressure

Δ PWP = differenced pore water pressure

* Lag has been derived from crosscorrelation of Rain–PWP

To verify, and possibly to refine the lag of 2–3 days (Figure 48) between rainfall and according peak of the water table in a first step, the correlation of monthly sections was calculated. A 6-hour sampling was applied to the data, so that a lag with a resolution of ± 6 hours could be determined. Table 5 shows the attained results of the monthly correlations (selected diagrams are attached in Appendix VIII). In several months it wasn't possible to calculate meaningful

crosscorrelations due to multiple gaps in one or even both data series. E.g., in fall 2010 and spring 2011 the heater of the precipitation gauge was out of order, leading to long gaps. Excluding lags calculated from months, in which the temperature dropped below 0 °C, the lag between rainfall and peak in pore water pressure varies from 1.25 days to 6 days, with a mean of approximately 2.75 days. In October 2009 and 2010, considerably longer lags of 12.5 and 8.75 days, respectively, display the influence of snowfall and snowmelt. However, due to the varying lengths of snowfall and periods with temperatures below freezing – thus periods in which snow is stored – it is impossible to derive a significant value (lag), which represents all such periods.

Table 6: Results of the crosscorrelation analysis of short data intervals (10–28 days) with no or negligible gaps. The lag varies between 1.25 and 6 days and averages 2.5 days.

Start- & end-date [mm/dd/yy]**	Interval length [days]	R_{XY} (Rain–PWP)	R_{XY} (Rain– Δ PWP)	Lag* [days]
05/01/09–05/10/09	10	0.29	0.28	2.25
06/23/09–07/02/09	10	0.34	0.55	2.5
07/01/09–07/14/09	14	0.27	0.39	1.75
07/15/09–07/30/09	16	0.27	0.64	2.0
08/01/09–08/11/09	11	0.3	0.58	2.5
09/01/09–09/11/09	11	0.35	0.52	3.25
11/02/09–11/11/09	10	0.35	0.38	1.75
05/26/10–06/08/10	14	0.32	0.62	1.25
07/15/10–08/11/10	28	0.2	0.48	2.5
07/22/10–08/01/10	11	0.3	0.64	2.5
04/11/11–04/20/11	10	0.48	0.62	1.5
06/15/11–06/29/11	15	0.2	0.45	2.5
07/12/11–07/26/11	14	0.32	0.52	3.0
09/17/11–09/27/11	11	0.65	0.6	6.0

PWP = absolute pore water pressure

Δ PWP = differenced pore water pressure

* Lag has been derived from crosscorrelation of Rain–PWP

** Interval starts at 00:00:00 on start-date and ends at 18:00:00 on end-date

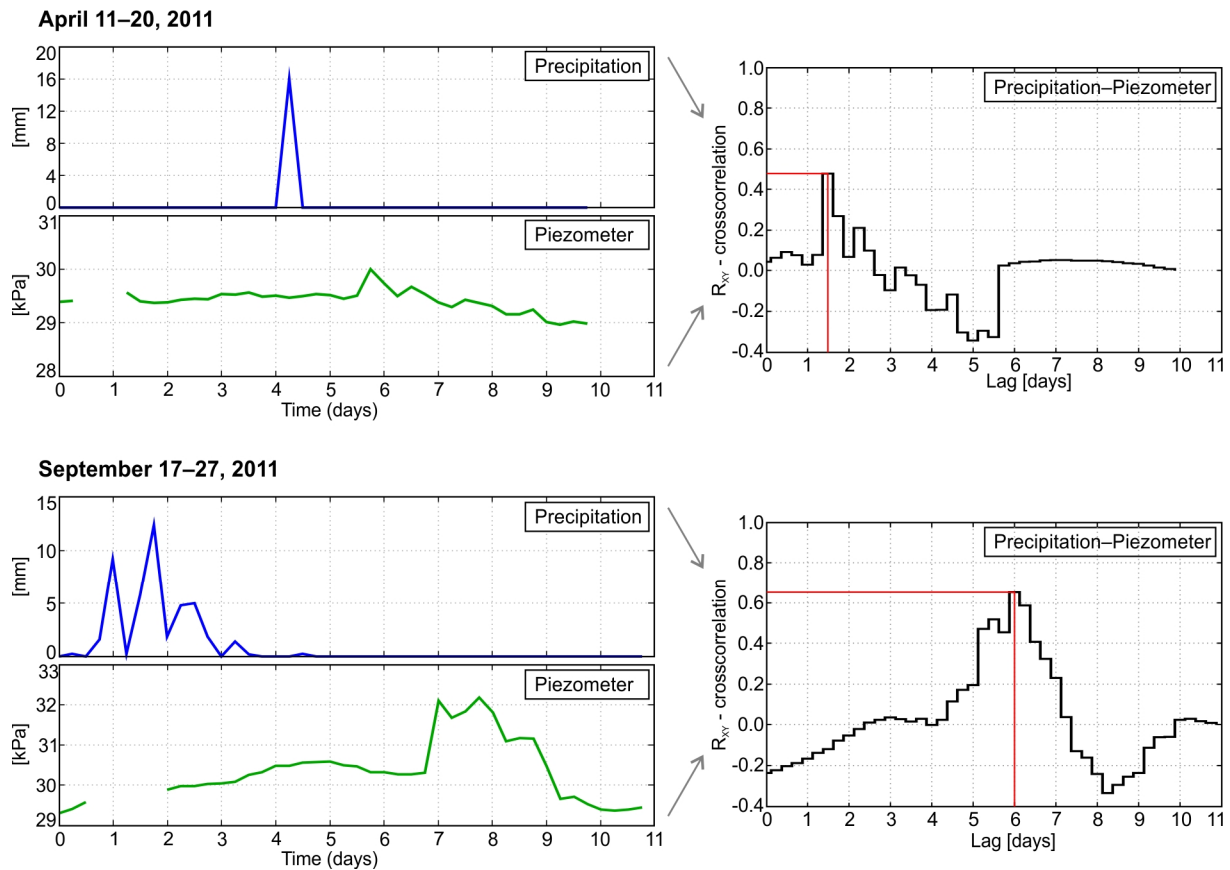


Figure 50: Two sample crosscorrelations calculated from precipitation and pore water pressure data, which have been sampled in a 6-hour interval over a period of 10, respectively 11 days. Since just a single event (rainfall) happened in each of the samples, the correlation is comparably high.

To overcome problems in the correlation analysis arising from too many gaps in the data series, several shorter intervals (10–28 days) with no or negligible gaps have been selected and crosscorrelations calculated from them. The calculated values are listed in Table 6 and a selection of according correlation diagrams is pictured in Figure 50. The results differ hardly from the ones attained from the monthly sections. The lag between rainfall and peak in pore water pressure varies from 1.25–6.0 days and averages 2.5 days. In summary, the crosscorrelation analysis of precipitation and pore water pressure over intervals of various lengths (10 days to 1 year) yielded rather homogeneous results, with lags varying only slightly (with one exception in September 2011), averaging about 2.5 days.

6.5 TSA – threshold derivation and discussion of results

Already the visual evaluation and comparison of the various data series provided some valuable information. It clearly shows the influence of the precipitation on the water table – measured as pore water pressure by the piezometer in B4. On the one hand, following snowmelt of snow-rich years (2009 and 2010) a distinctive rise in pore water pressure (rise of water table by 0.8 m at maximum) can be observed. On the other hand, a similar behavior is evident after rainfall-

rich periods as well, with a maximum water table rise of 0.7 m. Additionally, a response of the deformation measurements (GNSS) to precipitation and thus to an elevated water table, can be identified in the visual evaluation, too. A small increase in the displacement rate (mm-range) is noticeable at several points in time in the data series following periods of intense rainfall and/or snowmelt. These observations led to the deduction of a first conservative threshold: If the water pressure surpasses 32 kPa in piezometer B4 and remains at this elevated level for several days, small movements/accelerations can be expected in the GNSS measurements.

The evaluation of shorter data series allowed verifying and refining these initial results. The analysis of a 60-day interval (Figure 46) exemplarily illustrated the relation between rainfall (not necessarily limited to heavy rainfall events) and variation in pore water pressure in great detail, and also revealed additional information regarding the relation between rainfall/pore water pressure and deformation measurements and between GNSS sensors themselves. The pore water pressure reacts to rainfall with a temporal delay of several days, while a reaction of the GNSS can't yet be quantified with certainty. Though a temporal delay between rainfall/rise of water table and GNSS movement seems to be visible after some precipitation events, at least in one of the GNSS sensors at a time, it can't be defined more precisely by simple visual analysis. Yet, a comparison of the data of the three GNSS sensors between themselves shows a very similar behavior of sensors 2 and 3, while GNSS 1 differs from them and moves even less (only 1 cm over the 3-year observation period for sensor 1, three times as much for the other two).

Auto- and crosscorrelations calculated from data series of various lengths yielded some additional information and specified the above-described observations. The analysis of precipitation and pore water pressure confirmed the results of the visual interpretation: The temporal delay, with which the pore water pressure reacts to preceding rainfall, averages 2.5–2.75 days. This delay varies only little, except for times during snowfall and snowmelt; then the lag – temporal delay – strongly depends on the duration over which the precipitation is “stored” as snow. The lag between rainfall or pore water pressure and GNSS displacement measurements couldn't be specified by means of correlation analysis either, even though some similar characteristics were notified visually. This is due to the extremely small movement rates of only a few millimeters at maximum – attributed to a single “extreme rainfall/snowmelt event” – which, however, are still within the GNSS's noise, thus preventing significant results.

The correlation analysis of the data of the three GNSS sensors verified the first impressions: The calculated crosscorrelation showed a very strong similarity between the data sets from GNSS 2 and GNSS 3, while the crosscorrelation of either with GNSS 1 is distinctly lower. This different behavior can be explained by the sensors' location. GNSS 1 is located at the very edge of the Aggenalm landslide, where even smaller movements occur, while GNSS 2 and GNSS 3 are situated centrally, at the main sensor node and at the Lampl Alm, where the movement rates are slightly higher. In addition, the strong correlation between GNSS 2 and GNSS 3 as well as the attained lag, 0 (no temporal delay), confirm the very homogeneous and also simultaneous

movements, especially in the lower two-thirds of the slope, where the mechanism of the Aggenalm landslide has been classified as slide.

In summary, by applying TSA methods to the data it was possible to better describe and to partly quantify the cause-and-effect chain between trigger factors (precipitation/pore water pressure) and landslide displacement, and also to derive a first threshold, which was incorporated into the alpEWAS Control software. Once the pore water pressure surpasses the set threshold (32 kPa) an e-mail alert is sent to the experts/administrators automatically, who evaluate the severity and then decide depending on the situation, if further measures have to be taken (in consultation with the municipality). The threshold evaluated by the TSA, however, is much too conservative for early warning. Therefore a numerical model was set up to obtain information about the system behavior beyond the previously observed relationships, whose results are described in the succeeding Chapter 7.

7. Numerical model of the Aggenalm landslide

Upon analyzing the newly gathered data and adapting the geological model, a new numerical model has been accordingly set up and calculated using the geosensor network's data for validation purposes. This has been done even though numerical simulations of the Aggenalm landslide already existed (JUNG 2007, TADAYONFAR 2011), which, however, were each based on the old geological model by JUNG (2007) and didn't include the new information acquired in course of the alpEWAS project and by the GSN, either. Subsequently, the new model is then used as a predictive tool for landslide behavior to simulate extreme events – e.g., water tables that haven't been observed so far – in order to deduce thresholds for such events.

In the beginning of this chapter, the underlying processes and methodology of the used modeling software are outlined. This is followed by a description of the modeling strategy, the model's structure and the parameter acquisition as well as studies, which were conducted as part of the validation process. Finally, the results of the validated model and the simulation of the extreme events are presented.

7.1 Basic principles

In the last few decades, the application range of numerical models and the variety of available numerical codes has expanded greatly. As STARFIELD & CUNDALL (1988: 99) point out, this is mostly due to the rapid advancement in computer technology and the accompanying easy access to versatile and powerful computer packages as well as due to increasing possibilities to incorporate the underlying geology and structures into the model. At the same time a shift in application from predominately experimental research to practical engineering took place.

Nowadays, many different programs are state-of-the-art and are widely used in the field of geosciences and geomechanics. They allow analyzing complex factors such as nonlinear behavior, inhomogeneity, anisotropy, inclusion of discontinuities, fluid flow, material softening, time-dependent behavior, and many others, while they remain always data-dependent and thus strongly depend on the available input data. A great amount of data seems to be useful but one has to keep in mind that at the same time this increases the complexity of a model (HOLLING 1978: 60ff.), which may then reduce the clarity and general utility. Therefore one should always consider this interdependence, and balance data input against utility.

7.1.1 Numerical modeling techniques

As mentioned before in Chapter 3.5.2 STEAD et al. (2006: 217) discriminate between three different numerical modeling levels. Ordered after their sophistication these are: kinematic & limit-equilibrium analysis models (Level I), continuum & discontinuum numerical methods (Level II), and hybrid finite/discrete element models with fracture approaches (Level III).

Level II methods can again be roughly classified by their three underlying numerical computation techniques according to KONIETZKY (2001: 9):

- Type of material description: continuum vs. discontinuum approach
- Type of spatial discretization: domain vs. boundary method
- Type of time discretization: explicit vs. implicit solution

The rock or soil mass can be treated in two different ways, either using a continuum or a discontinuum approach. Which of the two is used best, depends on several factors, such as type and structure of material, scale of the problem, and purpose of the analysis. Using discontinuum mechanical formulations (DEM – distinct element method, DDA – discontinuous deformation analysis) the rock mass is subdivided into individual blocks that interact with one another. Different algorithms can be used to describe the blocks' interactions, but all have to fulfill certain requirements such as automatic surveillance of contacts and complete description of all kinematic movement patterns (rotation, displacement, establishment or loss of contacts). The blocks can be discretized internally either by finite element (FE) or finite difference (FD) methods to allow deformation of the individual blocks. (WILL & KONIETZKY 1998: 157f., KONIETZKY 2001: 9f.)

In rock mechanics, the mostly discontinuous rock mass can most often be described as a mosaic of joint-bounded blocks but depending on the scale it is either modeled as a continuum or discontinuum, though the discontinuum approach is preferred most of the time (BENKO 1998: 32ff.). If a rock mass is strongly jointed (no predominant joint sets) and the problem is rather large-scaled, the cumulative effects of the discontinuities on the rock mass can be taken into account and the problem can be solved with a continuum approach. Whereas, soil mechanical problems are predominantly analyzed using a holistic, continuum mechanical approach. Exceptions to that are for example fast moving landslides, such as debris flows or rock falls, at which a discontinuum model is more suitable to describe the involved mechanisms.

In domain methods, such as the finite element method (FEM), finite difference method (FDM) or discrete element method (DEM), the modeled rock mass (continuum or discontinuum) is discretized into a finite number of elements (geometrically simple zones) which require a complete cross-linking with nodes (grid¹⁹). All domain methods are based on the solution of sets of algebraic equations, whose resulting equations are the same for either FEM or FDM, even though they have been derived in different ways (ITASCA CONSULTING GROUP INC. 2011b: 1-1). The nodal forces are then translated to displacements at the individual nodes using a stiffness matrix (KONIETZKY 2001: 9). Boundary element methods (BEM) on the contrary do not need to be completely discretized. It is sufficient to divide only the surface or excavation of the rock

¹⁹ The grid is not restricted exclusively to rectangular forms, which are most often associated with FD methods, but can have any shape as can the boundaries (ITASCA CONSULTING GROUP INC. 2011b: 1-1f.).

mass into small elements, in order to apply appropriate boundary conditions, while the rest is treated as a continuum (AMANN 2006: 136f.).

Generating the grid is always easier in BEM (less discretization necessary) and the computational effort is usually lower, at least for simple problems, than in domain methods. Contrariwise differential methods (domain) have the advantage that rock mass properties such as inhomogeneity and nonlinear behavior can be easily incorporated in the material law. This is very inefficient or not possible at all in boundary methods. (KONIETZKY 2001: 9f.)

The third and most important sub-classification of Level II codes is the type of time discretization applied in the solution method. If the equation of motion is evaluated at an initially unknown state ($t + \Delta t$), this is called implicit. On the contrary, in the explicit solution scheme, the equation of motion is solved for a known point in time (t) (WILL & KONIETZKY 1998: 158f.). Table 7 summarizes the major differences between explicit and implicit solution schemes by comparing an explicit FD program with an implicit FE code.

Table 7: Comparison of explicit and implicit solution methods. The explicit method is used by finite difference (FD) methods such as FLAC while implicit solution methods are most commonly used by finite element programs (after ITASCA CONSULTING GROUP INC. 2011b: 1-4, Table 1.1 and KONIETZKY 2001: 10, Tab. 1).

Explicit solution method in FD	Implicit solution method in FE
Timestep must be smaller than a critical value to ensure numerical stability	Timestep can be arbitrarily large, with unconditionally stable schemes
Small amount of computational effort per timestep but many operations to reach solution	Large amount of computational effort per timestep but few global operations necessary
No significant numerical damping introduced for dynamic solution	Numerical damping dependent on timestep present with unconditionally stable schemes
No iterations necessary to follow nonlinear constitutive law	Iterative procedure necessary to follow nonlinear constitutive law
Provided that the timestep criterion is always satisfied, nonlinear laws are always followed in a valid physical way	Always necessary to demonstrate that the above-mentioned procedure is stable and follows the physically correct path (in case of path-sensitive problems)
No matrices are ever formed and memory requirements are always at a minimum; no bandwidth limitations	Stiffness matrices must be stored and associated problems such as bandwidth must be overcome; usually requiring large memory
Since no matrices are formed, large displacements and strains are accommodated without additional computational effort	Additional computing effort is needed following large displacements and strains

In FE programs it is common to generate a global stiffness matrix from the element matrices, therefore using an implicit, matrix-oriented solution scheme. However, this is uncommon in

explicit FD codes. Here a time-marching method to solve the algebraic equations is used (WYLLIE et al. 2004: 221), as it is relatively efficient to regenerate the FD equations at each step (Figure 51). Explicit methods are especially suitable for nonlinearities and dynamic systems with strong deformations while an implicit solution scheme is preferably applicable for linear elastic, static problems (KONIETZKY 2001: 11). A more detailed description of the different solution schemes, their advantages as well as disadvantages and their application range can be found, e.g., in KONIETZKY et al. (1994), WILL & KONIETZKY (1998), KONIETZKY (2001), ITASCA CONSULTING GROUP INC. (2011b).

7.1.2 FLAC and the finite difference method (FDM)

According to DESAI & CHRISTIAN (1977) in ITASCA CONSULTING GROUP INC. (2011b: 1-1) and ODEN (1991: 3ff.) the FDM method is probably the oldest numerical technique used to solve sets of differential equation when initial and/or boundary values are given. The code FLAC has been developed by Itasca and was first released in 1986 (www-09). Nowadays, two different versions – 2D and 3D – of the FLAC program exist on the market. Only the two-dimensional version of the program²⁰ will be discussed further on as it has been selected to simulate the Aggenalm landslide.

The name *FLAC* stands for ‘Fast Lagrangian Analysis of Continua’ and the code is based on an explicit finite difference solution method. FLAC – as most FD programs – utilizes an explicit, dynamic solution scheme. The calculation sequence embodied is pictured in Figure 51. In this calculation procedure, new velocities and displacements are derived from stresses or forces by the equation of motion. From the velocities new strain rates are deduced and new stresses from the strain rates.

Every cycle equals one timestep (t), which is so small that no passing of information from one element to a neighboring element is physically possible. In this basic principle of the explicit solution scheme, each box (equilibrium equation or stress/strain relation) updates all of its grid variables from known values that remain fixed during the box’s calculation cycle. For instance, the constitutive equation uses the velocities that remain frozen for the operation and computes new stresses for each element, meaning there is no influence on the velocities by the newly calculated stresses (due to the very small timestep). After several cycles (timesteps) it is of course possible for disturbances to propagate across several elements, which are updated after each cycle. (ITASCA CONSULTING GROUP INC. 2011b: 1-2f.)

The term Lagrangian in the code’s name refers to the Lagrangian formulation that is used in this program. Since no global stiffness matrix needs to be formed, the coordinates can easily be

²⁰ The first numerical analysis of the Aggenalm landslide performed by JUNG (2007) utilized two programs by Rocscience (www-18), *Slide* and *Phase2*, the former a ‘2D limit-equilibrium slope stability analysis program’, the latter a ‘2D finite element analysis program’. Phase2 offers a great variety of modeling options and uses the shear strength reduction method especially in slope stability analysis. In the numerical analysis by TADAYONFAR (2011) the FLAC program was applied but was still based on the first, thus “old” geological model. In this thesis, Phase2 was only used marginally in the initial stage as a quick backup modeling tool during the parameter studies.

updated at each timestep in large-strain mode. This means that the incremental displacements are added to the coordinates so that the grid, representing the material, moves and becomes deformed. Contrariwise, the material moves and becomes deformed in relation to a fixed grid, when utilizing an Eulerian formulation. (ITASCA CONSULTING GROUP INC. 2011b: 1-4)

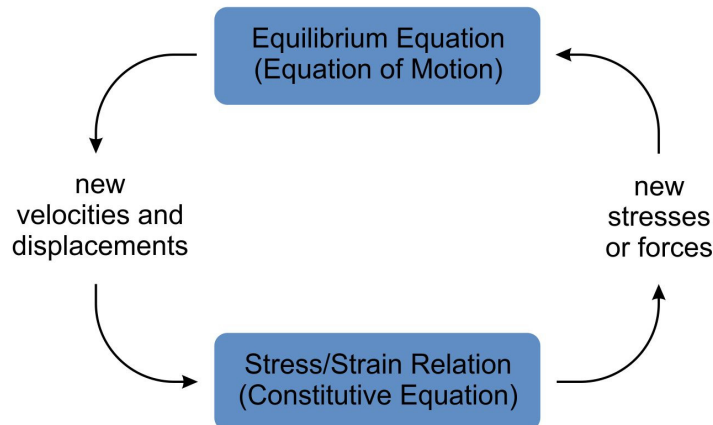


Figure 51: Basic calculation cycle in explicit solution schemes (ITASCA CONSULTING GROUP INC. 2011b: 1-3, Figure 1.1).

The FLAC program offers a versatile application spectrum and can simulate the behavior of many different materials such as soils, rocks, structural elements, and buildings, and their influence on each other. FLAC offers several built-in constitutive models, optional facilities and available structure elements as well as a program-specific language – FISH.

The basic version of FLAC offers a total of 14 constitutive models to represent geomechanical material behavior that can be arranged into 3 model groups: null, elastic, and plastic model group. The material model *null* is used to represent material that is removed or excavated. The second group – elastic material model group – consists of an *elastic, isotropic*, and *elastic, transversely isotropic* model. Both material models are suitable for elastic, isotropic material that exhibit linear stress-strain behavior, with the second being able to simulate layered elastic media with different elastic moduli in directions normal and parallel to the layers. The third group – the plastic model group – is the largest of the three and consists of the following 11 models: *Drucker-Prager*, *Mohr-Coulomb*, *ubiquitous-joint*, *strain-hardening/softening*, *bilinear strain-hardening/softening ubiquitous-joint*, *double-yield*, *modified Cam-clay*, *Hoek-Brown*, *modified Hoek-Brown*, *Cysoil*, and *simplified Cysoil* model. While some of these models are specifically suitable for certain applications or materials, models such as the *Mohr-Coulomb* or (*modified*) *Hoek-Brown* offer a wide application range and are most commonly used to model geologic materials. The former is the most conventional model to represent shear failure in soils and/or rocks (ITASCA CONSULTING GROUP INC. 2011c: 1-3ff.).

Additionally, an *interface* model is available to insert planes into the grid upon which slip and/or separation are allowed. Even though joint-dominated problems call for more suitable programs, using a discontinuum approach, it is possible to integrate simple joints and faults while still having the advantages of a continuum program.

Several different structures, such as liners, piles, bolts, just to name a few, can be easily added and modeled using the structural element logic of FLAC. Furthermore, static, dynamic, creep, seepage, and thermal modes are additions that can be easily incorporated into FLAC. Another powerful tool is the built-in programming language FISH (short for FLACish). It enables the user to write their own programs to extend FLAC's functions including implementation of new constitutive material laws/models and to plot and print user-defined plots.

7.1.3 Mohr-Coulomb model

This section briefly describes the basics of the constitutive Mohr-Coulomb (MC) model, which has been chosen to describe the material's behavior in the numerical simulation of the Aggenalm landslide. It is the most commonly used material model to simulate shear failure in soils and/or rocks in geomechanical modeling. Reasons for the popularity of the model are most certainly the small number of necessary input parameters – shear (G) and bulk (K) moduli²¹ for elasticity, cohesion (c) and angle of friction (ϕ) for plasticity, and the angle of dilatancy (ψ) – that are also comparably easy to come by. The MC model thereby represents a good approximation of soil and rock behavior while the computation time still tends to be relatively fast compared to other more complex material models.

In the elasto-plastic MC material model incorporated in FLAC, the failure envelope corresponds to the MC failure criterion, at which, when satisfied, the material either yields by shear or tension (tension cutoff). It uses a nonassociated shear flow rule and an associated tensile flow rule. Subsequently, the main underlying equations of the MC model are given, while a more detailed and complete presentation of this constitutive MC model in regards to its implementation in FLAC as well as several application examples can be found in ITASCA CONSULTING GROUP INC. (2011c: 1-30ff.). All of the following equations have been taken from this description.

FLAC utilizes the principal stresses, σ_1 , σ_2 , σ_3 , with the out-of-plane stress, σ_{zz} , as one of them. The principal stresses and according directions are calculated from the stress-tensor components and ordered so that

$$\sigma_1 \leq \sigma_2 \leq \sigma_3 \quad (7-1)$$

Eq. 7-1 is fulfilled (with compressive stresses being negative).

²¹ FLAC utilizes the shear and bulk moduli as stiffness moduli, which can be calculated from the input values, E and ν , Young's modulus and Poisson's ratio, respectively.

The associated principal strain increments $\Delta e_1, \Delta e_2, \Delta e_3$ are composed of elastic (superscript e) and plastic (superscript p) parts according to Eq. 7-2:

$$\Delta e_i = \Delta e_i^e + \Delta e_i^p \quad i = 1,3 \quad (7-2)$$

Only during plastic flow are the plastic components nonzero. Then, the incremental expression of Hooke's law in terms of principal stress and strain can be expressed by Eq. 7-3:

$$\begin{aligned} \Delta \sigma_1 &= \alpha_1 \Delta e_1^e + \alpha_2 (\Delta e_2^e + \Delta e_3^e) \\ \Delta \sigma_2 &= \alpha_1 \Delta e_2^e + \alpha_2 (\Delta e_1^e + \Delta e_3^e) \\ \Delta \sigma_3 &= \alpha_1 \Delta e_3^e + \alpha_2 (\Delta e_1^e + \Delta e_2^e) \end{aligned} \quad (7-3)$$

where $\alpha_1 = K + 4G/3$ and $\alpha_2 = K - 2G/3$, with G (Eq. 7-15) and K (Eq. 7-14) being the shear and bulk modulus, respectively (ITASCA CONSULTING GROUP INC. 2011c: 1-30).

By applying the convention of Eq. 7-1, the Mohr-Coulomb failure criterion can be pictured in the σ_1 - σ_3 -plane (Figure 52).

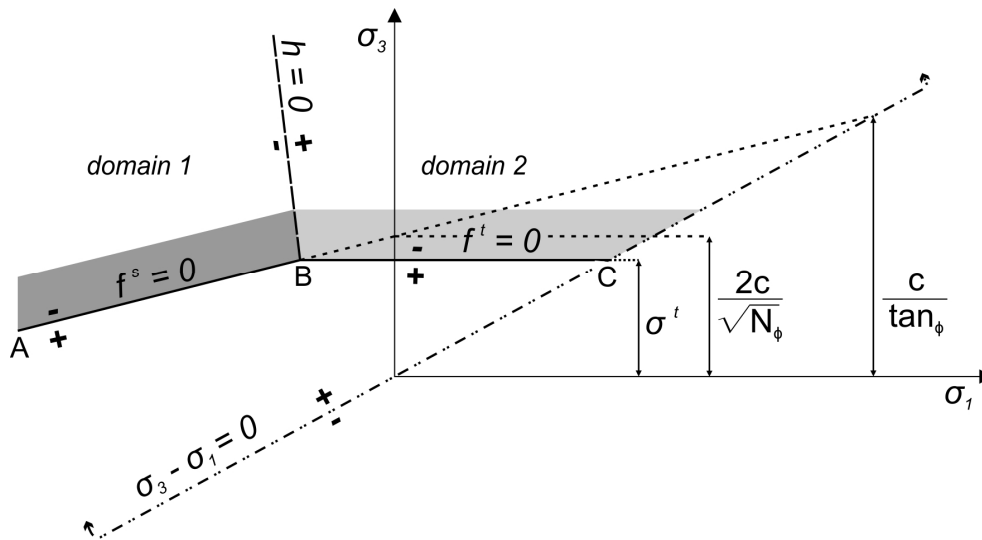


Figure 52: Mohr-Coulomb failure criterion represented in the σ_1 - σ_3 -plane in FLAC according to ITASCA CONSULTING GROUP INC. (2011c: 1-31, Figure 1.6) and domains used in the definition of the flow rule according to ITASCA CONSULTING GROUP INC. (2011c: 1-33, Figure 1.7).

Once the MC failure criterion is met, the material yields either by shear or by tension. Failure due to shear can be expressed by the MC shear yield function (Eq. 7-4), which is defined from point A to point B (Figure 52).

$$f^s = \sigma_1 - \sigma_3 N_\phi + 2c\sqrt{N_\phi} \quad (7-4)$$

Here, in the shear yield function (Eq. 7-4), only σ_1 and σ_3 (major and minor principal stresses) are active, while σ_2 has no effect. Thus, shear yield is detected if $f^s < 0$ (ITASCA CONSULTING GROUP INC. 2011a: 3-104). Once the normal stress becomes tensile, the MC criterion loses its physical validity and then, from B to C the tension yield function (Eq. 7-5) defines the failure envelope due to tension, at which tensile yield is detected if $f^t > 0$.

$$f^t = \sigma^t - \sigma_3 \quad (7-5)$$

In the two preceding equations, ϕ stands for the friction angle, c for cohesion, σ^t for tensile strength and N_ϕ is obtained by Eq. 7-6:

$$N_\phi = \frac{1 + \sin \phi}{1 - \sin \phi} \quad (7-6)$$

It is also noteworthy that the tensile strength, σ^t , of a material with friction ($\phi \neq 0$) in the tension yield function (Eq. 7-5) cannot exceed the value σ_{\max}^t , which can be calculated by

$$\sigma_{\max}^t = \frac{c}{\tan \phi} \quad (7-7)$$

As above-mentioned, the MC material model in FLAC uses a nonassociated shear flow rule and an associated tension flow rule. The shear potential function, g^s , is given by Eq. 7-7:

$$g^s = \sigma_1 - \sigma_3 N_\psi \quad (7-8)$$

where ψ stands for the dilation angle and N_ψ is defined by Eq. 7-9:

$$N_\psi = \frac{1 + \sin \psi}{1 - \sin \psi} \quad (7-9)$$

The tensile potential function, g^t , following an associated flow rule is given by the following formulation, Eq. 7-10:

$$g^t = -\sigma_3 \quad (7-10)$$

The transition region (edge) between the composite yield functions in the three-dimensional stress space has to be defined separately. For this case – a shear-tension edge – the flow rules

are given a unique definition in FLAC, which is illustrated in Figure 52 and requires the introduction of an additional function. This function, $h(\sigma_1, \sigma_3) = 0$, forms the diagonal between the representation of $f^s = 0$ and $f^t = 0$ in the σ_1 - σ_3 -plane and is defined as follows by Eq. 7-11:

$$h = \sigma_3 - \sigma^t + \alpha^p (\sigma_1 - \sigma^p) \quad (7-11)$$

with two constants, α^p and σ^p , that can be calculated by Eq. 7-12 and Eq. 7-13, respectively.

$$\alpha^p = \sqrt{1 + N_\phi^2} + N_\phi \quad (7-12)$$

$$\sigma^p = \sigma^t N_\phi - 2c\sqrt{N_\phi} \quad (7-13)$$

Whenever the Mohr-Coulomb failure criterion is met, the corresponding point in the σ_1 - σ_3 -plane can be either drawn in domain 1 or 2 (negative or positive domain of $h = 0$) as pictured in Figure 52. Shear failure occurs when the stress point is located in domain 1. Using a flow rule that has been derived from the shear potential function, g^s (Eq. 7-8), the stress point is taken back to the failure curve, $f^s = 0$. When tensile failure happens, the process is very similar: The stress point is then located in the positive domain (domain 2) and is taken back to $f^t = 0$ applying a flow rule derived using g^t , the tensile potential. (ITASCA CONSULTING GROUP INC. 2011c: 1-30ff.)

7.2 Modeling approach and strategy

The numerical modeling that has been conducted as part of this work aims to determine threshold values, primarily for extreme events which haven't been observed during the project's runtime. Due to the continuous research at the Aggenalm landslide and the installation of the alpEWAS monitoring system during the past few years, it has been possible to resort to a lot of already existing data concerning geology, build-up, deformation measurements, etc. (Chapter 4 and 5). Thus, only a few additional tests, such as shear tests, had to be conducted specifically for the numerical model, whose results will be described in the following subchapter.

In landslide modeling, several approaches are commonly applied to answer respective questions. To create a good initial model, which coincides with the actual conditions, such as monitoring data, movement pattern, etc., so-called back-analyses are frequently used. Back-analyses are an effective method to gain fitting material parameters (e.g., soil shear strength) that may not be well represented by laboratory testing – such as structural fabric, inhomogeneity, effects of slickensides, etc. – or can't even be obtained due to lack of appropriate samples (TANG et al. 1999: 73). This can be attempted, firstly, by modeling an initial state (constructed slope before movement occurred) with the aim to achieve the present conditions at the slope as model output while calibrating the parameters at the same time. Secondly, the calibration of parameters itself may be referred to as a back-analysis (not using a constructed but the present slope). Once the

model and parameters are validated, it is easy to perform calculations in order to evaluate the model's/slope's evolution in the future. Then, sensitivity analyses to get an understanding of the influences of the different parameters and to derive threshold values can be conducted. Other calculations often performed are stability analyses, where the factor of safety is determined and/or remedial actions are included into the model.

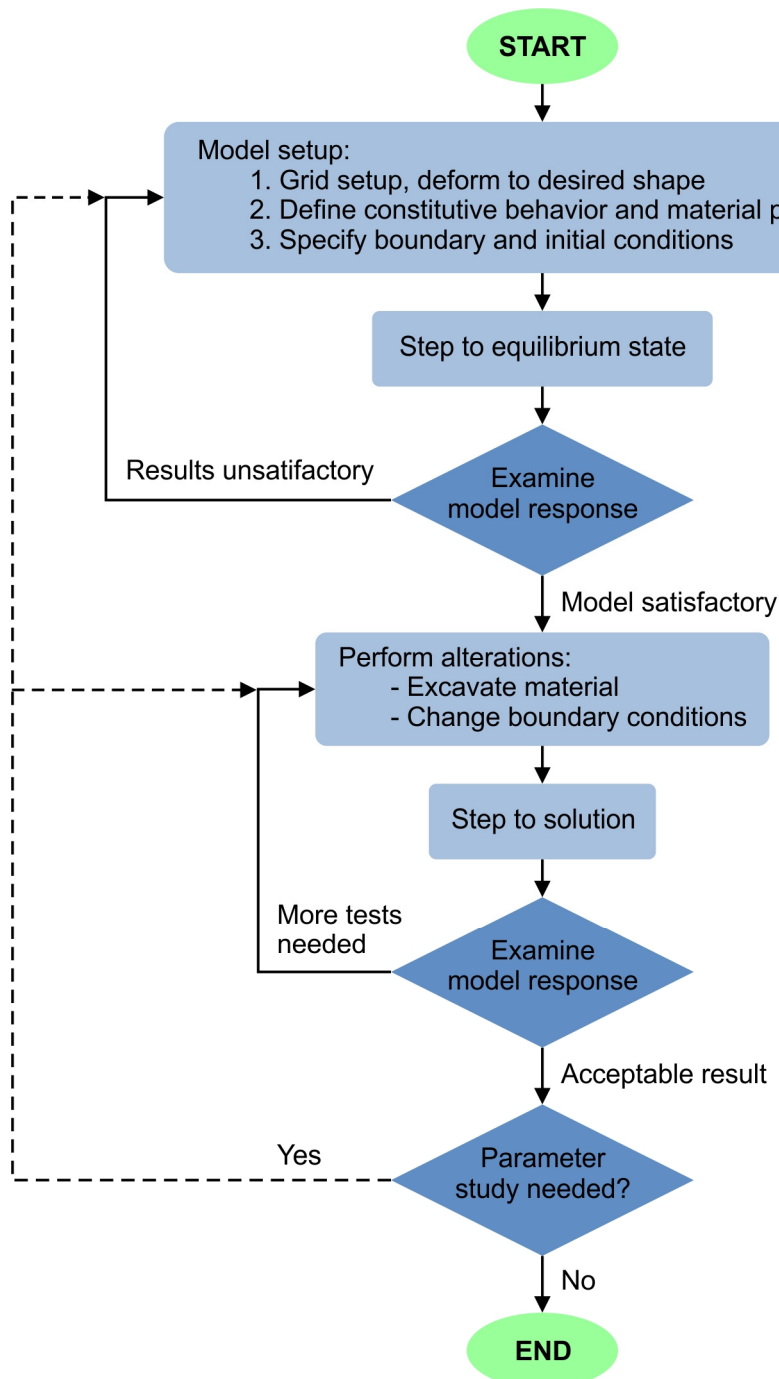


Figure 53: Typical solution procedure in numerical modeling as suggested by ITASCA CONSULTING GROUP INC. (2011a: 2-53, Figure 2.39).

JUNG (2007) and TADAYONFAR (2011) have already performed numerical analyses of the Aggenalm landslide, the former using a limit-equilibrium (Slide) and a FE program (Phase2) both by Rocscience (www-18) and the latter realizing Jung's model in the FD code FLAC by Itasca. Since both performed back-analyses based on a reconstructed pre-landslide geometry (old land surface pictured in Figure 28 in Chapter 4.6.4.1), it was waived to do such an analysis with the same code (FLAC). Rather, the focus was on adapting these existing models to the new findings from the studies in the framework of the alpEWAS project and to model the further development of the movement as well as to derive thresholds.

Thus, a new grid – representing the geometry of the Aggenalm landslide as it is assumed today – has been constructed, based on the new geological model as described and depicted in Chapter 4.6.4.2. Once the grid was constructed and the constitutive material model and boundary conditions set, the model was brought to an initial force-equilibrium state, following the typical solution procedure used in numerical modeling as described by ITASCA CONSULTING GROUP INC. (2011a: 2-52ff.) and illustrated in Figure 53. Using this model (at equilibrium), a back-analysis and parameter study was performed first, to find the parameter sets that best represent the current movement pattern of the Aggenalm landslide. For this initial model the parameter sets of the different geological units (especially Kössen formation, debris/quaternary) and structures (joints) were varied. Afterwards, the slope's possible evolution was modeled and a sensitivity analysis was undertaken, now varying only material properties of the Kössen marls. Additionally, several water tables were introduced to simulate the slope's behavior with water tables several meters higher than observed so far. From the results of these analyses, then threshold values were derived. The input code for the complete numerical analysis is attached in Appendix IX.

7.3 Model setup

In this subchapter the first steps of the numerical analysis – the model setup and the material parameter determination – are described. Although it was tried to model the actual conditions as accurately as possible, it is not always feasible or even advisable to do so due to model-technical reasons, such as extremely long computation time. Therefore some simplifications were implemented, which will be mentioned below in the according passages.

7.3.1 Geometry

The geometry of the numerical model was set up in accordance with section 1 – cross section south in Figure 29, in which all available data has been considered. This section has been chosen as a basis instead of Jung's section updated to today's knowledge or section 2, because of the information available along each section (course of the profile lines in Figure 11 and geological sections in Figure 28 and Figure 29). The decisive factor has been the location of the only, still functional piezometer in B4, which provides the information on the water level and is implemented in section 1.

7.3.1.1 Setup of grid

A grid or finite difference mesh composed of a total of 340,000 quadrilateral elements, each associated with four gridpoints at the corners, has been used for the numerical analyses. With a regular cell width of $1.0 \text{ m} \times 1.0 \text{ m}$ and 1,000 zones horizontally and 340 zones vertically, the model domain is then 1,000 m by 340 m (Figure 54).

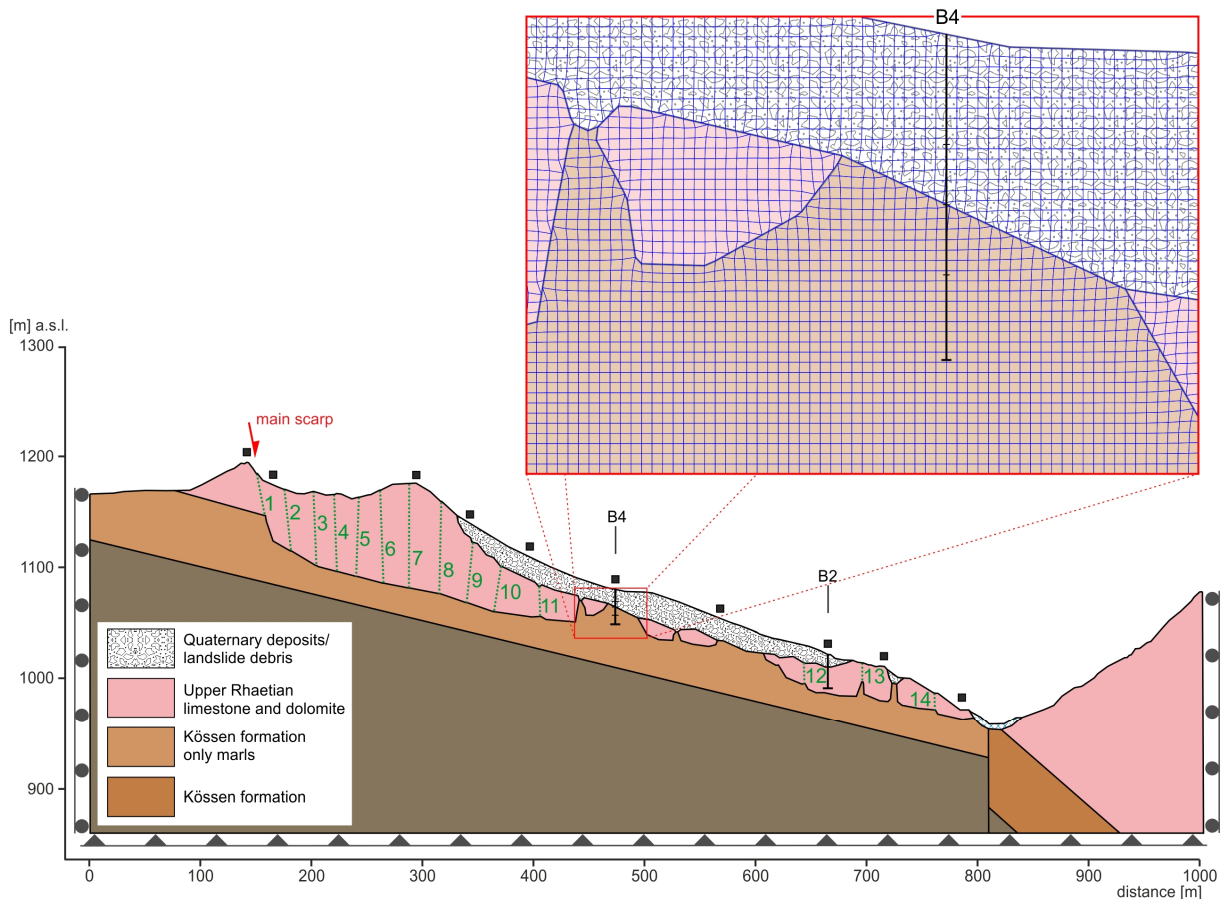


Figure 54: Setup of geometry and geology used as a basis for the numerical simulation. In comparison to the geological section south in Figure 29 some geometrical simplifications have been implemented. The green dotted lines show the joints and their according reference numbers as used in the FLAC input code. The $1 \times 1 \text{ m}$ grid is too dense to be depicted over the complete slope using this scale, but can be seen in the detail inserted above. The boundary conditions are pictured as well, fixed in x - and y -direction at the base and on the sides only in x -direction.

As different parameters can be assigned to each zone the associated level of detail and thus significantly the computation time increases with a concurrent high number of zones. Depending mostly on the computer and its processing power, the computation time for one calculation cycle (calculation of one parameter variation over 100,000 timesteps²²) varied between 4.5 and almost 10 hours. Nevertheless, in order to be able to vary the water table within reasonable level

²² Timesteps refer to calculation cycles as pictured in Figure 51 and don't correspond to "real" time.

changes, such a fine-spaced grid was used which allows changes of 1 m (due to zone width – as each zone can have different parameters). Figure 54 depicts a detail of the grid (insert), after the material boundaries have been inserted. Only toward the material/model boundaries, the 1×1 m zones are deformed in order to meet the boundaries' geometry.

7.3.1.2 Implementation of material boundaries

After preparing the grid, the different material boundaries were inserted into it as was the profile line building the model's surface (Appendix VII). As it can be seen in Figure 54, not much has been simplified compared to the geological cross section in Figure 29. A few details – such as the basis of the Upper Rhaetian formation or the talus at the scarp and blocks in the main landslide body – have been idealized (straightened) or left out. One of the major adjustments has been made within the Kössen formation. The Kössen formation below the Aggenalm landslide, where the landslide's shear surface is thought to be within the marls, was defined as marls only. Since the intermediary banks of limestone or marly limestone as described in Chapter 4.5.1.2 have thicknesses ranging from only a few centimeters to maximum 25 cm, it was not possible nor reasonable to incorporate these into the model. This would have needed a much finer-spaced grid and thus increased the computation time significantly. Instead, this simplification was considered in the parameter analyses of the material properties of the Kössen marls, which might be slightly higher than the properties of the material in reality (Chapter 7.3.2). Summarizing, only geometrical changes that don't have an influence on the model's output or can't be compensated by parameter modifications have been performed.

7.3.1.3 Insertion of joints

Even though FLAC is a continuum code, it is possible to incorporate simple joints geometries as so-called interface elements that are characterized by Coulomb sliding and/or tensile separation (ITASCA CONSULTING GROUP INC. 2011b: 3-1). An interface is realized by a normal- and a shear-stiffness spring between two planes which, in this case, contact each other. Several joints – all located within the Upper Rhaetian formation, especially at the ridge below the scarp – were implemented in the model of the Aggenalm landslide. The location and general orientation of the joints were determined from the detailed mapping performed by JUNG (2007) and WOYTOWITZ (2010). The orientation and progress of the joints below surface were interpreted taking all gathered information into consideration. For referencing, all joints have been numbered in ascending order starting the scarp (Figure 54, Appendix IX).

7.3.1.4 Definition of boundary conditions

The base of the model is fixed in x- as well as in y-direction (Figure 54). The left and right edge of the modeled cross section are only fixed in x-direction to prohibit horizontal movements, while vertical deformation (settling) is licit. The dimensions of the model have been chosen so that on each side it reaches at least 100 m into stable ground (outside of landslide's boundary).

Thus, movements should have faded toward the edge and boundary effects don't superpose the landslide's movements.

7.3.1.5 Implementation of water table

One reason for choosing such a fine-spaced grid has been the implementation of water tables. Since the maximum fluctuation of the phreatic water table in B4 (Chapter 5.3.4.3) over the complete observation period has only been about 1 m, it seemed necessary to be able to simulate such small changes. Therefore, as each zone can have different parameters, a 1 m grid was chosen, which allows such small changes of 1 m. Nonetheless some simplifications and assumptions had to be accepted concerning the water table(s), because of the little information available. As the piezometer B4 is the only functional piezometer and it is known from the mapping that above the scarp is a zone of soil wetting, where the Kössen formation comes (close) to surface, these points have been connected to build the water table. Toward the toe of the landslide the water table has been connected to the Gassenbach since at the toe several zones of soil wetting/seepage and/or small trickles can be observed (Figure 55).

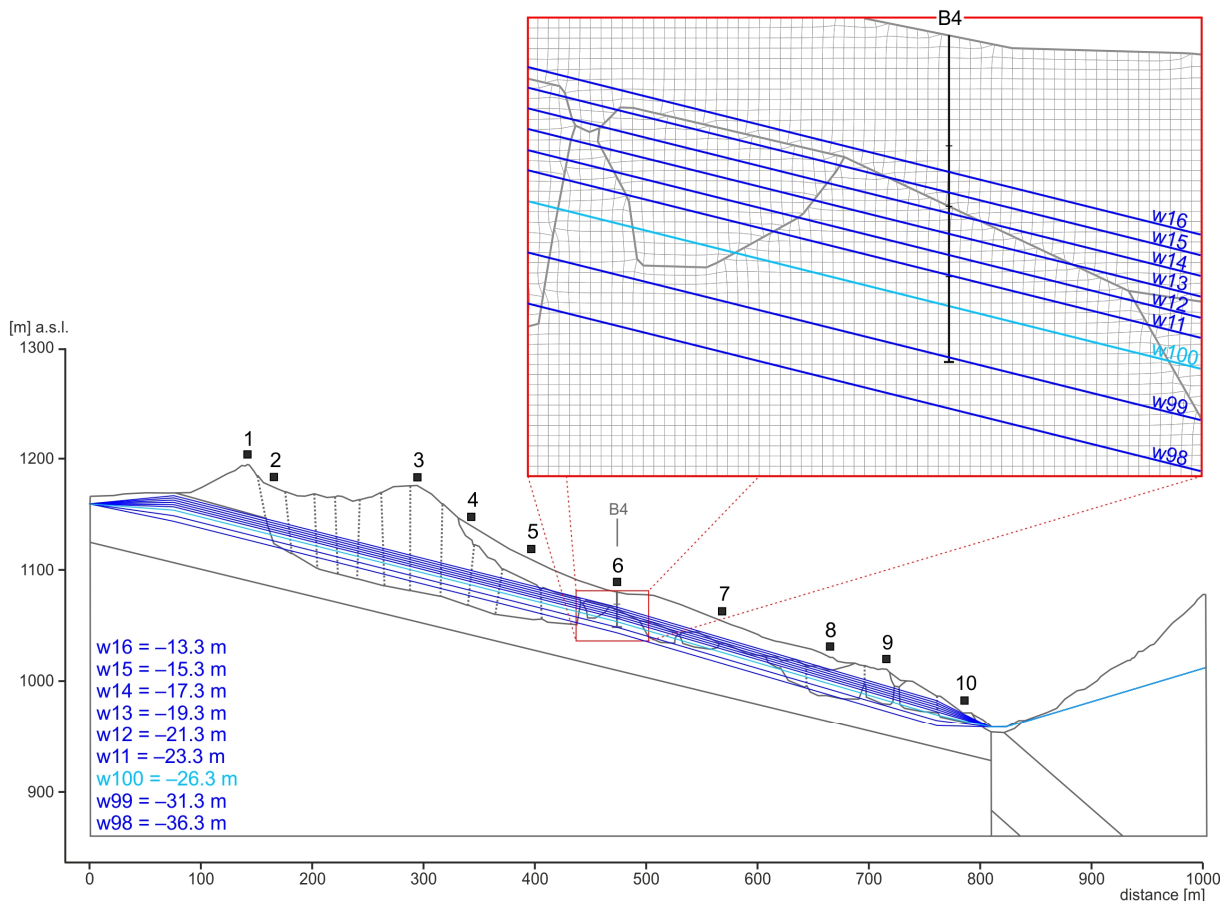


Figure 55: Applied water tables, with w100 (light blue) representing the mean water table measured in B4. The insert shows the water tables in the vicinity of B4 depicted on top of the grid. Note that a cell/zone cannot be divided by the water table but is either saturated or not. Additionally, a total of 10 (1-10) monitoring points to record the deformations on surface are pictured.

Figure 55 depicts the water tables implemented in the model for the parameter variation (w100) and the threshold derivation (w11–w99). Over the monitoring period a mean water table of about -26.5 m was measured by the piezometer in B4, thus it was implemented, named w100, at this depth. Due to the spacing of the grid, only a resolution of 1 m at maximum can be achieved, thus the actual water table in the numerical model is calculated at a depth of -26.0 m. The small discrepancies between measured, implemented and calculated water table are due to the grid's resolution, nevertheless the absolute changes between the different water table depths remain constant at either 5 m (w98–w99–w100), 3 m (w100–w11) or 2 m (w11–w12– ... – w16).

7.3.2 Material parameters

Due to the numerical analyses of the old geological profile of the Aggenalm landslide, parameter sets for the different materials already exist. So, as a basis for the new analyses, the material parameters acquired from the sensitivity analyses by JUNG (2007) and TADAYONFAR (2011) applying the programs Phase2, respectively FLAC, were used. Afterwards, the material properties were varied nonetheless, in order to best represent the observed displacements and movement characteristics of the slope.

Table 8: Material parameters used in the numerical simulation of the Aggenalm landslide. The values correspond to the ones determined and applied by JUNG (2007) and TADAYONFAR (2011). Below, in brackets, the variation ranges or adjusted values are listed. Bulk and shear moduli are calculated from the Young's modulus and Poisson's ratio (Eq. 7-14, 7-15).

	Talus	Debris, Quaternary	Upper Rhaetian f.	Kössen limestone	Kössen marls	Plattenkalk
Density ρ [g/cm ³]	2.2 (2.5)	2.2 (2.5)	2.75	2.7	2.7 (2.4)	2.7
Cohesion c [kPa]	10	10	3050	2490	40 (0–40)	3520
Friction angle ϕ [°]	35	35	30	30.5	23 (16–31)	33.5
Tensile strength σ^t [MPa]	0	0	10	10	0.1	10
Young's modulus E [GPa]	0.05 (0.25, 0.5)	0.02 (0.1, 0.2)	7.9	7.0	5.9 (2.0, 4.0)	13.8
Poisson's ratio ν [–]	0.2	0.2	0.2	0.2	0.2	0.2
Bulk modulus K [GPa]	0.028 (0.14, 0.28)	0.011 (0.06, 0.11)	4.4	3.9	3.28 (1.11, 2.22)	7.65
Shear modulus G [GPa]	0.021 (0.1, 0.21)	0.008 (0.04, 0.08)	3.28	2.95	2.46 (0.83, 1.67)	5.75

In FLAC, when using the MC constitutive model, one needs the following material parameters to define rock and soil masses: density (ρ), cohesion (c), friction angle (ϕ), tensile strength (σ^t), dilation angle (ψ), and bulk (K) and shear (G) moduli. As mentioned above, the initial properties were adopted mainly from the previous analyses of the Aggenalm landslide. They have been cross-checked and validated with values of comparable materials (e.g. limestones, dolomites, etc.), taken from, e.g., KULHAWY (1975), VUTUKURI et al. (1978), and the database stored in the program Phase2. However, a special focus was laid on the marls' parameters (more in Chapter 7.3.2.1), since the field investigations and observations but also the existing simulations showed a great influence of the parameters of the Kössen formation (marls) on the development of the slide in the model output.

The bulk and shear moduli – two elastic constants – describe the isotropic material behavior in the elastic range. They are used in FLAC, rather than the Young's modulus (E) and the Poisson's ratio (ν), from which K and G are calculated (Eq. 7-14, 7-15), since “it is believed that bulk and shear moduli correspond to more fundamental aspects of material behavior” (ITASCA CONSULTING GROUP INC. 2011a: 3-101f., 3-140). The equations are defined as:

$$K = \frac{E}{3(1-2\nu)} \quad (7-14)$$

$$G = \frac{E}{2(1+\nu)} \quad (7-15)$$

K = bulk modulus [GPa]

G = shear modulus [GPa]

E = Young's modulus [GPa]

ν = Poisson's ratio [-]

Table 8 summarizes the properties of the materials defined within the numerical model of the Aggenalm landslide. If parameter variations have been performed in the course of the analyses, the varied values or parameter ranges are listed as well.

7.3.2.1 Properties of the Kössen marls – shear box testing

A special focus was laid on the determination of suitable material properties of the Kössen marls. From previous studies as well as the observations in the field at the Aggenalm landslide the conclusion can be drawn that the Kössen marls are primarily responsible for the Aggenalm's predisposition to sliding. On the one hand due to its more or less slope-parallel orientation and on the other hand because of its material properties. The Kössen marls are affected easily by weathering (long-term) and changing pore water pressures (short-term), which both lead to a reduction of the shear strength. Such a reduction in shear strength makes them prone for the onset of instabilities or can be the reason for the continuing of a movement.

In several publications the following parameters for marls or comparable materials in general and Kössen marls in particular are listed (Table 9). The values show quite some variability, with the cohesion ranging from 0–80 kPa and the friction angle from 15–42°, if considering all listed materials. However, the values of the Kössen marls also vary over a considerable range (c : 5.5–41.9 kPa and ϕ : 16.5–29.4°). Thus, as it was possible to sample the marls of the Kössen formation, direct shear tests were conducted in order to determine “site-specific” shear parameters.

Table 9: Collection of geotechnical parameters of Kössen marl and comparable soil and rock material as published by different authors.

Density ρ [g/cm ³]	Cohesion c [kPa]	Friction angle ϕ [°]	Probed rock/soil material, source
1.79–2.09	1–27	18–25	Upper Lias clay (Lower Jurassic) ANDERSON & RICHARDS (1992: 426f., Table 13.5)
1.80–2.50	2–80	25–42	Keuper marls ANDERSON & RICHARDS (1992: 426f., Table 13.5)
1.75–2.10	0–25	15–32.5	Fine-grained, inorganic, plastic soil DIN 1055-2 (2010: 10f., Tabelle 4 & 5)
1.66–2.11	21.3–41.2	16.5–29.4	Kössen marls REIBMÜLLER (1997: Anhang 4, Tabelle 6)
1.98–2.29	5.5–41.9	23–24	Kössen marls SCHORMAIR (2003: 49, Tab. 3)

Sampling and test preparations

The samples for the shear test were taken at the landslide’s toe at the outcrop of the Kössen formation next to the Gassenbach (as pictured in Figure 12 and described in Chapter 4.5.1.2). At this outcrop the Kössen formation is dominated by marls, which are tectonically extremely stressed and also weathered, most strongly close to the surface. Therefore, to gather less weathered material, it was tried to take samples from as deep below surface as possible, since it is assumed that most of the landslide’s shear zone is not quite as strongly weathered. Due to the conditions at the outcrop, only a sampling depth of about 0.5–0.75 m below surface was realizable. According to ISRM (1981: 94) the sampled material can be classified as moderately to highly weathered (W3–W4).

Two different types of samples – disturbed and undisturbed – were taken. Initially, it was tried to retrieve as many undisturbed samples as possible, but only four – more or less undisturbed specimen – were successfully extracted. These were taken by pressing a cylindrical steel cutter (\emptyset : 7.12 cm, height, h : 2.0 cm) manually into the marls, while trying not to alter the soil’s

density nor fabric. Prior, the sampling area was prepared, so that the sample could be taken perpendicular to the layering of the Kössen formation, in order to measure shear strength parallel to its plane of bedding (assumed orientation of shear zone). After the ring was completely buried in the Kössen marls, it was etched and cut off with material protruding and then wrapped in plastic foil for preservation of the natural water content. Due to the small number of undisturbed specimen, an additional 5 kg of the material (disturbed sample) were retrieved.

In preparation of the shear test, all material protruding the cylindrical steel cutter was cut off the undisturbed samples. For the disturbed samples a similar procedure came to use. Here, the material was built in to the liner manually. For comparative reasons, it was tried to achieve a similar density as the one of the undisturbed samples. According to DIN 18137-3 (2002: 9), the maximum grain size should not exceed one fifth of the sample's height, thus approx. 4 mm. Rock chips, clearly bigger than accepted by the DIN were removed, but as the material is rather foliated, many pieces exceeding 4 mm in one of their axes were left in the sample. This was done due to several reasons: First, the undisturbed samples may contain some bigger chips and are composed of strongly foliated material with flake sizes exceeding the maximum 4 mm, as well. Therefore, to be able to compare the results, the samples should be as similar as possible. Secondly, it is assumed, that the foliated material becomes adjusted during the installation process, so that most of the flakes are oriented with their shortest axis parallel to the sample's height and thus no jamming occurs. Once the ring, containing the sample (\varnothing : 7.12 cm, approx. height 2.0 cm) was prepared, it was set on top of the shear box and the sample was pushed into the sample frame using a punch with the same diameter as the ring.

Test procedure and results

The shear tests were performed as drained direct shear tests in accordance with DIN 18137-3 (2002) using the shear apparatus by Wille Geotechnik (www-19) as pictured in Figure 56 and described in HOLZHAUSER (2011) in great detail. Following the above-mentioned description, the sample was built in the shear box, which consisted of a split sample-frame. The frame's top part was fixed while the lower part was slidable, so that the shear plane was gained by the gap between the split sample-frame (apparatus according to Krey). Since the sample was placed between two filter stones (porous plates) to facilitate drainage, the influences due to pore pressure changes were kept at a minimum. Once the normal load started to be applied, the water container was filled with water to ensure saturated conditions. The specimen were then consolidated by applying a normal load (continuous increase of normal stress in 10 kN/m² increments per minute) via the hydraulic load piston until the preset normal load, N (set as normal stress, σ_n), was reached. The sample was then stressed at the preset normal stress until the accompanying compression (settlement) was below 0.001 mm/h, but at least for 180 minutes.

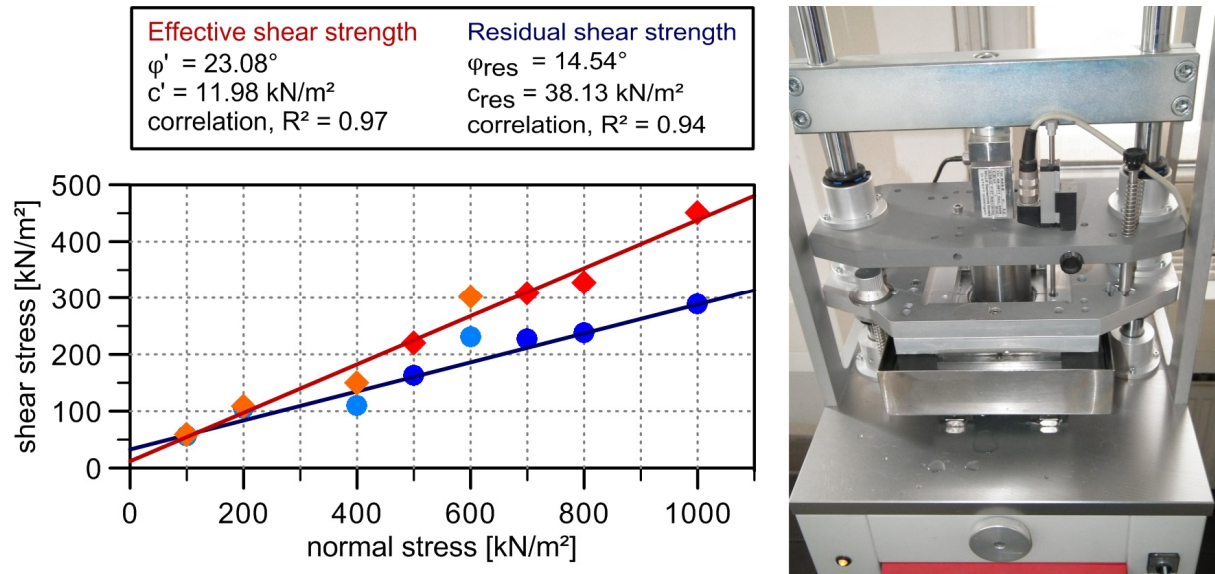


Figure 56: Results of the direct shear tests performed with the apparatus by Wille Geotechnik incorporating the results of eight tests performed at different normal stresses. Depicted are the shear planes for both, the effective (red) and residual (blue) shear strengths. The orange and light-blue marks represent the results of the undisturbed samples, while the red and blue marks are results from the disturbed samples.

Once the consolidation phase ended, the shear phase started automatically, increasing the shear force, S , until the sample failed, thus forming the shear plane, while keeping the normal load, N , constant, at the preset value and increasing the shear distance continuously by 0.008 mm per minute²³. Both, the shear force and the according shear distance, were recorded automatically every 5 seconds. The according shear stress, σ_s , can be calculated by Eq. 7-16:

$$\sigma_s = \frac{S}{A} \quad (7-16)$$

σ_s = shear stress [kN/m²]

S = shear force [kN]

A = area of shear surface overlap (corrected to account for shear displacement) [m²]

Since the area of the shear surface decreases with increasing shear distance, this has to be considered in the calculation of the shear stress by using the reduced area of shear plane A_{red} , which is given by Eq. 7-17 for round shear frames/samples.

²³ This shear velocity was chosen in accordance with DIN 18137-3 (2002: 14, Tabelle 1), which suggests several velocities depending on the sample's plasticity index. As a reference, the range of the plasticity index as determined by REIBMÜLLER (1997: 97f.) was applied.

$$A_{\text{red}} = 0.5\pi r(2r - \Delta l) \quad (7-17)$$

A_{red} = reduced area of shear surface [m²]

r = radius of shear frame/sample [m]

Δl = shear displacement [m]

After the maximum shear stress has been reached, the shearing continues nevertheless up to a shear displacement of 20 mm (the first few tests were sheared over 25 mm, which is the apparatus's maximum). This has been done, so that also residual shear parameters can be calculated from the tests, even though they cannot be determined as accurately as in a ring shear test with greater shear displacements.

The evaluation of the test data was performed using the program Winbod 32 (version 1.88) by Wille Geotechnik (www-19). In order to be able to calculate the effective and residual cohesion and friction angle, at least three shear tests, each performed using a different normal load, are needed. The data can be evaluated by plotting the normal stress versus the shear stress (maximum shear stress for effective shear strength and shear stress after 20 mm shear displacement for residual shear strength). The linear regression through these points then allows determining the angle of friction from the gradient and the cohesion from the intersection with the y-axis. Winbod 32 calculates the parameters φ and c by Eq. 7-18 and Eq. 7-19 as described in the software's manual in accordance with the summation convention in Eq. 7-20.

$$\varphi = \tan^{-1} \left(\frac{\sigma_n \sigma_s - T \sigma_n \sigma_s}{\sigma_n^2 - T \sigma_n^2} \right) \quad (7-18)$$

$$c = \frac{\sigma_s - \sigma_n * \tan \varphi}{T} \quad (7-19)$$

$$\sum_{i=1}^T x_i = x \quad (7-20)$$

φ = friction angle [°]

c = cohesion [kN/m²]

σ_n = normal stress [kN/m²]

σ_s = shear stress [kN/m²]

T = number of tests

From the samples taken at the Aggenalm landslide a total of 13 individual shear tests, applying normal stresses ranging between 100 and 1000 kN/m², were performed. Four of these were done using undisturbed samples (orange and light-blue marks in Figure 56) while for the rest the disturbed sample material was used. Similar results were attained for both sample qualities, with an effective friction angle varying from 21.6 to 24.5° and the effective cohesion from 6.7 to 19.3 kN/m². Figure 56 depicts the results of the four undisturbed samples combined with an

equal number of disturbed samples, for which $\phi' = 23^\circ$ and $c' = 12 \text{ kN/m}^2$. Additional information regarding the installation parameters and results of the individual tests as well as several plots, depicting the change of the shear strength parameters in dependence to which individual tests were combined and diagrams of shear stress versus shear distance, are attached in Appendix X.

Taking these results and the parameters from literature studies into consideration, it was chosen to start the numerical analysis with the parameters listed in Table 8 (Kössen marls: $\phi = 23^\circ$ and $c = 20 \text{ kN/m}^2$) and then slowly adjusting the parameters within the listed ranges during the sensitivity analyses. During the sensitivity analyses the cohesion of the Kössen marls was changed individually in 5 kN/m^2 increments between $0\text{--}40 \text{ kN/m}^2$. The friction angle was varied

between $16\text{--}31^\circ$ and increased in increments of $1\text{--}3^\circ$, performing analyses with $16^\circ, 19^\circ, 21^\circ, 22^\circ, 23^\circ, 25^\circ, 28^\circ,$ and 31° . The range of the covered shear parameter variation of the Kössen marls is illustrated in Figure 57.

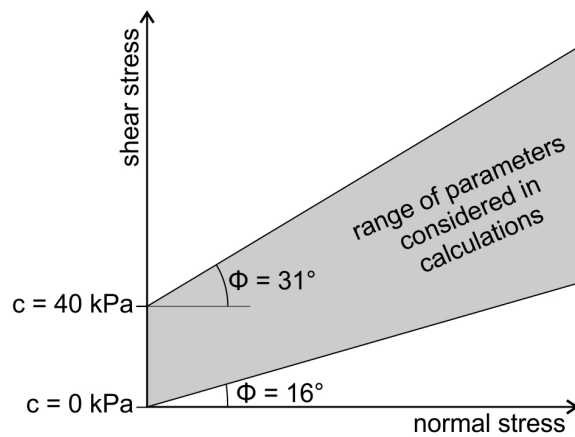


Figure 57: Range of cohesion and friction angle of the Kössen marls considered in the sensitivity analyses depicted in a σ_n - σ_s -diagram.

7.3.2.2 Joint properties

The interfaces or joints introduced into the model are represented by two planes/sides that are connected by shear (k_s) and normal (k_n) stiffness springs. A good approximation for k_s and k_n is to set it to ten times the equivalent stiffness of the stiffest neighboring zone, thus in this case, of the Upper Rhaetian formation. The apparent stiffness of a zone in the normal direction is then determined by Eq. 7-21:

$$k_n = k_s \leq 10 * \max \left[\frac{K + \frac{4}{3}G}{\Delta z_{\min}} \right] \quad (7-21)$$

where K and G are the bulk and shear moduli (Eq. 7-14, 7-15) of the Upper Rhaetian formation, respectively, and Δz_{\min} is the smallest width of an adjoining zone in the normal direction (approximately 1.5 m in the model of the Aggenalm landslide). In this equation, the $\max []$ notation indicates that the maximum value (stiffest) of all adjacent zones should be used.

It is also possible to derive the shear and normal stiffness from tests on real joints or to back-calculate it from the deformability and joint structure in the rock mass and the deformability of the intact rock (ITASCA CONSULTING GROUP INC. 2011b: 3-11ff.). In this case, due to the lack of laboratory tests or suitable parameters, the approximation above, applying Eq. 7-21, has been used. Additionally, parameters defining the joint's friction angle, cohesion and dilation angle are needed and were approximated using comparable values as they can, e.g., be found in KULHAWY (1975). Furthermore they were then adjusted during the parameter studies. Table 10 gives a summary of the joint parameters used in the numerical modeling.

Table 10: Joint parameters and parameter variations applied to the numerical model. The shear and normal stiffness have been calculated by Eq. 7-21 using the bulk and shear moduli of the Upper Rhaetian formation listed in Table 8.

Parameter	Value
Cohesion c [kPa]	0
Friction angle ϕ [°]	25 (5, 15)
Dilation angle ψ [°]	1 (0)
Shear stiffness k_s [GPa/m]	55 (5.5)
Normal stiffness k_n [GPa/m]	55 (5.5)

7.3.2.3 Seismicity

If the modeled area is located within a seismically active area, a rated value of ground acceleration, a_g , has to be taken into consideration, as it might influence the slope's mechanics. According to DIN 4149 (2005: 12, Bild 2), four zones (0–3), ordered by increasing intensity, are distinguished. The Aggenalm landslide is situated in earthquake zone “0”, the lowest intensity interval, for which the rated value of a_g is set zero. Thus, a static analysis is possible as no ground acceleration needs to be implemented.

7.3.2.4 Properties of water tables

For the modeling of the Aggenalm landslide the water tables have been implemented as tables, one at a time instead of a flow analysis, since only little information is available and the only trusted information is from B4 where the resulting pore pressures are calculated by the product of gravity, water density and the vertical depth below the water table. At the same time the mass density of the materials below the phreatic water surface is adjusted to its wet density (saturated) by using a FISH function (Appendix IX, part 3).

7.4 Results of parameter studies and sensitivity analyses

The aim of the parameter study has been to find the material property sets that best represent the today's movement characteristics of the Aggenalm landslide, and thus validate the numerical model. Thereby it was tried to achieve a movement behavior of the numerical slope that shows the following main characteristics:

- Homogeneous movement pattern along the profile from scarp to toe. Small, more or less incessant displacement rates as observed by the LfU and during the alpEWAS project as pictured in Figure 25 and Appendix III.
- Deep-seated shear surface – most likely within the Kössen marls – as hardly any movement was detected by the inclinometer and TDR, while the surface measurement systems display a rather continuous displacement, though very slow (Chapter 5.3).
- Movement characteristics of the Upper Rhaetian formation at slope's top third should display a slightly stronger vertical component to represent the drifting mechanism. Sinking of Upper Rhaetian limestone and dolomite blocks into the underlying plastic Kössen marls while also moving continuously downhill (Chapter 4.6.4.2, Figure 29 and Appendix III).

Initially, parameters identical and/or similar to the ones used in the old numerical models by JUNG (2007) and TADAYONFAR (2011) were applied as listed in Table 8. Depending on the calculation's output, material properties were then varied, one at a time, until the above-mentioned characteristics were satisfied. The change of properties has been performed analogous to the procedure described in the strength reduction method, making big changes at first and then, depending on the implications, adding steps in between. During all of the parameter studies the "mean" water table (w100) was applied. Afterwards, some changes were performed at a slightly higher water table (w11) to check if the parameter variations have a similar effect on the model's output. Only in the threshold derivation, the water table was then varied while the material parameters were fixed at the best-suited values.

7.4.1 Parameter variations of Quaternary deposits and joints

In order to reach the above-mentioned requirements on the slope's behavior, the Quaternary's (talus and debris/Quaternary, summarized as Quaternary deposits) and the joints' properties had to be adapted. Even though, the properties of the Quaternary deposits were already set quite high, several "secondary" shallow movements within the Quaternary deposits, especially at the steepest parts of the slope (above B4 and at the toe) superposed the movement of the deep-seated Aggenalm landslide (Figure 58). Therefore the properties, density as well as bulk and shear moduli, were set at partly unrealistically high values. The density was changed to 2.5 g/cm³ and the bulk and shear moduli were multiplied by 5 and 10, respectively.

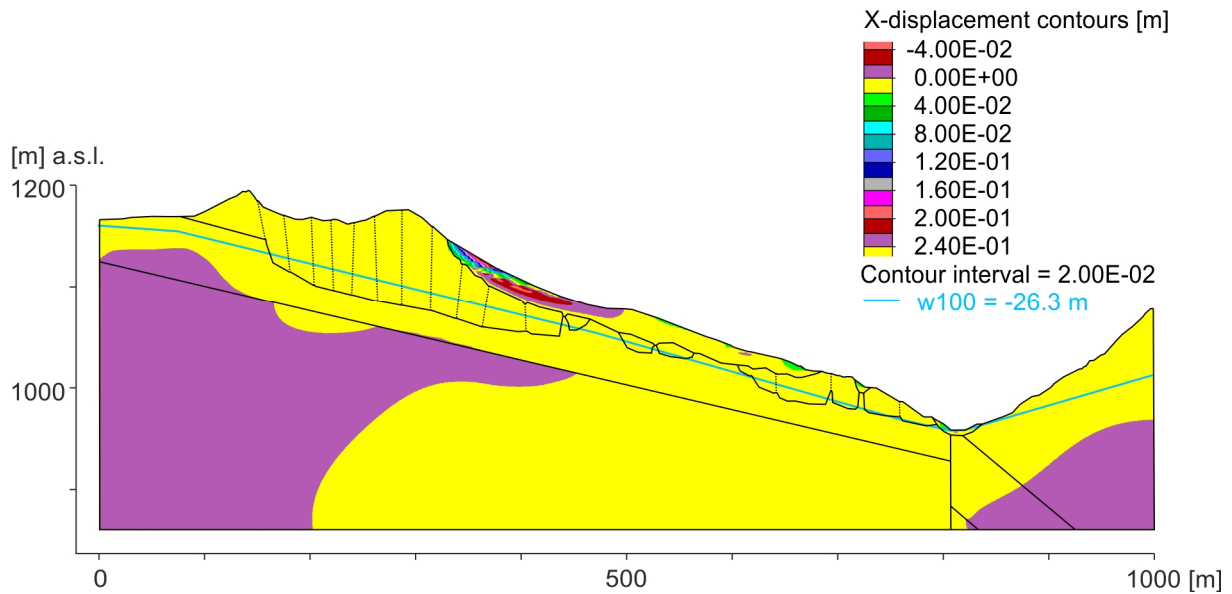


Figure 58: X-displacement contour plot of the Aggenalm landslide after 100,000 steps before adjusting the properties of the Quaternary deposits. The Quaternary deposits' properties are set to their initial values as listed in Table 8. The movements mostly occur within these deposits, especially in the steepest parts of the slope (below Upper Rhaetian formation ridge and at the toe of the landslide) and thus superimpose the displacements within the deeper parts of the landslide.

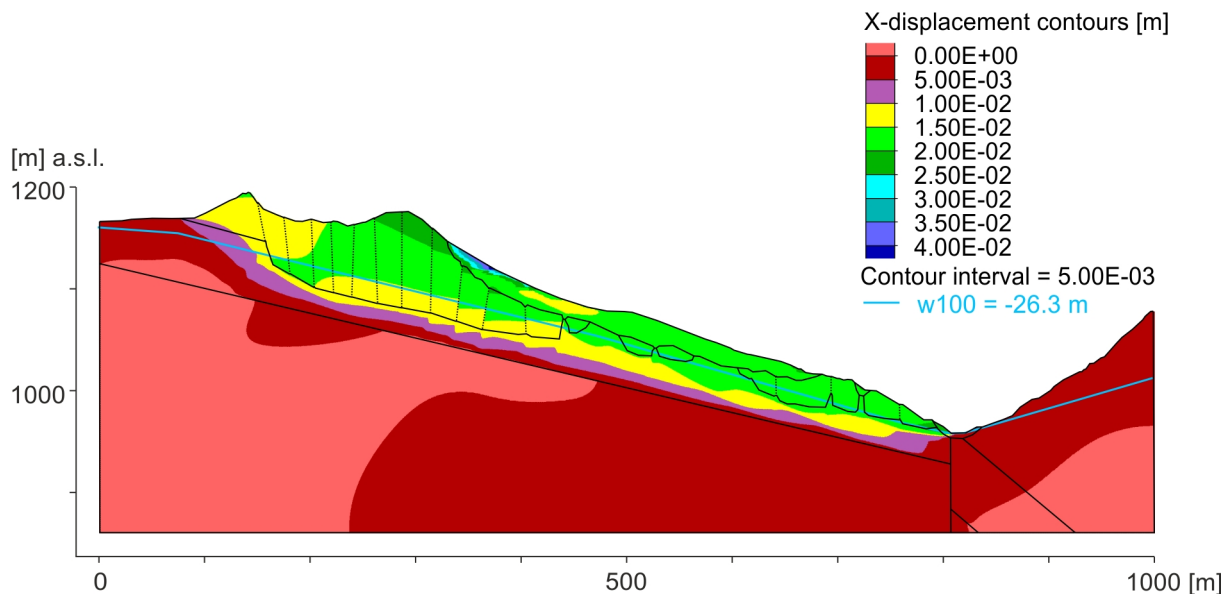


Figure 59: X-displacement contour plot of the Aggenalm landslide after adjusting the Quaternary deposits' properties (calculation over 100,000 steps). Here, the density was set to 2.5 g/cm^3 and the bulk and shear moduli to 10 times their initial value. Thereby the maximum displacements were reduced from approximately 24 cm (in Figure 58) to only 4 cm and thus the distribution of x-displacements over the Aggenalm slope becomes clearly visible.

While the change of the density alone didn't have a strong effect, the bulk and shear moduli set at 10 times the original value did show a significant improvement. With the combination of the

two adaptations the interference was kept at a minimum (Figure 59), so that these properties ($\rho = 2.5 \text{ g/cm}^3$; $G, K = G, K * 10$) were chosen for all successive calculations. By this adjustment the maximum displacements were decreased from approx. 24 cm to only 4 cm after 100,000 timesteps.

With the initially chosen properties of the joints (all joints were given identical values) hardly any vertical displacement along the joints has been observed. Due to the assumed mechanism – sinking of stiff Upper Rhaetian limestone and dolomite slabs into the plastically deforming Kössen marls underneath – a slightly stronger vertical component in displacements in the upper third of the slope was expected, as implied by the geodetic survey results, too (Appendix III). Therefore, the parameters friction angle, dilatancy, and normal- and shear-stiffness were varied. The performed variations are listed in Table 10. The best results were gained applying a lower friction angle of 15° as well as 0° for the angle of dilation, while not changing any of the other initial values.

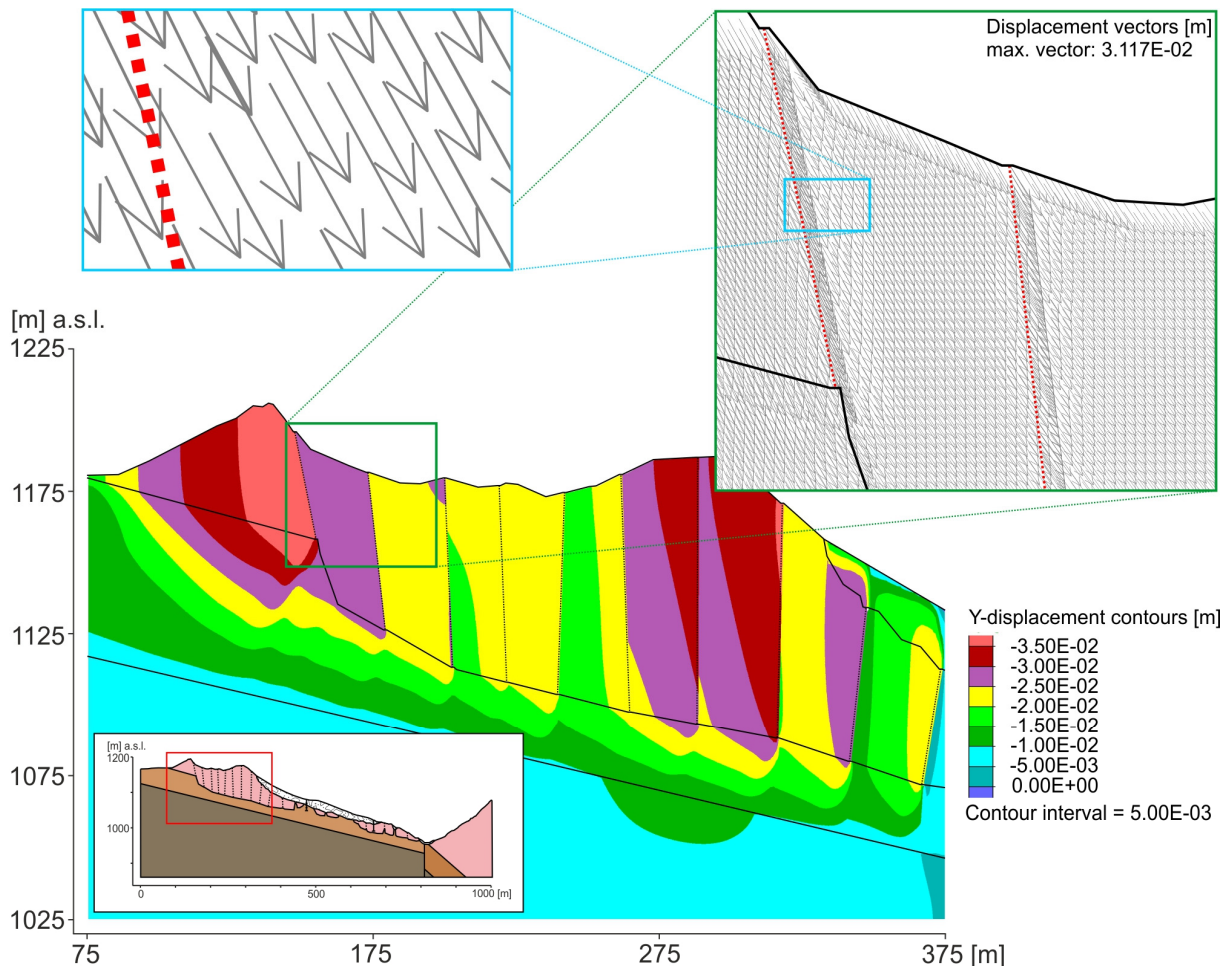


Figure 60: Y-displacement contour plot and displacement vectors (insert) for the slope's upper third after 100,000 cycles. In the y-displacements of the slope's upper third the differential movement of each of the limestone/dolomite slabs can be seen. The displacement vectors are clearly steeper than the slope's incline mean incline. This is due to fact that the stiff Upper Rhaetian blocks sink into the plastically deforming marls underneath while slowly drifting downslope as well.

Applying these values a slightly higher vertical displacement can be observed in the slope's upper third – in the jointed Upper Rhaetian formation – as pictured in the insert of Figure 60. The contour plot of the y-displacements shows that the individual blocks of Upper Rhaetian formation move differentially with vertical displacements diverging at each of the joints' sides, again after 100,000 calculation cycles. More figures, also showing this behavior, are depicted in Chapter 7.5, in the presentation of the final, verified model.

7.4.2 Change of properties of marls and sensitivity analysis

As the complete landslide is underlain by the marl-dominated Kössen formation, the influence of the parameters of the Kössen marls on the movements were of greatest interest and thus a detailed analysis was performed. The analyses aimed to not only evaluate the parameter sets that best represent today's observations within the simplified numerical model, but also to assess the landslide's sensitivity to variations of these. As already described in Chapter 7.3.2.1, the marls' shear parameters (cohesion and friction angle) are strongly affected by weathering. According to REIßMÜLLER (1997: 98ff.), the friction angle decreases by approx. 50 % from fresh (W1) to completely weathered/residual soil (W5), with the strongest decrease from W1 to W2 as well as W4 to W5 (ISRM 1981). A similar dependency also applies for the cohesion, which decreases even more, before it again increases slightly from W4 to W5.

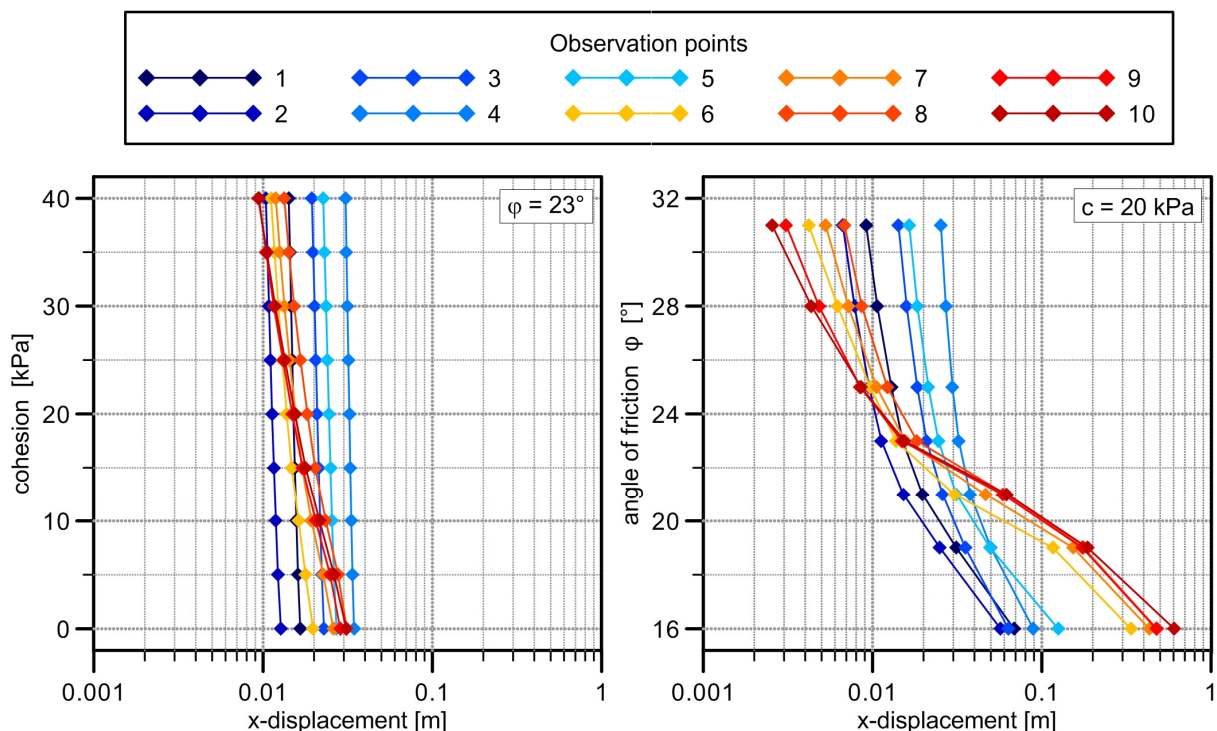


Figure 61: Influence of Kössen marls' cohesion and angle of friction on the x-displacements, observed at 10 different observation points scattered across the slope after 100,000 calculation cycles.

Therefore, both parameters were varied individually, as was the Young's modulus, while applying a constant water table (mean water table, w_{100}) and the earlier determined properties of the joints and Quaternary deposits as described in the preceding subchapters. The Young's modulus of the Kössen marls was set to 2, 4, and 5.9 GPa, respectively. The best results were attained applying a Young's modulus of $E = 4$ GPa.

The cohesion, varied between 0 and 40 kPa in 5 kPa increments, doesn't have much influence on the modeling results. The contour plots in Figure 62, applying the two extremes, picture this quite well. For both, the maximum displacements (in x-direction) occur within the Quaternary (between observation points 4 and 5) and don't exceed 4.5 cm. A small difference can be observed in the distribution of the x-displacements across the slope. The displacements accelerate slightly more in the lower part of the slope when no cohesion is applied. Figure 61 depicts the behavior of the slope to variable cohesions in summary. At the top five observation points (1-5), the displacements only increase marginally (mm-range) with decreasing cohesion. At the lower points (6-10), a small acceleration can be observed, which is the highest for point 10 with a variation in x-displacement of approx. 2 cm between the two extremes.

Kössen marl: variable cohesion

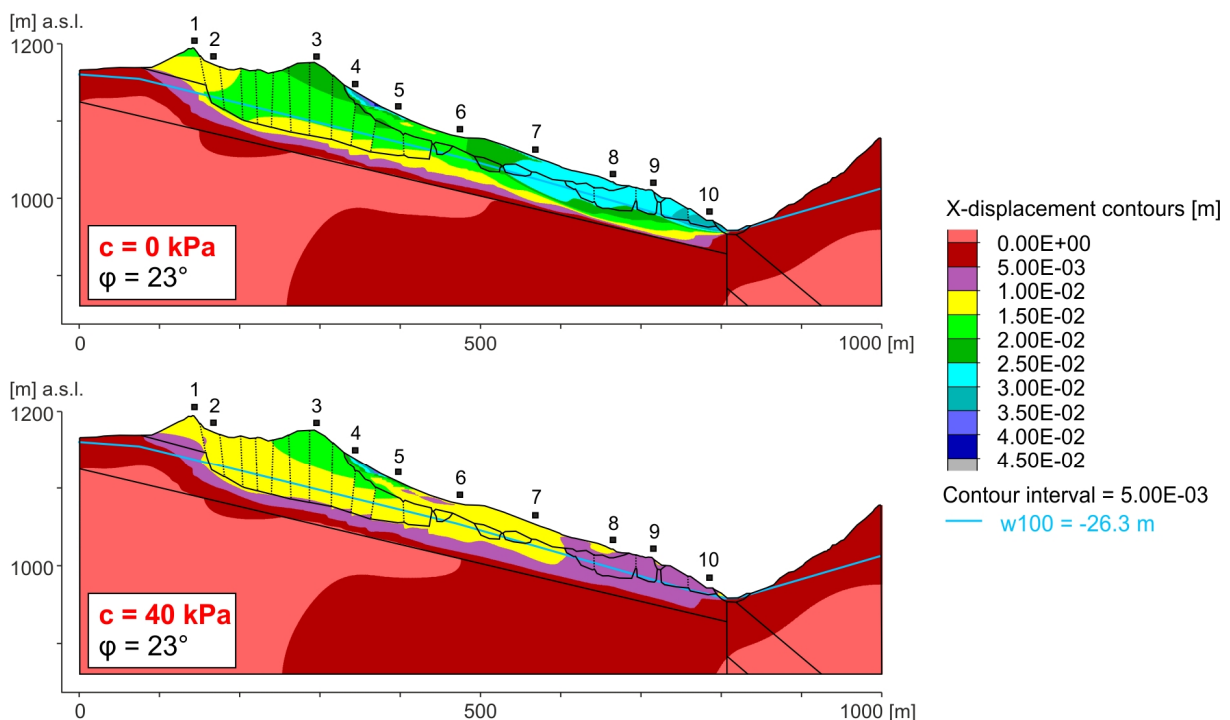


Figure 62: Contour plots of the x-displacements applying a cohesion of 0 kPa for the Kössen marls (top), respectively 40 kPa (bottom) after 100,000 cycles. Both plots show displacements of up to 4.5 cm and only the distribution of displacements varies slightly between the two plots.

The results show that the slope's behavior is much more sensitive to varying friction angles. Again, the two extremes, 16° and 31° , are pictured in Figure 63 for comparison. At first sight,

it becomes obvious that the x-displacements are very different for the two extremes. Using the high friction angle, the displacements vary between a few millimeter and approx. 2,5 cm (due to 10 cm contour interval not clearly visible in this plot). This changes extremely for the friction angle of 16° , at which the displacements surpass 60 cm. Also the distribution of the displacements changes drastically. The highest displacements are reached in the lower half of the landslide, especially at the toe, while in the top half the displacements hardly exceed 10 cm. The sensitivity to only small reductions of the friction angle can be seen best in Figure 61. While the displacements at the observation points 1 to 5 increase more or less consistently with decreasing friction angle, the displacements of the lower half (points 6–10) accelerate strongly, especially once the friction angle falls below 23° .

Kössen marl: variable friction angle

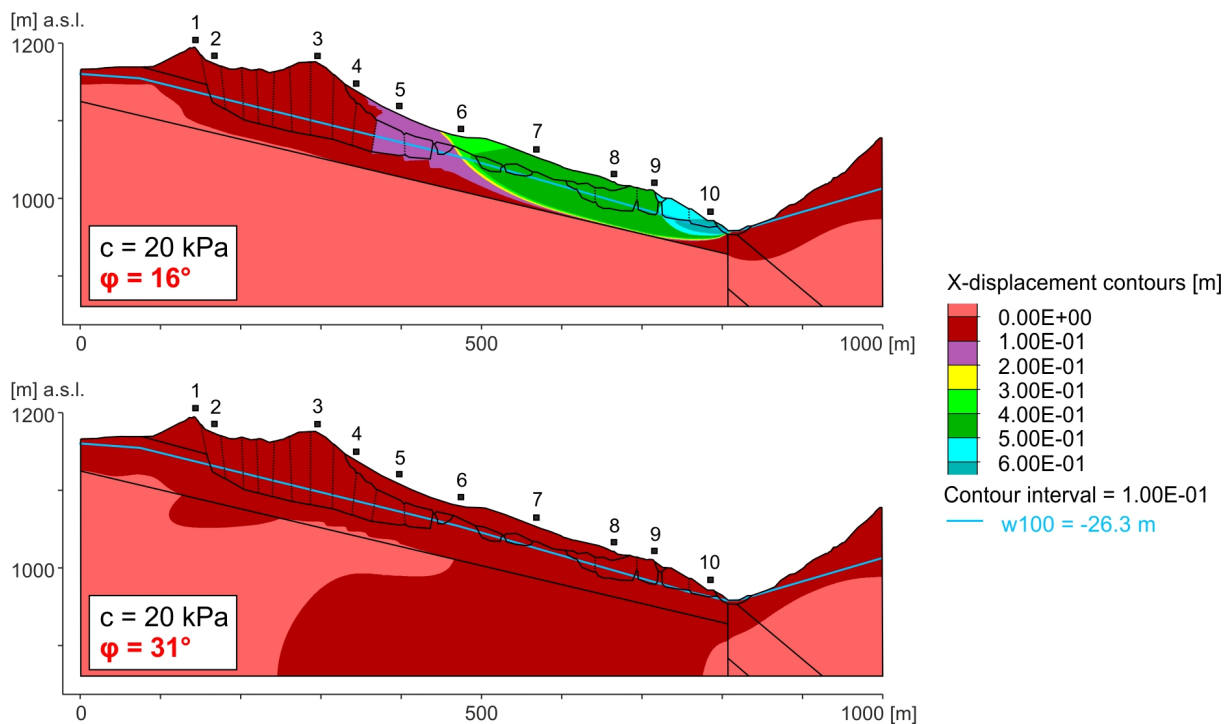


Figure 63: Contour plots of the x-displacements while applying a friction angle of 16° (top), respectively 31° (bottom) after 100,000 steps. The friction angle has great influence on the modeling results. When set to 16° , the x-displacements reach a maximum of approx. 60 cm, concentrated to the bottom half of the landslide, while the top hardly accelerates. On the contrary, with a high friction angle (31°) the displacements are distributed evenly over the slope, with a maximum of approx. 2.5 cm.

In order to meet the above-mentioned prerequisites for the calibrated model, a cohesion and a friction angle were chosen, at which the distribution of x-displacements across the slope is as homogeneously as possible. As a friction angle a value of 23° was selected, since the displacements at the observation points varied the least. For the cohesion a value of 20 kPa was chosen.

Pictures, representing the final model, including the set values for the Kössen marls' properties, are depicted and described in the following subchapter.

7.5 Final model

Here, the results of all the previously described parameter variations are combined into a verified model of the Aggenalm landslide. Table 11 summarizes the varied parameters and the approved values, meeting the mentioned requirements. Applying these, a more or less homogeneous movement over the complete slope (Aggenalm landslide) was achieved, as it has been observed by the displacement monitoring on surface, such as the geodetic survey.

Table 11: Material properties used in the verified and final model of the Aggenalm landslide. Listed are only the materials and its properties adjusted during the parameter variation. The values used for the final model are printed bold, while the applied parameter ranges during the sensitivity analyses are italicized.

	Talus	Debris, Quaternary	Kössen marls		Joints
Density ρ [g/cm ³]	2.5 (2.2)	2.5 (2.2)	2.4 (2.7)	Friction angle ϕ [°]	15 (5, 25)
Cohesion c [kPa]	–	–	20 (0, 5, 10, ..., 35, 40)	Dilation angle ψ [°]	0 (1)
Friction angle ϕ [°]	–	–	23 (16, 19, 21, 25, 28, 31)	Shear stiffness k_s [GPa/m]	55 (5.5)
Young's modulus E [GPa]	0.5 (0.05, 0.25)	0.2 (0.02, 0.1)	4.0 (2.0, 5.9)	Normal stiffness k_n [GPa/m]	55 (5.5)
Bulk modulus K [GPa]	0.28 (0.028, 0.14)	0.11 (0.011, 0.06)	2.22 (1.11, 3.28)		
Shear modulus G [GPa]	0.21 (0.021, 0.1)	0.08 (0.008, 0.04)	1.67 (0.83, 2.46)		

Figure 64 displays the x- and y-displacements and Figure 65 the according displacement vectors. The x-displacements are distributed rather homogeneously across the Aggenalm landslide, with a maximum within the Quaternary material at the toe (observation point 10) and above B4 around observation points 4 and 5. Except for these minor “secondary effects” the x-displacements are ranging between 1 and 1.5 cm after 100,000 calculation timesteps. Toward the base of the Kössen formation (marls) the displacements are relatively sharply defined (purple contour), which may indicate the development of a discrete shear zone parallel to the formation's inclination (see also Figure 66). This weak zone is located still within the Kössen marls, more or less at its basis.

The y-displacements (Figure 64) are not distributed as homogeneously as the x-displacements, but rather concentrated to the upper half of the slope. There they display the sinking of the hard and stiff Upper Rhaetian formation into the underlying Kössen marls. This behavior is also visible in Figure 65 and Figure 66, in which the displacement vectors and the development of shear planes are plotted, respectively.

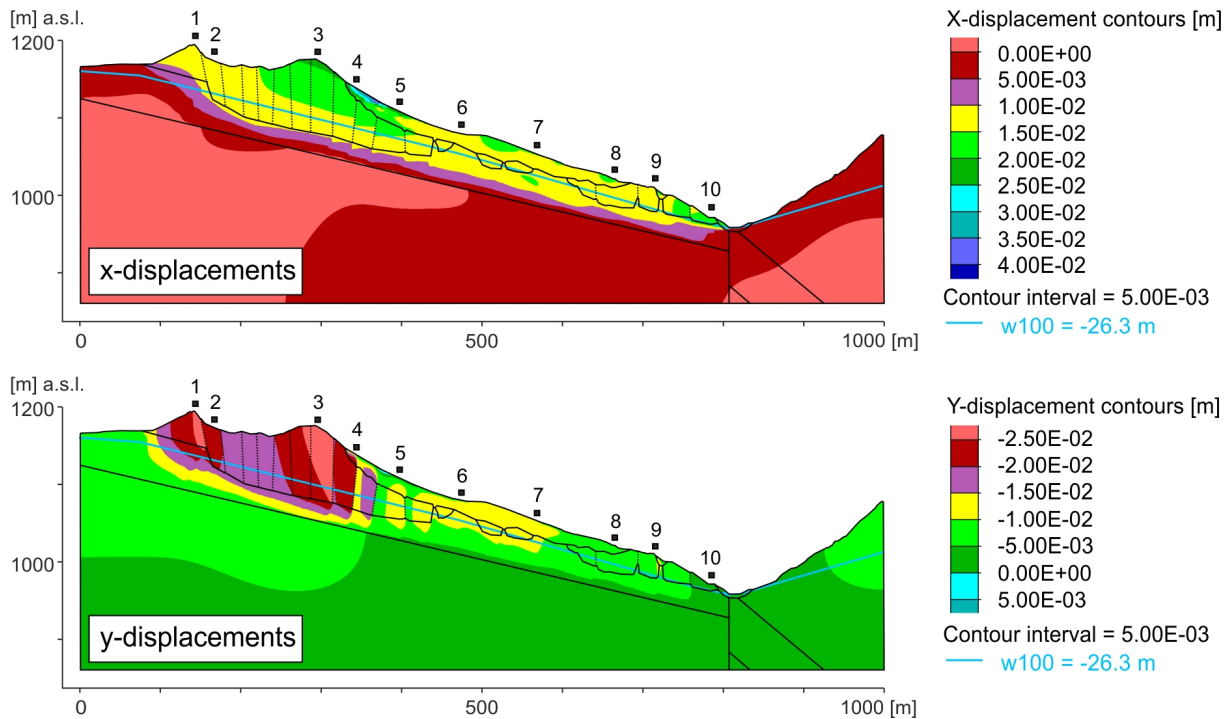


Figure 64: X- and y-displacement contour plots of the verified numerical model. The x-displacements are distributed homogeneously. On the downside, still within the Kössen marls, the movements are more or less sharply defined (purple contour). The y-displacements are concentrated to the slope's upper half, displaying the sinking of the limestone and dolomites into the plastically deforming Kössen marls.

In the top third of the slope, the displacement vectors (detail 1 in Figure 65) are steeper than the general slope due to the mechanism and thus the higher y-displacements in this part of the Aggenalm landslide. In the lower part of the slope, dominated by Quaternary deposits, the vectors merge into a slope parallel orientation (detail 2), suggesting a sliding on the shear plane at the basis of the Kössen marls. Solely at the toe of the landslide the orientation of the displacement vectors changes once again: they flatten out (detail 3). This can be interpreted as a bulging and thus steepening of the landslide's toe, as it has been also observed and described in Chapter 4.6.2.1.

In Figure 66 the plastic indicators are pictured. In this plot, zones, in which the stresses satisfy the yield criterion (Mohr-Coulomb) and plastic flow occurs, are marked while differentiating between yield in elastic, shear, and tension. After the calculated 100,000 timesteps, a zone developed at the base of the Kössen formation (pink asterisks), which indicates that these elements

are actively yielding in shear. The insert in Figure 66 shows how differentiated the actively yielding elements are, especially when looking at it in detail. Below the blocks of Upper Rhaetian formation, which sink into the Kössen marls (indicated by exemplary yellow arrows), several shear planes (depicted by elements at yield in shear) developed. Most of them can be clearly connected to the basal shear plane with which they then merge. At some of the blocks one can also make out shear bands that are oriented toward the opposite direction (upslope), which were caused by the slightly heterogeneous downward movement of the limestone and dolomite slabs. Due to slight tilting of these blocks, the stresses on the downside corner increase, thus leading to such oriented shear bands. These results also acknowledge the suggested and expected behavior, especially in the slope's upper part.

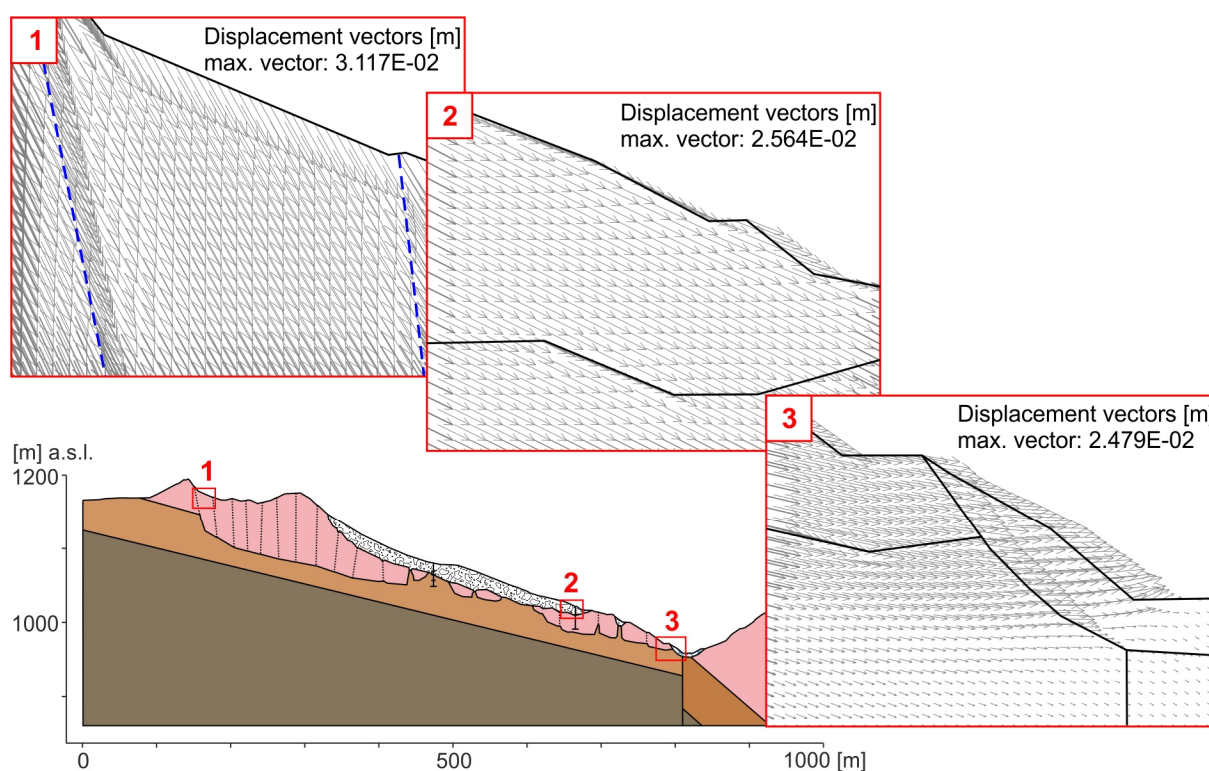


Figure 65: Displacement vectors of the Aggenalm landslide at selected areas. While in the top third of the slope (1) the movements have a stronger vertical component, they are more or less parallel to the slope's incline in the middle and lower parts (2) before the displacement vectors flatten out at the toe (3), which also suggests bulging.

What becomes also visible in Figure 64 and especially in Figure 66 is the extent of the Aggenalm landslide. Several shear zones developed within the Kössen formation behind the ridge with the main scarp, running from the surface expression of the Kössen formation (several elements yielded in tension) through the marls before joining the basal shear zone. The plots of the x- and y-displacement display distinct movements in the ridge above the main scarp, too (outside of the landslide's dimensions according to Figure 15). This suggests that the landslide's dimensions are greater than assumed, even though the extensometer installed at the scarp shows

that movements occur between the two anchor points, which are located at the scarp and at a block below the scarp. Therefore, the movements of the area uphill of the scarp must be lower than of the parts below the main scarp.

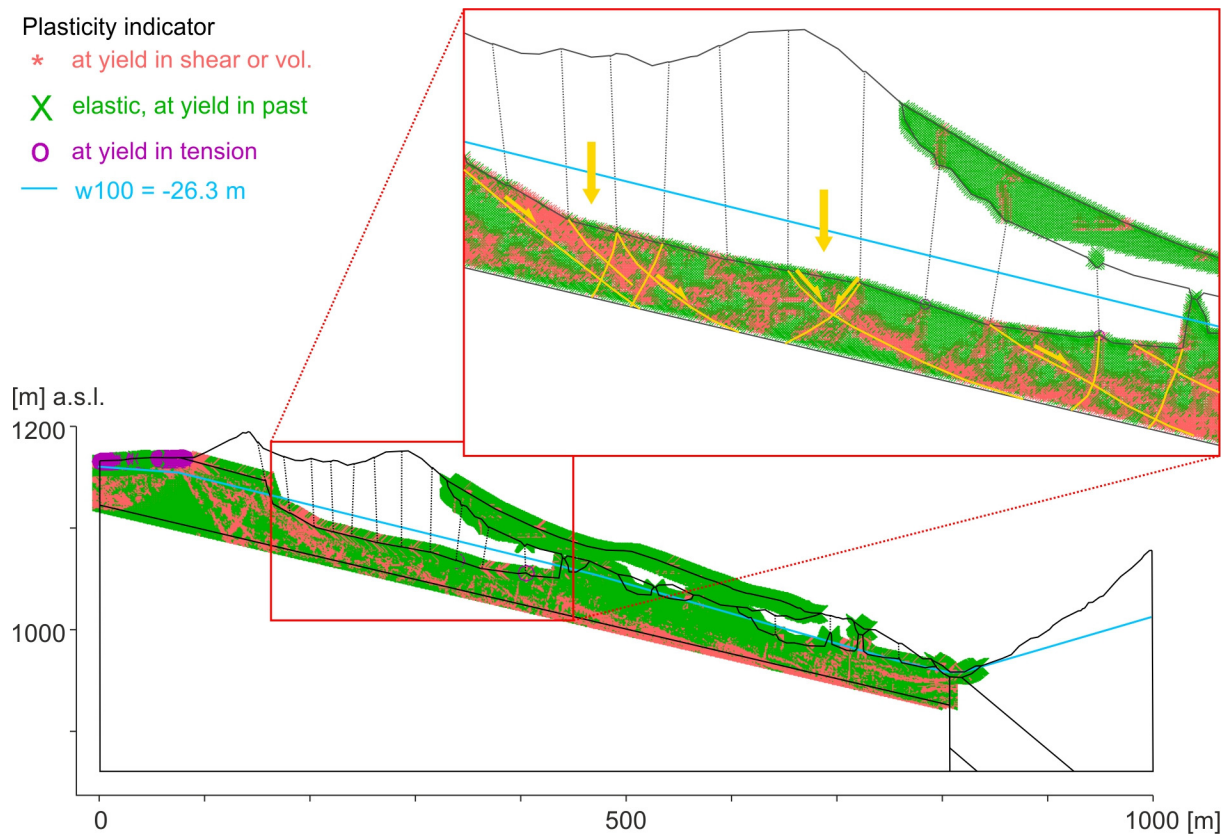


Figure 66: Plasticity indicators, displaying zones where yield in shear or tension occurs (after 100,000 cycles). The zones, which yield due to shear are mostly within the Kössen marls, but also within the debris and talus. Connecting element at yield in shear, one can draw a main shear zone at the basis of the Kössen formation, but also several subsidiary shear planes (highlighted in the detail) that developed due to the sinking of the Upper Rhaetian formation blocks into the underlying Kössen marls.

7.6 Threshold derivation

In order to derive threshold values for the onset of a distinct acceleration of the Aggenalm landslide, the water table has been raised in 2- to 3-meter increments (over most of the slope with an exception at the Gassenbach due to geometric constraints). All applied water tables are described in Chapter 7.3.1.5 and pictured in Figure 55.

With a rising water table height the distribution of the movements changes in comparison to the movement pattern in the final, verified model, applying the mean water table, w100. The part of the Aggenalm landslide below B4 (observation points 6–10) accelerates more strongly than the upper half of the Aggenalm as it can be seen in x-displacement contour plot (a) in Figure 67. When increasing the water table by 5 m this phenomenon starts to become more and more

apparent. This can also be pictured in the plots of plasticity indicators (b) and maximum shear strain-rate (c) in Figure 67, in which a shear plane develops in the lower half of the landslide after a 9 m water table rise. The shear plane (zone of shear yield) proceeds along the base of the Kössen marls and surfaces in the middle of the slope around B4 (observation point 6) as well as in the Gassenbach at the toe.

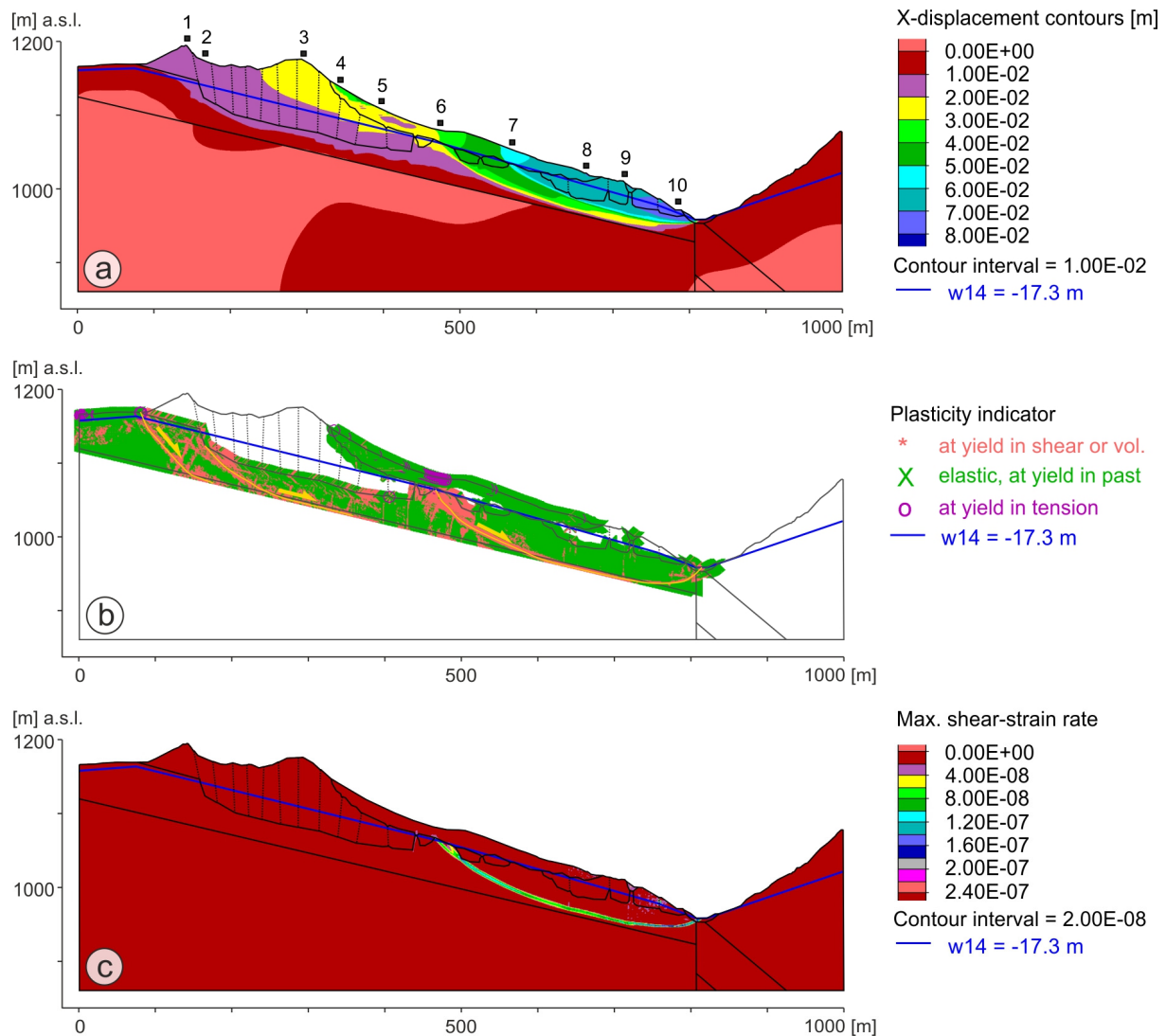


Figure 67: Results of the numerical analysis applying a high water table, w14 (+9 m), while keeping all other parameters constant. a) pictures the x-displacement contours and b) the plastic indicators. c) shows a contour plot of the maximum shear-strain rate, in which the most dominant shear surface becomes visible.

Plotting the x-displacements of all 10 observation points against the rising water table confirms this changing movement pattern. To emphasize the changing movement pattern, the observation points (1–5) at the top half of the slope – on top of the massive Upper Rhaetian formation blocks – are plotted in blue colors, while for the observation points (6–10), situated in the lower part,

yellow to red colors have been used in Figure 68. The top points (1–5) only show a very low and continuous increase in x-displacements over the complete 23-meter rise of the water table, without any acceleration. The x-displacements increased by approx. 1 cm at each of the observation points (1.0–3.0 cm at lowest water table (w98) to 1.7–4.0 cm at highest water table (w16)) over the complete water table variation. The behavior of the lower half of the slope, points 6–10, differs clearly. The x-displacements vary between 0.7 and 1.2 cm at the lowest water table, w98. Up to a water level of w11–w12 (equals a rise of 13–15 m) the displacements increase rather continuously and homogeneously. Above that level, they then clearly accelerate, reaching displacements varying from 6–12 cm at w16, thus decoupling their x-displacements over the complete rise of 23 m.

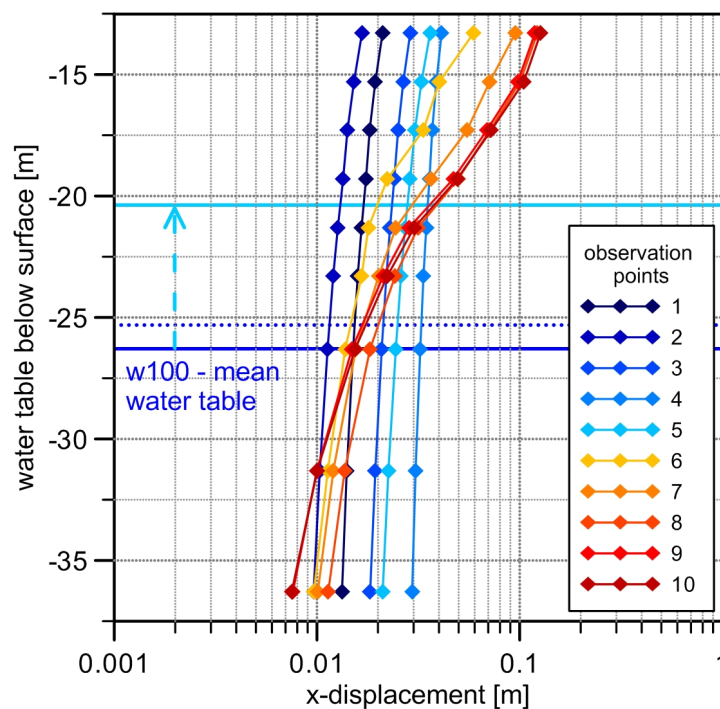
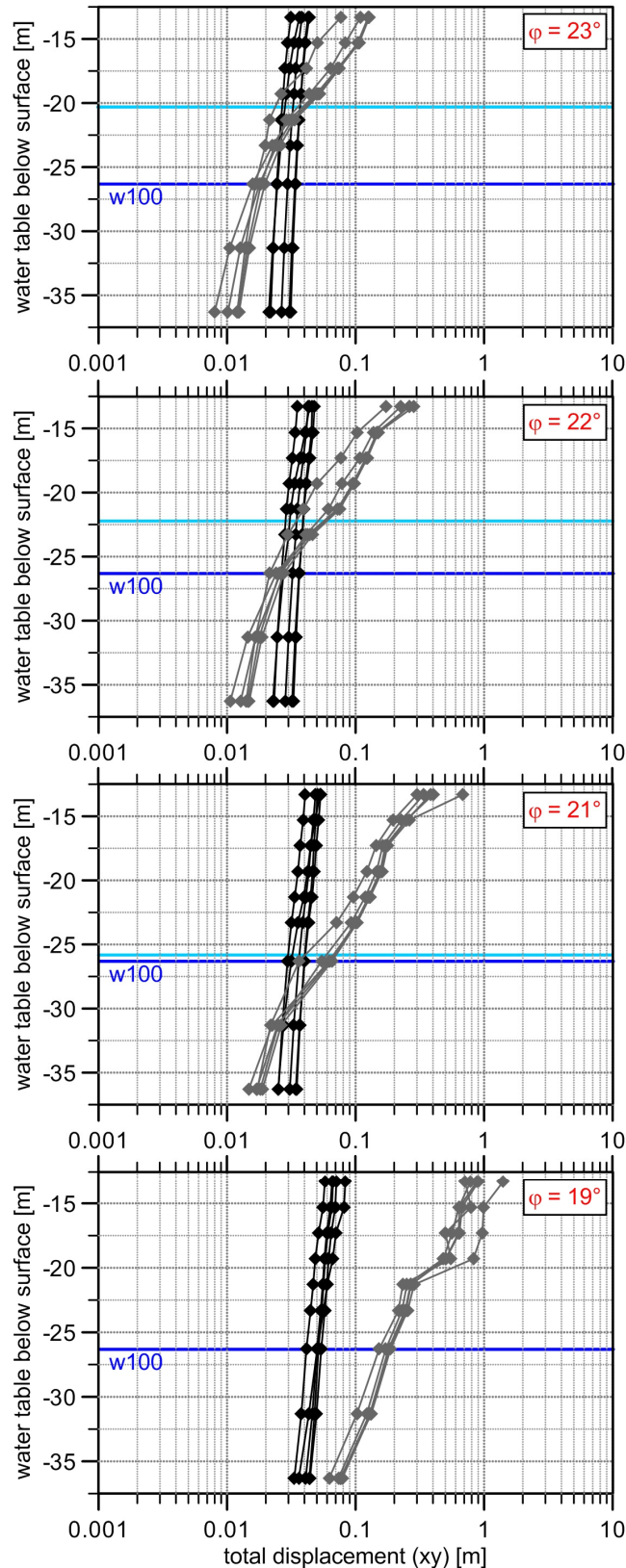


Figure 68: X-displacements at the 10 observation points at different water tables. The solid blue line marks the mean water table and the blue-dotted line the maximum water table rise observed so far. The light-blue line correlates to a 6 m water level rise, which is necessary to start changing the slope's movement behavior.

Due to this movement behavior a threshold for the onset of stronger movements at the Aggenalm landslide has been set at approx. 6 m above the mean water table, w100. The above-mentioned changing movement pattern can first be observed when increasing the water table by 5 m to w12, which then becomes very obvious at w13. Besides, the 2 m increase from w12 to w13 shows the strongest acceleration in x-displacements. Hence, the threshold has been defined at the transition between these two scenarios. In Figure 68 the light-blue line marks this 6 m increase and also illustrates that a great amount of rainfall, possibly combined with strong

snowmelt, is needed to reach such a water level, as up to now only a maximum increase of 1 m has been observed (blue-dotted line).

Not only can a rising water table lead to an acceleration of the Aggenalm landslide, but also a change of material properties, to which the slope's stability is sensitive to. The previous sensi-



tivity analysis (Chapter 7.4.2) has unfolded that the Aggenalm slope is very sensitive to variations of the friction angle of the Kössen marls, whereas the cohesion doesn't have much influence. Therefore, Figure 69 depicts the xy-displacements at different water table heights for four different friction angles (19°, 21°, 22°, and 23°). Again, the movement pattern is as described above: slowly and continuously increasing displacements at the top observation points (all black in this figure) and at the lower half of the slope, acceleration phases and displacements exceeding the ones at the upper half many times over. The lower the friction angle, the higher are the displacements and the less needs the water table to rise to result in strongly increasing movements in the lower part of the slope.

Figure 69: Total displacement (xy) plotted against water table height applying various friction angles of the Kössen marls (from top to bottom: 23°, 22°, 21°, and 19°). Observation points 1–5 are plotted black and points 6–10 gray. The light-blue line marks the height of an approximate threshold at each friction angle.

The resulting threshold water table is illustrated again with the light-blue line in Figure 69. Decreasing the friction angle by only 1° to 22° already lowers the needed water table rise to approximately 4 m. An additional decrease to 21° results in a threshold table about 1 m above the mean water table and therefore within the range of the maximum observed water table during the monitoring phase. A further decrease of the friction angle leads to even stronger displacements of the lower slope, thus the differing movement pattern of upper and lower slope sets in at a water level that is below the mean level, w100 (more than 10 m below for $\varphi = 19^\circ$).

7.7 Numerical modeling – discussion of results

By adapting the newly gathered information concerning the build-up of the Aggenalm landslide into the numerical model of the landslide, it has been possible to reproduce most of the phenomena measured by the monitoring system as well as observed in the field. Most of the parameters used in the previous models could be adapted directly, whereas shear tests on the disturbed and undisturbed samples of the Kössen marls indicated the most probable property range for the marls at the Aggenalm landslide (φ : $21.6\text{--}24.5^\circ$). Several parameter sets (Kössen marls, Quaternary/debris/talus, joints within Upper Rhaetian formation) were subject of sensitivity analyses to find the best representation of the observed phenomena. This analysis showed that displacements of the Aggenalm landslide are especially sensitive to variations of the Kössen marls' friction angle, but hardly influenced by a changing cohesion.

The verified model reproduces many of the observed phenomena and also verifies the assumed mechanism of the Aggenalm landslide. It shows very homogeneous movement across the complete slope, with a slightly stronger vertical component at the top part of the slope, illustrating the sinking of the stiff Upper Rhaetian formation into the underlying, plastically deforming Kössen marls, thus representing the spreading mechanism in this slope's part. At the lower half of the slope the displacement vectors are oriented parallel to the slope and strata and the movements are sharply confined at the base of the Kössen marls forming a shear plane. This shear plane isn't limited to this part but continues at the base of the Kössen marls all the way to the outcrop above the landslide's main scarp. Several secondary shear planes resulting from the sinking and differential movements of the hard rock slabs in the slope's upper half merge with the main shear plane.

Furthermore, the modeling results show that an increase of the groundwater table (or decrease of friction angle) clearly results in increasing displacement rates and a concomitant concentration of plastic deformation within the marly layers, thus triggering a landslide. However, this process is focused on the slope's lower half. In the model, the upper half is hardly affected by a rising water table (nor decreasing friction angle) and doesn't alter its above-mentioned movement characteristics, only the displacements of the spreading increase slightly and continuously. Therefore, the displacement pattern of the complete slope changes significantly with a rising water table and the displacements of the lower part multiply. The main shear plane then still surfaces in the debris-dominated lower part, around B4. However, to trigger a slide of the lower

part, the water table needs to rise to an extremely high level, which can only be caused by a very strong snowmelt and/or heavy rainfall. The description of the 1935 landslide event confirms the modeling results in the way that the movements were concentrated to the lower part of the slope and occurred during snowmelt season after a period of heavy rainfall (Chapter 4.6.1.1, Appendix II).

In the model, the transition between the water tables w12 (5 m) and w13 (7 m) marks the level that can possibly trigger a landslide – 6 m above the mean water table. However, up to now a maximum water table rise of only 1 m has been observed, even though several heavy rainfall events and snowmelt occurred (>100 L/24 h). The necessary water table rise quickly lowers when decreasing the friction angle of the Kössen marls by only 1 to 2° (Figure 69). Over time, this change can naturally occur due to weathering of the Kössen marls, especially at places close to the surface or along water-bearing joints and fissures. Therefore, assuming that the properties of the Kössen marls deteriorate over time by weathering processes, a significantly lower water table increase of only 1 m (2° decrease) can lead to failure.

8. Conclusion

In this thesis, the holistic interpretation and analysis of the data on the Aggenalm landslide collected throughout the alpEWAS project and within its framework have been described in great detail – aiming to derive appropriate thresholds for an early warning system. All of the objectives set at the beginning of this work have been achieved.

The results of the field investigations performed in 2007 through 2009 (drillings, geoelectric survey, etc., described in Chapter 4.6.3 on page 49ff.) showed large deviations from the primary model and thereby reinforced the need to incorporate the new findings into the geological sections and to adapt the understanding of the landslide's mechanism. The new results from the boring campaign and geoelectric survey led to the construction of several new cross sections. In the upper part of the Aggenalm landslide mainly the thickness of the Upper Rhaetian formation had to be adjusted from only 40–50 m to over 100 m, at parts due to the geoelectric surveys results (Chapter 4.6.3.3, Figure 27). Joints and faults divide the Upper Rhaetian formation into huge slabs, which sink into the underlying plastically deforming and decaying marls of the Kössen formation and slowly move downhill. Thus, the mechanism in this slope's part has been classified as spreading or *rock spread* according to CRUDEN & VARNES (1996: 38, Table 3-1).

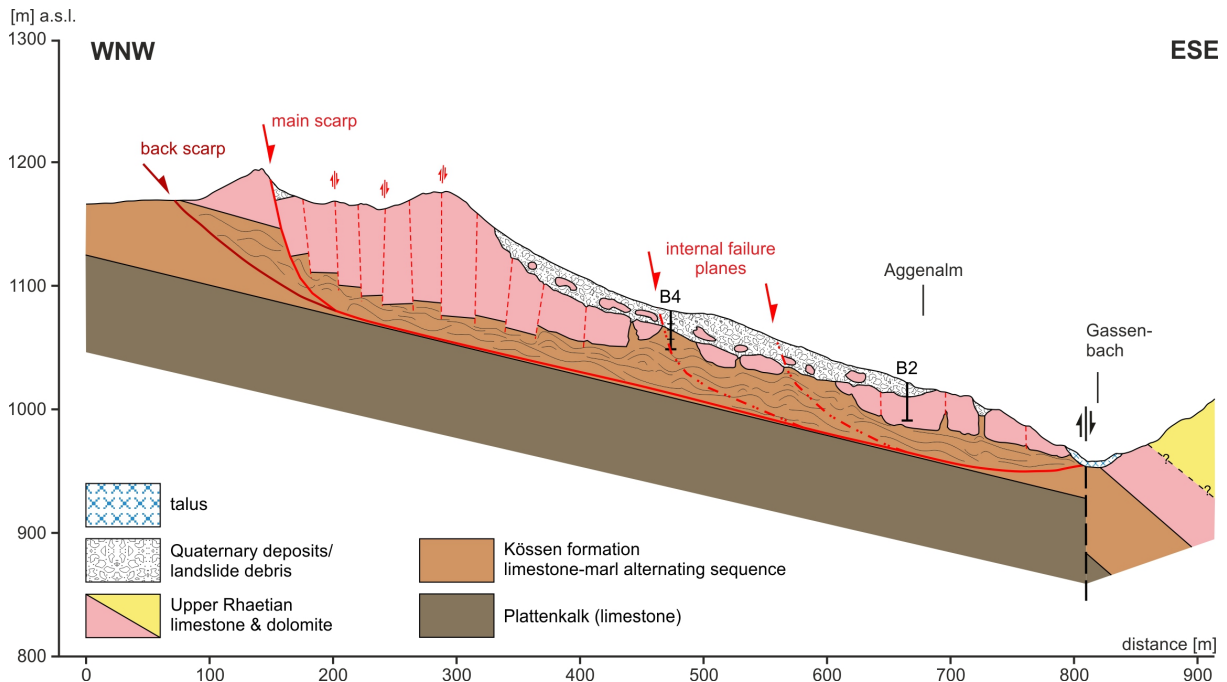


Figure 70: Geological section across the Aggenalm landslide incorporating the new information acquired during the field investigations and also updated by the results of the numerical model. The red dash-dotted lines mark possible internal failure planes that become dominant once the water table rises and/or the friction angle of the Kössen marls reduces.

Additionally, the results of the numerical model showed that the Aggenalm landslide's dimensions are greater than previously assumed. Several shear zones evolved within the Kössen formation above the main scarp, whose failure planes then join the basal shear zone, as pictured in Figure 70. This is also supported by the hillshade of the area (Figure 71), in which several back scarps are visible above the main scarp, even though not as prominently because this area has been strongly altered by the ski piste running along the main scarp.

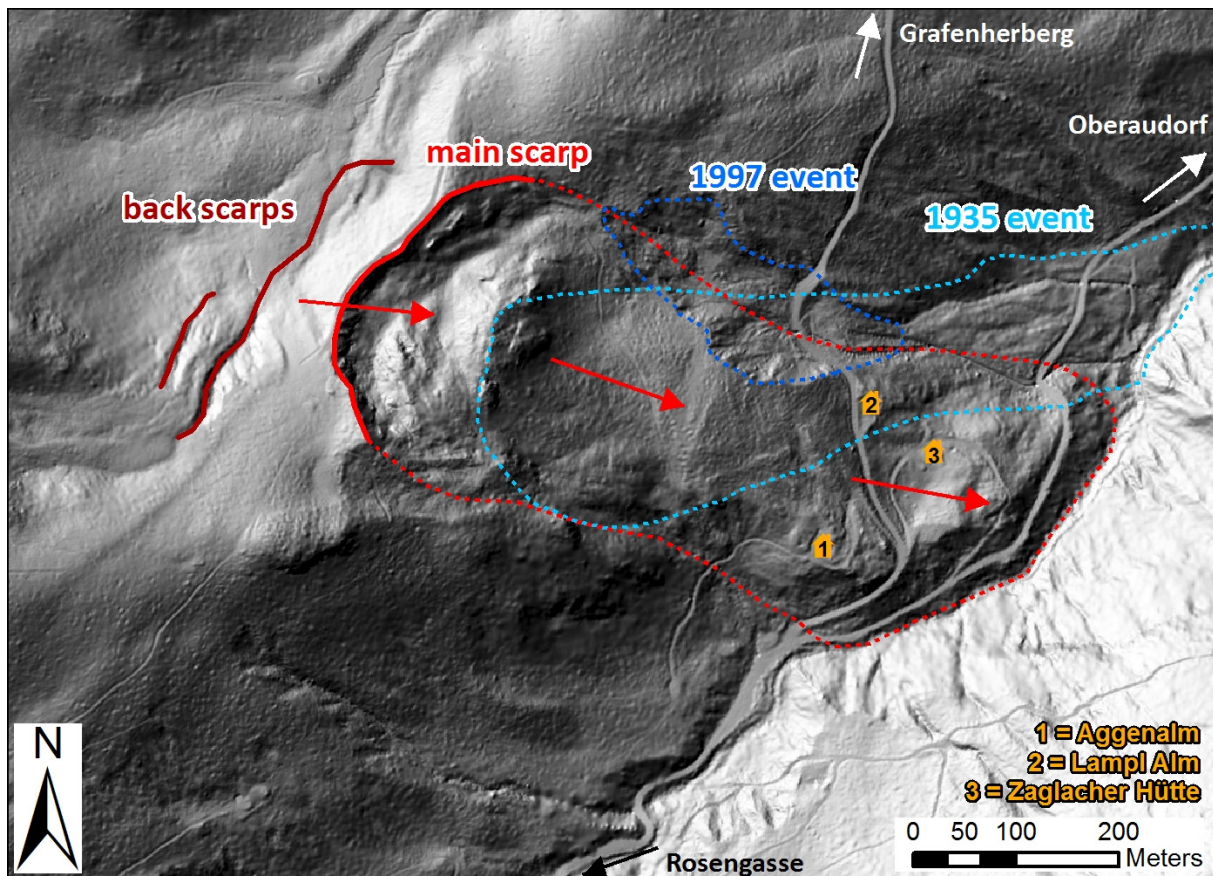


Figure 71: Enhanced hillshade model of the Aggenalm landslide based on a digital elevation model (DGM, 1 m laser scan). The back scarps have been traced in dark red. The blue-dotted lines show the extent of the two events in 1935 and 1997. Dotted red is the extent of the main Aggenalm landslide body, as previously assumed. However, due to the results from the numerical modeling, the landslide's dimensions have to be increased, reaching at least as far uphill as to the back scarps.

Toward the middle part of the slope, the thickness of the Upper Rhaetian formation decreases and generally becomes more and more disintegrated into individual blocks and slabs before it is then totally interrupted in the middle of the landslide (the interruption is favored by the slope's tectonic history as well as glacial and landslide evolution). Here, the subsidence and spreading of the downward-moving limestone blocks cause the underlying Kössen formation to bulge toward the surface, so that the Kössen formation is directly overlain by debris and Quaternary deposits (Figure 70). Further downhill, the Upper Rhaetian formation is again found

at, or close to the surface, displaying wide open cracks and a strong disintegration, which is likewise related to the subsidence into the underlying marls of the Kössen formation. The mechanism for the lower two-thirds of the Aggenalm slope has been classified as *debris slide* (CRUDEN & VARNES 1996: 38, Table 3-1), since it is presumed that the forces introduced by the movement of the Upper Rhaetian formation led to a detachment of the whole rock mass from its base and thus to the development of a shear zone within the Kössen formation.

In summary, the Aggenalm landslide can be characterized as an active, complex, homogeneously moving, extremely slow, deep-seated mass movement, with a rock spread at the top third of the slope transitioning to an extremely to very slow debris slide downhill, namely a *complex, extremely slow rock spread-debris slide* (Table 1, CRUDEN & VARNES (1996: 38, Table 3-1). This interpretation and classification of the Aggenalm landslide is supported by the results of the geodetic survey, the various alpEWS measurement systems, the GNSS correlation analysis, and the numerical modeling, which all illustrate quite homogeneous movements across the whole Aggenalm landslide, under the present conditions.

The data of the three main measuring systems of the alpEWAS GSN as well as additional sensors and its analyses have helped to characterize the Aggenalm landslide, its mechanism, and cause-and-effect chain more precisely and to derive first thresholds.

The results of the subsurface deformation measurement systems, TDR and inclinometer, are insignificant, caused by the insufficient depth of the installations, suggested by an, at the time of installation, plausible geological model (Chapter 5.3.3 on page 79ff.). The deformation measurement systems on surface, VTPS and GNSS, however, show reliable measurements, which are consistent with the results of the geodetic survey. Even though the displacements measured by the VTPS are not yet statistically significant, they seem to be highly plausible and correspond well with the movement rates detected by the other independent surface deformation measurement systems. The GNSS, which was included into the alpEWAS Control software, proved to be very reliable, detecting deformation with sub-centimeter accuracy, previously reserved for high-end receivers. Over the 3-year measurement period, GNSS 1 recorded a displacement of 1 cm in total, while the other two sensors, GNSS 2 and GNSS 3, registered 3 cm each (Chapters 5.3.1 and 5.3.2 on page 75ff.).

The results of all systems together, including data concerning the piezometric water table and precipitation, allowed a more precise evaluation of the movement characteristics and its dependencies. On this basis, statistically significant correlations between precipitation, groundwater level and deformation were identified by means of time series analysis. First results were attained simply by a visual evaluation of the data (Chapter 6.4.1 on page 93ff.). After the onset of snowmelt or after rainfall-rich periods a distinctive rise in pore water pressure (up to 0.8 m) was observed, as was a very small increase in the displacement rate (mm-range), which led to the deduction of a first conservative threshold: If the pore water pressure in piezometer B4 surpasses 32 kPa and remains at this elevated level for several days, small movements/accelerations can be expected in the GNSS measurements.

Crosscorrelations (Chapter 6.4.2 on page 99ff.) calculated from the data series revealed additional information: On the one hand, the correlation analyses showed that the GNSS sensors at the main sensor node and at the Lampl Alm (GNSS 2 and 3) are highly correlated, thus displaying a very similar movement pattern, and move simultaneously – without temporal delay. Contrariwise, the correlation of either of the sensors with GNSS 1 is distinctly lower. These results fit well with the findings of the other measurement systems and also support the classification of the slope's lower two-thirds as a slide. On the other hand, the temporal delay between precipitation and pore water pressure was determined and quantified by crosscorrelation analyses. Following rainfall the delay varies only slightly (1.25–6.0 days) and averages 2.5–2.75 days. The relation between trigger (rainfall/pore water pressure) and GNSS displacement measurements couldn't be specified by means of correlation analysis yet, even though very small acceleration phases in the wake of heavy rainfall and/or snowmelt were notified visually and also the analysis of historic events, 1935 and 1997, proves the influence of water to be relevant and nonambiguous. This is due to the extremely small movement rates of only a few millimeters at maximum – attributed to a single “extreme rainfall/snowmelt event” – which is still within the GNSS's noise, thus preventing significant results.

In summary, by applying TSA methods to the data it was possible to partly quantify the cause-and-effect chain between trigger factors (precipitation/pore water pressure) and landslide displacement, and also to derive a first threshold, which has been incorporated into the alpEWAS Control software. If the set threshold is exceeded, an e-mail alert is automatically sent to the experts/administrators, who evaluate the severity of the event and decide depending on the situation, if further measures have to be taken (in consultation with the municipality).

However, since this threshold, determined by the TSA, is much too conservative for early warning, a numerical model (Chapter 7 on page 109ff.) was used to obtain information about the system's behavior beyond the previously observed relationships. All information concerning the build-up of the Aggenalm landslide and relevant data gathered by the various systems were incorporated into the very detailed numerical model. Additionally, shear tests were performed on the marls of the Kössen formation (samples taken at the outcrop at the toe of the landslide), indicating their most probably property range (φ : 21.6–24.5°). Prior to simulating extreme events, the various parameter sets were subject of sensitivity analyses to find the combination, which best reproduced most of the phenomena measured by the monitoring system as well as observed in the field. Additionally, this analysis showed that the displacements of the Aggenalm landslide are especially sensitive to variations of the friction angle of the Kössen marls, but hardly influenced by a changing cohesion.

The thereby verified model reproduces many of the observed phenomena but also confirms the assumed mechanism of the Aggenalm landslide. The modeling results show a very homogeneous movement across the complete slope, with a slightly stronger vertical component at the top part of the slope, illustrating the sinking of the stiff Upper Rhaetian formation into the underlying, plastically deforming Kössen marls, thus representing the spreading mechanism in this

slope's part. At the lower half of the slope the displacement vectors are oriented parallel to slope and strata and the movements are sharply confined at the base of the Kössen marls forming a shear plane. Several secondary shear planes resulting from the sinking and differential movements of the hard rock slabs in the slope's upper half merge with the main shear surface.

Furthermore, the simulation of extreme events proved the dependence of an increased water table on the increasing displacement rate and a concomitant concentration of plastic deformation within the marls, thus triggering a landslide (Chapter 7.6 on page 140ff.). However, this process is focused on the slope's lower half, where the displacements multiply, while the upper half is hardly affected by a rising water table (nor decreasing friction angle) and doesn't alter its movement characteristics. Thus a rising water table changes the displacement pattern of the complete slope significantly. The resulting main shear plane then surfaces in the debris-dominated lower part, around B4 as illustrated by the dash-dotted lines in Figure 70. This is also confirmed by the description of the 1935 event, which describes the movements to be concentrated in the slope's lower part, too. At the same time, the simulation of various water levels also demonstrates that, in order to trigger a slide, a significant rise to an extremely high level is necessary (+6 m), which can only be caused by a very strong snowmelt and/or heavy rainfall.

The information regarding the cause-and-effect chain as well as the threshold values derived by the extensive analyses can be summarized as follows: A first, however conservative threshold was set at 32 kPa, at whose exceedance a very small acceleration can be expected. The second threshold, whose exceedance may lead to failure of the slope's lower part – thus suitable for an early warning system – was found to be at approximately 90 kPa, therefore 6 m above the mean water table (measured in B4). The temporal delay between cause (trigger) and effect – a prerequisite for an early warning system to prepare and to take measures – was determined by the TSA to be around 2–3 days for the water table's response to precipitation. This allows for ample warning time, even though the responding time of the accelerations couldn't yet be specified by these analyses.

Since up to now only a maximum water table rise of 1 m has been documented – even though several heavy rainfall events (>100 L/24 h) and snowmelt occurred – a catastrophic failure of the Aggenalm landslide seems very unlikely under the weather conditions experienced at the moment. However, the very low hazard potential currently coming from the Aggenalm landslide may change in future. Not only because of a possible change of weather conditions, but also due to a deterioration of the Kössen marls' properties, occurring naturally due to weathering effects, eventually amplified and expedited by the concurrently advancing disintegration of the overlaying strata. This affects the necessary rise of the water table tremendously, as the model reacts highly sensitive to changes of the Kössen marls' friction angle. If the friction angle decreases by only 2°, a significantly lower water table increase of approximately 1 m can already lead to failure (Figure 69).

9. Outlook and prerequisites for future projects

The threshold values obtained by time series analysis and numerical modeling enable the early warning system to issue an alert in advance of an acceleration or a catastrophic failure of the Aggenalm landslide. The latter, a catastrophic failure, which the threshold has been deduced from the numerical modeling, seems very unlikely under the conditions experienced at the moment while small acceleration phases have already been observed several times during the monitoring period. The rather conservative threshold derived from the TSA warns of a possible acceleration, which may lead to small secondary movements – such as debris flows and rotational and translational slides. The temporal delay of 2–3 days between rainfall and according peak in pore water pressure allows for an ample time in advance, to either raise the level of attentiveness toward possible road damage or blockage due to secondary movements and/or to take any other preparatory measures.

In future, additional analyses of the data series, whose acquisition has been continued by the now operating alpEWAS GSN 2.0, will hopefully allow a refining of the cause-and-effect chain – the relation between trigger and movement. Especially the relationship between precipitation/pore water pressure and deformation measurements couldn't be proved yet by sophisticated models, e.g., correlation analyses, even though the impact of water masses (e.g., snowmelt and/or heavy rainfall) is clear without ambiguity. In addition, several questions concerning the mechanism and development of the Aggenalm landslide are yet not fully exhausted, partially due to the little information regarding the shear zone (insufficient depth of several borings). For example, implementing a creep option into the numerical FLAC model could help to reproduce the movement characteristics within the Kössen marls in greater detail and to explore the time-dependent behavior and development of the slope. But also by applying a different code – for instance a distinct element code such as UDEC – joints can be defined more easily and additional information regarding the mechanism of the slope's upper third (sinking of Upper Rhaetian formation into plastically deforming Kössen marls) can possibly be derived.

At the same time, the Aggenalm landslide itself with the alpEWAS monitoring system installed on it serves as a great field test site. On the one hand, it is a good place to install, test, and calibrate new measurement techniques, since rich information on the build-up and mechanism of the Aggenalm landslide exist and the results of other measurement systems provide data for comparison. On the other hand the infrastructure of the alpEWAS GSN makes it easy to add new sensors due to its plug-in structure, thus providing options such as remote data access, data visualization and analysis, threshold implementation, and warning service. In addition, these plug-ins (further development during alpEWAS-Markt) allow a transfer of the whole system or individual components to a different monitoring site, e.g., another mass movement.

In order to gain a maximum of information from such a monitoring system – in regards to understanding the landslide's mechanism and behavior as well as the deduction of threshold values for an early warning system – it is a necessity to have a precise geologic model before

installation of the geosensor network. Thus the following workflow and prerequisites should be considered:

- Collecting as much information – geology and movement characteristics – about the site as possible by analyzing historic events, by performing a geological and geomorphological mapping, and by attaining additional material concerned with the build-up, etc.
- Performing laboratory tests and researching comparable materials and their properties in order to get suitable parameters for use in a numerical simulation.
- Geoelectric surveying of the mass movement prior or parallel to reconnaissance borings, so that it is possible to adjust the depths of borings, especially when not coring, as the shear zone is then hardly or not at all detectable in the cuttings. The length of the geoelectric survey profile has to be selected so that the shear zone is clearly penetrated.
- Installing the geosensor network. Sensors should be chosen depending on the monitoring task at hand, the landslide's characteristics, and planned analyses, e.g.:
 - Depending on landslide's mechanism and velocity an inclinometer, in-place inclinometer, TDR system, or any combination of these at one or several sites is possible. However, TDR is best installed individually.
 - Depending on the landslide's complexity piezometers should be installed in several boreholes and if relevant at different depths to allow a characterization of groundwater patterns as well as various water tables and their interdependence as well as individual relation to rainfall and movements.
 - Depending on the size and mechanism of the landslide, several sensors to measure on-surface movements, such as GNSS, should be distributed across the mass movement. Ideally continuous measurements, since these permit time series analysis, even with short data series.
 - Depending on the size and climatic zone of the landslide, it is necessary to eventually have more than one weather station and to add a heater to be able to continue measuring precipitation once temperatures drop below freezing.
- Storing the data in a data logger on an interim basis to minimize data gaps due to disruptions in, e.g., the WLAN connection to a central station.
- Analyzing the data with only little temporal delay to acquisition, for instance by means of time series analysis, as this eventually allows altering the recording frequency and performing adjustments on the sensors.
- Implementing first threshold values early into the warning system to be able to test the reliability of the system. However, a continuous adaptation to new results is necessary.

10. Bibliography

- AGLIARDI, F., CROSTA, G., ZANCHI, A. & RAVAZZI, C. (2009): Onset and timing of deep-seated gravitational slope deformations in the eastern Alps, Italy.– *Geomorphology*, **103** (1): 113–129.
- ALCAMO, J., MORENO, J., NOVÁKY, B., BINDI, M., COROBOV, R., DEVOY, R., GIANNAKOPOULOS, C., MARTIN, E., OLESEN, J. & SHVIDENKO, A. (2007): Europe.– In: PARRY, M., CANZIANI, O., PALUTIKOF, J., VAN DER LINDEN, P. & HANSON, C. [eds.]: *Climate change 2007: Impacts, adaptation and vulnerability: Working Group II contribution to the Fourth Assessment Report of the IPCC Intergovernmental Panel on Climate Change*.– 976 pp., Cambridge, UK (Cambridge University Press), 541–580.
- ALEOTTI, P. (2004): A warning system for rainfall-induced shallow failures.– *Eng. Geol.*, **73** (3–4): 247–265.
- ALFIERI, L., SALAMON, P., PAPPENBERGER, F., WETTERHALL, F. & THIELEN, J. (2012): Operational early warning systems for water-related hazards in Europe.– *Environmental Science & Policy*, **21**: 35–49.
- AMANN, F. (2006): *Großhangbewegung Cuolm Da Vi (Graubünden, Schweiz)*.– Doctoral thesis, Naturwissenschaftliche Fakultät, Friedrich-Alexander-Universität Erlangen-Nürnberg, 207 pp.
- AMPFERER, O. (1939): Über einige Formen der Bergzerreiung.– *Sitzungsberichte d. mathem.-naturw. Kl., Abt. I*, **148** (1–2): 1–14.
- AMPFERER, O. (1940): Zum weiteren Ausbau der Lehre von den Bergzerreiungen.– *Sitzungsberichte d. mathem.-naturw. Kl., Abt. I*, **149** (1–2): 51–70.
- AMPFERER, O. (1941): Bergzerreiungen im Inntalraume.– *Sitzungsberichte d. mathem.-naturw. Kl., Abt. I*, **150** (3–6): 97–114.
- ANDERSON, M. & RICHARDS, K. (1992): *Slope stability*.– 648 pp., Chichester, New York, etc. (Wiley & Sons).
- ANDERSON, O., ORD, J. & ROBINSON, E. [eds.] (1985): *Time Series Analysis: Theory and Practice 6: Hydrological, Geophysical, and Spatial Applications*.– In: *Proceedings of the International Conference on Time Series Analysis, Toronto, Canada, August 10–14, 1983*.– 308 pp., Amsterdam, New York (Elsevier).
- ARATTANO, M. & MARCHI, L. (2005): Measurements of debris flow velocity through cross-correlation of instrumentation data.– *Nat. Hazards Earth Syst. Sci.*, **5** (1): 137–142.
- AU, S. (1993): Rainfall and slope failure in Hong Kong.– *Eng. Geol.*, **36** (1–2): 141–147.
- AVO – ALMWIRTSCHAFTLICHER VEREIN OBERBAYERN (n.d.): *Almbuch "Aggen Alm" – Ursprünglich amtliche Almdokumentation*.– Miesbach.
- BADOUX, A., GRAF, C., RHYNER, J., KUNTNER, R. & MCARDELL, B. (2009): A debris-flow alarm system for the Alpine Illgraben catchment: design and performance.– *Nat. Hazards*, **49** (3): 517–539.
- BALTZER, A. (1875): *Ueber Bergstürze in den Alpen*.– 50 pp., Zürich (Verlag der Schabelitz'schen Buchhandlung, C. Schmidt).
- BARBOUR, S. & KRAHN, J. (2004): *Numerical Modelling – Prediction or Process*.– *Geotechnical News*: 44–52.

- BARON, I., AGLIARDI, F., AMBROSI, C. & CROSTA, G. (2005): Numerical analysis of deep-seated mass movements in the Magura Nappe; Flysch Belt of the Western Carpathians (Czech Republic).– *Nat. Hazards Earth Syst. Sci.*, **5** (3): 367–374.
- BASHER, R. (2006): Global early warning systems for natural hazards: systematic and people-centered.– *Philosophical Transactions of the Royal Society A: Mathematical, Physical and Engineering Sciences*, **364** (1845): 2167–2182.
- BAUR, F. (2010): Untersuchung der Aggenalm-Hangbewegung mittels Geoelektrik – Profil Ost.– Unpublished bachelor's thesis, Chair of Engineering Geology, Technische Universität München, 45 pp., Munich.
- BELL, R., MAYER, J., POHL, J., GREIVING, S. & GLADE, T. (2010): Integrative Frühwarnsysteme für gravitative Massenbewegungen (ILEWS). Monitoring, Modellierung, Implementierung.– 271 pp., Essen (Klartext).
- BENKO, B. (1998): Numerical modelling of complex slope deformations.– Canadian theses, Thèses canadiennes, 366 pp., Ottawa (National Library of Canada).
- BERNRIEDER, J. (1991): Unser Audorf, Chronik II. Teil.– 1014 pp., Oberaudorf (Meißner-Druck GmbH).
- BMU – BUNDESMINISTERIUM FÜR UMWELT, NATURSCHUTZ UND REAKTORSICHERHEIT (2008): Klimawandel in den Alpen. Fakten – Folgen – Anpassung.– 91 pp., Niestetal.
- BRANDHOFF, T. (2010): Auswertung und Reproduzierbarkeit von Inklinometermessungen.– Unpublished bachelor's thesis, Chair of Engineering Geology, Technische Universität München, 55 pp., Munich.
- BRÜCKL, E. & BRÜCKL, J. (2006): Geophysical models of the Lesachriegel and Gradenbach deep-seated mass-movements (Schober range, Austria).– *Eng. Geol.*, **83** (1–3): 254–272.
- BRUNETTI, M., PERUCCACCI, S., ROSSI, M., LUCIANI, S., VALIGI, D. & GUZZETTI, F. (2010): Rainfall thresholds for the possible occurrence of landslides in Italy.– *Nat. Hazards Earth Syst. Sci.*, **10** (3): 447–458.
- BUSS, E. & HEIM, A. (1881): Der Bergsturz von Elm, den 11. September 1881.– 163 pp., Zürich (Wurster).
- CAINE, N. (1980): The Rainfall Intensity: Duration Control of Shallow Landslides and Debris Flows.– *Geografiska Annaler, Series A, Physical Geography*, **62** (1–2): 23–27.
- CAMPBELL, R. (1975): Soil Slips, Debris Flows, and Rainstorms in the Santa Monica Mountains and Vicinity, Southern California.– U.S. Geological Survey Professional Paper, **851**: 1–51.
- CAPPARELLI, G. & VERSACE, P. (2011): FLAIR and SUSHI: two mathematical models for early warning of landslides induced by rainfall.– *Landslides*, **8** (1): 67–79.
- CHLEBORAD, A.; BAUM, R. & GODT, J. (2006): Rainfall thresholds for forecasting landslides in the Seattle, Washington, area – Exceedance and probability.– In: U.S. Geological Survey Open-File Report, **2006–1064**.– 31 pp., Reston (USGS).
- CORNFORTH, D. (2005): Landslides in practice – Investigations, analysis, remedial/preventive options in soils.– 596 pp., Hoboken (Wiley).
- COROMINAS, J. & MOYA, J. (1999): Reconstructing recent landslide activity in relation to rainfall in the Llobregat River basin, Eastern Pyrenees, Spain.– *Geomorphology*, **30** (1–2): 79–93.

- CROSTA, G. & AGLIARDI, F. (2002): How to obtain alert velocity thresholds for large rock-slides.– *Physics and Chemistry of the Earth*, **27**: 1557–1565.
- CROSTA, G., FRATTINI, P. & AGLIARDI, F. (2013): Deep seated gravitational slope deformations in the European Alps.– *Tectonophysics*, **605**: 13–33.
- CRUDEN, D. (1991): A simple definition of a landslide.– *Bull. Int. Assoc. of Eng. Geol.*, **43**: 27–29.
- CRUDEN, D. & COUTURE, R. (2010): More comprehensive characterization of landslides: Review and additions.– In: WILLIAMS, A. [ed.]: *Geologically active: Proceedings of the 11th IAEG congress.*– 11th IAEG congress, Auckland, New Zealand, September 5–10, 2010.– 4590 pp., Boca Raton (CRC Press), 1033–1042.
- CRUDEN, D. & VARNES, D. (1996): Landslide types and processes.– In: TURNER, A. & SCHUSTER, R. [eds.]: *Landslides – Investigation and mitigation.*– 673 pp., Washington D.C. (National Academy Press), 36–75.
- DAI, F. & LEE, C. (2001): Frequency-volume relation and prediction of rainfall-induced landslides.– *Eng. Geol.*, **59** (3–4): 253–266.
- DAVIS (2012): *Vantage Pro2 Console Manual.*– 53 pp., (Davis Instruments Corp).
- DETOURNAY, C. & HART, R. [eds.] (1999): *FLAC and numerical modeling in geomechanics.*– International FLAC Symposium on Numerical Modeling in Geomechanics, Minneapolis, Minnesota, USA, 1-3. September 1999.– 512 pp., Rotterdam, Brookfield (Balkema).
- DIN 18137-3 (2002): *Bestimmung der Scherfestigkeit – Teil 3: Direkter Scherversuch.*– 33 pp., Berlin (Beuth Verlag GmbH).
- DIN 4149 (2005): *Bauten in deutschen Erdbebengebieten – Lastannahmen, Bemessung und Ausführung üblicher Hochbauten.*– 82 pp., Berlin (Beuth Verlag GmbH).
- DIN 1055-2 (2010): *Einwirkungen auf Tragwerke – Teil 2: Bodenkenngrößen.*– 14 pp., Berlin (Beuth Verlag GmbH).
- DKKV – DEUTSCHES KOMITEE KATASTROPHENVORSORGE E.V. (2010): *Emerging Challenges for Early Warning Systems in context of Climate Change and Urbanization.*– 38 pp., Cop-pet, Switzerland (HDN).
- DOWDING, C. SU, M. & O'CONNOR, K. (1989): Measurements of Rock Mass Deformation with Grouted Coaxial Antenna Cables.– *Rock Mech. and Rock Eng.*, **22**: 1–23.
- DRAMIS, F. & SORRISO-VALVO, M. (1994): Deep-seated gravitational slope deformations, related landslides and tectonics.– *Eng. Geol.*, **38**: 231–243.
- EBERHARDT, E. (2006): From cause to effect: using numerical modelling to understand rock slope instability mechanisms.– In: EVANS, S., SCARASCIA MUGNOZZA, G., STROM, A. & HERMANN, R. [eds.]: *Proceedings of the NATO Advanced Research Workshop on Massive Rock Slope Failure: New Models for Hazard Assessment*, Celano, Italy, June 16–21, 2002.– NATO Science Series IV, **49**: 662 pp., Dordrecht (Springer), 85–101.
- EBERHARDT, E., BONZANIGO, L. & LOEW, S. (2007): Long-term investigation of a deep-seated creeping landslide in crystalline rock. Part II. Mitigation measures and numerical modelling of deep drainage at Campo Vallemaggia.– *Can. Geotech. J.*, **44** (10): 1181–1199.
- EBERHARDT, E., THURO, K. & LUGINBUEHL, M. (2005): Slope instability mechanisms in dipping interbedded conglomerates and weathered marls – the 1999 Rufi landslide, Switzerland.– *Eng. Geol.*, **77** (1–2): 35–56.

- EISBACHER, G. & CLAGUE, J. (1984): Destructive mass movements in high mountains. Hazard and management.– Geological Survey of Canada Paper, **84** (16): 230 pp., Ottawa (Canadian Govt. Pub. Centre).
- FALK, M. (2012): A First Course on Time Series Analysis – Examples with SAS.– 364 pp., Berlin (epubli).
- FELLNER-FELDEGG, H. (1969): The Measurement of Dielectrics in the Time Domain.– J. Phys. Chem., **73**: 616–623.
- FERRARI, A., QUAN LUNA, B., SPICKERMANN, A., TRAVELLETTI, J., KRZEMINSKA, D., EICHENBERGER, J., VAN ASCH, T., VAN BEEK, R., BOGAARD, T., MALET, J. & LALOU, L. (2014): Techniques for the Modelling of the Process Systems in Slow and Fast-Moving Landslides.– In: VAN ASCH, T., COROMINAS, J., GREIVING, S., MALET, J. & STERLACCHINI, S. [eds.]: Mountain Risks: From Prediction to Management and Governance, Vol. 34.– 413 pp., Dordrecht (Springer Netherlands), 83–129.
- FESTL, J. (2008): Eignungsprüfung von Zement-Bentonit-Suspensionen als Injektionsgut bei TDR Deformationsmessungen.– Unpublished master's thesis, Chair of Engineering Geology, Technische Universität München, 54 pp., Munich.
- FESTL, J., SINGER, J. & THURO, K. (2011): The Aggenalm landslide – First Findings of the Acquired Monitoring Data.– In: EBERHARDT, E. & STEAD, D. [eds.]: Slope Stability 2011.– Proceedings of the International Symposium on Rock Slope Stability in Open Pit Mining and Civil Engineering, Vancouver, Canada, September 18–21, 2011.– paper CD-ROM (CARMA), paper no. 195, 7 pp.
- FESTL, J., SINGER, J. & THURO, K. (2012): The Aggenalm landslide – first findings of the monitoring data.– In: EBERHARDT, E., FROESE, C., TURNER, A. & LEROUEIL, S. [eds.]: Landslide and Engineered Slopes, Protecting Society Through Improved Understanding.– Proceedings of the 11th International and 2nd North American Symposium on Landslides and Engineered Slopes, Banff, Canada, June 3–8, 2012.– 2050 pp., London (Taylor & Francis Group), 907–912.
- FESTL, J., SINGER, J. & THURO, K. (2013): Grundwasserstandsschwellenwerte für eine tiefgreifende Hangbewegung mittels Zeitreihenanalyse und numerischen Modellen (Aggenalm, Bayrischzell).– In: THURO, K. (ed.): Veröffentlichungen der 19. Tagung für Ingenieurgeologie und des Forums für junge Ingenieurgeologen.– 19. Tagung für Ingenieurgeologie mit Forum für junge Ingenieurgeologen, Munich, March 13–15, 2013.– 660 pp., <http://nbn-resolving.de/urn/resolver.pl?urn:nbn:de:bvb:91-epub-20130320-1138068-0-8>, 179–184.
- FLORIS, M. & BOZZANO, F. (2008): Evaluation of landslide reactivation: A modified rainfall threshold model based on historical records of rainfall and landslides.– Geomorphology, **94** (1–2): 40–57.
- FOPPE, K., KNAACK, L. & PAWEL, B. (2009): Zeitabhängige Messgrößen – verborgene Schätze in unseren Daten. Beiträge zum 85. DVW-Seminar am 7. und 8. September 2009 in Kassel.– Schriftenreihe des DVW, **59**: 223 pp., Augsburg (Wißner).
- FÜBL, S. (2009): Überprüfung des Einflusses der Suspensionsüberdeckung auf TDR Deformationsmessungen.– Unpublished bachelor's thesis, Chair of Engineering Geology, Technische Universität München, 32 pp., Munich.
- GALLEMANN, T. (2012): Geodätische Überwachung der Rutschung Aggenalm im Sudelfeld, 9. Folgemessung am 11.05.2012.– LfU unpublished internal report, 9 pp.

- GANSS, O. (1950): Sedimentation und Tektonik in den Kalkalpen zwischen Schliersee und dem Inntal.– *Z. deutsch. Geol. Ges.*, **102**: 203–211.
- GARCÍA, A., HÖRDT, A. & FABIAN, M. (2010): Landslide monitoring with high resolution tilt measurements at the Dollendorfer Hardt landslide, Germany.– *Geomorphology*, **120** (1–2): 16–25.
- GILGEN, H.J. (2006): *Univariate time series in geosciences.*– 718 pp., Berlin, London (Springer).
- GLABSCH, J., HEUNECKE, O. & SCHUHBÄCK, S. (2009): Monitoring the Hornbergl landslide using a recently developed low cost GNSS sensor network.– *Journal of Applied Geodesy*, **3** (3): 179–192.
- GLADE, T., CROZIER, M. & SMITH, P. (2000): Applying Probability Determination to Refine Landslide-triggering Rainfall Thresholds Using an Empirical “Antecedent Daily Rainfall Model”.– *Pure and Applied Geophysics*, **157** (6–8): 1059–1079.
- GOKCEOGLU, C. & SEZER, E. (2009): A statistical assessment on international landslide literature (1945–2008).– *Landslides*, **6** (4): 345–351.
- GORE, A. (2006): *An inconvenient truth.*– 325 pp., New York (Rodale).
- GRAF, C., BADOUX, A., DUFOUR, F., FRITSCHI, B., MCARDELL, B., RHYNER, J., KUNTNER, R., TEYSSEIRE, P. & NIGG, U. (2007): Alarmsystem für murgangfähige Wildbäche – Beispiel Illgraben.– *Wasser Energie Luft*, **99** (2): 119–128.
- GRANA, V. & TOMMASI, P. (2014): A deep-seated slow movement controlled by structural setting in marly formations of Central Italy.– *Landslides*, **11** (2): 195–212.
- GRUBER, S. & HAEBERLI, W. (2007): Permafrost in steep bedrock slopes and its temperature-related destabilization following climate change.– *J. Geophys. Res.*, **112** (F2): 1–10.
- GWINNER, M.P. (1971): *Geologie der Alpen.*– 477 pp.; Stuttgart (Schweizerbart).
- HAEBERLI, W. & MAISCH, M. (2007): Klimawandel im Hochgebirge.– In: ENDLICHER, W. & GERSTENGARBE, F. [eds.]: *Der Klimawandel – Einblicke, Rückblicke und Ausblicke.*– 134 pp., Berlin, Potsdam (G & S Druck und Medien GmbH), 98–107.
- HAHN, F. (1912): Versuch einer Gliederung der austroalpinen Masse westlich der österreichischen Traun.– *Verh. geol. Reichsanst.*, **15**: 51–58.
- HAHN, F. (1914): Ergebnisse neuer Spezialforschungen in den deutschen Alpen. 3. Die Kalkalpen Südbayerns.– *Geol. Rdsch.*, **5**: 112–145.
- HASEMANN, W. (1929): *Geologie des Brunnstein- und Traithengebietes in den oberbayerischen Alpen. Mit einer geol. Karte 1:25000.*– Doctoral thesis, Ludwig-Maximilians-Universität, 46 pp., Munich.
- HATEM, M. & THURO, K. (2008): Untersuchungen des Bergsturzes von Goldau 1806 mit Hilfe einer Distinkten Elemente Modellierung.– In: MARSCHALLINGER, R. & WANKER, W. [eds.]: *Geomonitoring, FE-Modellierung, Sturzprozesse und Massenbewegungen – Beiträge zur COG Fachtagung Salzburg 2008.*– 197 pp., Heidelberg (Wichmann), 75–91.
- HEIM, A. (1882a): Der Bergsturz von Elm.– *Z. dt. geol. Ges.*, **34** (1): 74–115.
- HEIM, A. (1882b): *Über Bergstürze.*– 31 pp., Zürich (Wurster & Cie).
- HEIM, A. (1919): *Geologie der Schweiz – Band I: Molasseland und Juragebirge.*– 704 pp., Leipzig (Chr. Herm. Tauchnitz).

- HEIM, A. (1921/1922): *Geologie der Schweiz – Band II: Die Schweizer Alpen.*– 1018 pp., Leipzig (Chr. Herm. Tauchnitz).
- HEIM, A. (1932): *Bergsturz und Menschenleben.*– 218 pp., Zürich (Fretz & Wasmuth Verlag).
- HEINIMANN, H., HOLLENSTEIN, K., KIENHOLZ, H., KRUMMENACHER, B. & MANI, P. (1998): *Methoden zur Analyse und Bewertung von Naturgefahren.*– In: Bundesamt für Umwelt, Wald und Landschaft (BUWAL) [ed.]: *Umwelt-Materialien Nr. 85, Naturgefahren.*– 248 pp., Bern (BUWAL).
- HEPP, K. (2010): *Untersuchung der Aggenalm-Hangbewegung mittels Geoelektrik – Profil West.*– Unpublished bachelor's thesis, Chair of Engineering Geology, Technische Universität München, 46 pp., Munich.
- HIPEL, K. & MCLEOD, I. (1994): *Time Series Modelling of Water Resources and Environmental Systems.*– 1013 pp., Amsterdam (Elsevier).
- HOLLING, C. (1978): *Adaptive Environmental Assessment and Management.*– International Series on Applied Systems Analysis, **3**: 377 pp., Chichester, New York, etc. (Wiley & Sons).
- HOLZHAUSER, P. (2011): *Bestimmung der Scherfestigkeit an veränderlich festen Gesteinen in Hinblick auf Hangbewegungsphänomene.*– Münchner geowissenschaftliche Abhandlungen Reihe B, **17**: 122 pp., München (Verlag Dr. Friedrich Pfeil).
- HONG, Y., HIURA, H., SHINO, K., SASSA, K., SUEMINE, A., FUKUOKA, H. & WANG, G. (2005): *The influence of intense rainfall on the activity of large-scale crystalline schist landslides in Shikoku Island, Japan.*– *Landslides*, **2** (2): 97–105.
- HUGGEL, C., CLAGUE, J. & KORUP, O. (2012): *Is climate change responsible for changing landslide activity in high mountains?*– *Earth Surf. Process. Landforms*, **37** (1): 77–91.
- HUNGR, O., LEROUEIL, S. & PICARELLI, L. (2014): *The Varnes classification of landslide types, an update.*– *Landslides*, **11** (2): 167–194.
- HUSAINI, O. & RATNASAMY, M. (2001): *An early warning system for active landslides.*– *Quarterly Journal of Engineering Geology and Hydrogeology*, **34** (3): 299–305.
- HUTCHINSON, J. (1988): *General Report: Morphological and Geotechnical Parameters of Landslides in Relation to Geology and Hydrogeology.*– In: BONNARD, C. [ed.]: *Landslides – Proceedings of the Fifth International Symposium on Landslides, Lausanne, July 10–15, 1988, Part I.*– 809 pp., Rotterdam (Balkema), 3–35.
- IAEG COMMISSION ON LANDSLIDES – INTERNATIONAL ASSOCIATION OF ENGINEERING GEOLOGY (1990): *Suggested Nomenclature for Landslides.*– *Bull. Int. Assoc. Eng. Geol.*, **41**: 13–16.
- IAEG COMMISSION ON LANDSLIDES – INTERNATIONAL ASSOCIATION OF ENGINEERING GEOLOGY (1994): *A Suggested Method for Reporting Landslide Causes.*– *Bull. Int. Assoc. Eng. Geol.*, **50**: 71–74.
- IAEG COMMISSION ON LANDSLIDES – INTERNATIONAL ASSOCIATION OF ENGINEERING GEOLOGY (1995): *A Suggested Method for Describing the Rate of Movement of a Landslide.*– *Bull. Int. Assoc. Eng. Geol.*, **52**: 75–78.
- IDNDR – INTERNATIONAL DECADE FOR NATURAL DISASTER REDUCTION (1997): *International Decade for Natural Disaster Reduction. IDNDR Early Warning Programme. Report on Early Warning Capabilities for Geological Hazards.*– 35 pp., Geneva (IDNDR).

- IMRE, B., ALIG, C., SCHÖNENBERGER, I., SPRINGMAN, S. & HERMANN, S. (2009): Morphology and kinematic of a very large, deep-seated structural rock slide located in the Fusch Valley, Eastern Alps, Austria.– *Geomorphology*, **112** (3–4): 277–294.
- INTRIERI, E., GIGLI, G., MUGNAI, F., FANTI, R. & CASAGLI, N. (2012): Design and implementation of a landslide early warning system.– *Eng. Geol.*, **147/148**: 124–136.
- ISRM – INTERNATIONAL SOCIETY FOR ROCK MECHANICS (1981): Basic geotechnical description of rock masses.– *Int. J. Rock Mech. Min. Sci. & Geomech. Abstr.*, **18** (1): 87–110.
- ITASCA CONSULTING GROUP INC. (2011a): FLAC – Fast Lagrangian Analysis of Continua, Version 7.0, User's Guide.– 364 pp., Minneapolis (Itasca).
- ITASCA CONSULTING GROUP INC. (2011b): FLAC – Fast Lagrangian Analysis of Continua, Version 7.0, Theory and Background.– 126 pp., Minneapolis (Itasca).
- ITASCA CONSULTING GROUP INC. (2011c): FLAC – Fast Lagrangian Analysis of Continua, Version 7.0, Constitutive Models.– 210 pp., Minneapolis (Itasca).
- JAHN, A. (1964): Slopes morphological features resulting from gravitation.– *Zeitschrift für Geomorphologie, Supplementband*, **5**: 59–72.
- JING, L. & HUDSON, J. (2002): Numerical methods in rock mechanics.– *Int. J. Rock Mech. Min. Sci.*, **39** (4): 409–427.
- JUNG, S. (2007): Untersuchung der Hangbewegung Aggenalm östlich des Sudelfelds zwischen Bayrischzell und Oberaudorf.– Unpublished diploma thesis, Chair of Engineering Geology, Technische Universität München, 82 pp., Munich.
- KANE, W. & BECK, T. (1994): Development of a Time Domain Reflectometry System to Monitor Landslide Activity.– In: BURNS, S. [ed.]: *Proceedings, 45th Highway Geology Symposium*.– 45th Highway Geology Symposium, Portland, OR, USA, August 17–19, 1994.– 274 pp., Portland (Portland State University), 163–173.
- KANE, W. & BECK, T. (1996): An Alternative Monitoring System for Unstable Slopes.– *Geotechnical Instrumentation News*, **14** (3): 29–31.
- KEAREY, P., BROOKS, M. & HILL, I. (2002): *An introduction to geophysical exploration*.– 262 pp., Oxford (Blackwell Science).
- KEEFER, D., WILSON, R., MARK, R., BRABB, E., BROWN, W., ELLEN, S., HARP, E., WIECZOREK, G., ALGER, C. & ZATKIN, R. (1987): Real-Time Landslide Warning During Heavy Rainfall.– *Science*, **238** (4829): 921–925.
- KEUSEN, H. (2006): Naturgefahren: Die neue Herausforderung für die Gesellschaft.– *Bull. angew. Geol.*, **11** (2): 57–63.
- KIESLINGER, A. (1957): Josef Stiny.– *Mitt. Geol. Ges. Wien*, **50**: 389–430.
- KONIETZKY, H. (2001): Numerische Simulation in der Geomechanik mittels expliziter Verfahren.– Habilitation, Veröffentlichungen des Instituts für Geotechnik der Technischen Universität Bergakademie Freiberg, **2001-2**: 358 pp., Freiberg (Institut für Geotechnik).
- KONIETZKY, H., HART, R. & BILLAUX, D. (1994): Mathematische Modellierung von geklüftetem Fels.– *Felsbau*, **12** (6): 395–400.
- KREISS, J. & NEUHAUS, G. (2006): *Einführung in die Zeitreihenanalyse*.– 388 pp., Berlin, New York (Springer).

- KRISTENSEN, L., BLIKRA, L. & HOLE, J. (2010): Åknes: State of instrumentation and data analysis, report 02.2010.– 43 pp, www.aknes.no/sites/default/files/Aaknesrapport02_2010.pdf.
- KULHAWY, F. (1975): Stress deformation properties of rock and rock discontinuities.– *Eng. Geol.*, **9**: 327–350.
- KVELDSVIK, V., EINSTEIN, H., NILSEN, B. & BLIKRA, L. (2009): Numerical Analysis of the 650,000 m² Åknes Rock Slope based on Measured Displacements and Geotechnical Data.– *Rock Mech. Rock Eng.*, **42** (5): 689–728.
- LACASSE, S. & NADIM, F. (2009): Landslide Risk Assessment and Mitigation Strategy.– In: SASSA, K. & CANUTI, P. [eds.]: *Landslides – Disaster Risk Reduction*.– 650 pp., Berlin, Heidelberg (Springer), 31–61.
- LAGOMARSINO, D., SEGONI, S., FANTI, R. & CATANI, F. (2013): Updating and tuning a regional-scale landslide early warning system.– *Landslides*, **10** (1): 91–97.
- LAROCQUE, M., MANGIN, A., RAZACK, M. & BANTON, O. (1998): Contribution of correlation and spectral analyses to the regional study of a large karst aquifer (Charente, France).– *Journal of Hydrology*, **205** (3–4): 217–231.
- LATELIN, O., BOLLINGER, D., HEGG, C. & KREUSEN, H. (2001): The Analysis of the 1999 Landslides in Switzerland.– In: KÜHNE, M., EINSTEIN, H., KRAUTER, E., KLAPPERICH, H., PÖTLER, R. & KÜHNE, M. [eds.]: *Proceedings of the United Engineering Foundation International Conference on Landslides – Causes, impacts and countermeasures*, Davos, Switzerland, June 17–21, 2001.– 636 pp., Essen (Verl. Glückauf), 159–167.
- LEBOURG, T., HERNANDEZ, M., ZERATHE, S., EL BEDOUI, S., JOMARD, H. & FRESIA, B. (2010): Landslides triggered factors analysed by time lapse electrical survey and multidimensional statistical approach.– *Eng. Geol.*, **114** (3–4): 238–250.
- LEE, J. & LEE, K. (2000): Use of hydrologic time series data for identification of recharge mechanism in a fractured bedrock aquifer system.– *Journal of Hydrology*, **229** (3–4): 190–201.
- LFU – BAYERISCHES LANDESAMT FÜR UMWELT (2009a): Projekt Georisken im Klimawandel, Vorhaben Gefahrenhinweiskarte Bayerische Alpen. Steinschlag-Felssturz-Rutschung-Hanganbruch. Alpenanteil Landkreis Rosenheim.– 58 pp., UmweltSpezial, Munich (Bayer. LfU).
- LFU – BAYERISCHES LANDESAMT FÜR UMWELT (2009b): Projekt Georisken im Klimawandel, Vorhaben Gefahrenhinweiskarte Bayerische Alpen. Steinschlag-Felssturz-Rutschung-Hanganbruch. Alpenanteil Landkreis Miesbach.– 52 pp., UmweltSpezial, Munich (Bayer. LfU).
- LFU – BAYERISCHES LANDESAMT FÜR UMWELT (2010): Rutschung.– 3 pp., (Bayer. LfU).
- LOLLINO, G., ARATTANO, M., ALLASIA, P. & GIORDAN, D. (2006): Time response of a landslide to meteorological events.– *Nat. Hazards Earth Syst. Sci.*, **6** (2): 179–184.
- LOLLINO, G., ARATTANO, M. & CUCCUREDDU, M. (2002): The use of the automatic inclinometric system for landslide early warning: the case of Cabella Ligure (North-Western Italy).– *Physics and Chemistry of the Earth, Parts A/B/C*, **27** (36): 1545–1550.
- MALAIÉ VON, V. (1951): Die Landwirtschaft des Landkreises Rosenheim im allgemeinen, die Almwirtschaft im besonderen und die Massnahmen zu ihrer Förderung.– Doctoral thesis, Fakultät für Landwirtschaft, Technische Hochschule München, 221 pp., Munich.

- MARCATO, G., MANTOVANI, M., PASUTO, A., ZABUSKI, L. & BORGATTI, L. (2012): Monitoring, numerical modelling and hazard mitigation of the Moscardo landslide (Eastern Italian Alps).– *Eng. Geol.*, **128**: 95–107.
- MARGOTTINI, C., CANUTI, P. & SASSA, K. (2013): *Landslide Science and Practice. Volume 2: Early Warning, Instrumentation and Monitoring. Proceedings of the Second World Landslide Forum, Rome, 3–9. October 2011.*– 685 pp., Berlin, Heidelberg, etc. (Springer).
- MARKLSEDER, F. (1935): Bergrutsch am Tatzelwurm.– *Anzeiger für Oberaudorf und Kiefersfelden – Heimatzeitung des Inngaues*, **26** (17): 2.
- MATSUURA, S., ASANO, S. & OKAMOTO, T. (2008): Relationship between rain and/or meltwater, pore-water pressure and displacement of a reactivated landslide.– *Eng. Geol.*, **101** (1–2): 49–59.
- MATSUURA, S., ASANO, S., OKAMOTO, T. & TAKEUCHI, Y. (2003): Characteristics of the displacement of a landslide with shallow sliding surface in a heavy snow district of Japan.– *Eng. Geol.*, **69** (1–2): 15–35.
- MAYER, J., GLADE, T., THIEBES, B. & BELL, R. (2010): Integrative Frühwarnsysteme.– In: BELL, R., MAYER, J., POHL, J., GREIVING, S. & GLADE, T. [eds.]: *Integrative Frühwarnsysteme für gravitative Massenbewegungen (ILEWS). Monitoring, Modellierung, Implementierung.*– 271 pp., Essen (Klartext), 17–31.
- MEHNERT, L. (2009): Optimierung von TDR Deformationsmessungen durch die Verwendung von Zement-Zuschlägen in der Hinterfüllung.– Unpublished bachelor's thesis, Chair of Engineering Geology, Technische Universität München, 25 p., Munich.
- MIKKELSEN, E. (2003): Advances in inclinometer data analysis.– In: MYRVOLL, F. [ed.]: *Proceedings of the Sixth International Symposium on Field Measurements in Geomechanics, Oslo, Norway, September 15–18, 2003.*– 812 pp., Lisse, Exton (Balkema), 555–567.
- N.N. & HEIM, A. (1887): *Das Unglück in Zug vom 5. Juli 1887.*– 50 pp., Zürich (Cäsar Schmidt).
- NADIM, F., CEPEDA, J., SANDERSEN, F., JAEDICKE, C. & HEYERDAHL, H. (2009): Prediction of rainfall-induced landslides through empirical and numerical models.– In: PICARELLI, L., TOMMASI, P., URCIUOLI, G. & VERSACE, P. [eds.]: *Rainfall-induced landslides: mechanisms, monitoring techniques and nowcasting models for early warning systems, Proceedings of the 1st Italian Workshop on Landslides (IWL 2009), Naples, June 8–10, 2009.*– 249 pp., Naples (CIRIAM), 206–215.
- NEUNER, H. & FOPPE, K. (2009): Grundlagen der Zeitreihenanalyse im Zeitbereich.– In: FOPPE, K., KNAACK, L. & PAWEL, B. (eds.): *Zeitabhängige Messgrößen – verborgene Schätze in unseren Daten. Beiträge zum 85. DVW-Seminar am 7. und 8. September 2009 in Kassel.*– Schriftenreihe des DVW, **59**: 223 pp., Augsburg (Wißner), 25–54.
- NITTEL, S., LABRINIDIS, A. & STEFANIDIS, A. (2008): *GeoSensor networks.*– Second International Conference, GSN 2006, Boston, MA, USA, October 1–3, 2006.– 270 pp. Berlin (Springer).
- OCCC – ORGANE CONSULTATIF SUR LES CHANGEMENTS CLIMATIQUES (2008): *Das Klima ändert – was nun? Der neue UN-Klimabericht (IPCC 2007) und die wichtigsten Ergebnisse aus Sicht der Schweiz.*– 47 pp., Bern (Occc).
- O'CONNOR, K. & DOWDING, C. (1999): *Geomeasurements by pulsing TDR cables and probes.*– 402 pp., Boca Raton (CRC Press).

- ODEN, J. (1991): Finite Elements: An Introduction.– In: CIARLET, P. & LIONS, J. [eds.]: Handbook of Numerical Analysis, Vol. II – Finite Element Methods (Part 1).– 928 pp., Amsterdam, New York, etc. (North-Holland), 3–15.
- OKAMOTO, T., LARSEN, J., MATSUURA, S., ASANO, S., TAKEUCHI, Y. & GRANDE, L. (2004): Displacement properties of landslide masses at the initiation of failure in quick clay deposits and the effects of meteorological and hydrological factors.– *Eng. Geol.*, **72** (3–4): 233–251.
- PARRY, M., CANZIANI, O., PALUTIKOF, J., VAN DER LINDEN, P. & HANSON, C. (2007): Climate change 2007: Impacts, adaptation and vulnerability: Working Group II contribution to the Fourth Assessment Report of the IPCC Intergovernmental Panel on Climate Change.– 976 pp., Cambridge, UK (Cambridge University Press).
- PETLEY, D. (2012): Global patterns of loss of life from landslides.– *Geology*, **40** (10): 927–930.
- PICARELLI, L. & VINALE, F. (2009): Numerical analyses of rainfall-induced landslides. The case of Nocera Inferiore, March 2005.– Technical report, 28 pp., (Centro Euro-Mediterraneo per i cambiamenti climatici).
- PLANALP – PLATFORM ON NATURAL HAZARDS OF THE ALPINE CONVENTION [ed.] (2012): Alpine strategy for adaptation to climate change in the field of natural hazards.– 20 pp., Bern (PLANALP).
- PLANK, S. (2012): Pre-survey suitability analysis of the differential and persistent scatterer synthetic aperture radar interferometry method for deformation monitoring of mass movements and subsidence.– Doctoral thesis, Chair of Engineering Geology, Technische Universität München, 164 pp., Munich.
- POLEMIO, M. & PETRUCCI, O. (2000): Rainfall as a Landslide Triggering Factor: An Overview of Recent International Research.– In: BROMHEAD, E., DIXON, N. & IBSEN, M. [eds.]: Landslides: in research, theory and practice – Proceedings of the 8th International Symposium on Landslides, Cardiff, June 26–30, 2000.– 1684 pp., London (Thomas Telford), 1219–1226.
- PROKEŠOVÁ, R., MEDVEĐOVÁ, A., TÁBOŘÍK, P. & SNOPKOVÁ, Z. (2013): Towards hydrological triggering mechanisms of large deep-seated landslides.– *Landslides*, **10** (3): 239–254.
- REIBMÜLLER, M. (1997): Die Geologie des Oberen Rottachtales zwischen Bodenschneid, Stolzenberg und Siebligrat sowie Geotechnische Eigenschaften verwitterter Kössener Mergel.– Unpublished diploma thesis, Lehrstuhl für Allgemeine, Angewandte und Ingenieur-Geologie, Technische Universität München, 128 pp., Munich.
- REYNOLDS, J.M. (1997): An introduction to applied and environmental geophysics.– 796 pp., Chichester, New York, etc. (Wiley & Sons).
- RIEDMÜLLER, G. (2003): Classification Schemes of Unstable Slopes – An Overview.– *Felsbau*, **21** (2): 13–18.
- RÖHRL, J. (2010): Erstellen von Kalibrierkurven für die in den Bohrungen der Hangbewegung Aggenalm eingebauten Zement-Bentonit-Suspensionen.– Unpublished diploma thesis, Chair of Engineering Geology, Technische Universität München, 47 pp., Munich.
- SASSA, K. (2013): Early Warning of Landslides.– In: SASSA, K., ROUHBAN, B., BRICEÑO, S., MCSAVENEY, M. & HE, B. [eds.]: Landslides: Global Risk Preparedness.– Berlin, Heidelberg (Springer), 27–42.
- SCHLITGEN, R. (2001): Angewandte Zeitreihenanalyse.– Lehr- und Handbücher der Statistik 203 pp., Munich (Oldenbourg).

- SCHMIDT-THOMÉ, P. (1964): Alpenraum.– In: BAYERISCHES GEOLOGISCHES LANDESAMT (LfU) [ed.]: Erläuterungen geol. Kt. Bayern 1:500000, 2nd ed.– 344 pp., Munich (LfU), 244–297.
- SCHÖNWIESE, C. (2007): Wird das Klima extremer? Eine statistische Perspektive.– In: ENDLICHER, W. & GERSTENGARBE, F. [eds.]: Der Klimawandel – Einblicke, Rückblicke und Ausblicke.– 134 pp., Berlin, Potsdam (G & S Druck und Medien GmbH), 60–66.
- SCHORMAIR, N. (2003): Geologische Kartierung des Gebietes zwischen Aggenalm und Tatzelwurmwasserfall, Sudelfeld.– Unpublished diploma thesis, Lehrstuhl für Allgemeine, Angewandte und Ingenieurgeologie, Technische Universität München, 58 pp., Munich.
- SEGALINI, A., GIANI, G.P. & FERRERO, A.M. (2009): Geomechanical studies on slow slope movements in Parma Apennine.– *Eng. Geol.*, **109** (1–2): 31–44.
- SIMONI, A., BERTI, M., GENERALI, M., ELMI, C. & GHIROTTI, M. (2004): Preliminary result from pore pressure monitoring on an unstable clay slope.– *Eng. Geol.*, **73** (1–2): 117–128.
- SINGER, J. (2010): Development of a Continuous Monitoring System for Instable Slopes Using Time Domain Reflectometry.– Unpublished doctoral thesis, Chair of Engineering Geology, Technische Universität München, 189 pp., Munich.
- SINGER, J., RIEDMANN, M., LANG, O., ANDERSSOHN, J., THURO, K., WUNDERLICH, T., HEUNECKE, O. & MINET, C. (2012): Corner reflector SAR interferometry as an element of a landslide early warning system.– Poster presentation, EGU 2012.
- SINGER, J., THURO, K. & SAMBETH, U. (2006): Development of a Continuous 3D-Monitoring System for Unstable Slopes using TDR.– *Felsbau*, **24** (3): 16–23.
- SOHRABY, K., MINOLI, D. & ZNATI, T.F. (2007): Wireless sensor networks. Technology, protocols, and applications.– 307 pp., Hoboken, (Wiley-Interscience).
- STARFIELD, A.M. & CUNDALL, P.A. (1988): Towards a Methodology for Rock Mechanics Modelling.– *Int. J. Rock Mech. Min. Sci. & Geomech. Abstr.*, **25** (3): 99–106.
- STEAD, D., EBERHARDT, E. & COGGAN, J. (2006): Developments in the characterization of complex rock slope deformation and failure using numerical modelling techniques.– *Eng. Geol.*, **83** (1–3): 217–235.
- STINI, J. (1952a): Neuere Ansichten über "Bodenbewegungen" und über ihre Beherrschung durch den Ingenieur.– *Geologie und Bauwesen*, **19**: 31–54.
- STINI, J. (1952b): Talzuschub und Wildbachverbauung.– *Geologie und Bauwesen*, **19**: 135–136.
- STINI, J. (1941): Unsere Täler wachsen zu.– *Geologie und Bauwesen*, **13**: 71–79.
- STINI, J. (1942): Nochmal der "Talzuschub".– *Geologie und Bauwesen*, **14**: 10–14.
- STINY, J. (1938a): Die Rutschanfälligkeit des Baugeländes und seine Untersuchung.– *Geologie und Bauwesen*, **10**: 112–123.
- STINY, J. (1938b): Über die Regelmäßigkeit der Wiederkehr von Rutschungen, Bergstürzen und Hochwasserschäden in Österreich.– *Geologie und Bauwesen*, **10**: 9–48.
- STINY, J. (1929): Faltungen und Überschiebungen durch Gleitung (Rutschung größten Maßstabes).– *Centralblatt für Mineralogie, Geologie und Paläontologie*, **2** (4): 116–125.
- STINY, J. (1942): Talzuschub und Bauwesen.– *Die Bautechnik*, **20** (9): 80–81.

- STINÝ, J. (1910): Die Muren. Versuch einer Monographie mit besonderer Berücksichtigung der Verhältnisse in den Tiroler Alpen.– 139 pp., Innsbruck (Verlag der Wagner'schen Universitätsbuchhandlung).
- STÖRZBACH, S. (2009): Untersuchung der Hangbewegung am Sudelfeld mittels Geoelektrik.– Unpublished master's thesis, Chair of Engineering Geology, Technische Universität München, 45 pp., Munich.
- TADAYONFAR, G. (2011): Numerische Modellierung der geologischen und mechanischen Prozesse der Hangbewegung am Sudelfeld.– Doctoral thesis, Chair of Engineering Geology, Technische Universität München, 121 pp., Munich.
- TANG, W., STARK, T. & ANGULO, M. (1999): Reliability in back analysis of slope failures.– *Soils and foundations*, **39** (5): 73–80.
- TERZAGHI, K. (1925): Erdbaumechanik auf bodenphysikalischer Grundlage.– 399 pp., Vienna (Deuticke).
- TERZAGHI, K. (1947): Theoretical soil mechanics.– 510 pp., New York (Wiley and Sons).
- TERZAGHI, K. (1950): Mechanism of landslides.– In: PAIGE, S. [ed.]: *Application of Geology to Engineering Practice*, Berkeley Volume.– 327 pp., New York (Geological Society of America), 83–123.
- THE MATHWORKS, INC. (2008): *MATLAB (R) 7 – Data Analysis*.– 211 pp., Natick (The MathWorks, Inc.).
- THORNES, J. & ALCÁNTARA-AYALA, I. (1998): Modelling mass failure in a Mediterranean mountain environment: climatic, geological, topographical and erosional controls.– *Geomorphology*, **24** (1): 87–100.
- THURNER, A. (1961): Die Baustile der tektonischen Einheiten der Nördlichen Kalkalpen.– *Z. dt. Geol. Ges.*, **113** (2-3): 367–389.
- THURO, K., SINGER, J. & FESTL, J. (2013): A Geosensor Network Based Monitoring and Early Warning System for Landslides.– In: MARGOTTINI, C., CANUTI, P. & SASSA, K. [eds.]: *Landslide Science and Practice*, Vol. 2: Early Warning, Instrumentation and Monitoring. Proceedings of the Second World Landslide Forum, Rome, October 3–9, 2011.– 685 pp., Berlin, Heidelberg, etc. (Springer), 79–86.
- THURO, K., SINGER, J., FESTL, J., WUNDERLICH, T., WASMEIER, P., REITH, C., HEUNECKE, O., GLABSCH, J. & SCHUHBÄCK, S. (2010a): New landslide monitoring techniques – developments and experiences of the alpEWAS project.– *Journal of Applied Geodesy*, **4** (2): 69–90.
- THURO, K., SINGER, J., FESTL, J., WUNDERLICH, T., WASMEIER, P., REITH, C., HEUNECKE, O., GLABSCH, J. & SCHUHBÄCK, S. (2011a): Entwicklung und Erprobung eines integrativen 3D-Frühwarnsystems für alpine instabile Hänge – alpEWAS – Final report in the framework of the BMBF/DFG special geoscientific program 'Geotechnologien'.– 80 pp., Munich.
- THURO, K., WUNDERLICH, T. & HEUNECKE, O. (2006): Entwicklung und Erprobung eines integrativen 3D-Frühwarnsystems für alpine instabile Hänge.– unpubl. project proposal in the framework of the BMBF/DFG special geoscientific program 'Geotechnologien', 38 pp.

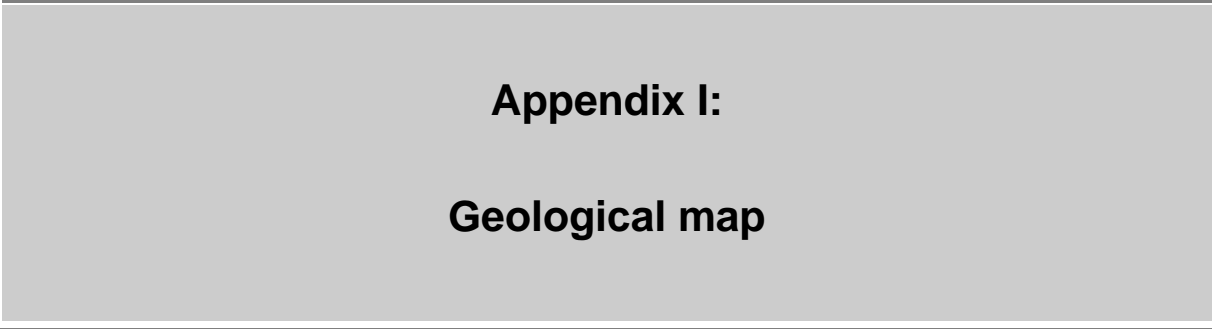
- THURO, K., WUNDERLICH, T. & HEUNECKE, O. (2007): Development and Testing of an Integrative 3D Early Warning System for Alpine Instable Slopes (alpEWAS).– In: STROINK, L. [ed.]: Geotechnologies Science Report No. 10, Kick-Off-Meeting, Technische Universität Karlsruhe, October 10, 2007.– 136 pp., 101–112.
- THURO, K., WUNDERLICH, T., HEUNECKE, O., FESTL, J., REITH, C., SCHUHBÄCK, S., SINGER, J., WASMEIER, P. & GLABSCH, J. (2010b): Systemarchitektur und Layout eines Frühwarnsystems für alpine instabile Hänge "alpEWAS".– In: MARSCHALLINGER, R., WANKER, W. & ZOBL, F. [eds.]: Beiträge zur COGeo 2010, Salzburg, June 11, 2010.– 18 pp., http://www.cogeo.at/publications/cogeo2010/cogeo2010_0001.pdf.
- THURO, K., WUNDERLICH, T., HEUNECKE, O., SINGER, J., SCHUHBÄCK, S., WASMEIER, P., GLABSCH, J. & FESTL, J. (2009): Low cost 3D early warning system for instable alpine slopes – the Aggenalm Landslide monitoring system.– *Geomechanik und Tunnelbau*, **2** (3): 221–237.
- THURO, K., WUNDERLICH, T., HEUNECKE, O., SINGER, J., WASMEIER, P., SCHUHBÄCK, S., FESTL, J., REITH, C. & GLABSCH, J. (2011b): Marktreifeentwicklung eines flexiblen, modular aufgebauten Geosensornetzwerks zur Überwachung von Hang-, Deich- und Bauwerksbewegungen – alpEWAS Markt – Final report in the framework of the BMBF/DFG special geoscientific program 'Geotechnologies'.– 48 pp., Munich.
- THURO, K., WUNDERLICH, T., HEUNECKE, O., SINGER, J., WASMEIER, P., SCHUHBÄCK, S., FESTL, J., REITH, C. & GLABSCH, J. (2014): Low Cost 3D Early Warning System for Alpine Instable Slopes: The Aggenalm Landslide Monitoring System.– In: WENZEL, F. & ZSCHAU, J. [eds.]: Early Warning for Geological Disasters.– 379 pp., Berlin, Heidelberg (Springer), 289–306.
- TURNER, A. & JAYAPRAKASH, G. (1996): Introduction.– In: TURNER, A. & SCHUSTER, R. [eds.]: Landslides – Investigation and mitigation.– 673 pp., Washington D.C. (National Academy Press), 3–11.
- UNEP – UNITED NATIONS ENVIRONMENT PROGRAMME, DEWA – DIVISION OF EARLY WARNING AND ASSESSMENT (2012): Early Warning Systems. A State of the Art Analysis and Future Directions.– 63 pp., Nairobi (UNEP).
- UNISDR – UNITED NATIONS INTERNATIONAL STRATEGY FOR DISASTER RISK REDUCTION (2006): Developing Early Warning Systems: A Checklist.– 10 pp., Bonn (UNISDR).
- UNISDR – UNITED NATIONS INTERNATIONAL STRATEGY FOR DISASTER REDUCTION (2009): 2009 UNISDR Terminology on Disaster Risk Reduction.– 30 pp., Geneva (UNISDR).
- VAN ASCH, T. & BUMA, J. (1997): Modelling groundwater fluctuations and the frequency of movement of a landslide in the Terres Noires region of Barcelonnette (France).– *Earth Surf. Process. Landforms*, **22** (2): 131–141.
- VAN ASCH, T., BUMA, J. & VAN BEEK, L. (1999): A view on some hydrological triggering systems in landslides.– *Geomorphology*, **30** (1–2): 25–32.
- VAN ASCH, T., MALET, J., VAN BEEK, L. & AMITRANO, D. (2007): Techniques, issues and advances in numerical modelling of landslide hazard.– *Bulletin de la Société Géologique de France*, **178** (2) : 65–88.
- VARNES, D. (1978): Slope movement types and processes.– In: SCHUSTER, R. & KRIZEK, R. [eds.]: Landslides, analysis and control.– Special report – Transportation Research Board, National Research Council, **176**: 234 pp., Washington (National Academy of Sciences), 11–33.

- VARNES, D., RADBRUCH-HALL, D. & SAVAGE, W. (1989): Topographic and Structural Conditions in Areas of Gravitational Spreading of Ridges in the Western United States.– U.S. Geological Survey Professional Paper, **1496**: 1–28.
- VITA, P. DE, REICHENBACH, P., BATHURST, J., BORGA, M., CROSTA, G., CROZIER, M., GLADE, T., GUZZETTI, F., HANSEN, A. & WASOWSKI, J. (1998): Rainfall-triggered landslides: a reference list.– *Environmental Geology*, **35** (2–3): 219–233.
- VUTUKURI, V., LAMA, R. & SALUJA, S. (1978): Handbook on mechanical properties of rocks. Testing techniques and results, Vol. II.– 481 pp., Clausthal (Trans Tech Publications).
- WALLER, G. (n.d.): Die Brücke – Erlebtes und Erlauschtes vom Leben auf dem Berg.– 19 pp.
- WASMEIER, P. (2009): Grundlagen der Deformationsbestimmung mit Messdaten bildgebender Tachymeter.– Doctoral thesis, Chair of Geodesy, Technische Universität München, 153 pp., Munich.
- WEIDNER, S. (2000): Kinematik und Mechanismus tiefgreifender alpiner Hangdeformationen unter besonderer Berücksichtigung der hydrogeologischen Verhältnisse.– Doctoral thesis, Naturwissenschaftliche Fakultät, Friedrich-Alexander-Universität Erlangen-Nürnberg, 246 pp.
- WIECZOREK, G. (1996): Landslide triggering mechanisms.– In: TURNER, A. & SCHUSTER, R. [eds.]: *Landslides – Investigation and mitigation*.– 673 pp., Washington D.C. (National Academy Press), 76-90.
- WIECZOREK, G., ELLEN, S., LIPS, E. & CANNON, S. (1983): Potential for debris flow and debris flood along the Wasatch Front between Salt Lake City and Willard, Utah, and measures for their mitigation.– U.S. Geological Survey Open-File Report, **83-635**: 76 pp.
- WIECZOREK, G. & GUZZETTI, F. (2000): A review of rainfall thresholds for triggering landslides.– In: CLAPS, P. & SICCARDI, F. [eds.]: *Proceedings of the 1st Plinius Conference on Mediterranean Storms, Maratea, October 14–16, 1999*.– 649 pp., Consenza (Editoriale Bios), 407–414.
- WILLERICH, S. (2013): Charakterisierung tiefgründiger Hangbewegungen vor dem Hintergrund der Gefahrenzonierung am Beispiel Algund/Südtirol.– Doctoral thesis, Münchner Geowissenschaftliche Abhandlungen, **19**: 286 pp., Munich (Verlag Dr. Friedrich Pfeil).
- WILL, J. & KONIETZKY, H. (1998): Neue Techniken der Numerik zur Berechnung von Felsböschungen.– *Felsbau*, **16** (3): 155–167.
- WOLFF, H. (1985): Geologische Karte von Bayern 1 : 25 000, Erläuterungen zum Blatt Nr. 8338 Bayrischzell.– 190 pp., Munich (Bayer. LfU).
- WOYTOWITZ, F. (2008): Untersuchung des Einflusses der Koaxialkabel-Zuleitungslänge auf TDR Deformationsmessungen.– Unpublished bachelor's thesis, Chair of Engineering Geology, Technische Universität München, 24 pp., Munich.
- WOYTOWITZ, F. (2010): Entwurf und Installation eines ad-hoc multi-hop Sensornetzwerkes für die Hangbewegung Aggenalm bei Bayrischzell.– Unpublished master's thesis, Chair of Engineering Geology, Technische Universität München, 44 pp., Munich.
- WP/WLI (1993a): Multilingual landslide glossary.– 59 pp., Richmond (Bi-Tech Publishers).
- WP/WLI (1993b): A Suggested Method for Describing the Activity of a Landslide.– *Bull. Int. Assoc. Eng. Geol.*, **47**: 53–57.

- WP/WLI (1990): A Suggested Method for Reporting a Landslide.– Bull. Int. Assoc. Eng. Geol., **41**: 5–12.
- WP/WLI (1991): A Suggested Method for a Landslide Summary.– Bull. Int. Assoc. Eng. Geol., **43**: 101–110.
- WWA ROSENHEIM – WASSERWIRTSCHAFTSAMT ROSENHEIM (n.d.): Talzuschub Gassenbach – Aggraben, Östliches Sudelfeld Gemeinde Oberaufdorf.– internal report, 2 pp.
- WYLLIE, D., MAH, C. & HOEK, E. (2004): Rock slope engineering.– 431 pp., London, New York (Spon Press).
- YIN, Y., WANG, H., GAO, Y. & LI, X. (2010): Real-time monitoring and early warning of landslides at relocated Wushan Town, the Three Gorges Reservoir, China.– Landslides, **7** (3): 339–349.
- ZANGERL, C., PRAGER, C., BRANDNER, R., BRÜCKL, E., EDER, S., FELLIN, W., TENSCHERT, E., POSCHER, G. & SCHÖNLAUB, H. (2008): Methodischer Leitfaden zur prozessorientierten Bearbeitung von Massenbewegungen.– Geo.Alp, **5**: 1–51.
- ZAY, K. (1807): Goldau und seine Gegend, wie sie war und was sie geworden.– 390 pp., Zürich (Orell Füssli & Co).
- ZEIMETZ, P., ELING, C. & KUHLMANN, H. (2009): Analyse von GPS-Referenzstationsbeobachtungen mit Methoden der Zeitreihenanalyse.– In: FOPPE, K., KNAACK, L. & PAWEL, B. (eds.): Zeitabhängige Messgrößen – verborgene Schätze in unseren Daten. Beiträge zum 85. DVW-Seminar am 7. und 8. September 2009 in Kassel.– Schriftenreihe des DVW, **59**: 223 pp., Augsburg (Wißner), 193–210.
- ZISCHINSKY, U. (1968): Über Bergzerreißung und Talzuschub.– Geol Rundsch, **58** (2): 974–983.
- ZISCHINSKY, U. (1969): Über Sackungen.– Rock Mechanics, **1** (1): 30–52.

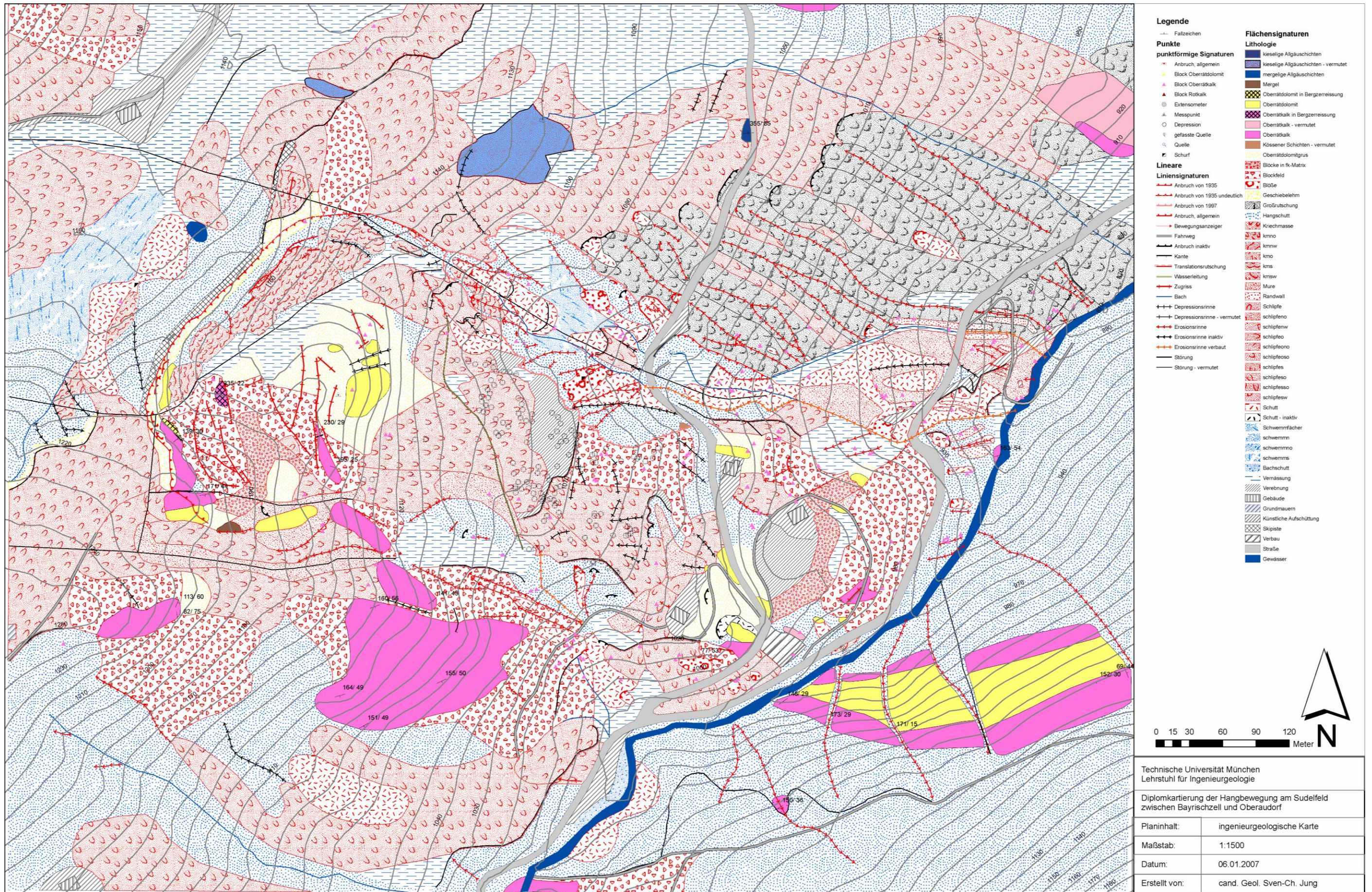
11. URL Resources

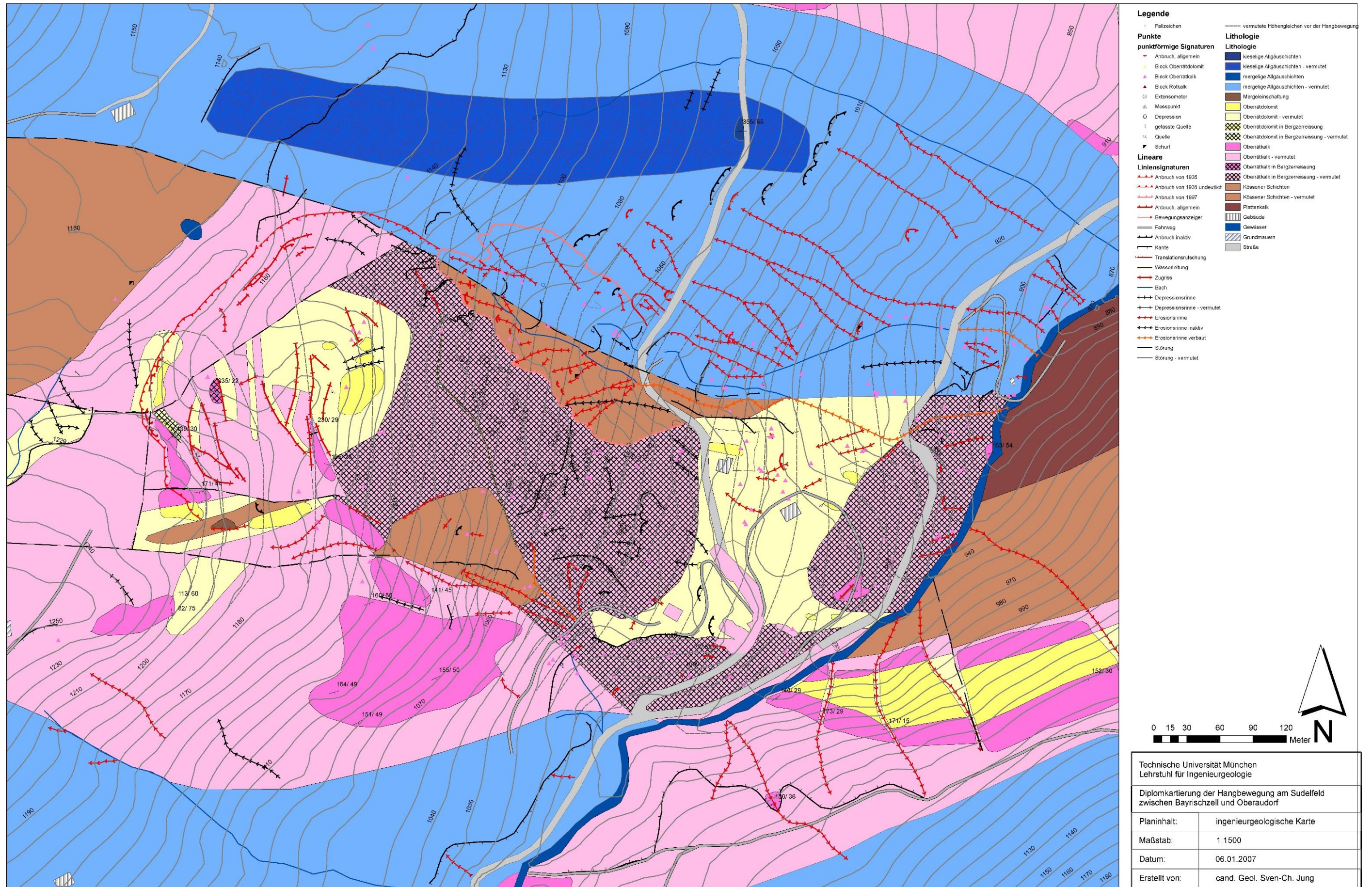
- www-01: <http://www.alpconv.org/en/default.html>, last accessed on May 1, 2013.
- www-02: <http://www.alpewas.de/>, last accessed on May 8, 2013.
- www-03: <http://www.ardmediathek.de/das-erste/brennpunkt/hochwasseralarm-der-kampf-gegen-die-flut?documentId=15030748>, last accessed on June 4, 2013.
- www-04: <http://www.sommer.at/referenzen/warnsysteme/warnsystem-steinbruch-spitz.html>, last accessed on May 12, 2013.
- www-05: <http://www.suedtirolnews.it/d/artikel/2010/04/12/zugunglueck-im-vinschgau-opferstammen-aus-suedtirol.html>, last accessed on June 11, 2013.
- www-06: <http://www.stol.it/Artikel/Chronik-im-Ueberblick/Lokal/Chronologie-des-Ungluecks-Video>, last accessed on June 11, 2013.
- www-07: <http://www.slews.de>, last accessed on June 18, 2013.
- www-08: <http://rainfallthresholds.irpi.cnr.it>, last accessed on July 1, 2013.
- www-09: <http://www.itascacg.com/about/history.html>, last accessed on July 1, 2013.
- www-10: <http://www.bayernaltas.de>, last accessed on July 2, 2013.
- www-11: <http://www.lfu.bayern.de/geologie/massenbewegungen/georisk/index.htm>, last accessed on August 18, 2013.
- www-12: <http://www.agrarkulturerbe.de>, cue 'Aggenalm', last accessed on August 18, 2013.
- www-13: <http://www.davisnet.com>, last accessed on November 11, 2013.
- www-14: http://www.leica-geosystems.com/de/de/lgs/_8346.htm?cid=3305, last accessed on January 22, 2011.
- www-15: http://www.humboldtmg.com/crack_monitor_plus.html, last accessed on February 4, 2014.
- www-16: www.ni.com, last accessed on February 16, 2014.
- www-17: www.sisgeo.com, last accessed on February 17, 2014.
- www-18: <http://www.rocscience.com>, last accessed on June 3, 2014.
- www-19: <http://www.wille-geotechnik.de>, last accessed on June 29, 2014.
- www-20: <http://www.mathworks.de/products/matlab>, last accessed on August 14, 2014.



Appendix I:
Geological map

Appendix I shows the two geological and morphological maps by JUNG (2007), who did the mapping of the Aggenalm landslide in course of his Diploma thesis in 2007. The geological map, uncovered of the Quaternary, was used as a basis for the map in Figure 11.





Appendix II:

Description of 1935 landslide

In this appendix the complete article from May 4, 1935, published in the weekly newspaper *Anzeiger von Oberaudorf und Kiefersfelden – Heimatzeitung des Inngaus* concerning the happenings at the Aggenalm landslide can be found. The text has been freely translated into English by the author.

Anzeiger für Oberaudorf und Kiefersfelden – Heimatzeitung des Inngauses; vol. 26, ed. 17, Saturday, May 4, 1935:

„(Bergrutsch am Tatzelwurm). Am Morgen des Ostermontags machte sich am Aggeralpl [Aggenalm] oberhalb des Tatzelwurms zwischen den dort liegenden Hütten der Beginn eines Erdbebens bemerkbar. Kurze Zeit darauf begannen bereits größere Strecken Weideland in den Gassenbach abzurutschen und sich dort zu stauen. Bis zum Abend hatte die Geländebewegungen schon einen derartigen Umfang angenommen, daß die zahlreichen freiwilligen Helfer dem Vordringen der Erdmassen machtlos gegenüberstanden. Der Gassenbach wurde bis zu einer Tiefe von 5 Metern mit Gestein, Felsblöcken und Bäumen aufgefüllt. Die beiden Brücken zum Aggeralpl²⁴ und zur Gassenalm waren ebenso wie die oberen Teile der Straße spurlos verschwunden. Die abgerutschte Fläche wurde am Abend des Ostermontags auf etwa vier Tagwerk Weideland und etwa zwei bis drei Tagwerk Wald geschätzt.

Die Bewegung der gewaltigen Erdmassen kam auch am Dienstag nicht zum Stillstand. Die Erdmassen bewegten sich vielmehr mit einer Geschwindigkeit von etwa 4 Metern in der Stunde abwärts und hatten in den Nachmittagsstunden den Gassenbach in einer Länge von 1 ½ km vollkommen ausgefüllt. Die Murre hatte um diese Zeit auch schon den Auerbach erreicht und verschüttet, der sich ebenfalls ein neues Bett bahnen muß.

Bis Dienstag Nachmittag sind schätzungsweise eine Million Kubikmeter Erdmassen in Bewegung geraten. Man rechnet aber damit, daß der Erdbeben zunächst nicht zum Stillstand gelangen dürfte, sondern wie aus den Rissen und Sprüngen der Abbruchstelle zu schließen ist, noch weiter um sich greifen wird. Über die Ursachen des riesigen Bergrutsches können nur Mutmaßungen geäußert werden. Man nimmt an, daß durch die starken Regenfälle der letzten Zeit unter dem Hang liegende Erdschichten ins Rutschen geraten sind.

Bis Dienstag nachmittag waren etwa 20 Tagwerk Alm- und Weidegrund völlig vermurrt. Arbeiter des hiesigen Forstamtes sind damit beschäftigt, dem Gassenbach ein neues Flußbett zu schaffen. Die Betonbrücke nach Bayrischzell, an der sich die Erdmassen stauten, ist unter der Mure ebenfalls völlig verschwunden.

Meldung vom Donnerstag: Die im Gebiete des Tatzelwurms abgerutschten Erdmassen sind nunmehr durch das Aufhören der Niederschläge nahe zum Stillstand gekommen. Die Hauptmure hatte sich bis Donnerstag früh noch ganz langsam fortbewegt. Durch die Beendigung der Schneeschmelze hat sich die Wasserbildung vermindert und übt nicht mehr Druck aus wie bei Beginn des Erdbebens. Die Kommission der Sektion für Wildbachverbauung in Rosenheim, die bis Mittwoch an Ort und Stelle weilte, ist der Ansicht, daß wohl noch mehr Erdmassen abrutschen werden, jedoch erst wieder beim Eintritt einer Schlechtwetterperiode. Eine Gefahr für den großen Tatzelwurmwasserfall, der etwa 20 Minuten weit von dem Bergrutschgebiet entfernt ist, besteht vorerst nicht. Es ist aber Vorsorge getroffen, im Notfall durch Sprengungen dem Bach einen anderen Abfluss zu geben.

Man ist nunmehr damit beschäftigt, das durch die Gewalt der Murren mitgerissene Holz, ausgerissene Baumstämme usw. wegzuräumen, damit keine Stauung eintritt und das Wasser freien Abfluss hat. Die Möglichkeit zu einer sogenannten Wildbachverbauung ist hier nicht gegeben, da es sich um eine abgelagerte Moräne handelt, die sich in gewissen Zeitabständen immer wieder in Bewegung setzen wird, wie das auch schon früher der Fall war, wenn auch nicht in dem gegenwärtigen Ausmaß.“

²⁴ Lampl Alm according to the nomenclature used in this thesis – hut No. 2 in Figure 15.

Anzeiger für Oberaudorf und Kiefersfelden – Heimatzeitung des Inngaues; vol. 26, ed. 17, Saturday, May 4, 1935:

‘(Landslide at the Tatzelwurm). On Easter Monday morning [April 22, 1935] the start of a landslide became noticeable between the alpine cabins at the Aggeralpl [Aggenalm area] above the Tatzelwurm. Shortly after, major parts of pasture started to slide into the Gassenbach creek and accumulating thereabout. By evening, the movements had already assumed such proportions that the numerous volunteers faced the advance of the debris masses powerless. The Gassenbach was filled with rocks, boulders, and trees up to a depth of 5 meters. The two bridges leading to the Aggeralpl²⁴ and Gassenalm as well as the upper parts of the road had disappeared. On the evening of Easter Monday the area affected by the landslide was estimated to be about four days’ work of pasture and two to three days’ work of forest.

Neither on Tuesday did the movement of these huge masses come to a stand. Rather, the debris masses moved with a velocity of 4 meters per hour downhill and completely filled the Gassenbach over a length of 1 ½ km until the afternoon. The debris flow had already reached and overwhelmed the Auerbach creek by this time, which had to pave itself a new bed, too.

By Tuesday afternoon, an estimated one million cubic meters of earth masses were set in motion. It is expected, however, that the landslide won’t come to a halt at first, but as can be concluded from the cracks and fissures at the scarp, will continue to spread. About the causes of the huge landslide only conjectures can be expressed. It is believed that due to the heavy preceding rains the strata below the slope started to slip.

By Tuesday afternoon about 20 days’ work of alpine pasture were destroyed by debris flows. Workers of the local forestry office are busy constructing a new riverbed for the Gassenbach. The concrete bridge to Bayrischzell, at which the debris masses accumulated, has been covered completely.

Message from Thursday: The slid instable masses came to a halt almost completely because of the cessation of rainfall. The main debris flow was still moving very slowly on Thursday morning. Due to the end of the snowmelt the formation of water decreases and therefore doesn’t exert as much pressure as at the onset of the landslide. The Commission of the Department of torrents in Rosenheim, who stayed in place until Wednesday, is of the opinion that probably more earth masses will become instable and slide off, but only after another period of bad weather. For the time being, there is no threat to the big Tatzelwurm waterfall, which is about 20 minutes away from the landslide area. There is, however, made provision to blast a new drain for the Gassenbach in case of an emergency.

One is now busy to clear the wood entrained by the debris flows, as well as the uprooted tree trunk, etc., so that no jamming occurs and the water can freely drain. The possibility of a torrent control is not given here, since it is a deposited moraine, which will be set in motion at certain intervals, as it was already the case previously, though not to the current extent.’

Appendix III:

LfU geodetic survey, extensometers

This Appendix compiles the graphics showing the results of the geodetic survey conducted by the LfU as well as the wire extensometers over the last eleven years. Figure 24 and Figure 25 in Chapter 4.6.3 picture the location of the individual measurement systems or survey points. A more detailed description and analysis of the individual results is given by GALLEMANN (2012).

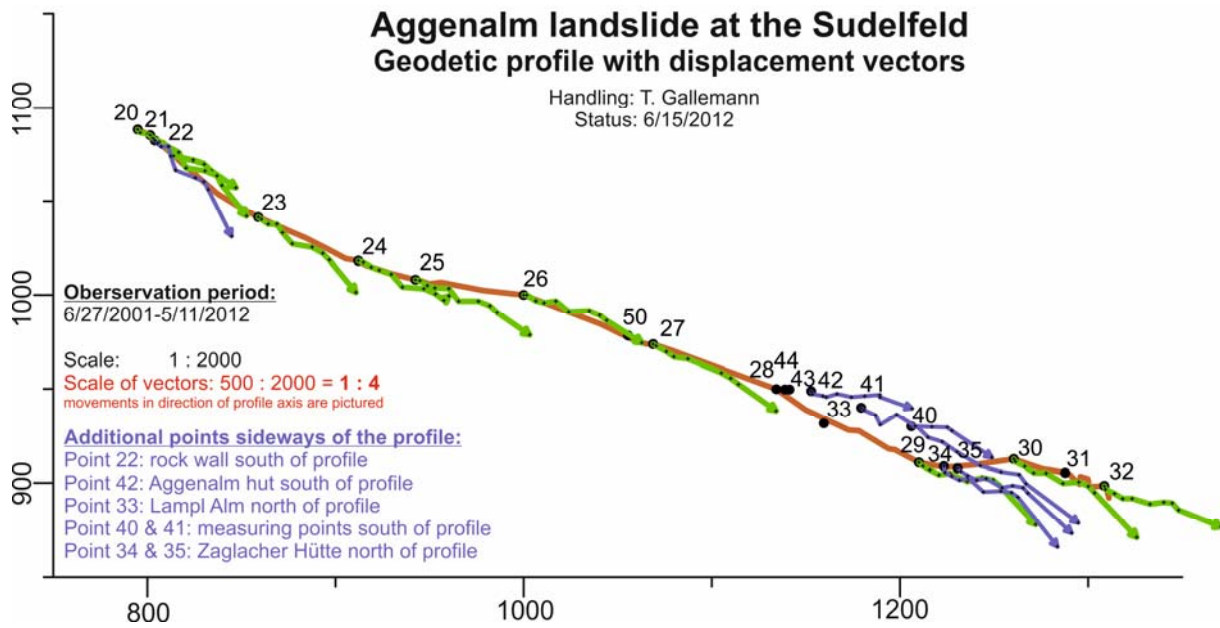


Figure III-1: Displacement vectors at the measuring points along the geodetic profile conducted by the LfU (adapted from GALLEMANN 2012).

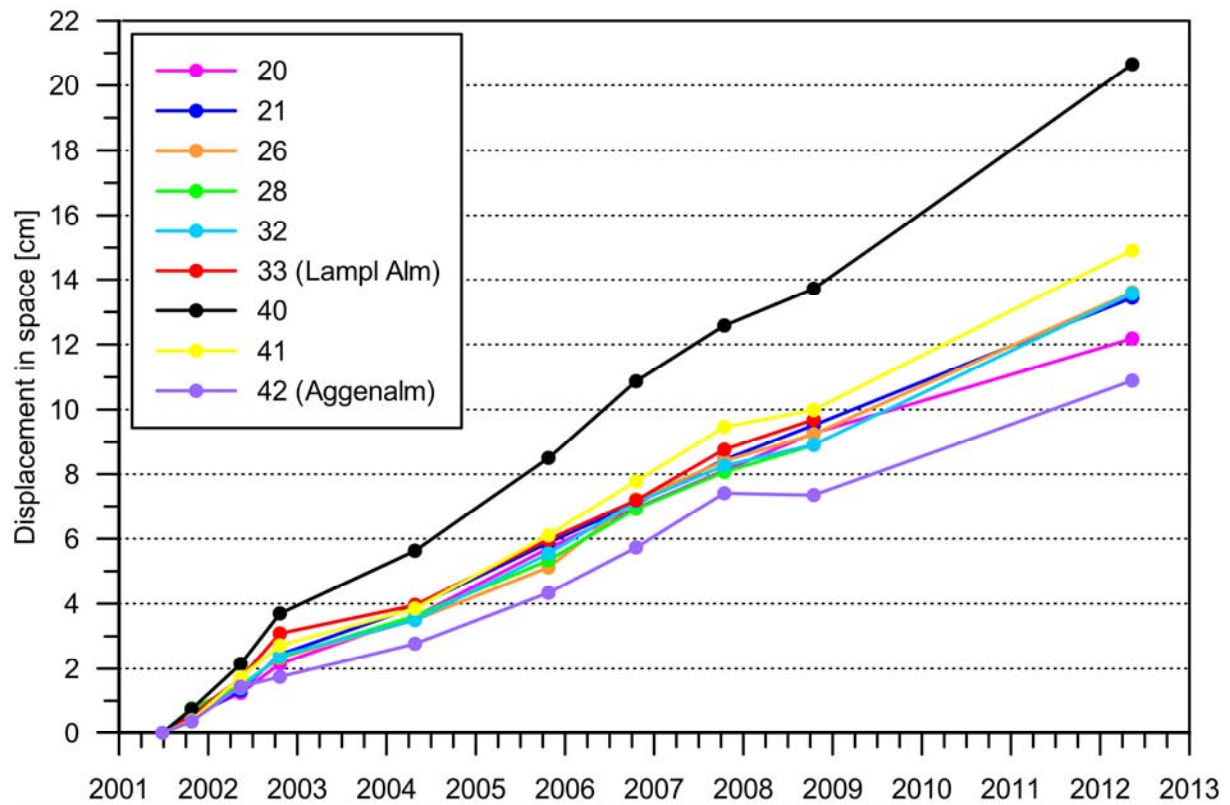


Figure III-2: Development of displacement in space for selected measuring points of the geodetic survey conducted by the LfU (adapted from GALLEMANN 2012: 6, Fig. 5).

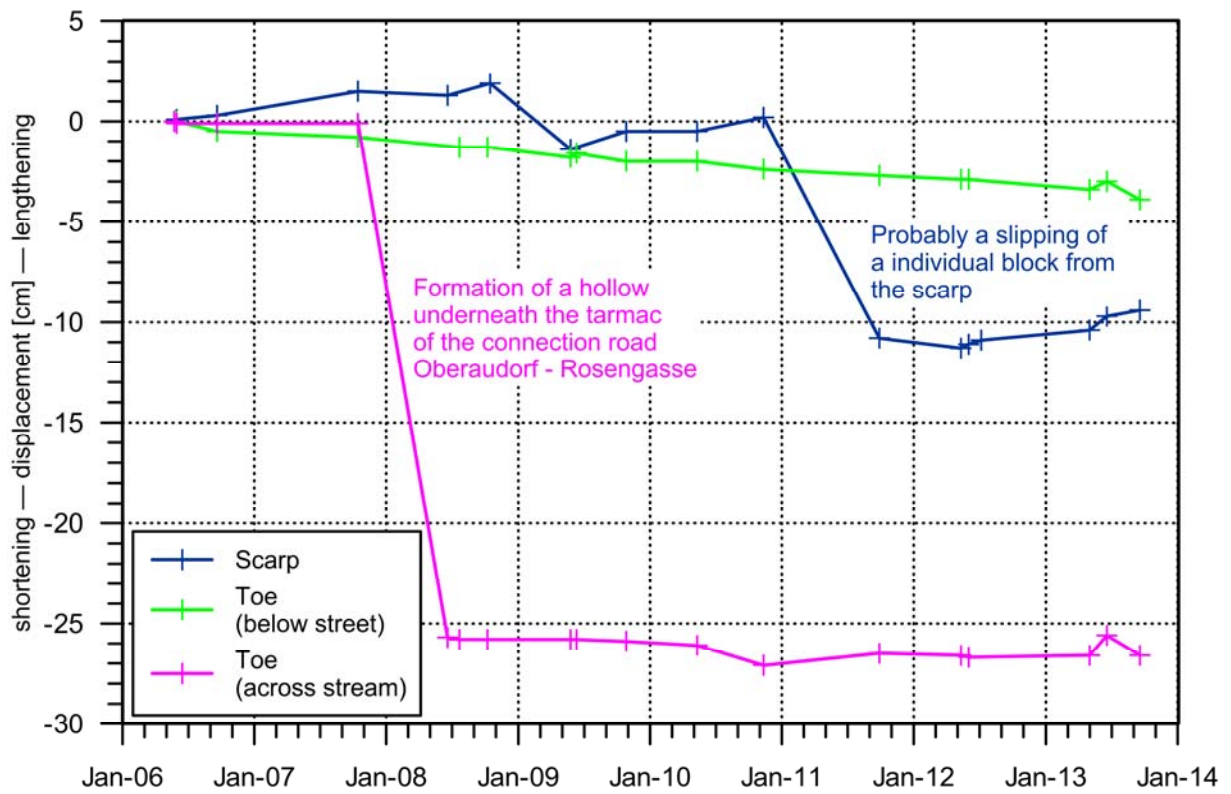


Figure III-3: Displacement of the extensometer at the scarp and toe of the Aggenalm landslide (adapted from GALLEMANN 2012: 8, Fig. 6)

Appendix IV:

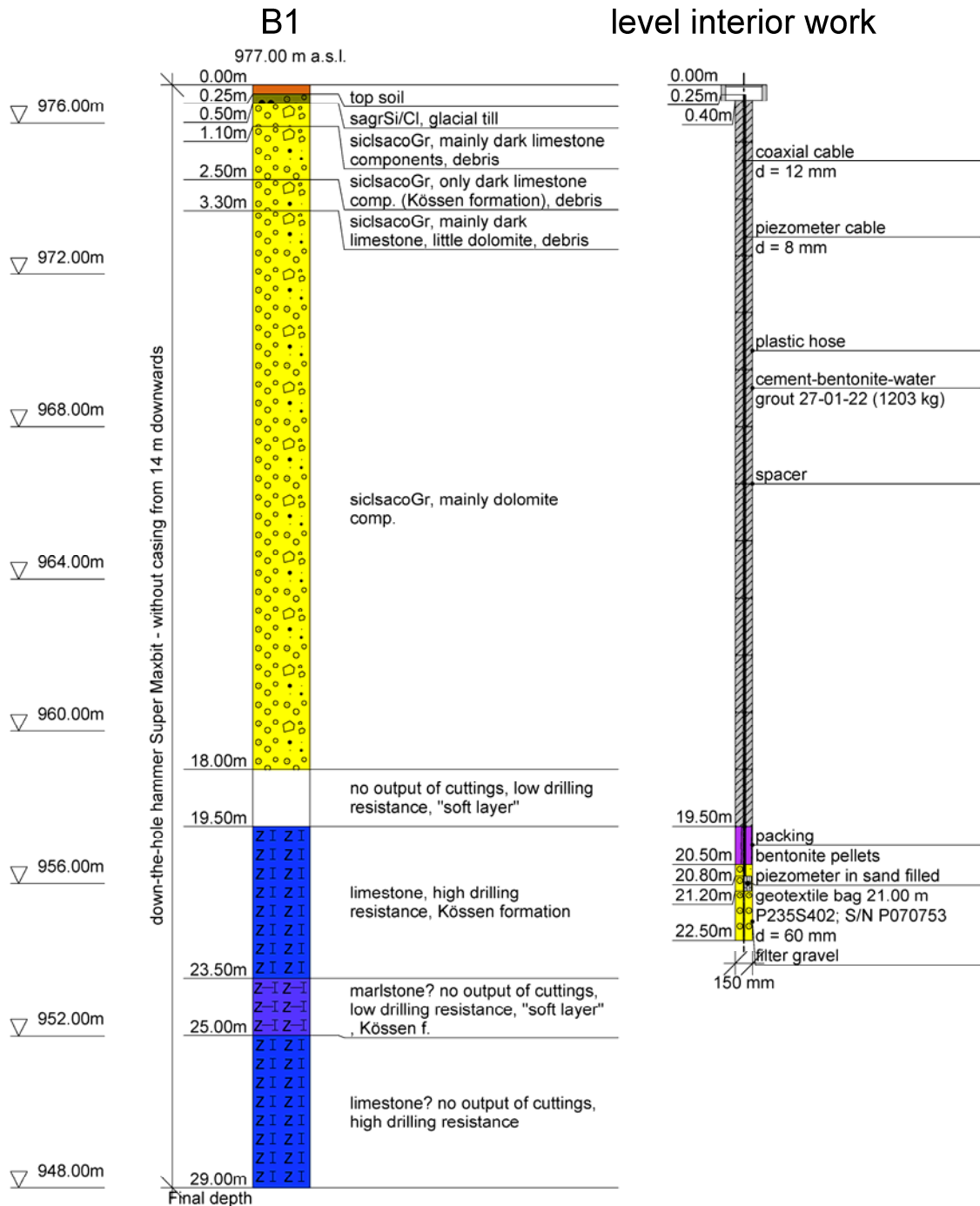
Boring logs and installation setup

Appendix IV displays the boring logs of all seven boring sites. Only at KB1 a core boring was performed but had to be abandoned due to mechanical problems. At all the other sites (B1–B6) a rotating rock drilling method with an reverse air-flushing was used and only the ejected rock chips at an approximated depth were documented. The installation setup for either TDR, inclinometer, piezometer, or any combination of these is pictured next to the boring logs. Additionally, the photographs of the coring of KB1 are pictured as well, following the boring log of KB1.



Boring log
DIN 4023

Project: alpEWAS - Aggenalm landslide	
Drill hole: B1	Date: 3/22/2009
Coordinates: 4504726 / 5280884	Scale: 1: 150 / 1: 50
Date(s) drilled: July 02-08, 2008	Logged by: Singer, Festl

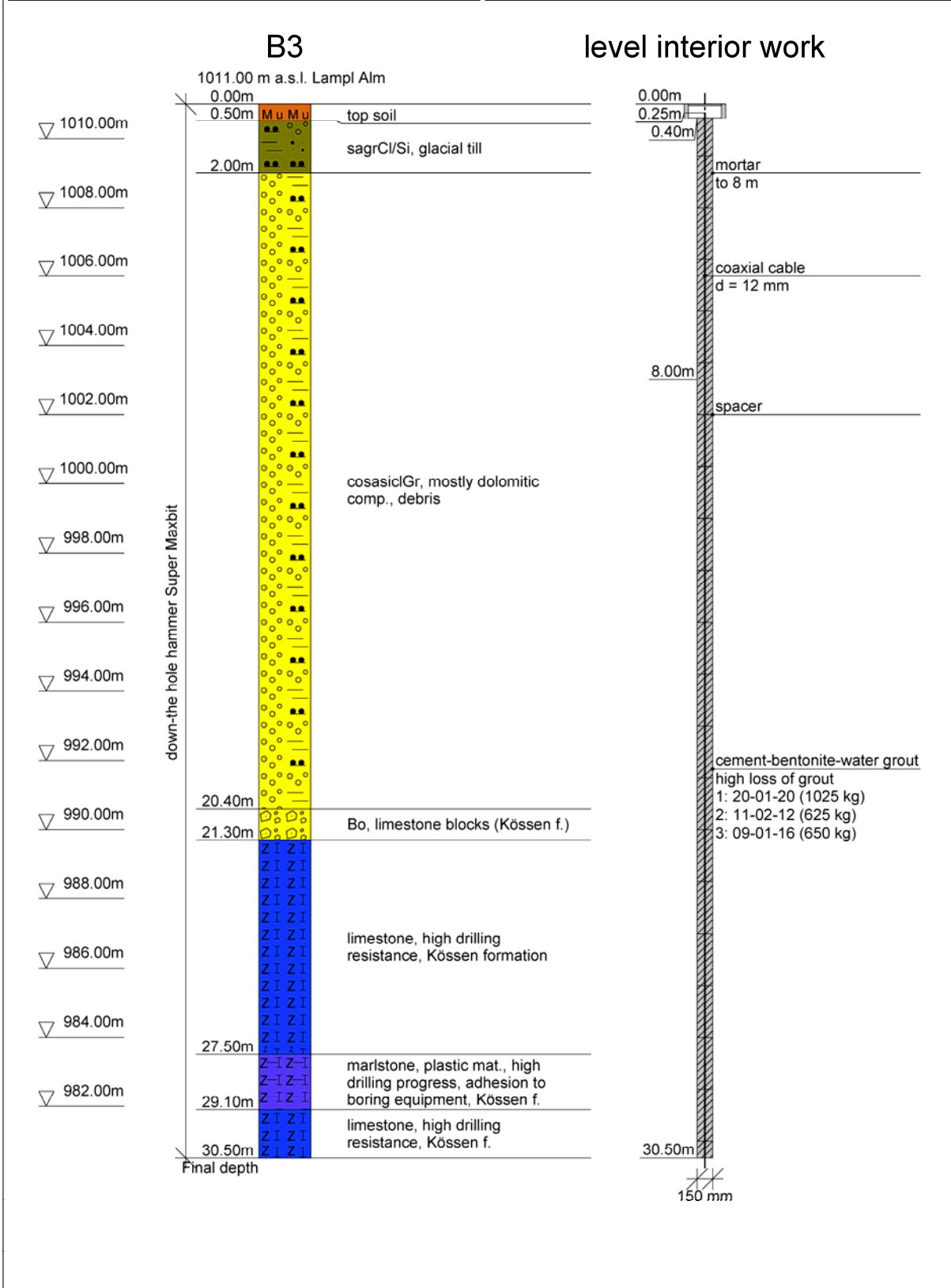


Dumping of the boring hole before installation at 22.5 m depth



Boring log
DIN 4023

Project: alpEWAS - Aggenalm landslide	
Drill hole: B3	Date: 3/22/2009
Coordinates: 4504613 / 5280913	Scale: 1: 150 / 1: 50
Date(s) drilled: July 23-28, 2008	Logged by: Singer, Festl

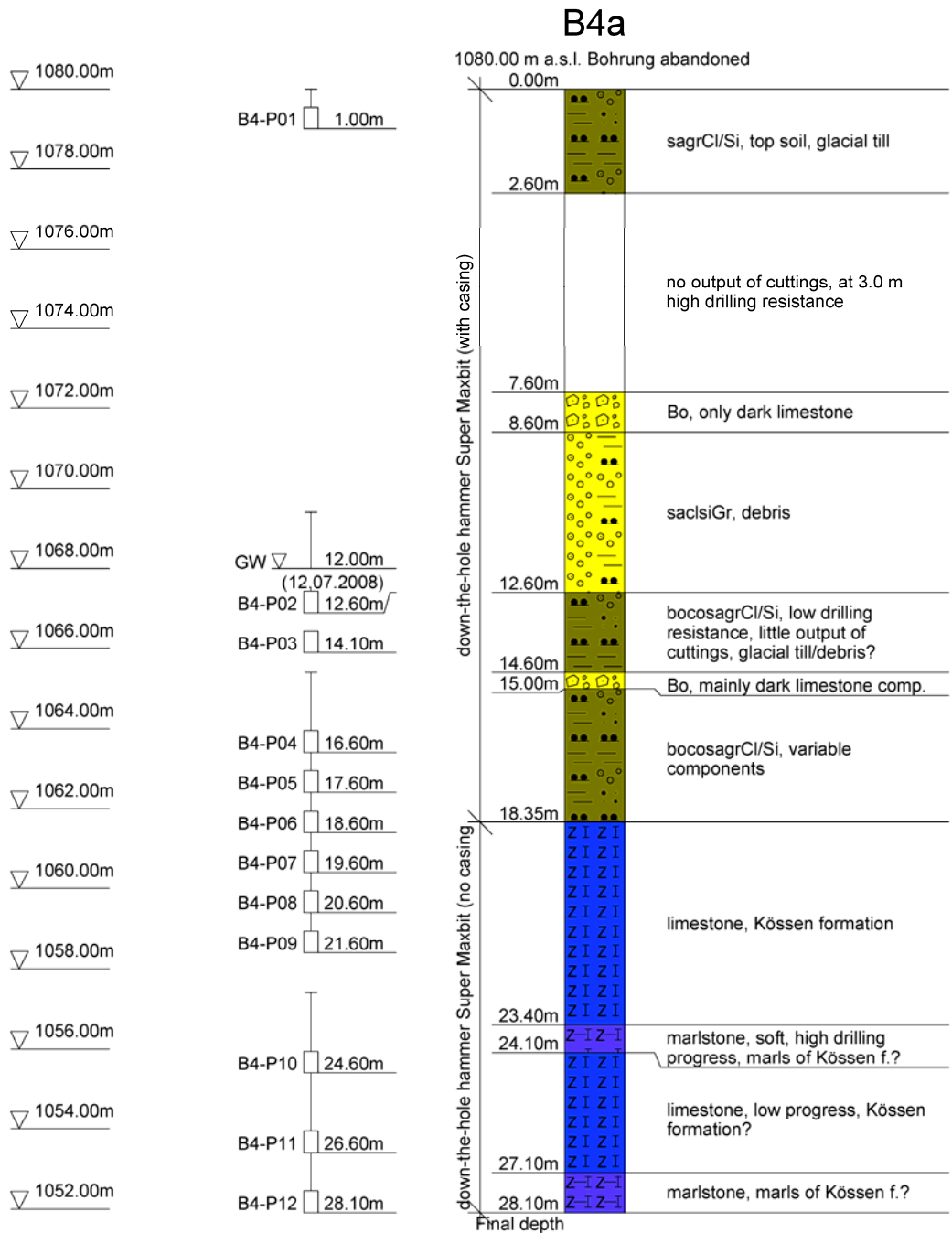




Boring log
DIN 4023

Project: alpEWAS - Aggenalm landslide

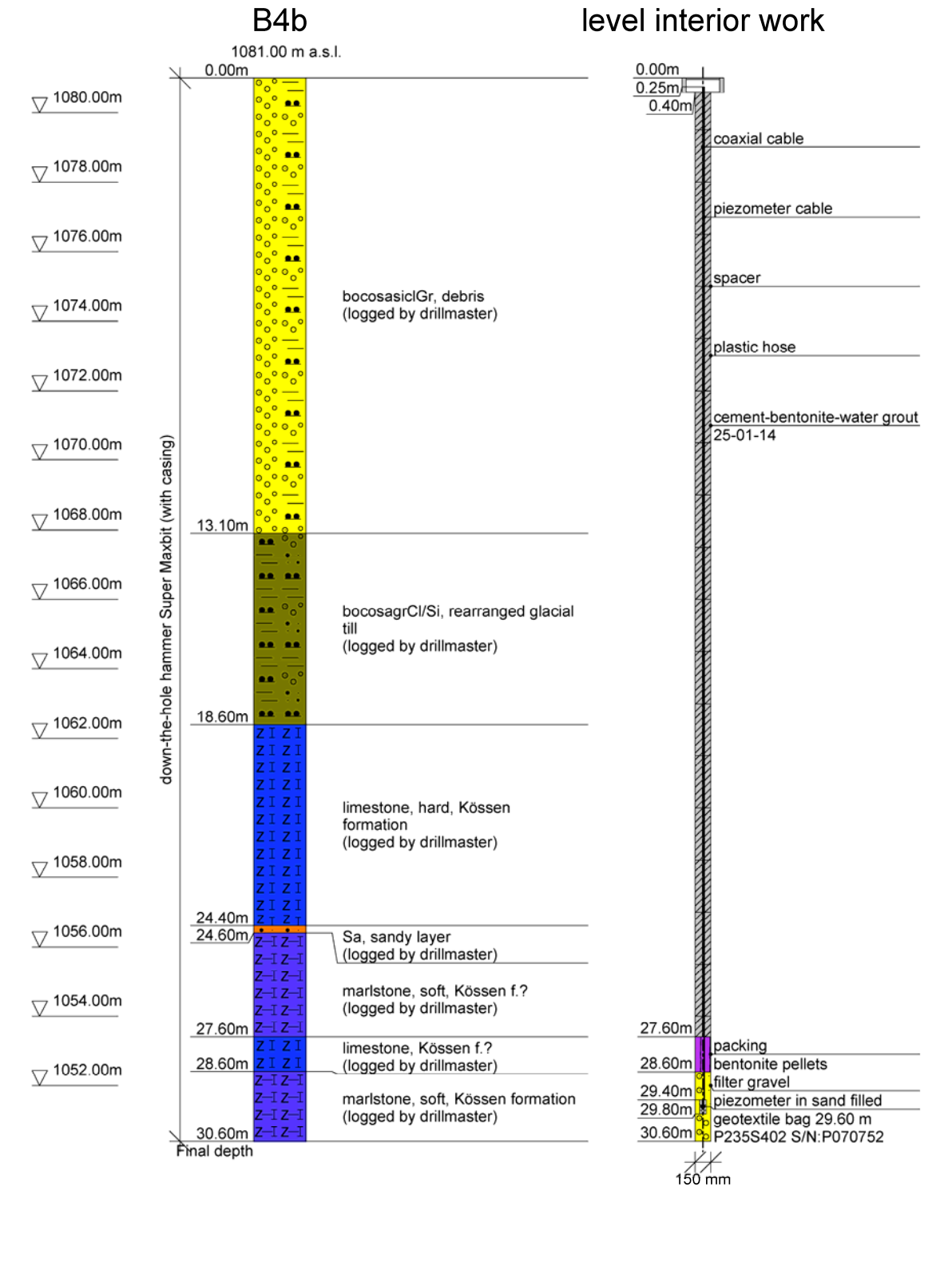
Drill hole: B4a	Date: 3/22/2009
Coordinates: 4504412 / 5280890	Scale: 1: 150
Date(s) drilled: July 12-16, 2008	Logged by: Singer, Festl





Boring log
DIN 4023

Project: alpEWAS - Aggenalm landslide	
Drill hole: B4b	Date: 3/22/2009
Coordinates: 4504411 / 5280896	Scale: 1: 150 / 1: 50
Date(s) drilled: August 5-8, 2008	Logged by: Singer, Festl





Boring log
DIN 4023

Project: alpEWAS - Aggenalm landslide

Drill hole: B5

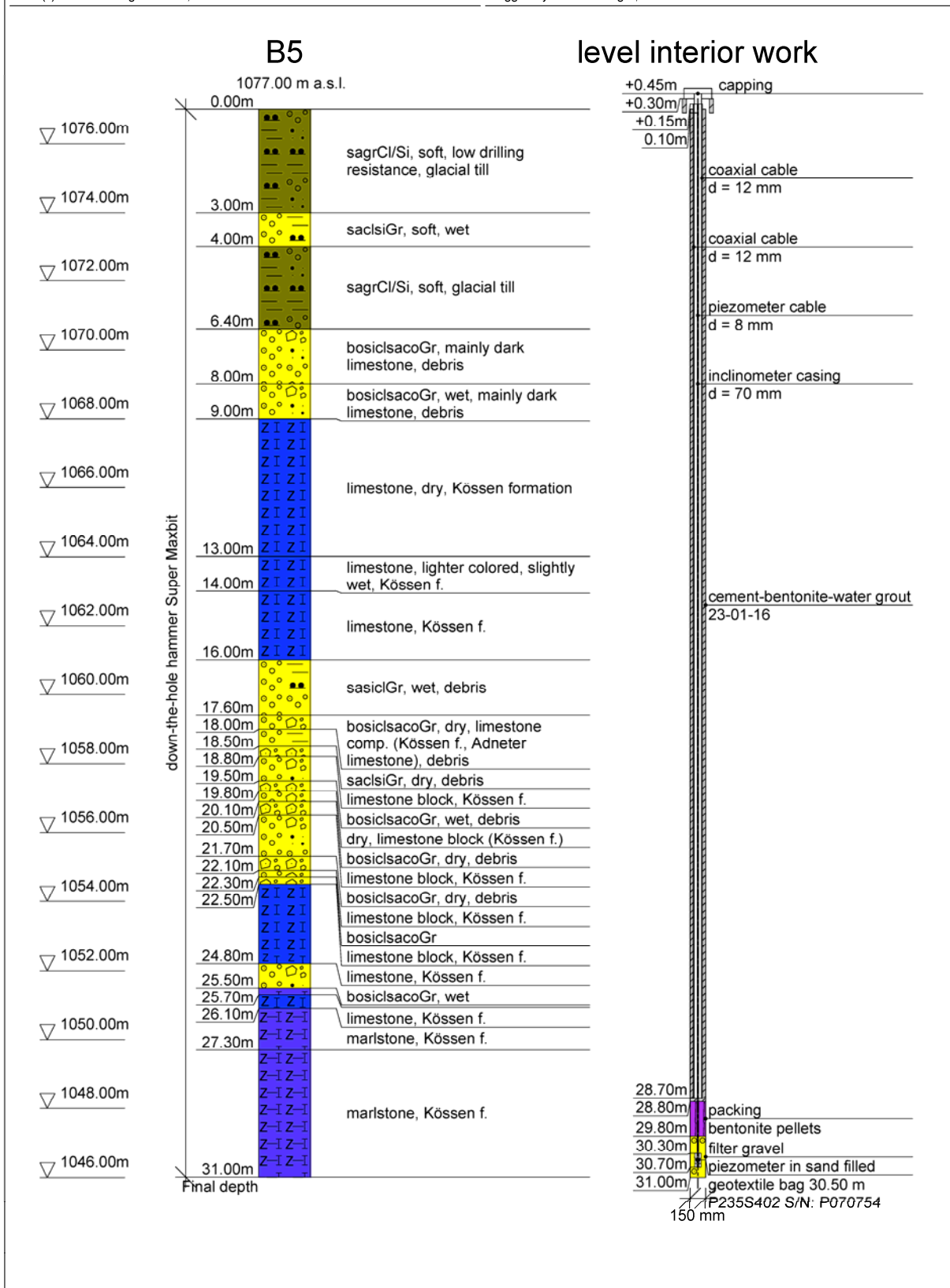
Date: 3/22/2009

Coordinates: 4504453 / 5280955

Scale: 1: 150 / 1: 50

Date(s) drilled: August 11-22, 2008

Logged by: Singer, Festl

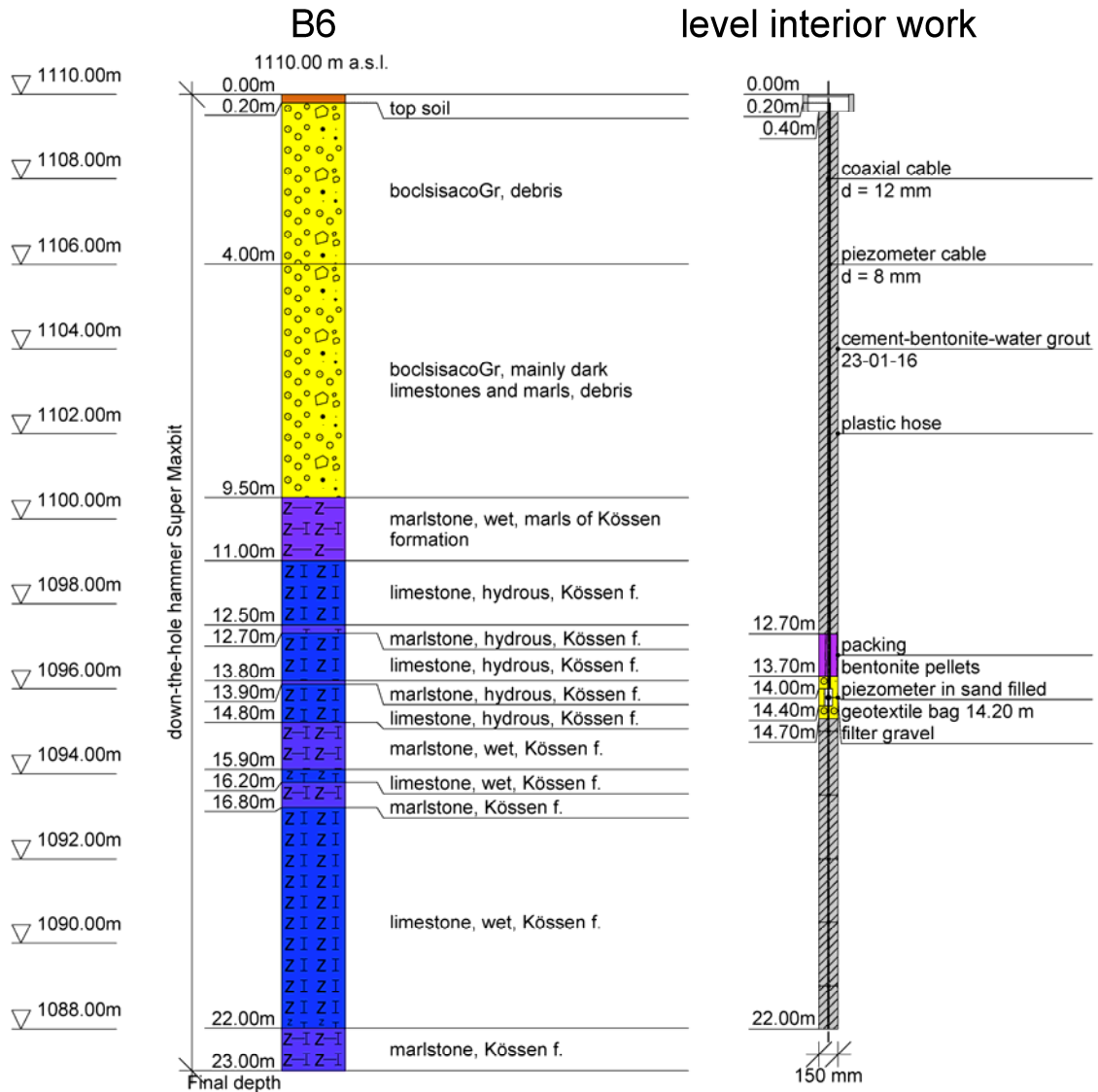




Boring log
DIN 4023

Project: alpEWAS - Aggenalm landslide

Drill hole: B6	Date: 3/22/2009
Coordinates: 4504360 / 5281088	Scale: 1: 150 / 1: 50
Date(s) drilled: August 23-25, 2008	Logged by: Singer, Festl





Boring log
DIN 4023

Project: alpEWAS - Aggenalm landslide

Drill hole: KB1

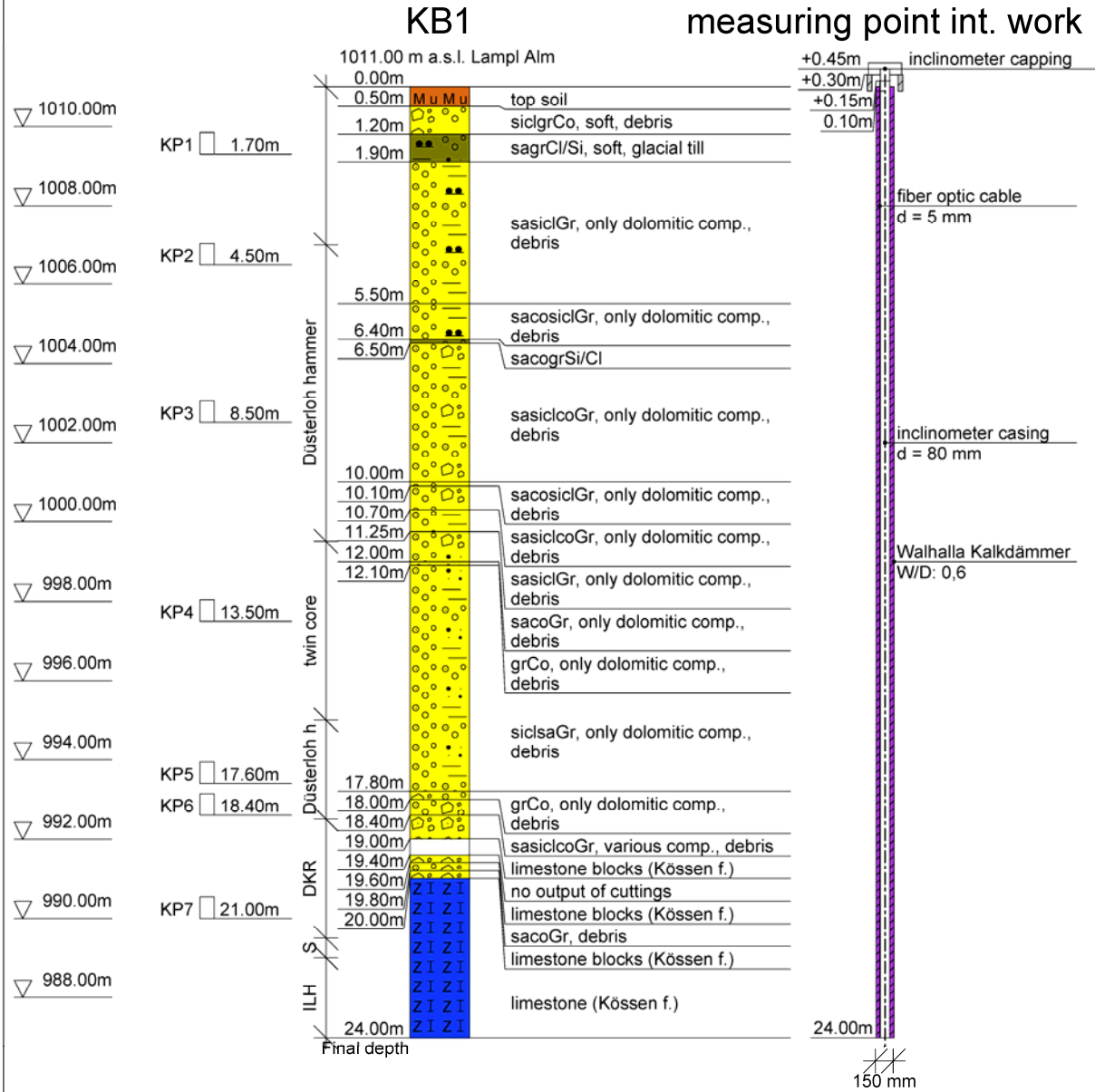
Date: 3/22/2009

Coordinates: 4504613 / 5280911

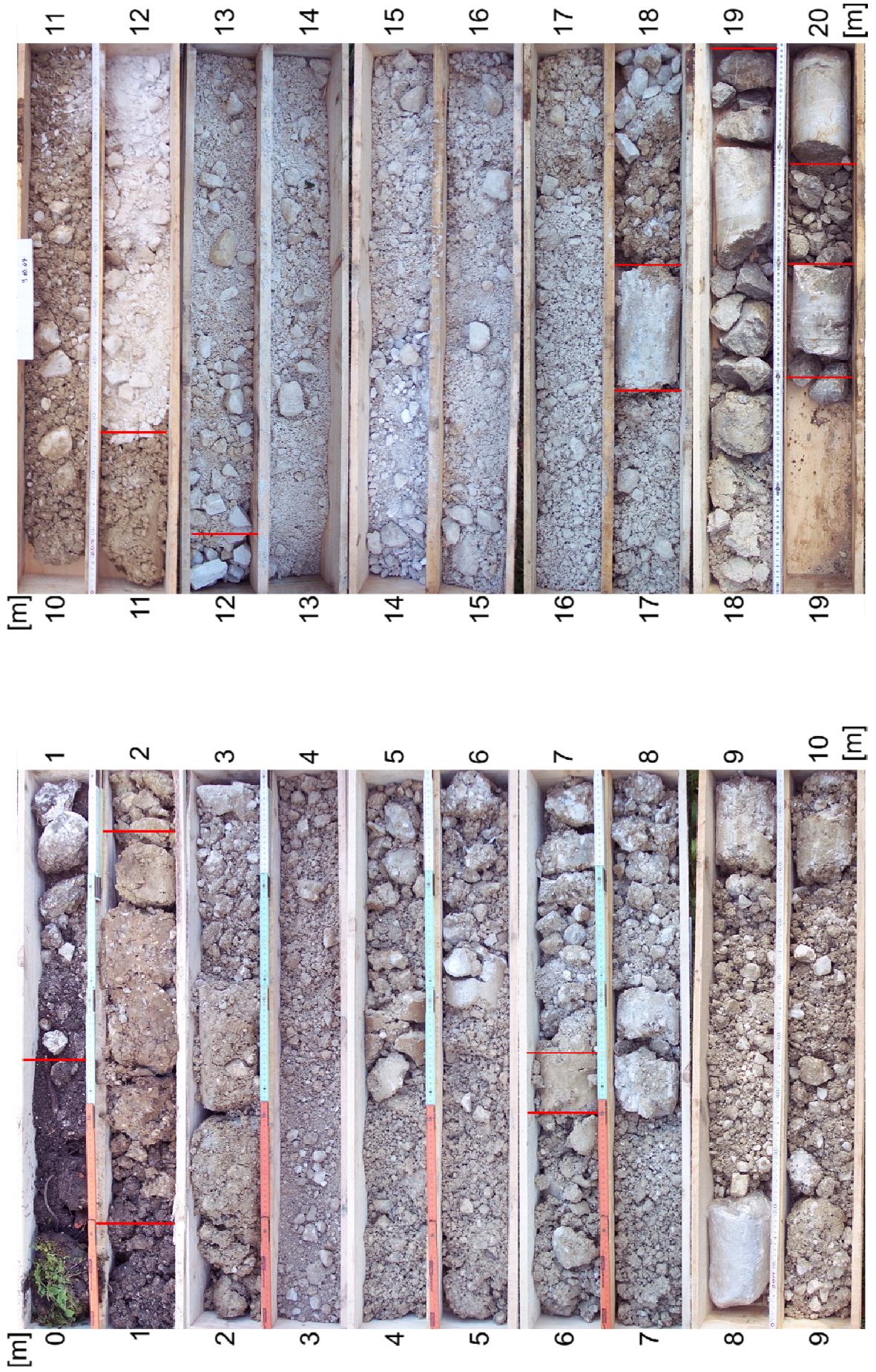
Scale: 1: 150 / 1: 50

Date(s) drilled: October 08-14, 2007

Logged by: Singer



Corings of KB1 (Drilling performed in October 2007)



Appendix V:

Goelectric survey – sections

In this Appendix the complete sections (location see Figure 24, Chapter 4.6.3) of the goelectric survey and their approximate interpretation are presented. The measuring campaign was conducted within the framework of the master's thesis by STÖRZBACH (2009). For the goelectric sounding (resistivity) a multi electrode system with electrodes at a 4 m interval (max. length of a section: 400 m) based on the Schlumberger array was used. Due to the distinct topography and steepness of major parts of the Aggenalm landslide a topographic correction was introduced to the data analysis.

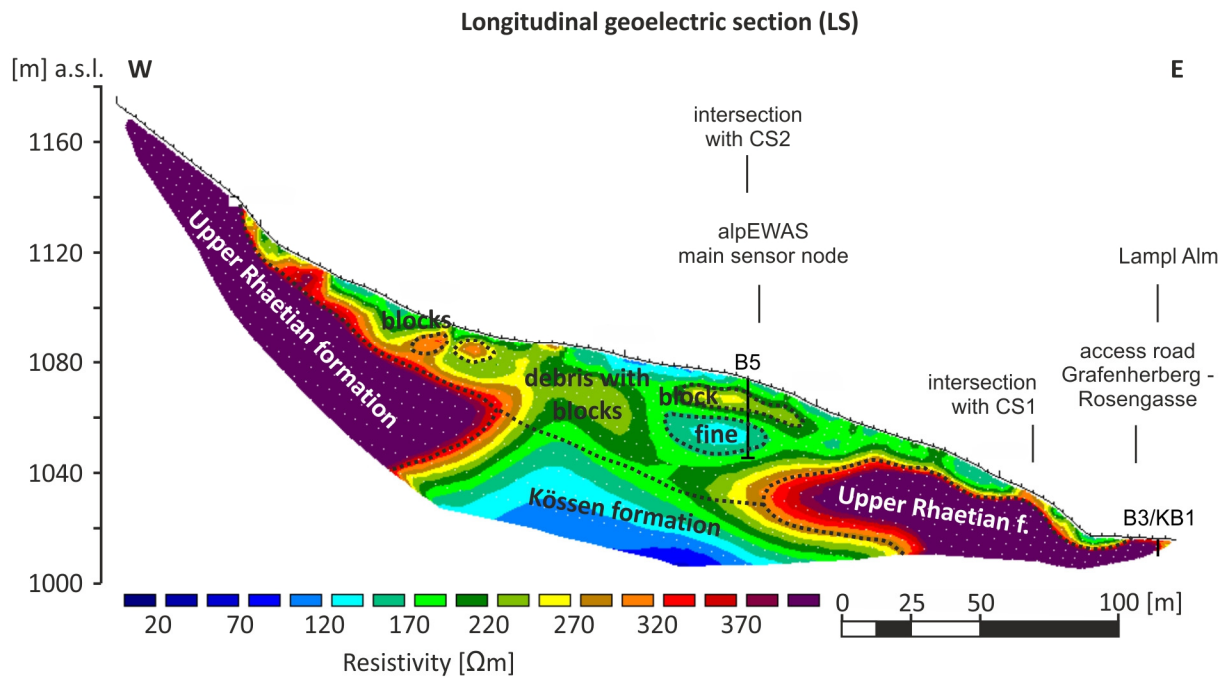


Figure V-1: Longitudinal goelectric section (LS) adapted from STÖRZBACH (2009: 32, Fig. 20).

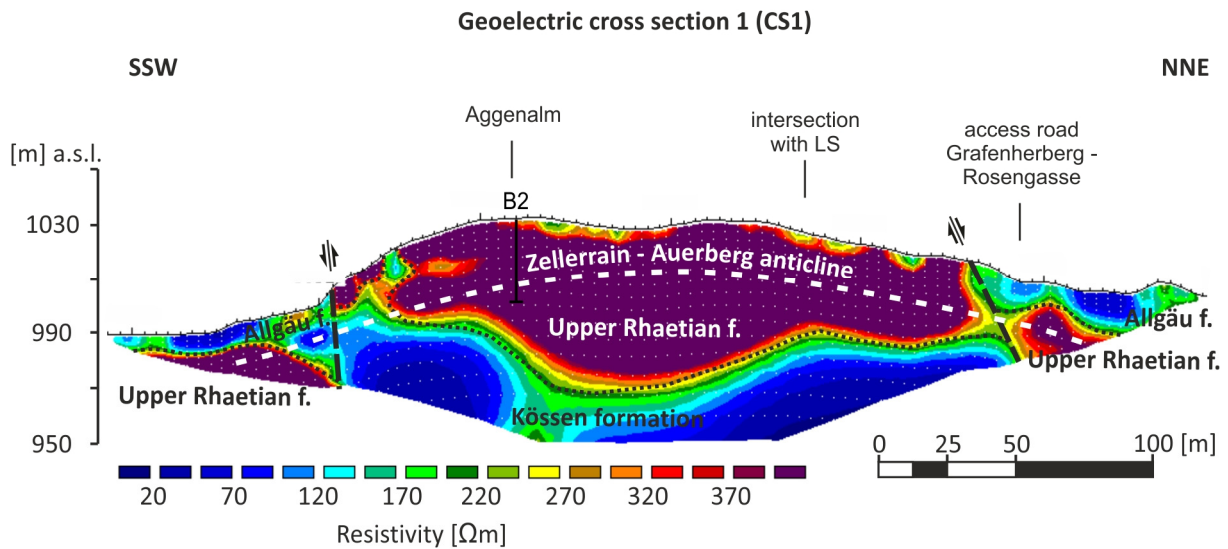


Figure V-2: Goelectric cross section (CS1) adapted from STÖRZBACH (2009: 35, Fig. 22).

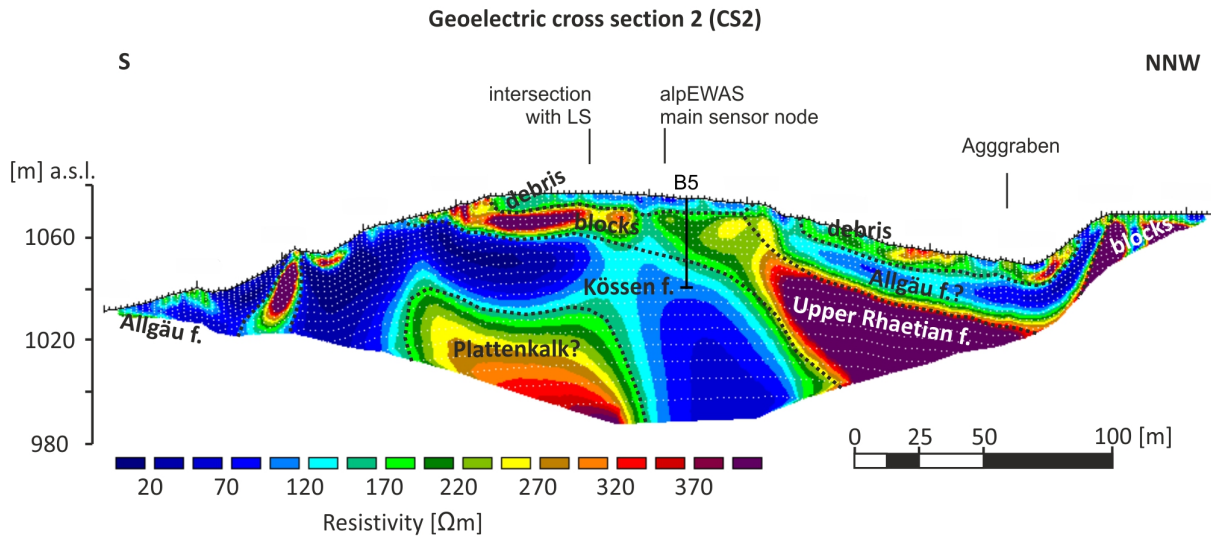


Figure V-3: Geoelectric cross section (CS2) adapted from STÖRZBACH (2009: 38, Fig. 24).

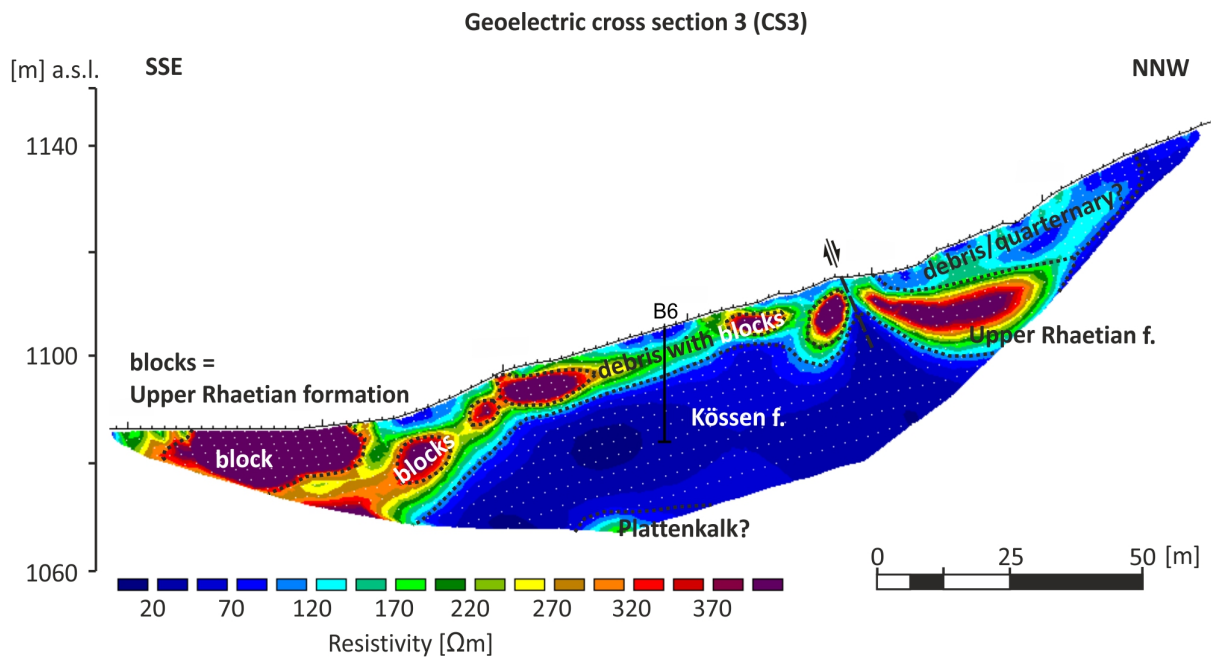


Figure V-4: Geoelectric cross section (CS3) adapted from STÖRZBACH (2009: 42, Fig. 27).

Appendix VI:

Results of inclinometer measurements – plots

In this Appendix several plots depict the results of the inclinometer measurements. At the beginning of the alpEWAS project, once the grouting had hardened sufficiently after installation of the inclinometer casings, a reference reading was taken for both sites on October 14, 2008. This was about one and a half months after installation for B5 and about one year for KB1. A new reference reading was taken on July 16, 2009, since the site at B5 had to be reconstructed and the casing was therefore shortened by approximately half a meter. Additionally, all further measurements were conducted using a new inclinometer probe (marked “TU”), thus all further measurements at KB1 and B5 are referenced to the new reference reading, in order to eliminate probe-specific errors. Using the two reference readings vice versa has been tested and showed only small differences between two readings taken at the same day with the two different probes – within the system’s noise.

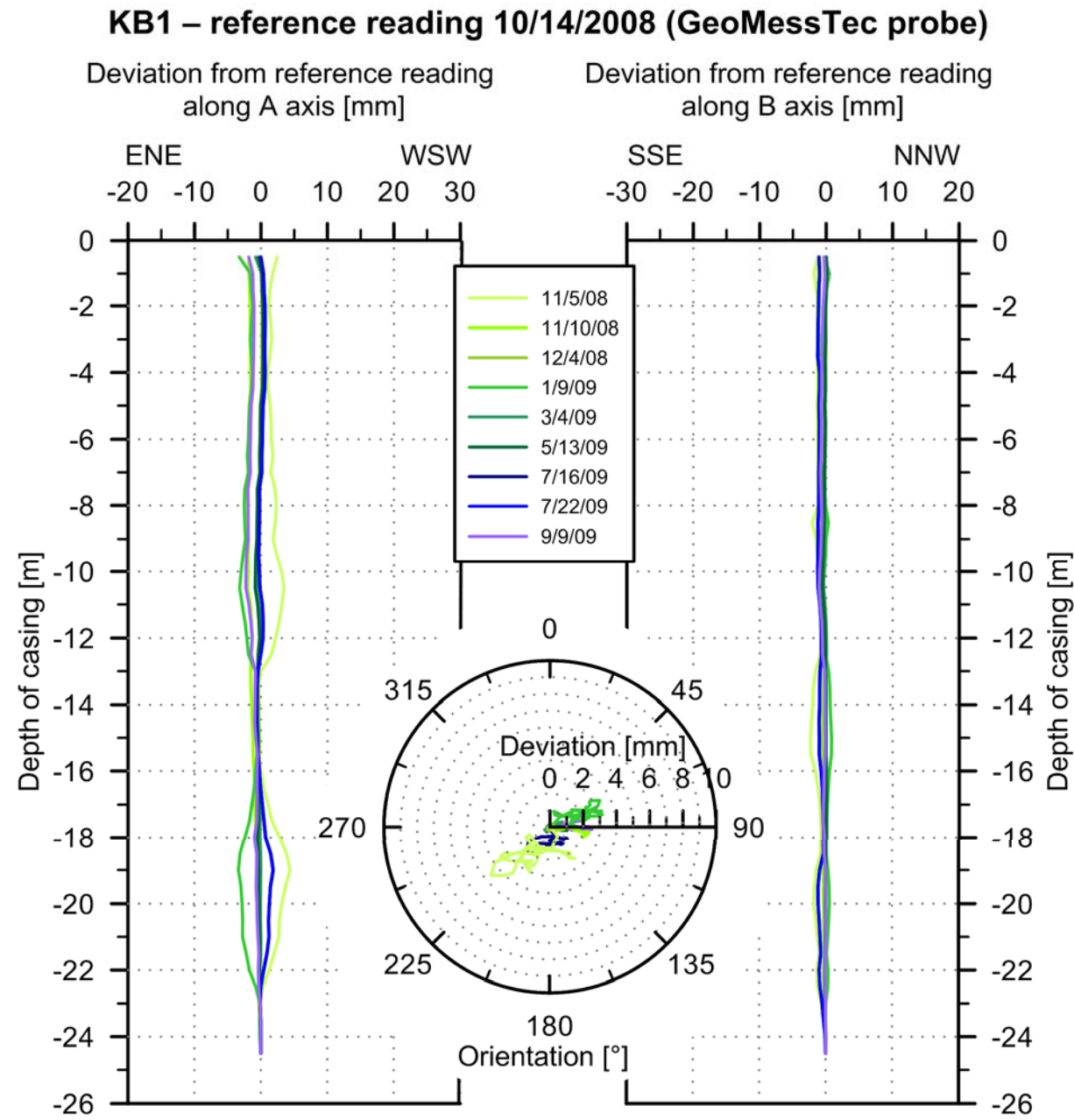


Figure VI-1: Results of the inclinometer measurements in borehole KB1. For all consecutive readings, starting with the reference reading on October 14, 2008, a SISGEO probe was used. The graphic on the left shows the results parallel the A axis, on the right along the B axis over the complete length of the borehole (depth 24.5 m). In the middle, a polar plot depicts the change in orientation over the measurement length.

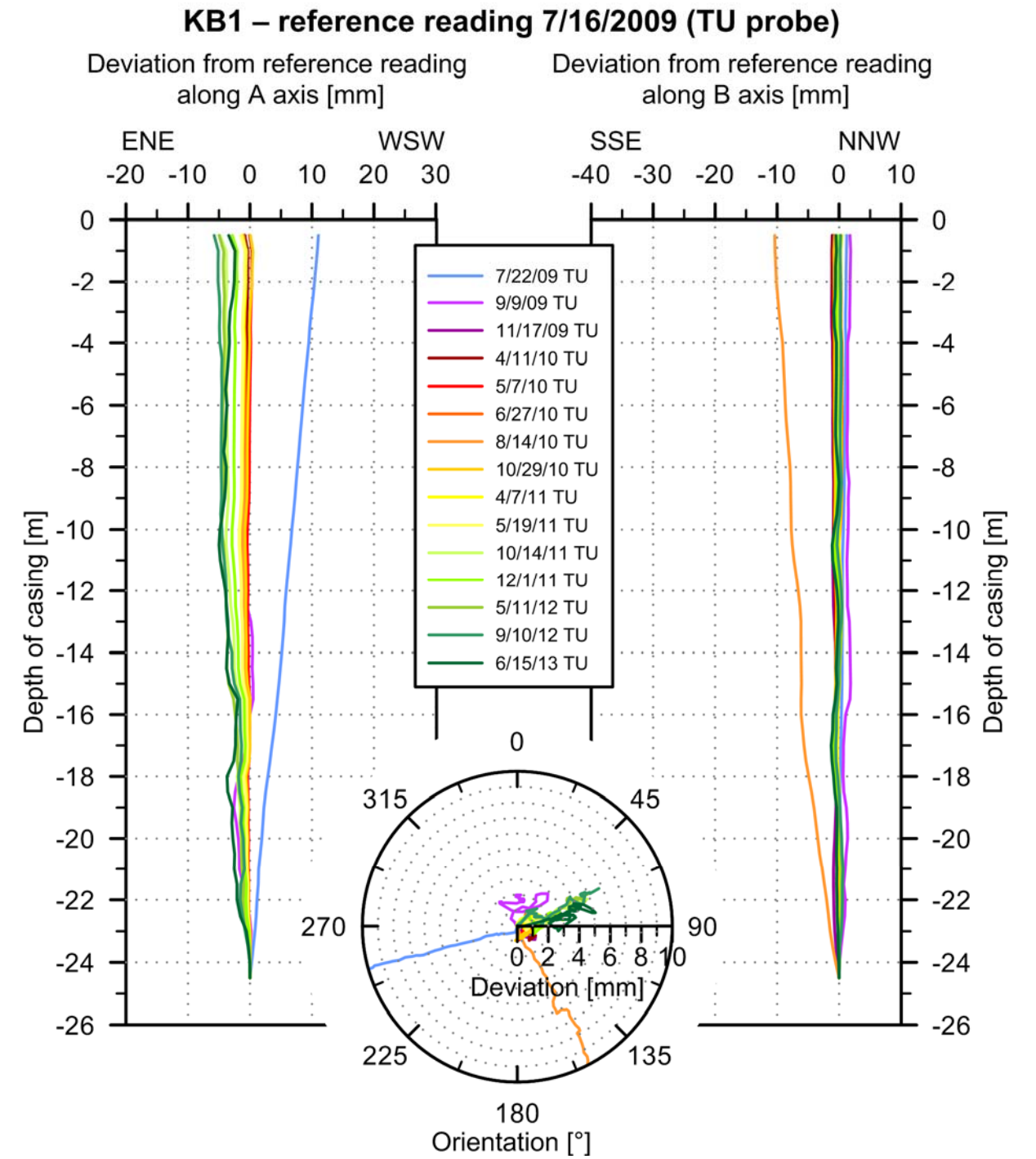


Figure VI-2: Results of the inclinometer measurements in borehole KB1. For all consecutive readings, starting with the reference reading on July 16, 2009, the TU probe was used. The graphic on the left shows the results parallel the A axis, on the right along the B axis over the complete length of the borehole (depth 24.5 m). In the middle, a polar plot depicts the change in orientation over the measurement length. At two of the measurements (7/22/2009 and 8/14/2010) errors occurred during measurements.

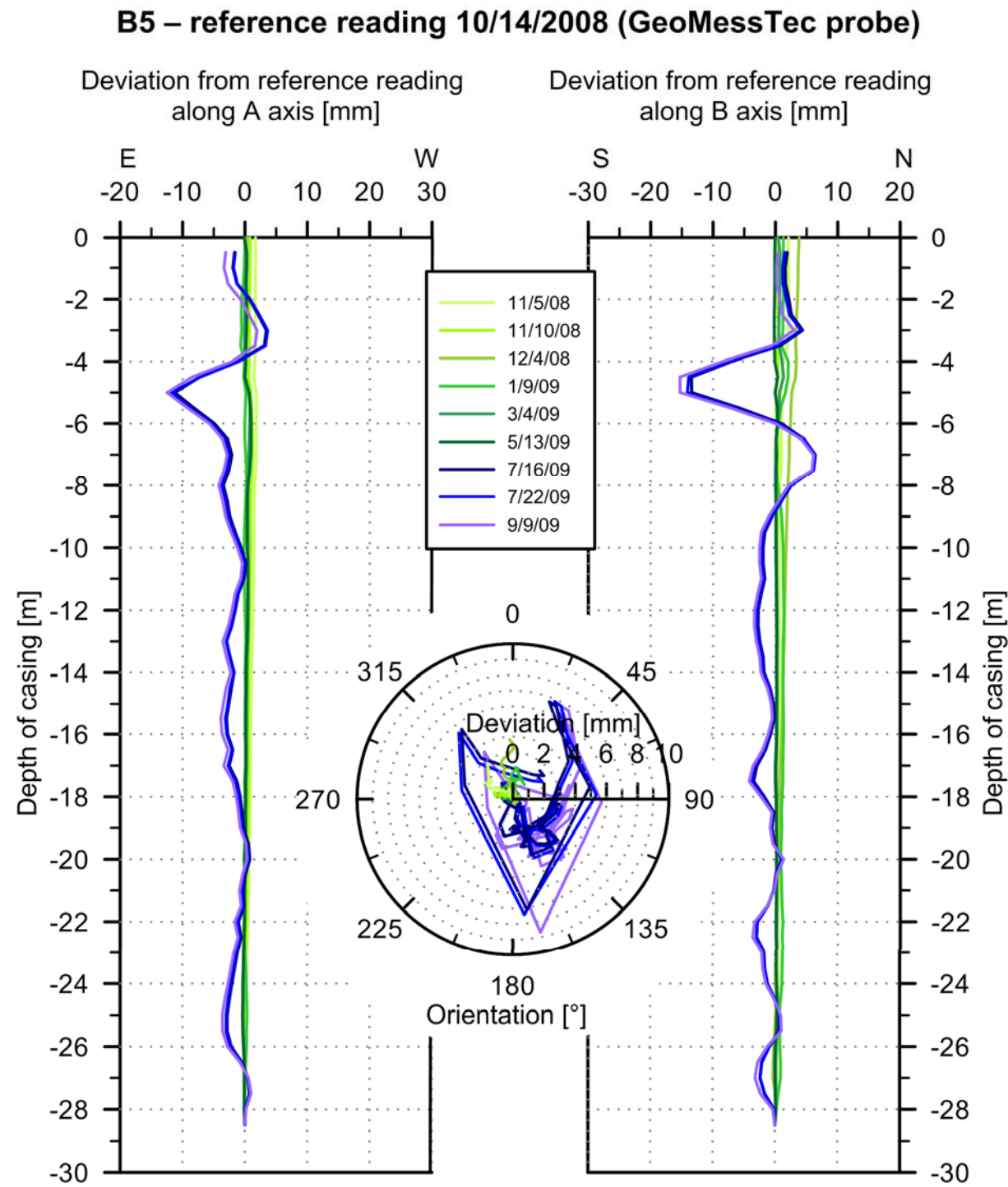


Figure VI-3: Results of the inclinometer measurements in borehole B5. For all consecutive readings, starting with the reference reading on October 14, 2008, a SISGEO probe (marked “GeoMessTec”) was used. The graphic on the left shows the results parallel the A axis, on the right along the B axis over the complete length of the borehole (depth 29 m/28.5 m from July 2009 onwards). In the middle, a polar plot depicts the change in orientation over the measurement length. After shortening the inclinometer casing by approximately 0.5 m during reconstruction in the beginning of July 2009 a deformation of up to 10-15 mm, especially at a depth of -5.0 m, can be seen, which has to be mostly attributed to said reconstruction. In comparison, no deformation can be seen in the inclinometer measurements in KB1 at this time (Figure VI-1).

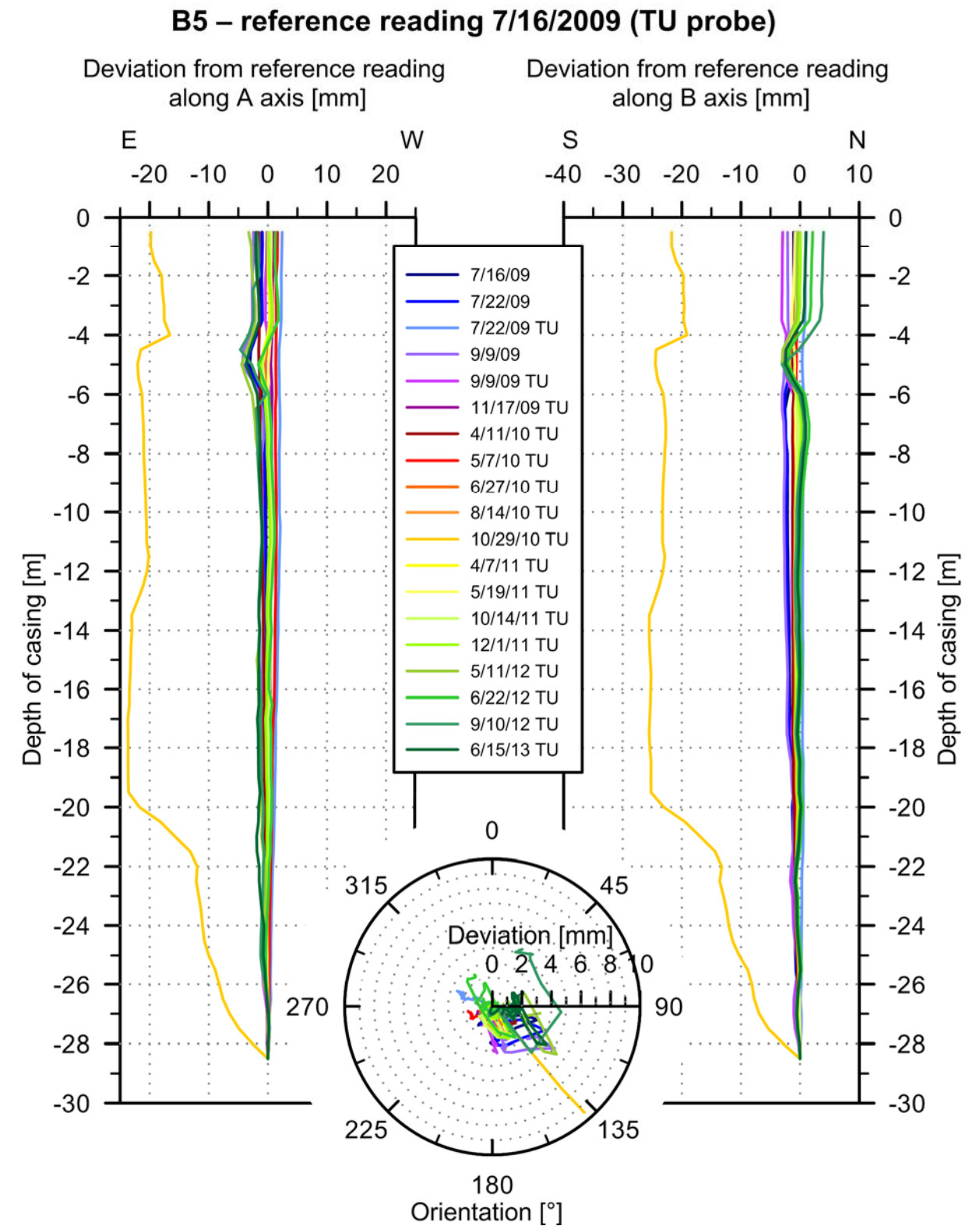


Figure VI-4: Results of the inclinometer measurements in borehole B5. For all consecutive readings, starting with the reference reading on July 16, 2009, the TU probe was used (all measurements after reconstruction). The graphic on the left shows the results parallel the A axis, on the right along the B axis over the complete length of the borehole (depth 28.5 m). In the middle, a polar plot depicts the change in orientation over the measurement length. On October 29, 2010 an erroneous measurement was taken.

Appendix VII:

TSA – time series analysis, programming code

This Appendix contains the programming code for the time series analysis (TSA) of the alpEWAS GSN's monitoring data generated with MATLAB by MathWorks. It is divided into several parts. In the first part, the data files (GNSS, piezometer, and weather data) are loaded into the program. Outliers and faulty data are removed, the data sets are filtered and smoothed, and various alterations are calculated, e.g., building 6-, 12-, 24-hour rainfall sums, summation curves, and relative pore pressure change (differenced pore pressure). In part II the prepared data sets, whether altered (smoothed, filtered, etc.) or original, are cut to a time period that can then be loaded into the tstool-toolbox. With the toolbox, the data sets are plotted and auto- and crosscorrelations are calculated. The third part contains several functions that have been specifically written for this analysis.

Time Series analysis – MATLAB programming code

Part 1: Import of data, conversion to MATLAB

Written by Judith Festl, Christoph Reith, and Stefan Schubbäck in course of the alpEWAS project, last revised July 2013

%% Import of GPS/GNSS, rainfall and piezometric data from the individual excel-files, %% formatting and filtering of data sets

```
clc; clear all; close all;
path([cd '\02 Funktionen'], path);
% Path to folder containing all functions written for this analysis is set. The newly written functions
% are attached in Part III. Functions provided by MathWorks in their function pool are not printed
% here. All other files, including excel-files need to be in the superior folder.
```

% Setting of „zero“ date

```
t0 = datenum('01-Jan-2009 00:00:00',0);
% The time/date is converted to a MATLAB-time, measured in seconds for all following calculations,
% starting with zero on January 1, 2009 at 00:00:00.
```

% Import of GPS data from station 1 (above scarp of Agggraben debris flow)

```
filename_P1=fullfile(cd,'\GPS_Berg_09-11.xlsx');
Daten1=GPS_in(filename_P1);
Daten_P1=Daten1;
Speicher.Punktnummer='GPS';
% Content of each column in the excel-file:
%      x No      x Date x Time
%      1 Time (text format)  2 Easting (raw data)  3 Easting (filtered)  4 Easting (trend)
%      6 Northing (raw data)  7 Northing (filtered)  8 Northing (trend)  10 Height (raw data)
%      11 Height (filtered)  12 Height (trend)
% ONLY the raw data will be used. The raw data will be filtered and sampled in this code.
```

% Deletion of blanks

```
f1=find(Daten_P1(:,2)~=0 & Daten_P1(:,5)~=0 & Daten_P1(:,8)~=0);
Daten_P1=Daten_P1(f1,:);
```

% Finding time doublets (to be deleted - not averaged)

```
f2= Daten_P1(2:end,1)-Daten_P1(1:end-1,1) ~=0;
Daten_P1=Daten_P1(f2,:);
```

% Date/Time conversion to zero date: 01-Jan-2009 00:00:00

```
f3=find(Daten_P1(:,1)>=t0);
Daten_P1=Daten_P1(f3,:);
t_P1=Daten_P1(:,1); R_P1=Daten_P1(:,2); H_P1=Daten_P1(:,6); h_P1=Daten_P1(:,10);
% if applying conversion to pre-filtered data → change columns from 2, 6, and 10 to 3, 7, and 11.
tt_P1=(t_P1-t0)*86400;
```

% Filtering of GNSS 1

% Deletion of outliers

```
[t_R_P1,R2_P1]=gM_Schwellenfilter(R_P1,tt_P1);
[t_H_P1,H2_P1]=gM_Schwellenfilter(H_P1,tt_P1);
[t_h_P1,h2_P1]=gM_Schwellenfilter(h_P1,tt_P1);
```

% Moving Average of P1

```
[t_R2_P1,R3_P1]=gleitendes_Mittel(t_R_P1,R2_P1,100);           % 100, corresponds to approx. 1 day
[t_H2_P1,H3_P1]=gleitendes_Mittel(t_H_P1,H2_P1,100);
[t_h2_P1,h3_P1]=gleitendes_Mittel(t_h_P1,h2_P1,100);
```

% Detrending

```
R4_P1=detrend(R3_P1);
H4_P1=detrend(H3_P1);
h4_P1=detrend(h3_P1);
```

% Deletion of time doublets (no averaging)

```
[t_R3_P1,R5_P1]=DuplettenLoeschen(t_R2_P1,R4_P1);
[t_H3_P1,H5_P1]=DuplettenLoeschen(t_H2_P1,H4_P1);
[t_h3_P1,h5_P1]=DuplettenLoeschen(t_h2_P1,h4_P1);
```

% Transformation in timeseries-objects

```
RechtswertGPS_P1=timeseries(R5_P1,t_R3_P1);
HochwertGPS_P1=timeseries(H5_P1,t_H3_P1);
HoeheGPS_P1=timeseries(h5_P1,t_h3_P1);
```

% Import of GPS data from station 2 (at main sensor node)

```
filename_P2=fullfile(cd,'\GPS_Mittelstation_09-11.xlsx');
Daten2=GPS_in(filename_P2);
Daten_P2=Daten2;
Speicher.Punktnummer='GPS';
f4=find(Daten_P2(:,2)~=0 & Daten_P2(:,5)~=0 & Daten_P2(:,8)~=0);
Daten_P2=Daten_P2(f4,:);
f5= Daten_P2(2:end,1)-Daten_P2(1:end-1,1) ~=0;
Daten_P2=Daten_P2(f5,:);
f6=find(Daten_P2(:,1)>=t0);
Daten_P2=Daten_P2(f6,:);
t_P2=Daten_P2(:,1); R_P2=Daten_P2(:,2); H_P2=Daten_P2(:,6); h_P2=Daten_P2(:,10);
tt_P2=(t_P2-t0)*86400;
[t_R_P2,R2_P2]=gM_Schwellenfilter(R_P2,tt_P2);
[t_H_P2,H2_P2]=gM_Schwellenfilter(H_P2,tt_P2);
[t_h_P2,h2_P2]=gM_Schwellenfilter(h_P2,tt_P2);
[t_R2_P2,R3_P2]=gleitendes_Mittel(t_R_P2,R2_P2,100);
[t_H2_P2,H3_P2]=gleitendes_Mittel(t_H_P2,H2_P2,100);
[t_h2_P2,h3_P2]=gleitendes_Mittel(t_h_P2,h2_P2,100);
R4_P2=detrend(R3_P2);
H4_P2=detrend(H3_P2);
h4_P2=detrend(h3_P2);
[t_R3_P2,R5_P2]=DuplettenLoeschen(t_R2_P2,R4_P2);
[t_H3_P2,H5_P2]=DuplettenLoeschen(t_H2_P2,H4_P2);
[t_h3_P2,h5_P2]=DuplettenLoeschen(t_h2_P2,h4_P2);
RechtswertGPS_P2=timeseries(R5_P2,t_R3_P2);
HochwertGPS_P2=timeseries(H5_P2,t_H3_P2);
HoeheGPS_P2=timeseries(h5_P2,t_h3_P2);
```

% Import of GPS data from station 3 (at Lampl Alm)

```

filename_P3=fullfile(cd,'\GPS_Lampl-Alm_09-11.xlsx');
Daten3=GPS_in(filename_P3);
Daten_P3=Daten3;
Speicher.Punktnummer='GPS';
f7=find(Daten_P3(:,2)~=0 & Daten_P3(:,5)~=0 & Daten_P3(:,8)~=0);
Daten_P3=Daten_P3(f7,:);
f8= Daten_P3(2:end,1)-Daten_P3(1:end-1,1) ~=0;
Daten_P3=Daten_P3(f8,:);
f9=find(Daten_P3(:,1)>=t0);
Daten_P3=Daten_P3(f9,:);
t_P3=Daten_P3(:,1); R_P3=Daten_P3(:,2); H_P3=Daten_P3(:,6); h_P3=Daten_P3(:,10);
tt_P3=(t_P3-t0)*86400;
[t_R_P3,R2_P3]=gM_Schwellenfilter(R_P3,tt_P3);
[t_H_P3,H2_P3]=gM_Schwellenfilter(H_P3,tt_P3);
[t_h_P3,h2_P3]=gM_Schwellenfilter(h_P3,tt_P3);
[t_R2_P3,R3_P3]=gleitendes_Mittel(t_R_P3,R2_P3,100);
[t_H2_P3,H3_P3]=gleitendes_Mittel(t_H_P3,H2_P3,100);
[t_h2_P3,h3_P3]=gleitendes_Mittel(t_h_P3,h2_P3,100);
R4_P3=detrend(R3_P3);
H4_P3=detrend(H3_P3);
h4_P3=detrend(h3_P3);
[t_R3_P3,R5_P3]=DuplettenLoeschen(t_R2_P3,R4_P3);
[t_H3_P3,H5_P3]=DuplettenLoeschen(t_H2_P3,H4_P3);
[t_h3_P3,h5_P3]=DuplettenLoeschen(t_h2_P3,h4_P3);
RechtswertGPS_P3=timeseries(R5_P3,t_R3_P3);
HochwertGPS_P3=timeseries(H5_P3,t_H3_P3);
HoeheGPS_P3=timeseries(h5_P3,t_h3_P3);

```

% Import of weather and piezometer data (rainfall gauge at main sensor node, piezometer at B4)

```

filename=fullfile(cd,'\alpEWAS_Data_09-11.xlsx');
[Daten4]=Piezo_in(filename);
Daten=Daten4;
Speicher.Punktnummer='Temp';
% Content of each column in the excel-file:
%      1 Timestamp                2 Piezo (B4) – w. press. kPa      3 Piezo (B4) – smoothed kPa
%      4 Piezo (B4) – corrected kPa  5 Barometric press. mbar        6 Temp. out °C
%      7 Rainfall mm
t=Daten(:,1);
P=Daten(:,2);
Psmooth=Daten(:,3);
Pcor=Daten(:,4);
D=Daten(:,5);
T=Daten(:,6);
Rain=Daten(:,7);

```

% Finding time doublets (to be deleted - not averaged)

```

f2=find(Daten(2:end,1)-Daten(1:end-1,1) ~=0);
Daten=Daten(f2,:);

```

% Date/Time conversion to zero date: 01-Jan-2009 00:00:00

```

tt=(t-t0)*86400;

```

% Calculation of rainfall summation curve and detrending

```
[D] = NaNdelete (Rain);
clear E;
Rain_o_NaN=D;
Rain_SK=Summenkurve(Rain_o_NaN);
plot(Rain_SK);
Rain_SKD=detrend(Rain_SK);
plot (Rain_SKD);
```

% Sampling of data

*% The amount of rainfall is summed up over 6-, 12-, 24-hour intervals, and the according timestamp
% is cut out. For the rainfall summation curve, detrended rainfall summation curve and the piezo-
% meter, the value at the according time interval is sampled and saved in a new data file.*

```
Timestep=6;
Rain_S6=Summieren(Rain,Timestep);
tt_S6=Zeitstempel_anpassen(tt,Timestep);
Pcor_A6=Zeitstempel_anpassen(Pcor,Timestep);
Rain_SK_A6=Zeitstempel_anpassen(Rain_SK,Timestep);
Rain_SKD_A6=Zeitstempel_anpassen(Rain_SKD,Timestep);
Timestep=12;
Rain_S12=Summieren(Rain,Timestep);
tt_S12=Zeitstempel_anpassen(tt,Timestep);
Pcor_A12=Zeitstempel_anpassen(Pcor,Timestep);
Rain_SK_A12=Zeitstempel_anpassen(Rain_SK,Timestep);
Rain_SKD_A12=Zeitstempel_anpassen(Rain_SKD,Timestep);
Timestep=24;
Rain_S24=Summieren(Rain,Timestep);
tt_S24=Zeitstempel_anpassen(tt,Timestep);
Pcor_A24=Zeitstempel_anpassen(Pcor,Timestep);
Rain_SK_A24=Zeitstempel_anpassen(Rain_SK,Timestep);
Rain_SKD_A24=Zeitstempel_anpassen(Rain_SKD,Timestep);
```

% Calculation of relative pore pressure change (differenced water pressure)

% Difference of pore pressure between time t+x and time t (6-, 12-, and 24-hour interval)

```
Pcor_A6_rel=delta(Pcor_A6);
Pcor_A12_rel=delta(Pcor_A12);
Pcor_A24_rel=delta(Pcor_A24);
```

% Filtering of data

% Moving average filter over original data with various filter lengths (value + (m-1) values in front)

```
m=5;
b1=[1/m 1/m 1/m 1/m 1/m];
a1=1;
Rain_SKD_gM5=filter(b1,a1,Rain_SKD);
Pcor_gM5=filter(b1,a1,Pcor);
m=10;
b2=[1/m 1/m 1/m 1/m 1/m 1/m 1/m 1/m 1/m 1/m];
a2=1;
Rain_SKD_gM10=filter(b2,a2,Rain_SKD);
Pcor_gM10=filter(b2,a2,Pcor);
m=12;
b3=[1/m 1/m 1/m 1/m 1/m 1/m 1/m 1/m 1/m 1/m 1/m 1/m];
a3=1;
Rain_SKD_gM12=filter(b3,a3,Rain_SKD);
```

```

Pcor_gM12=filter(b3,a3,Pcor);
m=24;
b4=[1/m 1/m 1/m 1/m 1/m 1/m 1/m 1/m 1/m 1/m 1/m 1/m 1/m 1/m 1/m 1/m 1/m 1/m...
    1/m 1/m 1/m 1/m 1/m 1/m 1/m];
a4=1;
Rain_SKD_gM24=filter(b4,a4,Rain_SKD);
Pcor_gM24=filter(b4,a4,Pcor);
m=48;
b5=[1/m 1/m 1/m 1/m 1/m 1/m 1/m 1/m 1/m 1/m 1/m 1/m 1/m 1/m 1/m 1/m 1/m 1/m...
    1/m 1/m 1/m 1/m 1/m 1/m 1/m 1/m 1/m 1/m 1/m 1/m 1/m 1/m 1/m 1/m...
    1/m 1/m 1/m 1/m 1/m 1/m 1/m 1/m 1/m 1/m 1/m 1/m 1/m 1/m];
a5=1;
Rain_SKD_gM48=filter(b5,a5,Rain_SKD);
Pcor_gM48=filter(b5,a5,Pcor);

% Moving average filter over sampled data with various filter lengths (value + (m-1) values in front)
m=2;
b6=[1/m 1/m];
a6=1;
Rain_SKD_A6_gM2=filter(b6,a6,Rain_SKD_A6);           %filter length = 2, data = 6h sum/sample
Rain_SKD_A6_gM2=filter(b6,a6,Rain_SKD_A6);
Pcor_A6_gM2=filter(b6,a6,Pcor_A6);
Pcor_A6_rel_gM2=filter(b6,a6,Pcor_A6_rel);
Rain_SKD_A12_gM2=filter(b6,a6,Rain_SKD_A12);        %filter length = 2, data = 12h sum/sample
Pcor_A12_gM2=filter(b6,a6,Pcor_A12);
Pcor_A12_rel_gM2=filter(b6,a6,Pcor_A12_rel);
m=4;
b7=[1/m 1/m 1/m 1/m];
a7=1;
Rain_SKD_A6_gM4=filter(b7,a7,Rain_SKD_A6);          %filter length = 4, data = 6h sums/samples
Pcor_A6_gM4=filter(b7,a7,Pcor_A6);
Pcor_A6_rel_gM4=filter(b7,a7,Pcor_A6_rel);

-----
% Transformation in timeseries objects
-----
Regen=timeseries(Rain,tt);
Luftdruck=timeseries(D,tt);
Temperatur=timeseries(T,tt);
PiezoOrig=timeseries(P,tt);
PiezoSmooth=timeseries(Psmooth,tt);
PiezoKorig=timeseries(Pcor,tt);
Regen_S6=timeseries(Rain_S6,tt_S6);
Regen_S12=timeseries(Rain_S12,tt_S12);
Regen_S24=timeseries(Rain_S24,tt_S24);
NSK=timeseries(Rain_SK,tt);
NSK_A6=timeseries(Rain_SK_A6,tt_S6);
NSK_A12=timeseries(Rain_SK_A12,tt_S12);
NSK_A24=timeseries(Rain_SK_A24,tt_S24);
PiezoKorig_A6=timeseries(Pcor_A6,tt_S6);
PiezoKorig_A12=timeseries(Pcor_A12,tt_S12);
PiezoKorig_A24=timeseries(Pcor_A24,tt_S24);
PiezoKorig_A6_rel=timeseries(Pcor_A6_rel,tt_S6);
PiezoKorig_A12_rel=timeseries(Pcor_A12_rel,tt_S12);
PiezoKorig_A24_rel=timeseries(Pcor_A24_rel,tt_S24);
PiezoKorig_A6_rel_gM2=timeseries(Pcor_A6_rel_gM2,tt_S6);
PiezoKorig_A6_rel_gM4=timeseries(Pcor_A6_rel_gM4,tt_S6);

```

```

PiezoKorig_A12_rel_gM2=timeseries(Pcor_A12_rel_gM2,tt_S12);
PiezoKorig_A6_gM2=timeseries(Pcor_A6_gM2,tt_S6);
PiezoKorig_A6_gM4=timeseries(Pcor_A6_gM4,tt_S6);
PiezoKorig_A12_gM2=timeseries(Pcor_A12_gM2,tt_S12);
PiezoKorig_gM5=timeseries(Pcor_gM5,tt);
PiezoKorig_gM10=timeseries(Pcor_gM10,tt);
PiezoKorig_gM12=timeseries(Pcor_gM12,tt);
PiezoKorig_gM24=timeseries(Pcor_gM24,tt);
PiezoKorig_gM48=timeseries(Pcor_gM48,tt);
NSKD=timeseries(Rain_SKD,tt);
NSKD_A6=timeseries(Rain_SKD_A6,tt_S6);
NSKD_A12=timeseries(Rain_SKD_A12,tt_S12);
NSKD_A24=timeseries(Rain_SKD_A24,tt_S24);
NSKD_gM5=timeseries(Rain_SKD_gM5,tt);
NSKD_gM10=timeseries(Rain_SKD_gM10,tt);
NSKD_gM12=timeseries(Rain_SKD_gM12,tt);
NSKD_gM24=timeseries(Rain_SKD_gM24,tt);
NSKD_gM48=timeseries(Rain_SKD_gM48,tt);
NSKD_A6_gM2=timeseries(Rain_SKD_A6_gM2,tt_S6);
NSKD_A6_gM4=timeseries(Rain_SKD_A6_gM4,tt_S6);
NSKD_A12_gM2=timeseries(Rain_SKD_A12_gM2,tt_S12);

```

%% Saving of filtered and sampled timeseries-objects

```

save('P02_Daten_alpEWAS.mat','RechtswertGPS_P1','HochwertGPS_P1','HoeheGPS_P1',...
'RechtswertGPS_P2',... 'HochwertGPS_P2','HoeheGPS_P2','RechtswertGPS_P3','HochwertGPS_P3',...
'HoeheGPS_P3','PiezoOrig','PiezoSmooth','PiezoKorig','PiezoKorig_A6','PiezoKorig_A12',...
'PiezoKorig_A24','PiezoKorig_gM5','PiezoKorig_gM10','PiezoKorig_gM12','PiezoKorig_gM24',...
'PiezoKorig_gM48','PiezoKorig_A6_gM2','PiezoKorig_A6_gM4','PiezoKorig_A12_gM2',...
'PiezoKorig_A6_rel','PiezoKorig_A12_rel','PiezoKorig_A24_rel','PiezoKorig_A6_rel_gM2',...
'PiezoKorig_A6_rel_gM4','PiezoKorig_A12_rel_gM2','Luftdruck','Temperatur','Regen',...
'Regen_S6','Regen_S12','Regen_S24','Regen_S6_gM2','Regen_S6_gM4','Regen_S12_gM2',...
'NSK','NSK_A6','NSK_A12','NSK_A24','NSKD','NSKD_A6','NSKD_A12','NSKD_A24',...
'NSKD_gM5','NSKD_gM10','NSKD_gM12','NSKD_gM24','NSKD_gM48','NSKD_A6_gM2',...
'NSKD_A6_gM4','NSKD_A12_gM2');

```


Time Series analysis – MATLAB programming code

Part II: Cutting of different data sets to various periods, TSA analysis

Written by Judith Festl, Christoph Reith, and Stefan Schubäck in course of the alpEWAS project, last revised July 2013

%% Cutting data sets to periods for TSA analysis – correlation analysis

% Data sets are cut to the period to be analyzed. The “edges” of the moving average filter are removed.

% Import of filtered and sampled data sets, saved in part I

clear all; close all
load(fullfile(cd,'P02_Daten_alpEWAS.mat'));

% Definition of time interval for further analysis and cutting of data sets

% In part I, t=0 has been defined as the January 1, 2009, 00:00:00. All dates have to be given in seconds starting at t=0 on the preset date. 2009, 2010, and 2011 have 365 days, 2012 has 366 days (leap year).

Beginn=31536000; *% insert start and end of time interval*
Ende=63071999;

% All data sets are cut to selected time interval

```
f1= find(RechtswertGPS_P1.Time > Beginn & RechtswertGPS_P1.Time < Ende);
RechtswertGPS_P1_t = RechtswertGPS_P1(f1);
f2= find(HochwertGPS_P1.Time > Beginn & HochwertGPS_P1.Time < Ende);
HochwertGPS_P1_t = HochwertGPS_P1(f2);
f3= find(HoeheGPS_P1.Time > Beginn & HoeheGPS_P1.Time < Ende);
HoeheGPS_P1_t = HoeheGPS_P1(f3);
f4= find(RechtswertGPS_P2.Time > Beginn & RechtswertGPS_P2.Time < Ende);
RechtswertGPS_P2_t = RechtswertGPS_P2(f4);
f5= find(HochwertGPS_P2.Time > Beginn & HochwertGPS_P2.Time < Ende);
HochwertGPS_P2_t = HochwertGPS_P2(f5);
f6= find(HoeheGPS_P2.Time > Beginn & HoeheGPS_P2.Time < Ende);
HoeheGPS_P2_t = HoeheGPS_P2(f6);
f7= find(RechtswertGPS_P3.Time > Beginn & RechtswertGPS_P3.Time < Ende);
RechtswertGPS_P3_t = RechtswertGPS_P3(f7);
f8= find(HochwertGPS_P3.Time > Beginn & HochwertGPS_P3.Time < Ende);
HochwertGPS_P3_t = HochwertGPS_P3(f8);
f9= find(HoeheGPS_P3.Time > Beginn & HoeheGPS_P3.Time < Ende);
HoeheGPS_P3_t = HoeheGPS_P3(f9);
f10= find(PiezoKorig.Time >= Beginn & PiezoKorig.Time < Ende);
xPiezoKorig_t = PiezoKorig(f10);
f11= find(Regen.Time >= Beginn & Regen.Time < Ende);
xRegen_t = Regen(f11);
f17= find(Regen_S6.Time > Beginn & Regen_S6.Time < Ende);
xRegen_S6_t = Regen_S6(f17);
f18= find(Regen_S12.Time > Beginn & Regen_S12.Time < Ende);
xRegen_S12_t = Regen_S12(f18);
```

```

f19= find(Regen_S24.Time > Beginn & Regen_S24.Time < Ende);
xRegen_S24_t = Regen_S24(f19);
f23= find(PiezoKorig_gM5.Time >= Beginn & PiezoKorig_gM5.Time < Ende);
xPiezoKorig_gM5_t = PiezoKorig_gM5(f23);
f24= find(PiezoKorig_gM10.Time >= Beginn & PiezoKorig_gM10.Time < Ende);
xPiezoKorig_gM10_t = PiezoKorig_gM10(f24);
f25= find(PiezoKorig_gM12.Time >= Beginn & PiezoKorig_gM12.Time < Ende);
xPiezoKorig_gM12_t = PiezoKorig_gM12(f25);
f26= find(PiezoKorig_gM24.Time >= Beginn & PiezoKorig_gM24.Time < Ende);
xPiezoKorig_gM24_t = PiezoKorig_gM24(f26);
f27= find(PiezoKorig_gM48.Time >= Beginn & PiezoKorig_gM48.Time < Ende);
xPiezoKorig_gM48_t = PiezoKorig_gM48(f27);
f28= find(PiezoKorig_A6.Time > Beginn & PiezoKorig_A6.Time < Ende);
xPiezoKorig_A6_t = PiezoKorig_A6(f28);
f29= find(PiezoKorig_A12.Time > Beginn & PiezoKorig_A12.Time < Ende);
xPiezoKorig_A12_t = PiezoKorig_A12(f29);
f30= find(PiezoKorig_A24.Time > Beginn & PiezoKorig_A24.Time < Ende);
xPiezoKorig_A24_t = PiezoKorig_A24(f30);
f31= find(PiezoKorig_A6_gM2.Time > Beginn & PiezoKorig_A6_gM2.Time < Ende);
xPiezoKorig_A6_gM2_t = PiezoKorig_A6_gM2(f31);
f32= find(PiezoKorig_A6_gM4.Time > Beginn & PiezoKorig_A6_gM4.Time < Ende);
xPiezoKorig_A6_gM4_t = PiezoKorig_A6_gM4(f32);
f33= find(PiezoKorig_A12_gM2.Time > Beginn & PiezoKorig_A12_gM2.Time < Ende);
xPiezoKorig_A12_gM2_t = PiezoKorig_A12_gM2(f33);
f34= find(PiezoKorig_A6_rel.Time > Beginn & PiezoKorig_A6_rel.Time < Ende);
xPiezoKorig_A6_rel_t = PiezoKorig_A6_rel(f34);
f35= find(PiezoKorig_A12_rel.Time > Beginn & PiezoKorig_A12_rel.Time < Ende);
xPiezoKorig_A12_rel_t = PiezoKorig_A12_rel(f35);
f36= find(PiezoKorig_A24_rel.Time > Beginn & PiezoKorig_A24_rel.Time < Ende);
xPiezoKorig_A24_rel_t = PiezoKorig_A24_rel(f36);
f37= find(PiezoKorig_A6_rel_gM2.Time > Beginn & PiezoKorig_A6_rel_gM2.Time < Ende);
xPiezoKorig_A6_rel_gM2_t = PiezoKorig_A6_rel_gM2(f37);
f38= find(PiezoKorig_A6_rel_gM4.Time > Beginn & PiezoKorig_A6_rel_gM4.Time < Ende);
xPiezoKorig_A6_rel_gM4_t = PiezoKorig_A6_rel_gM4(f38);
f39= find(PiezoKorig_A12_rel_gM2.Time > Beginn & PiezoKorig_A12_rel_gM2.Time < Ende);
xPiezoKorig_A12_rel_gM2_t = PiezoKorig_A12_rel_gM2(f39);
f40= find(NSK.Time >= Beginn & NSK.Time < Ende);
xNSK_t = NSK(f40);
f41= find(NSK_A6.Time > Beginn & NSK_A6.Time < Ende);
xNSK_A6_t = NSK_A6(f41);
f42= find(NSK_A12.Time > Beginn & NSK_A12.Time < Ende);
xNSK_A12_t = NSK_A12(f42);
f43= find(NSK_A24.Time > Beginn & NSK_A24.Time < Ende);
xNSK_A24_t = NSK_A24(f43);
f44= find(NSKD.Time >= Beginn & NSKD.Time < Ende);
xNSKD_t = NSKD(f44);
f45= find(NSKD_A6.Time > Beginn & NSKD_A6.Time < Ende);
xNSKD_A6_t = NSKD_A6(f45);
f46= find(NSKD_A12.Time > Beginn & NSKD_A12.Time < Ende);
xNSKD_A12_t = NSKD_A12(f46);
f47= find(NSKD_A24.Time > Beginn & NSK_A24.Time < Ende);
xNSKD_A24_t = NSK_A24(f47);
f48= find(NSKD_gM5.Time >= Beginn & NSKD_gM5.Time < Ende);
xNSKD_gM5_t = NSKD_gM5(f48);
f49= find(NSKD_gM10.Time >= Beginn & NSKD_gM10.Time < Ende);

```

```

xNSKD_gM10_t = NSKD_gM10(f49);
f50= find(NSKD_gM12.Time >= Beginn & NSKD_gM12.Time < Ende);
xNSKD_gM12_t = NSKD_gM12(f50);
f51= find(NSKD_gM24.Time >= Beginn & NSKD_gM24.Time < Ende);
xNSKD_gM24_t = NSKD_gM24(f51);
f52= find(NSKD_gM48.Time >= Beginn & NSKD_gM48.Time < Ende);
xNSKD_gM48_t = NSKD_gM48(f52);
f53= find(NSKD_A6_gM2.Time > Beginn & NSKD_A6_gM2.Time < Ende);
xNSKD_A6_gM2_t = NSKD_A6_gM2(f53);
f54= find(NSKD_A6_gM4.Time > Beginn & NSKD_A6_gM4.Time < Ende);
xNSKD_A6_gM4_t = NSKD_A6_gM4(f54);
f55= find(NSKD_A12_gM2.Time > Beginn & NSKD_A12_gM2.Time < Ende);
xNSKD_A12_gM2_t = NSKD_A12_gM2(f55);

```

% Resampling of GNSS data

% Different time intervals, dt, are used. Exemplarily, one resampling cycle is listed.

% applied time intervals:

% dt=3600, 1 hour

% dt=21600, 6 hours

% dt=43200, 12 hours

% dt=86400, 24 hours

```

t0=Beginn;
t1=Ende;
n=ceil((t1-t0)/dt);
for i=1:n
    t=t0+(i-1)*dt;
    f= find(RechtswertGPS_P1_t.Time>t-(dt/2) & RechtswertGPS_P1_t.Time < t+(dt/2));
    d=mean(RechtswertGPS_P1_t.Data(f));
    D(i,1)=d;
    T(i,1)=t;
end
xR_P1=timeseries(D,T); D=[];T=[];
for i=1:n
    t=t0+(i-1)*dt;
    f= find(RechtswertGPS_P2_t.Time>t-(dt/2) & RechtswertGPS_P2_t.Time < t+(dt/2));
    d=mean(RechtswertGPS_P2_t.Data(f));
    D(i,1)=d;
    T(i,1)=t;
end
xR_P2=timeseries(D,T); D=[];T=[];
for i=1:n
    t=t0+(i-1)*dt;
    f= find(RechtswertGPS_P3_t.Time>t-(dt/2) & RechtswertGPS_P3_t.Time < t+(dt/2));
    d=mean(RechtswertGPS_P3_t.Data(f));
    D(i,1)=d;
    T(i,1)=t;
end
xR_P3=timeseries(D,T); D=[];T=[];

```

% Saving of data as .mat-files

```
save('2010.mat','xPiezoKorig_t','xR_P1','xR_P2','xR_P3','xRegen_t','xRegen_S6_t','xRegen_S12_t',...  
'xRegen_S24_t','xPiezoKorig_gM5_t','xPiezoKorig_gM10_t','xPiezoKorig_gM12_t',...  
'xPiezoKorig_gM24_t','xPiezoKorig_gM48_t','xPiezoKorig_A6_t','xPiezoKorig_A12_t',...  
'xPiezoKorig_A24_t','xPiezoKorig_A6_gM2_t','xPiezoKorig_A6_gM4_t',...  
'xPiezoKorig_A12_gM2_t','xPiezoKorig_A6_rel_t','xPiezoKorig_A12_rel_t',...  
'xPiezoKorig_A24_rel_t','xPiezoKorig_A6_rel_gM2_t','xPiezoKorig_A6_rel_gM4_t',...  
'xPiezoKorig_A12_rel_gM2_t','xNSK_t','xNSK_A6_t','xNSK_A12_t','xNSK_A24_t','xNSKD_t',...  
'xNSKD_A6_t','xNSKD_A12_t','xNSKD_A24_t','xNSKD_gM5_t','xNSKD_gM10_t',...  
'xNSKD_gM12_t','xNSKD_gM24_t','xNSKD_gM48_t','xNSKD_A6_gM2_t','xNSKD_A6_gM4_t',...  
'xNSKD_A12_gM2_t');
```

% Analysis of timeseries-objects

```
% The timeseries-toolbox incorporated in MATLAB is used for the further analysis. The previously  
saved data files of the filtered, sampled, and cut data sets are loaded into the toolbox, 'tstool'.  
There, the data sets can be plotted versus time or autocorrelations or crosscorrelations can be  
calculated and plotted, too.
```

```
tstool
```

Time Series analysis – MATLAB programming code

Part III: Compilation of functions written for the analysis

Written by Judith Festl, Christoph Reith, and Stefan Schubäck in course of the alpEWAS project, last revised July 2013

%%% delta

```
function [C]=delta(Piezo)    % calculation of the relative pore pressure change between two intervals
n=length(Piezo);
C=zeros(n,1);
for i=1:n
    if i==1;
        C(1,i)=0;
    else
        C(i,1)=Piezo(i)-Piezo(i-1);
    end
end
end
```

%%% DuplettenLoeschen

```
function [x2,y2]=DuplettenLoeschen(x,y)    % Deletion of dublets
s=sortrows([x y],1);
f=find(s(2:end,1)-s(1:end-1,1)~=0);
x2=s(f,1); y2=s(f,2);
```

%%% gleitendes_Mittel

```
function [x2,z]=gleitendes_Mittel(x,y,Filterlaenge)    % moving average filter
if (gcd(Filterlaenge,2)==2) Filterlaenge=Filterlaenge+1; end
n=(Filterlaenge-1)/2;
c=length(y);    % read out length of time series
for i=1:n
    z(i,1)=y(i,1);
end
for i=(c-n+1):c
    z(i,1)=y(i,1);
end
for i=(1+n):(c-n)
    z(i,1)=sum(y(i-n:i+n,1))/Filterlaenge;
end
z=z((1+n):(c-n),:);
x2=x((1+n):(c-n),:);
figure; plot(x,y,'.');hold on; plot(x2,z,'r')
```

%% gM_Schwellenfilter

```
function [x2,y2]=gM_Schwellenfilter(R,tt)
% Deletion of outliers: Values exceeding the moving average by more than one time the threshold are
% deleted. Prior to this, extreme outliers are deleted (strong discrepancy from global mean).
Filterlaenge=5;      % filter length
Schwellenwert=0.2;   % threshold
m1=mean(R);
f1=find(abs(R-m1)<1);
R2=R(f1,:); tt2=tt(f1,:);
m2=mean(R2);
f2=find(abs(R2-m2)<0.5);
R3=R2(f2,:); tt3=tt2(f2,:);
m3=mean(R3);
f3=find(abs(R3-m3)<0.1);
R4=R3(f3,:); tt4=tt3(f3,:);
y=R4; x=tt4;
if (gcd(Filterlaenge,2)==2) Filterlaenge=Filterlaenge+1; end
n=(Filterlaenge-1)/2;
c=length(y);
for i=1:n
    z(i,1)=y(i,1);
end
for i=(c-n+1):c
    z(i,1)=y(i,1);
end
for i=(1+n):(c-n)
    z(i,1)=sum(y(i-n:i+n,1))/Filterlaenge;
end
D=y-z;
S=std(D);
x2=[];y2=[];xm2=[];
for i=1:c
    if abs(D(i))< S*Schwellenwert
        y2=[y2;y(i)];
        x2=[x2;x(i)];
    end
end
end
```

%% GPS_in

```
function [Daten]=GPS_in(filename) % import function for GPS data
import=uiimport(filename);
data=import.data;
textdata=import.textdata;
for i=2:length(textdata)
    Daten(i-1,1) = datenum(textdata{i,4}, 'dd.mm.yyyy HH:MM:SS');
end
aa=data(:,5:end);
Daten(:,2:size(aa,2)+1)=aa;
```

%% NaNdelete

```
function [D,E] = NaNdelete (Rain)           % Deletion of NaN-values (data gaps in rainfall data)
E=isnan(Rain);
D=[];
for i=1:size(Rain,1);
    if E(i)==0;
        D=[D; Rain(i,:)];
    else E(i)==1
        D=[D; 0];
    end
end
```

%% Summenkurve

```
function [C]=Summenkurve(Rain_o_NaN)       % Calculates the rainfall summation curve
n=length(Rain_o_NaN);
C=zeros(n,1);
for i=1:n
    if i==1;
        C(i,1)=Rain_o_NaN(i);
    else
        C(i,1)=sum(Rain_o_NaN(1:i));
    end
end
```

%% Summieren

```
function [B]=Summieren(Rain,Timestep)     % 6-, 12-, 24-hour rainfall sums are calculated
n=length(Rain);
L_B=n/Timestep;
B=zeros(L_B,1);
for i=1:L_B;
    B(i,1)=sum(Rain(i*Timestep-(Timestep-1):i*Timestep));
end
```

%% Zeitstempel_anpassen

```
function [C]=Zeitstempel_anpassen(tt,Timestep) % Adjusting the stamp to 6-, 12-, 24-hour periods
n=length(tt);
L_out=n/Timestep;
C=zeros(L_out,1);
for i=1:L_out;
    C(i,1)=tt(i*Timestep);
end
```


Appendix VIII:
Time series and correlation diagrams

In this Appendix several additional time series plots of shorter time spans are presented (e.g., 60-day periods in 2010 and 2011). These are followed by multiple crosscorrelation diagrams that have been calculated of the filtered and resampled rainfall and pore water pressure data (6-hour sampling interval), each over a length of one month.

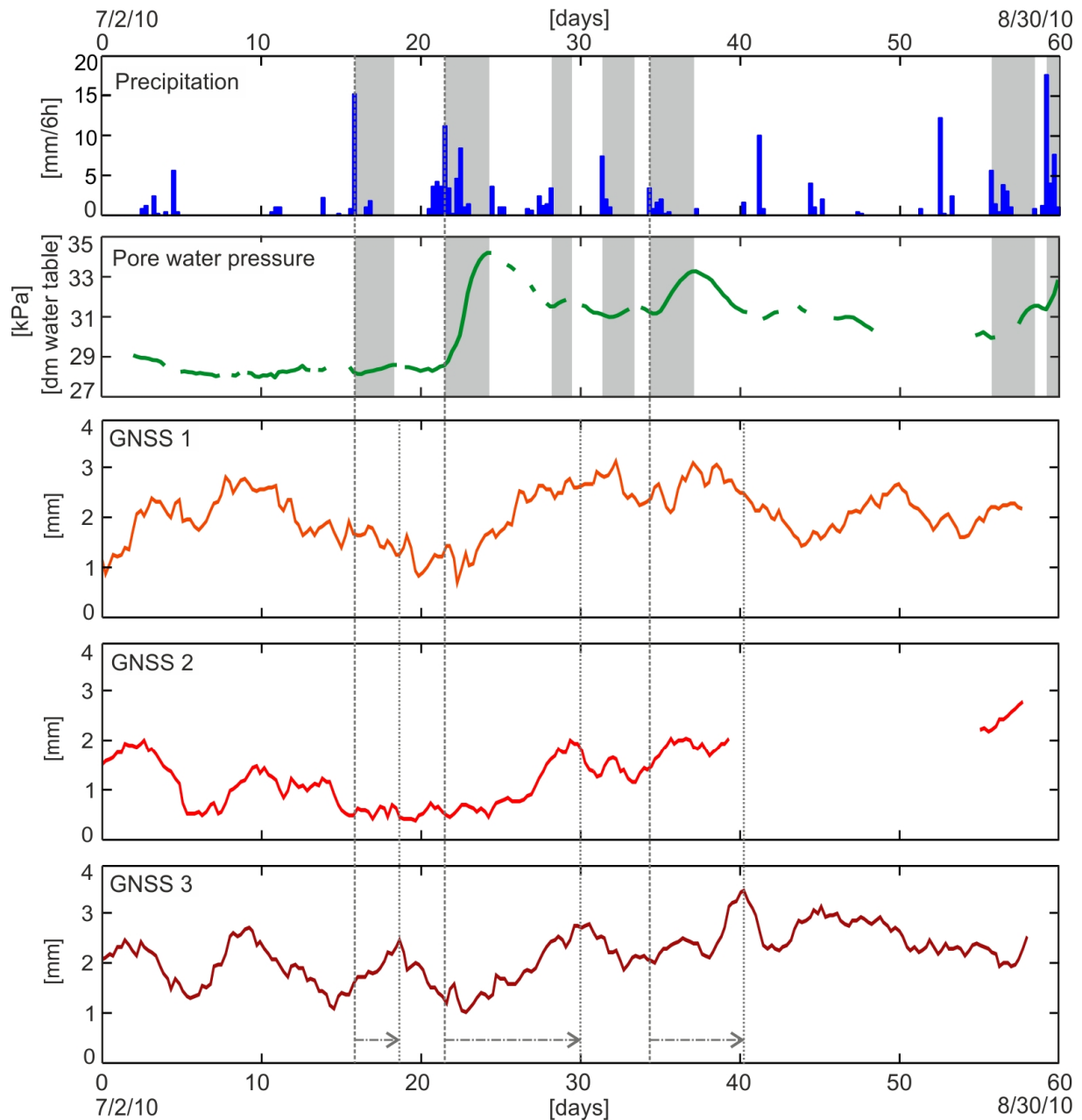


Figure VIII-1: Filtered and sampled (6-hour intervals) rainfall, pore water pressure, and displacement (Δ Easting in [mm]) of all three GNSS sensors over a 60-day period (July 2 to August 30, 2010). The response time between precipitation and rise of water level is shaded gray. Significant responses of the GNSS sensors to rainfall and thus to an elevated water level can't be derived properly, even though some dependencies, especially with GNSS 3, can be drawn visually.

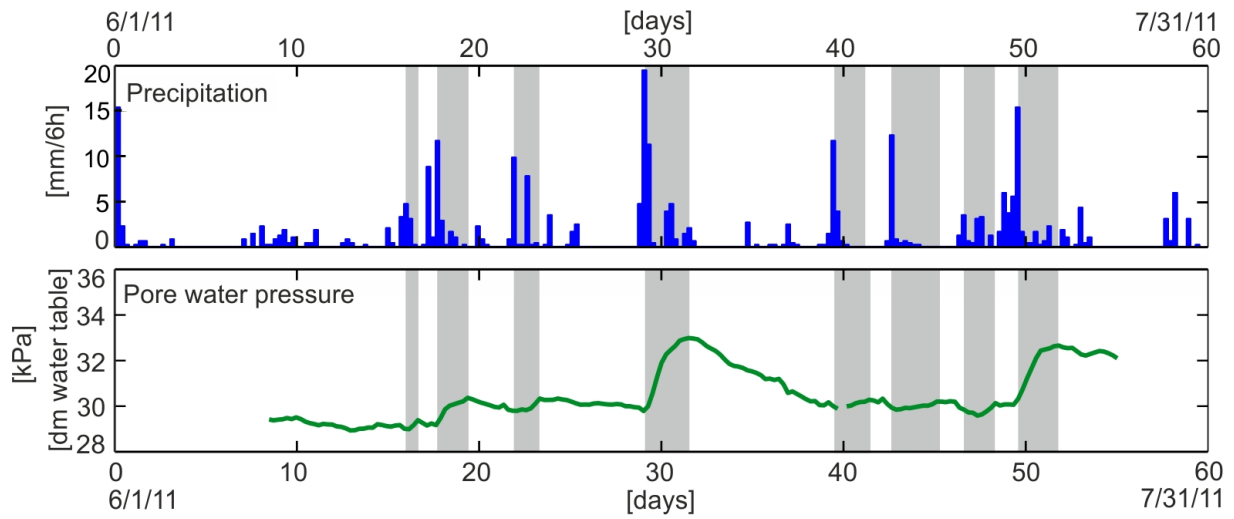


Figure VIII-2: Filtered and sampled (6-hour intervals) rainfall and pore water pressure over a 60-day period (June 1 to July 31, 2011). A major gap occurred in the GNSS data during this period, thus it was refrained from plotting the little data recorded during the last two weeks of this period. The response time between precipitation and rise of water level is shaded gray and shows very similar results to those deduced from the other plots.

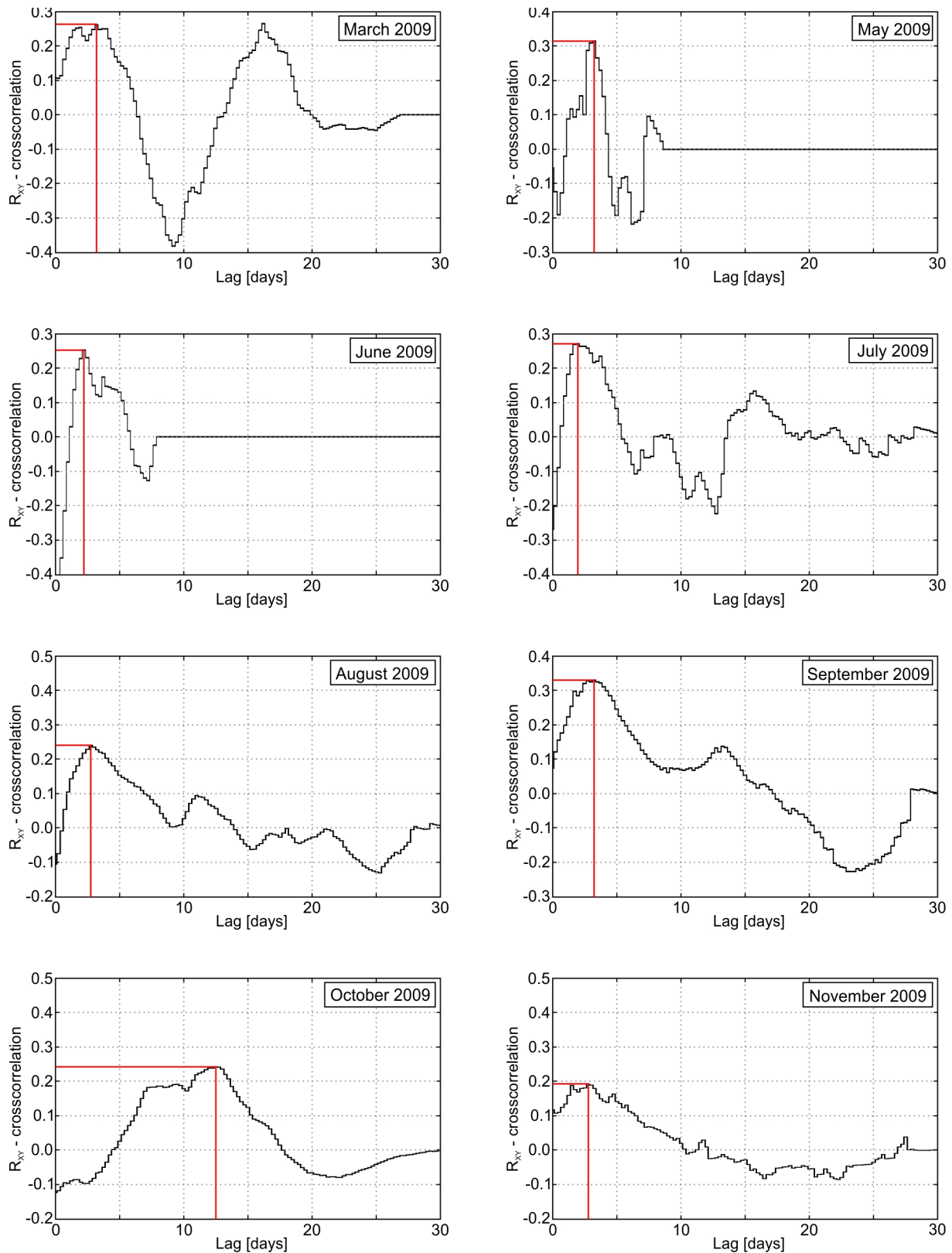


Figure VIII-3: Crosscorrelation diagrams of precipitation and pore water pressure data. The data series have been filtered and sampled applying a 6-hour interval. Each plot depicts the crosscorrelation function calculated over a 1-month period in 2009. The red line marks the highest correlation and thus the according lag, representing the response time of rise in pore water pressure to preceding precipitation.

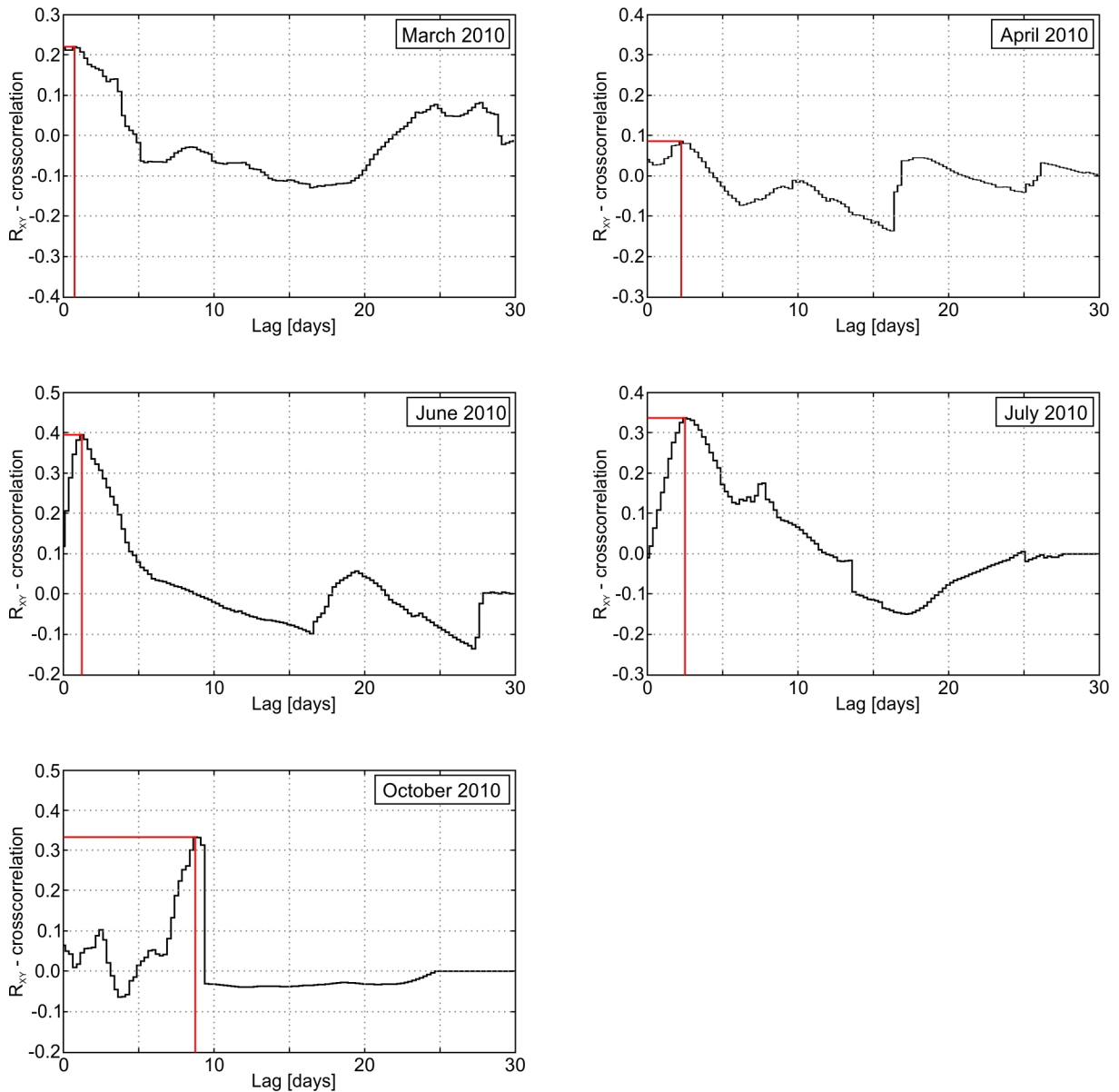


Figure VIII-4: Crosscorrelation diagrams of precipitation and pore water pressure data. The data series have been filtered and sampled applying a 6-hour interval. Each plot depicts the crosscorrelation function calculated over a 1-month period in 2010. The red line marks the highest correlation and thus the according lag, representing the response time of rise in pore water pressure to preceding precipitation.

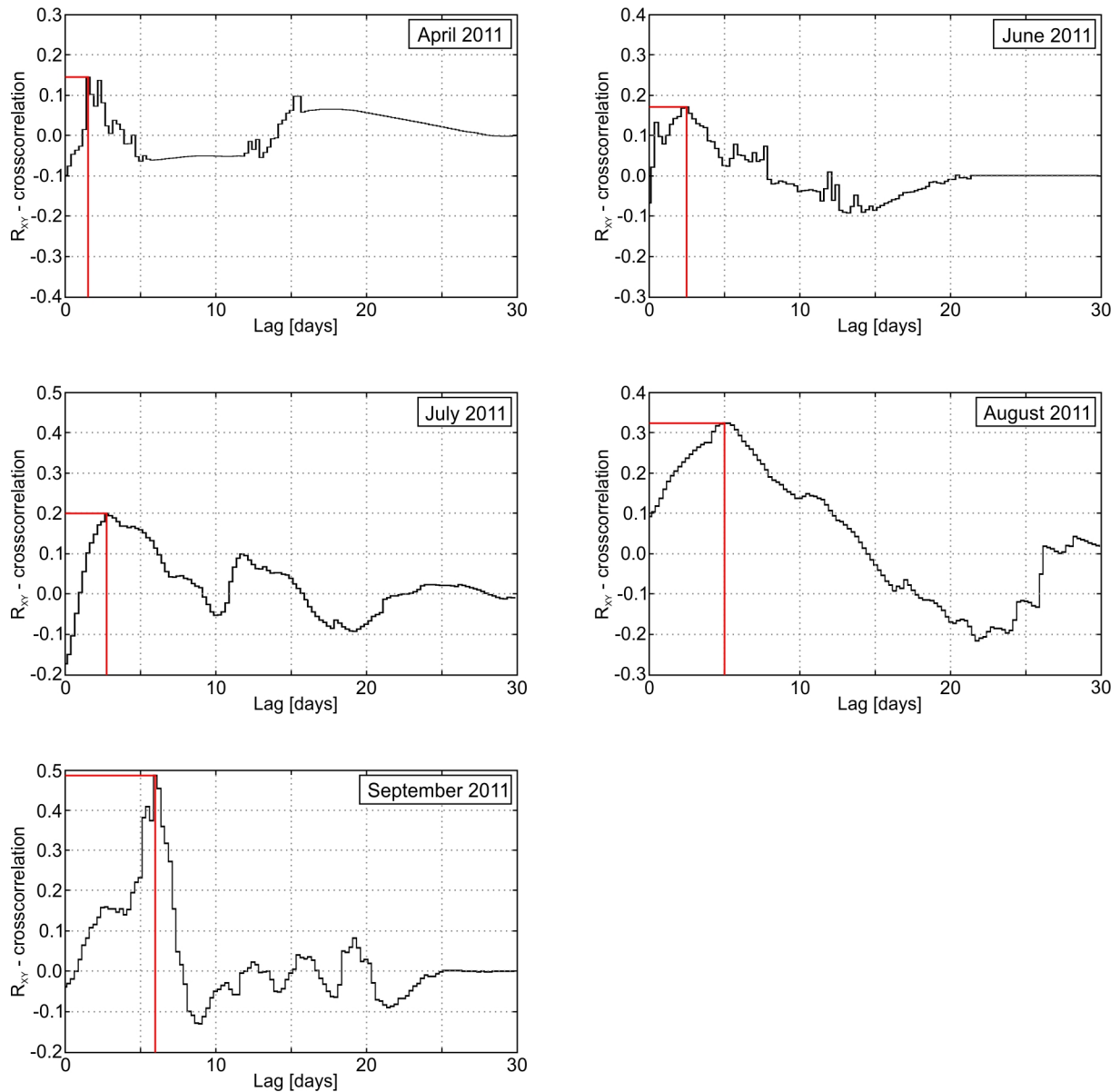


Figure VIII-5: Crosscorrelation diagrams of precipitation and pore water pressure data. The data series have been filtered and sampled applying a 6-hour interval. Each plot depicts the crosscorrelation function calculated over a 1-month period in 2011. The red line marks the highest correlation and thus the according lag, representing the response time of rise in pore water pressure to preceding precipitation.

Appendix IX:

Numerical modeling code

This Appendix contains the input code for the numerical model of the Aggenalm landslide generated with FLAC by Itasca. It is divided into several parts. The first part contains the setup of the grid, boundary conditions, and material definitions and is used to compute the initial force-equilibrium. In the second file, the joints are added, while in the third part the water table is generated and any accompanying material property changes are considered. The second and third part of the code have been used for the sensitivity and validation analyses, as well as for the simulation of extreme events. During the sensitivity and validation analyses one parameter at a time (joints in part 2 and rock mass properties in part 3) was changed while always applying the mean water table. For the simulation of extreme events the water table was then changed stepwise (part 3).

NUMERICAL MODELING OF THE AGGENALM LANDSLIDE**Part 1: Model setup – grid generation, geometry, constitutive model & initial equilibrium**

Written by Judith Festl, last revised June 2014

```

: *****
: *
: * Grid generation & constitutive model *
: * *****
: ; grid generation: mesh size 1 x 1 meter
: ; 340000 finite difference zones
grid 1000 340

: ; constitutive model: Mohr-Coulomb
model mohr

: *****
: *
: * Setup of slope's geometry *
: * *****
: ; assigning "real" coordinates to the grid
gen (0,860) (0,1200) (1000,1200) (1000,860) i=1,1001 j=1,341

: ; inserting topographic profile (line)
table 1 (-1.0,1164.6) (21.1,1165.4) (50.0,1167.8) (68.7,1167.6) (76.3,1167.7) &
(89.9,1168.0) (100.4,1172.8) (123.3,1185.1) (129.9,1187.8) (135.7,1192.2) (139.0,1191.9) &
(140.9,1193.1) (142.5,1192.7) (146.4,1187.6) (149.4,1183.1) (149.9,1183.1) (150.4,1183.1) &
(155.2,1176.9) (168.3,1171.2) (174.1,1168.8) (175.1,1168.8) (185.6,1165.1) (192.4,1164.8) &
(200.3,1166.8) (201.3,1166.8) (212.1,1163.6) (218.7,1164.2) (219.7,1164.2) (221.5,1165.0) &
(225.6,1164.6) (235.2,1160.2) (241.0,1161.7) (242.0,1161.7) (249.8,1163.8) (252.2,1164.0) &
(260.2,1168.1) (261.2,1168.1) (271.7,1173.3) (286.3,1174.1) (287.3,1174.1) (292.8,1174.4) &
(305.7,1166.7) (315.0,1157.9) (316.0,1157.9) (329.7,1145.3) (375.6,1117.4) (412.9,1099.4) &
(436.8,1089.4) (462.8,1080.8) (481.0,1077.0) (497.8,1076.5) (505.1,1075.7) (528.7,1067.7) &
(574.5,1049.4) (584.7,1046.1) (598.3,1040.7) (601.4,1038.7) (614.0,1034.7) (617.5,1034.2) &
(646.1,1027.6) (655.3,1024.1) (662.7,1020.3) (665.1,1020.3) (669.4,1016.8) (676.4,1015.5) &
(685.1,1015.1) (689.4,1013.4) (693.2,1012.9) (694.2,1012.9) (699.4,1011.0) (701.5,1010.9) &
(705.7,1009.4) (709.4,1010.0) (713.5,1009.6) (715.9,1007.0) (725.8,999.7) (731.2,999.2) &
(736.5,998.8) (758.1,985.6) (759.1,985.6) (761.6,985.4) (781.5,970.5) (789.3,970.5) (791.0,968.8) &
(800.1,963.8) (807.6,957.3) (821.2,957.6) (826.3,960.4) (831.7,963.4) (837.1,963.4) (857.0,970.8) &
(865.6,974.5) (873.0,982.9) (884.1,990.4) (890.8,991.7) (901.9,999.3) (905.1,1003.1) &
(914.0,1009.6) (929.2,1017.4) (931.5,1017.6) (933.4,1019.6) (935.1,1020.1) (936.8,1022.3) &
(938.8,1025.5) (942.8,1025.9) (949.3,1030.9) (952.9,1032.2) (964.0,1045.1) (969.5,1051.1) &
(979.5,1059.1) (989.1,1068.4) (991.6,1071.9) (996.6,1076.6) (1000.5,1076.8)
gen table 1

: ; inserting lower boundary debris/quaternary
table 2 (329.7,1145.3) (330.7,1135.4) (336.2,1129.4) (342.0,1125.3) (342.9,1121.5) (343.1,1121.3) &
(343.5,1121.3) (344.5,1121.3) (348.3,1119.9) (356.0,1109.9) (362.5,1107.4) (367.9,1099.6) &
(368.9,1099.6) (369.9,1099.6) (370.9,1099.6) (399.8,1085.2) (403.1,1081.5) (404.1,1081.5) &
(405.7,1083.0) (417.5,1078.3) (438.4,1073.2) (439.4,1069.5) (441.3,1068.6) (444.0,1071.4) &
(465.2,1066.3) (492.0,1053.2) (503.8,1051.4) (524.8,1042.5) (526.2,1040.6) (527.8,1040.7) &
(530.6,1042.7) (543.8,1043.2) (563.6,1033.0) (569.1,1032.6) (589.5,1023.2) (604.8,1021.4) &

```

(614.8,1020.5) (619.5,1017.4) (631.7,1018.5) (640.8,1013.0) (641.8,1013.0) (652.0,1012.6) &
(660.4,1009.1) (665.7,1009.1) (679.4,1012.8) (685.1,1015.1)
gen table 2

table 3 (715.9,1007.0) (717.7,999.7) (720.3,994.6) (724.5,993.8) (727.2,996.2) (731.2,999.2)
gen table 3

; inserting lower boundary of talus

table 4 (789.3,970.5) (794.6,962.0) (798.0,958.5) (801.0,955.9) (806.9,952.8) (818.5,952.1) &
(827.8,955.8) (837.1,963.4)
gen table 4

; inserting lower boundaries of Upper Rhaetian limestone and dolomite

table 5 (76.3,1167.7) (156.6,1145.3) (157.1,1145.3) (157.6,1145.3) (158.5,1140.1) (164.5,1122.4) &
(179.1,1113.4) (180.1,1113.4) (181.1,1113.4) (202.0,1100.2) (203.0,1100.2) (204.0,1100.2) &
(204.8,1099.4) (221.4,1095.1) (222.4,1095.1) (238.7,1090.7) (239.7,1090.7) (240.7,1090.7) &
(262.1,1084.4) (263.1,1084.4) (264.1,1084.4) (286.1,1080.2) (287.1,1080.2) (313.3,1075.1) &
(314.3,1075.1) (337.9,1067.0) (338.9,1067.0) (362.4,1058.8) (363.4,1058.8) (397.0,1054.1) &
(404.0,1054.6) (405.0,1054.6) (409.6,1051.8) (436.0,1049.6) (437.3,1057.9) (439.4,1069.5)
gen table 5

table 6 (441.3,1068.6) (444.6,1062.2) (445.5,1055.7) (452.2,1055.5) (461.1,1060.6) (465.2,1066.3)
gen table 6

table 7 (492.0,1053.2) (500.3,1038.2) (511.0,1033.7) (523.5,1033.1) (524.1,1038.0) (526.2,1040.6)
gen table 7

table 8 (527.8,1040.7) (530.9,1032.7) (541.2,1029.6) (555.8,1027.6) (562.0,1029.1) (563.6,1033.0)
gen table 8

table 9 (604.8,1021.4) (607.2,1015.7) (616.1,1010.6) (618.3,1010.9) (625.2,999.7) (639.4,993.7) &
(641.2,994.3) (642.2,994.3) (645.0,989.2) (652.2,986.0) (659.4,986.1) (673.1,983.2) (688.3,982.8) &
(693.2,995.7) (694.2,995.7) (694.8,994.0) (695.2,984.7) (709.4,978.7) (716.7,978.0) (719.0,980.4) &
(720.3,994.6)
gen table 9

table 10 (724.5,993.8) (725.3,977.9) (729.4,974.6) (760.0,968.1) (761.0,968.1) (783.7,961.7) &
(794.6,962.0)
gen table 10

gen line (818.5,952.1) (925.0,860.0)

; inserting lower boundaries of Koessen formation

gen line (-1,1123.4) (807.0,927.2)

gen line (807.1,883.0) (833.2,860)

; inserting of "fault" in the Gassenbach valley

gen line (806.9,-1) (806.9,952.8)

. *****
;
; * **Gravity & boundary conditions** *
;
; *****
; Calculations will be done in large strain mode. Base of model fixed in x- and y-direction. Sides fixed
; in x-direction. Movements in y-direction possible on sides.

```
set large
set grav=9.81
fix x i=1
fix x y j=1
fix x i=1001
```

```
. *****
;
; *           Assignment of material properties for initial equilibrium computation           *
; *****
;
; Material properties (strong material - high values) are assigned to each region to calculate the initial
; equilibrium; to bring the model to an initial equilibrium state. The command "solve" is used to
; calculate the equilibrium, which is reached once the stresses fall below 0.1 kN in FLAC. By doing
; so, the grid must "settle", and gaps (model) must close. Therefore high values are used, as only
; model-relevant movements should occur.
```

```
; high material properties used for all rock types for initial equilibrium computation
```

```
model mohr
prop dens=2700 bulk=8.E9 shear=6.E9 cohesion=5.E10 friction=35. dilation=1. &
tension=1.E7
```

```
; deletion of area above topography ("air")
```

```
model null region i=4 j=340
```

```
. *****
;
; *           Computation of initial force-equilibrium           *
; *****
;
hist unbal
solve
```

```
. *****
;
; *           Plot and documentation commands           *
; *****
;
; plot command to plot the "unbalanced force"
plot hist 1
```

```
; export of "unbalanced force" diagram "hist 1" in different formats
```

```
; export as pdf: best way to print as pdf is via the windows standard printer, therefore the pdf-printer
; must be set as the standard printer!
```

```
set plot win
```

```
copy unbal-force.pdf
```

```
; Export in emf-format, plot is automatically saved in the linked folder
```

```
set plot emf
```

```
copy Aggenalm_unbal-force.emf
```

```
; Export as ASCII file. It is saved as "filename.his" and can then be loaded into Excel for further analyses
; or plotting options. (Import in Excel - as a decimal point a "." is used in .his file -> must be set
; accordingly in Excel to assure proper import of data!)
```

```
set hisfile Aggenalm_unbal-force.his
```

```
hist write 1
```

```
. *****
;
; *           Saving of initial computations           *
; *****
;
save Aggenalm-00_ini.sav
```

NUMERICAL MODELING OF THE AGGENALM LANDSLIDE

Part 2: Model setup –material property assignation, implementation of joints, and adjustment of grid

Written by Judith Festl, last revised June 2014

```

; *****
; *
; *           Restoring geometry and settings after stepping to initial equilibrium           *
; * *****
restore Aggenalm-00_ini.sav

; *****
; *
; *           Resetting deformation to zero           *
; * *****
; Small deformations that occurred during initial force-equilibrium analysis are set back to zero so that
; the following analyses aren't influenced.
ini xdis=0 ydis=0

; *****
; *
; *           Summary of regions for parameter assignment           *
; * *****
; "Air" above profile line i=4 j=340
; Debris/quaternary i=500 j=200 und i=723 j=140
; Talus i=815 j=95
; Upper Rhaetian formation i=420 j=200; i=450 j=200; i=510 j=180; i=550 j=170; i=670 j=130;
; Upper Rhaetian formation i=740 j=120; i=950 j=100
; Koessen formation i=800 j=80 und i=850 j=10
; Plattenkalk i=770 j=10 und i=810 j=10

; *****
; *
; *           Assigning material properties           *
; * *****
; Now, the "real" material parameters are assigned. Not like during the initial force-equilibrium
; analysis, where identical, high parameters were assigned to all the different rock types.

; Deletion of area above topography ("air")
model null region i=4 j=340

; Plattenkalk
group 'Plattenkalk' region i=770 j=10
group 'Plattenkalk' region i=810 j=10
model mohr group 'Plattenkalk'
prop dens=2700 bulk=7.65E9 shear=5.74E9 cohesion=3.52E6 friction=33.5 dilation=1. &
tension=1.E7 group 'Plattenkalk'

; Koessen formation in shear zone (marls only!)
group 'Koessener Schichten bewegt' region i=800 j=80
model mohr group 'Koessener Schichten bewegt'
prop dens=2700 bulk=3.28E9 shear=2.46E9 cohesion=4.0E4 friction=29.5 dilation=1.E-2 &
tension=1.E5 group 'Koessener Schichten bewegt'

```

; ***Koessen formation (limestone only)***

```
group 'Koessener Schichten' region i=850 j=10
model mohr group 'Koessener Schichten'
prop dens=2700 bulk=3.9E9 shear=2.95E9 cohesion=2.49E6 friction=30.5 dilation=1. &
tension=1.E7 group 'Koessener Schichten'
```

; ***Upper Rhaetian formation (above scarp and at counterslope)***

```
group 'Oberrhaetkalk' region i=420 j=200
group 'Oberrhaetkalk' region i=950 j=100
model mohr group 'Oberrhaetkalk'
prop dens=2750 bulk=4.4E9 shear=3.28E9 cohesion=3.05E6 friction=30. dilation=1. &
tension=1.E7 group 'Oberrhaetkalk'
```

; ***Upper Rhaetian formation (landslide area)***

```
group 'Oberrhaetkalk aufgelockert' region i=450 j=200
group 'Oberrhaetkalk aufgelockert' region i=510 j=180
group 'Oberrhaetkalk aufgelockert' region i=550 j=170
group 'Oberrhaetkalk aufgelockert' region i=670 j=130
group 'Oberrhaetkalk aufgelockert' region i=740 j=120
model mohr group 'Oberrhaetkalk aufgelockert'
prop dens=2750 bulk=4.4E9 shear=3.28E9 cohesion=3.05E6 friction=30. dilation=1. &
tension=1.E7 group 'Oberrhaetkalk aufgelockert'
```

; ***Talus (Gassenbach)***

```
group 'Hangschutt' region i=815 j=95
model mohr group 'Hangschutt'
prop dens=2200 bulk=2.78E7 shear=2.1E7 cohesion=1.e4 friction=35. dilation=0. &
tension=0. group 'Hangschutt'
```

; ***Debris/Quaternary***

```
group 'Blockschutt/Quartaer' region i=500 j=200
group 'Blockschutt/Quartaer' region i=723 j=140
model mohr group 'Blockschutt/Quartaer'
prop dens=2200 bulk=1.1E7 shear=8.3E6 cohesion=1.E4 friction=35. dilation=0. &
tension=0. group 'Blockschutt/Quartaer'
```

```
. *****
;
; *                               Plot and documentation commands                               *
; *****
```

; ***Plotting the grid***

```
plot grid hold bo black
set plot win
copy grid.pdf
set plot emf
copy grid.emf
```

; ***Plotting geology without joints and water table***

```
plot group hold bo black
set plot win
copy group.pdf
;set plot emf
;copy group.emf
```

```

; *****
; *
; *                               Insertion of joints                               *
; * *****
; Joint 1 (Scarp)
; Initially, two lines (parallel joint) with a 1 m gap (minimal distance with 1 x 1 m grid) are drawn,
; which will later form the joint.
gen line (149.4,1183.1) (156.6,1145.3)
gen line (150.4,1183.1) (157.6,1145.3)

; The region between the two lines will now be deleted (model null).
model null i=158 j=286,288
model null i=157 j=288,292
model null i=156 j=292,297
model null i=155 j=297,303
model null i=154 j=303,308
model null i=153 j=308,313
model null i=152 j=313,318
model null i=151 j=318,323
model null i=150 j=323

; Starting and ending point must possibly be readjusted - set to the correct coordinates. With the
; coordinates x and y (real coordinates) the correct position is assigned to the according i and j
; nodes/points, to which these will be shifted.
ini x=156.6 y=1145.3 (i=158 j=286)
ini x=157.6 y=1145.3 (i=159 j=286)
ini x=150.4 y=1183.1 (i=152 j=323)
ini x=149.4 y=1183.1 (i=150 j=324)

; Now, the gap between the two lines must be closed again. To achieve this, the nodes on the right and
; left side must be moved on top of each other (This can be done asymmetrically - moving only one side
; - or symmetrically by shifting each side by 0.5 m (in case of 1 m grid). Here, the gridpoints are moved
; symmetrically, shifting the lines by 0.5 m /- 0.5 m in x-direction.
ini x add 0.5 i=158 j=287,288
ini x add 0.5 i=157 j=288,292
ini x add 0.5 i=156 j=292,297
ini x add 0.5 i=155 j=297,303
ini x add 0.5 i=154 j=303,308
ini x add 0.5 i=153 j=308,313
ini x add 0.5 i=152 j=313,318
ini x add 0.5 i=151 j=318,323
ini x add 0.5 i=150 j=323,324

ini x add -0.5 i=159 j=287,289
ini x add -0.5 i=158 j=289,293
ini x add -0.5 i=157 j=293,298
ini x add -0.5 i=156 j=298,304
ini x add -0.5 i=155 j=304,309
ini x add -0.5 i=154 j=309,314
ini x add -0.5 i=153 j=314,319
ini x add -0.5 i=152 j=319,323

; With the following command the interface/joint is created and parameters are assigned.
interface 1, ASIDE from 158,286 to 150,324 BSIDE from 159,286 to 152,323
int 1 kn=5.5E10 ks=5.5E10 friction=15. cohesion=0. dilation=0.

```


; Joint 2

gen line (174.1,1168.8) (180.1,1113.4)

gen line (175.1,1168.8) (181.1,1113.4)

model null i=181 j=254,260

model null i=180 j=260,269

model null i=179 j=269,279

model null i=178 j=279,288

model null i=177 j=288,297

model null i=176 j=297,306

model null i=175 j=306,309

ini x=181.1 y=1113.4 (i=182 j=254)

ini x=180.1 y=1113.4 (i=181 j=254)

ini x=174.1 y=1168.8 (i=175 j=310)

ini x=175.1 y=1168.8 (i=176 j=310)

ini x add 0.5 i=181 j=255,260

ini x add 0.5 i=180 j=260,269

ini x add 0.5 i=179 j=269,279

ini x add 0.5 i=178 j=279,288

ini x add 0.5 i=177 j=288,297

ini x add 0.5 i=176 j=297,306

ini x add 0.5 i=175 j=306,310

ini x add -0.5 i=182 j=255,261

ini x add -0.5 i=181 j=261,270

ini x add -0.5 i=180 j=270,280

ini x add -0.5 i=179 j=280,289

ini x add -0.5 i=178 j=289,298

ini x add -0.5 i=177 j=298,307

ini x add -0.5 i=176 j=307,310

interface 2, ASIDE from 181,254 to 175,310 BSIDE from 182,254 to 176,310

int 2 kn=5.5E10 ks=5.5E10 friction=15. cohesion=0. dilation=0.

; Joint 3

gen line (200.3,1166.8) (203.0,1100.2)

gen line (201.3,1166.8) (204.0,1100.2)

model null i=204 j=241,254

model null i=203 j=254,278

model null i=202 j=278,303

model null i=201 j=303,307

ini x=200.3 y=1166.8 (i=201 j=308)

ini x=201.3 y=1166.8 (i=202 j=308)

ini x=203.0 y=1100.2 (i=204 j=241)

ini x=204.0 y=1100.2 (i=205 j=241)

ini x add 0.5 i=204 j=242,254

ini x add 0.5 i=203 j=254,278

ini x add 0.5 i=202 j=278,303

ini x add 0.5 i=201 j=303,308

ini x add -0.5 i=205 j=242,255

ini x add -0.5 i=204 j=255,279

ini x add -0.5 i=203 j=279,304

ini x add -0.5 i=202 j=304,308

interface 3, ASIDE from 204,241 to 201,308 BSIDE from 205,241 to 202,308

int 3 kn=5.5E10 ks=5.5E10 friction=15. cohesion=0. dilation=0.

; Joint 4

gen line (218.7,1164.2) (221.4,1095.1)

gen line (219.7,1164.2) (222.4,1095.1)

model null i=222 j=236,259

model null i=221 j=259,285

model null i=220 j=285,304

ini x=218.7 y=1164.2 (i=220 j=305)

ini x=219.7 y=1164.2 (i=221 j=305)

ini x=221.4 y=1095.1 (i=222 j=236)

ini x=222.4 y=1095.1 (i=223 j=236)

ini x add 0.5 i=222 j=237,259

ini x add 0.5 i=221 j=259,285

ini x add 0.5 i=220 j=285,305

ini x add -0.5 i=223 j=237,260

ini x add -0.5 i=222 j=260,286

ini x add -0.5 i=221 j=286,305

interface 4, ASIDE from 222,236 to 220,305 BSIDE from 223,236 to 221,305

int 4 kn=5.5E10 ks=5.5E10 friction=15. cohesion=0. dilation=0.

; Joint 5

gen line (241.0,1161.7) (238.7,1090.7)

gen line (242.0,1161.7) (239.7,1090.7)

model null i=240 j=232,255

model null i=241 j=255,286

model null i=242 j=286,302

ini x=241.0 y=1161.7 (i=242 j=303)

ini x=242.0 y=1161.7 (i=243 j=303)

ini x=238.7 y=1090.7 (i=240 j=232)

ini x=239.7 y=1090.7 (i=241 j=232)

ini x add 0.5 i=240 j=233,256

ini x add 0.5 i=241 j=256,287

ini x add 0.5 i=242 j=287,303

ini x add -0.5 i=241 j=233,255

ini x add -0.5 i=242 j=255,286

ini x add -0.5 i=243 j=286,303

interface 5, ASIDE from 240,232 to 242,303 BSIDE from 241,232 to 243,303

int 5 kn=5.5E10 ks=5.5E10 friction=15. cohesion=0. dilation=0.

; Joint 6

gen line (260.2,1168.1) (263.1,1084.4)

gen line (261.2,1168.1) (264.1,1084.4)

model null i=264 j=225,243

model null i=263 j=243,272

model null i=262 j=272,301

model null i=261 j=301,308

ini x=260.2 y=1168.1 (i=261 j=309)

ini x=261.2 y=1168.1 (i=262 j=309)

ini x=263.1 y=1084.4 (i=264 j=225)

```
ini x=264.1 y=1084.4 (i=265 j=225)
ini x add 0.5 i=264 j=226,243
ini x add 0.5 i=263 j=243,272
ini x add 0.5 i=262 j=272,301
ini x add 0.5 i=261 j=301,309
ini x add -0.5 i=265 j=226,244
ini x add -0.5 i=264 j=244,273
ini x add -0.5 i=263 j=273,302
ini x add -0.5 i=262 j=302,309
```

```
interface 6, ASIDE from 264,225 to 261,309 BSIDE from 265,225 to 262,309
int 6 kn=5.5E10 ks=5.5E10 friction=15. cohesion=0. dilation=0.
```

; Joint 7

```
gen line (286.3,1174.1) (286.1,1080.2)
gen line (287.3,1174.1) (287.1,1080.2)
```

```
model null i=287 j=221,315
ini x=286.3 y=1174.1 (i=287 j=315)
ini x=287.3 y=1174.1 (i=288 j=315)
ini x=286.1 y=1080.2 (i=287 j=221)
ini x=287.1 y=1080.2 (i=288 j=221)
ini x add 0.5 i=287 j=222,315
ini x add -0.5 i=288 j=222,315
```

```
interface 7, ASIDE from 287,221 to 287,315 BSIDE from 288,221 to 288,315
int 7 kn=5.5E10 ks=5.5E10 friction=15. cohesion=0. dilation=0.
```

; Joint 8

```
gen line (315.0,1157.9) (313.3,1075.1)
gen line (316.0,1157.9) (314.3,1075.1)
```

```
model null i=314 j=216,225
model null i=315 j=225,273
model null i=316 j=273,298
ini x=315.0 y=1157.9 (i=316 j=299)
ini x=316.0 y=1157.9 (i=317 j=299)
ini x=316.0 y=1157.9 (i=317 j=298)
ini x=313.3 y=1075.1 (i=314 j=216)
ini x=314.3 y=1075.1 (i=315 j=216)
ini x add 0.5 i=314 j=217,226
ini x add 0.5 i=315 j=226,275
ini x add 0.5 i=316 j=274,299
ini x add -0.5 i=315 j=217,225
ini x add -0.5 i=316 j=225,273
ini x add -0.5 i=317 j=273,299
```

```
interface 8, ASIDE from 314,216 to 316,299 BSIDE from 315,216 to 317,298
int 8 kn=5.5E10 ks=5.5E10 friction=15. cohesion=0. dilation=0.
```

; Joint 9

```
gen line (343.5,1121.3) (337.9,1067.0)
gen line (344.5,1121.3) (338.9,1067.0)
```

```
model null i=339 j=208,213
```

```
model null i=340 j=213,223
model null i=341 j=223,232
model null i=342 j=232,242
model null i=343 j=242,252
model null i=344 j=252,261
ini x=343.5 y=1121.3 (i=344 j=262)
ini x=344.5 y=1121.3 (i=345 j=262)
ini x=337.9 y=1067.0 (i=339 j=208)
ini x=338.9 y=1067.0 (i=340 j=208)
ini x add 0.5 i=339 j=209,214
ini x add 0.5 i=340 j=214,224
ini x add 0.5 i=341 j=224,233
ini x add 0.5 i=342 j=233,243
ini x add 0.5 i=343 j=243,253
ini x add 0.5 i=344 j=253,261
ini x add -0.5 i=340 j=209,213
ini x add -0.5 i=341 j=213,223
ini x add -0.5 i=342 j=223,232
ini x add -0.5 i=343 j=232,242
ini x add -0.5 i=344 j=242,252
ini x add -0.5 i=345 j=252,261
```

```
interface 9, ASIDE from 339,208 to 344,262 BSIDE from 340,208 to 345,262
int 9 kn=5.5E10 ks=5.5E10 friction=15. cohesion=0. dilation=0.
```

; Joint 10

```
gen line (369.9,1099.6) (363.4,1058.8)
gen line (368.9,1099.6) (362.4,1058.8)
```

```
model null i=364 j=200,207
model null i=365 j=207,213
model null i=366 j=213,219
model null i=367 j=219,226
model null i=368 j=226,232
model null i=369 j=232,238
model null i=370 j=238,240
ini x=368.9 y=1099.6 (i=370 j=241)
ini x=369.9 y=1099.6 (i=371 j=241)
ini x=369.9 y=1099.6 (i=371 j=240)
ini x=362.4 y=1058.8 (i=364 j=200)
ini x=363.4 y=1058.8 (i=365 j=200)
ini x add 0.5 i=364 j=201,208
ini x add 0.5 i=365 j=208,214
ini x add 0.5 i=366 j=214,220
ini x add 0.5 i=367 j=220,227
ini x add 0.5 i=368 j=227,233
ini x add 0.5 i=369 j=233,239
ini x add 0.5 i=370 j=239,240
ini x add -0.5 i=365 j=201,207
ini x add -0.5 i=366 j=207,213
ini x add -0.5 i=367 j=213,219
ini x add -0.5 i=368 j=219,226
ini x add -0.5 i=369 j=226,232
ini x add -0.5 i=370 j=232,238
ini x add -0.5 i=371 j=238,240
```

interface 10, ASIDE from 364,200 to 370,241 BSIDE from 365,200 to 371,241
int 10 kn=5.5E10 ks=5.5E10 friction=15. cohesion=0. dilation=0.

; Joint 11

gen line (403.1,1081.5) (404.0,1054.6)
gen line (404.1,1081.5) (405.0,1054.6)

model null i=405 j=196,211
model null i=404 j=211,222
ini x=403.1 y=1081.5 (i=404 j=223)
ini x=404.1 y=1081.5 (i=405 j=223)
ini x=404.0 y=1054.6 (i=405 j=196)
ini x=405.0 y=1054.6 (i=406 j=196)
ini x add 0.5 i=405 j=197,211
ini x add 0.5 i=404 j=211,222
ini x add -0.5 i=406 j=197,212
ini x add -0.5 i=405 j=212,222

interface 11, ASIDE from 405,196 to 404,223 BSIDE from 406,196 to 405,223
int 11 kn=5.5E10 ks=5.5E10 friction=15. cohesion=0. dilation=0.

; Joint 12

gen line (640.8,1013.0) (641.2,994.3)
gen line (641.8,1013.0) (642.2,994.3)

model null region 642,135
ini x=640.8 y=1013.0 (i=642 j=154)
ini x=641.8 y=1013.0 (i=643 j=154)
ini x=641.2 y=994.3 (i=642 j=135)
ini x=642.2 y=994.3 (i=643 j=135)
ini x add 0.5 i=642 j=136,153
ini x add -0.5 i=643 j=136,153

interface 12, ASIDE from 642,135 to 642,154 BSIDE from 643,135 to 643,154
int 12 kn=5.5E10 ks=5.5E10 friction=15. cohesion=0. dilation=0.

; Joint 13

gen line (693.2,1012.9) (693.2,995.7)
gen line (694.2,1012.9) (694.2,995.7)

model null i=694 j=136,153
ini x=693.2 y=1012.9 (i=694 j=154)
ini x=694.2 y=1012.9 (i=695 j=154)
ini x add 0.5 i=694 j=137,154
ini x add -0.5 i=695 j=138,154
ini x add -0.3 i=695 j=137
ini y add 0.3 i=695 j=137

interface 13, ASIDE from 694,136 to 694,154 BSIDE from 695,136 to 695,154
int 13 kn=5.5E10 ks=5.5E10 friction=15. cohesion=0. dilation=0.

; Joint 14

gen line (758.1,985.6) (760.0,968.1)
gen line (759.1,985.6) (761.0,968.1)

```

model null i=761 j=109,114
model null i=760 j=114,123
model null i=759 j=123,126
ini x=758.1 y=985.6 (i=759 j=127)
ini x=759.1 y=985.6 (i=760 j=127)
ini x=760.0 y=968.1 (i=761 j=109)
ini x=761.0 y=968.1 (i=762 j=109)
ini x add 0.5 i=761 j=110,114
ini x add 0.5 i=760 j=114,123
ini x add 0.5 i=759 j=123,127
ini x add -0.5 i=762 j=110,115
ini x add -0.5 i=761 j=115,124
ini x add -0.5 i=760 j=124,127

```

```

interface 14, ASIDE from 761,109 to 759,127 BSIDE from 762,109 to 760,127
int 14 kn=5.5E10 ks=5.5E10 friction=15. cohesion=0. dilation=0.

```

```

. *****
;
; *
; Adjustment of grid *
; *****
; After inserting the joints into the grid, it is advisable to adjust the grid to minimize unfavorable
; geometries that occurred during the joint generation.
gen adjust

```

```

. *****
;
; *
; Plot and documentation commands *
; *****
; Plotting of grid with joints
plot grid hold iface blue
set plot win
copy grid_joint.pdf
set plot emf
copy grid_joint.emf

```

```

; Plotting of geology with joints but without water table
plot group hold iface blue
set plot win
copy group_joint.pdf
set plot emf
copy group_joint.emf

```

```

. *****
;
; *
; Saving the geometry with joints *
; *****
save Aggenalm-02_Endmodell.sav

```


NUMERICAL MODELING OF THE AGGENALM LANDSLIDE

Part 3: Implementation of “mean” water table, variation of material properties for sensitivity analyses, extreme event simulation (different water tables) & data output

Written by Judith Festl, last revised June 2014

```

; *****
; *
; Restoring geometry and settings as saved in part 2 *
; *****
; here the model as saved in part 2 is restored for further calculations. It is always the same, except
; for parameter changes that have been applied to the interface/joint properties. See list below for
; conducted joint property changes.
restore Aggenalm-02_Endmodell.sav

; *****
; *
; Resetting deformation to zero *
; *****
ini xdis=0 ydis=0

; *****
; *
; Assigning material properties *
; *****
; Below, the varying parameters are assigned to the materials, mostly to the marls of the Koessen
; formation in the landslide area. Cohesion and friction angle, but also the Young's modulus are changed.
; Also some parameter variations are applied to the talus and debris. Variations of the parameters of the
; joint properties are performed in part 2 already. Nonetheless, the following list lists all property
; variations performed and their range. Printed in bold letters are the parameters that best represent the
; movement characteristics and observations. All other material properties were already assigned in
; today's part 1 or 2 and don't need to be set again.

; List of parameter variations (printed in bold are the variables as used in the final model!)
; Koessen formation in shear zone (marls only!)
; Cohesion: 0, 5, 10, 15, 20, 25, 30, 35, 40 kPa
; Friction angle: 16, 19, 21, 22, 23, 25, 28, 31° (16.5, 19.5, 24.5, 26.5, 30° in first simulations as
; adapted from TADAYONFAR (2011)).
; Density: 2400, 2700 kg/m3
; Young's modulus: 2, 4, 5.9 GPa (doesn't appear directly in the assigned material properties but
; is used to calculate the bulk (K) and shear (G) moduli.
; Debris/Quaternary & Talus
; Density: 2200, 2500 kg/m3
; Young's modulus: multiplied times 5 and times 10
; Joints (variations performed in part 2)
; Friction angle: 5, 15, 25
; Shear and normal stiffness: 5.5E9, 5.5E10

; Talus (Gassenbach)
group 'Hangschutt' region i=815 j=95
model mohr group 'Hangschutt'
prop dens=2500 bulk=2.78E8 shear=2.1E8 cohesion=1.e4 friction=35. dilation=0. &
tension=0. group 'Hangschutt'

```

```
; Debris/Quaternary
group 'Blockschutt/Quartaer' region i=500 j=200
group 'Blockschutt/Quartaer' region i=723 j=140
model mohr group 'Blockschutt/Quartaer'
prop dens=2500 bulk=1.1E8 shear=8.3E7 cohesion=1.E4 friction=35. dilation=0. &
tension=0. group 'Blockschutt/Quartaer'
```

```
; Koessen formation in shear zone (marls only!)
group 'Koessener Schichten bewegt' region i=800 j=80
model mohr group 'Koessener Schichten bewegt'
prop dens=2700 bulk=2.2E9 shear=1.6E9 cohesion=2.E4 friction=23 dilation=0 &
tension=0 group 'Koessener Schichten bewegt'
```

```
. *****
;
; *
; Gravity *
; *****
set large
set grav=9.81
```

```
. *****
;
; *
; Water table *
; *****
; Here the water table is implemented into the model. "table 100" is the "mean" water table observed at
; the Aggenalm landslide. After introducing the table's geometry, a FISH routine is performed to
; calculate the wet density of all the material that is below the introduced water table.
```

```
water table 100 den=1000
table 100 (0,1158) (75.6,1152.3) (471.8,1052.6) (758.8,968.6) (807.6,957.3) (821.2,957.6) &
(1000.5,1011.3)
def wet_den
  loop i (1,izones)
    loop j (1,jzones)
      if model (i,j)>1 then
        xa=(x(i,j)+x(i+1,j)+x(i+1,j+1)+x(i,j+1))
        xc=0.25*xa
        ya=(y(i,j)+y(i+1,j)+y(i+1,j+1)+y(i,j+1))
        yc=0.25*ya
        if yc<table(1,xc) then
          density(i,j)=density(i,j)+300
        end_if
      end_if
    end_loop
  end_loop
end
wet_den
```

; The following list gives the coordinates for all the different water tables that were used in the model.
; Additionally, the table's depth below surface at B4 (location of piezometer) is given.

```
table 98 (0,1158) (75.6,1142.3) (471.8,1042.6) (758.8,958.6) (807.6,957.3) (821.2,957.6) &
(1000.5,1011.3)
table 99 (0,1158) (75.6,1147.3) (471.8,1047.6) (758.8,963.6) (807.6,957.3) (821.2,957.6) &
(1000.5,1011.3)
table 100 (0,1158) (75.6,1152.3) (471.8,1052.6) (758.8,968.6) (807.6,957.3) (821.2,957.6) &
(1000.5,1011.3)
```

table 11 (0,1158) (75.6,1155.3) (471.8,1055.6) (758.8,971.6) (807.6,957.3) (821.2,957.6) &
(1000.5,1011.3)
table 12 (0,1158) (75.6,1157.3) (471.8,1057.6) (758.6,973.7) (807.6,957.3) (821.2,957.6) &
(1000.5,1011.3)
table 13 (0,1158) (75.6,1159.3) (471.8,1059.6) (758.6,975.7) (807.6,957.3) (821.2,957.6) &
(1000.5,1011.3)
table 14 (0,1158) (75.6,1161.3) (471.8,1061.6) (758.6,977.7) (807.6,957.3) (821.2,957.6) &
(1000.5,1011.3)
table 15 (0,1158) (75.6,1163.3) (471.8,1063.6) (758.6,979.7) (807.6,957.3) (821.2,957.6) &
(1000.5,1011.3)
table 16 (0,1158) (75.6,1165.3) (471.8,1065.6) (758.6,981.7) (807.6,957.3) (821.2,957.6) &
(1000.5,1011.3)

```

; *****
; *
; * Assigning points for displacement monitoring *
; * *****
; At 10 points (location see text - at observation point 1 (above main scarp) hist 10 and 20, at observation
; point 2 hist 11 and 21, ... are recorded) the x- and y-displacements are recorded during the calculation.
; Here the location of each monitoring point is set.
hist 10 xdis i=144 j=334
hist 11 xdis i=166 j=314
hist 12 xdis i=296 j=314
hist 13 xdis i=344 j=279
hist 14 xdis i=397 j=248
hist 15 xdis i=476 j=219
hist 16 xdis i=568 j=194
hist 17 xdis i=668 j=160
hist 18 xdis i=716 j=150
hist 19 xdis i=787 j=111

hist 20 ydis i=144 j=334
hist 21 ydis i=166 j=314
hist 22 ydis i=296 j=314
hist 23 ydis i=344 j=279
hist 24 ydis i=397 j=248
hist 25 ydis i=476 j=219
hist 26 ydis i=568 j=194
hist 27 ydis i=668 j=160
hist 28 ydis i=716 j=150
hist 29 ydis i=787 j=111

```

```

; *****
; *
; * Calculation and saving of the model *
; * *****
; For most calculations the standard amount of steps, 100,000, was applied. The calculation stops
; automatically after 100,000 timesteps.
solve
save Aggenalm_w100-20-23.sav

```

```

; *****
; *
; * Restoring of saved file *
; * *****
restore Aggenalm_w100-20-23.sav

```

```
. *****  
,  
, *           Export of x- and y-displacements as .his-files and plotting of data           *  
, *****  
set hisfile x-w100-20-23_10.his  
hist write 10  
set hisfile x-w100-20-23_11.his  
hist write 11  
set hisfile x-w100-20-23_12.his  
hist write 12  
set hisfile x-w100-20-23_13.his  
hist write 13  
set hisfile x-w100-20-23_14.his  
hist write 14  
set hisfile x-w100-20-23_15.his  
hist write 15  
set hisfile x-w100-20-23_16.his  
hist write 16  
set hisfile x-w100-20-23_17.his  
hist write 17  
set hisfile x-w100-20-23_18.his  
hist write 18  
set hisfile x-w100-20-23_19.his  
hist write 19  
  
set hisfile y-w100-20-23_20.his  
hist write 20  
set hisfile y-w100-20-23_21.his  
hist write 21  
set hisfile y-w100-20-23_22.his  
hist write 22  
set hisfile y-w100-20-23_23.his  
hist write 23  
set hisfile y-w100-20-23_24.his  
hist write 24  
set hisfile y-w100-20-23_25.his  
hist write 25  
set hisfile y-w100-20-23_26.his  
hist write 26  
set hisfile y-w100-20-23_27.his  
hist write 27  
set hisfile y-w100-20-23_28.his  
hist write 28  
set hisfile y-w100-20-23_29.his  
hist write 29  
  
pl hi 10 11 12 13 14 15 16 17 18 19  
set plot win  
copy x-w100-20-23.pdf  
pl hi 20 21 22 23 24 25 26 27 28 29  
copy y-w100-20-23.pdf
```

Appendix X:

Direct shear test

The parameters recorded during installation and run of the direct shear tests on the Kössen marls are part of this Appendix. Additionally, the resulting diagrams, such as the plots of normal-stress versus shear-stress and the shear-displacement shear-stress diagrams are presented. Four of the total 13 samples were taken as undisturbed samples, while the remaining were disturbed and built in the shear box. The natural water content of the samples was analyzed only hours after sampling, and then again right before each shear test of the installed sample. All samples were kept in an air-tight container to hinder drying.

Table X-1: Installation setup and results of the individual direct shear tests on samples of the Kössen marls.

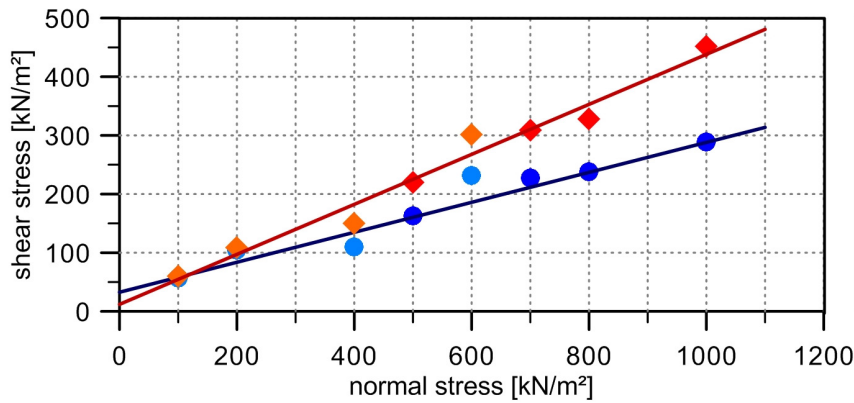
Direct shear test (in accordance with DIN 18137, part 1)											
Project:		alpEWAS/PhD thesis					Type of material:		Kössen marls		
Samples taken by:		J. Festl					Type of sample:		undisturbed & disturbed		
Sampling date:		October 19, 2012					Testing dates:		Oct.-Dec. 2012		
Sampling location:		Toe of landslide, Gassenbach					Diameter of ring:		71.2 mm		
Depth:		approx. 0.5 m below surface					Area:		39.81 cm ²		
Sample		Installation					Shear test				
Type	ID	m _w [g]	h ₀ [mm]	ρ _w [g/cm ³]	w [%]	ρ _d [g/cm ³]	σ _n [kN/m ²]	d _{s-tot.} [mm]	σ _{s-max.} [kN/m ²]	d _{s-max.} [mm]	σ _{s-res.} [kN/m ²]
undisturbed	1	173.5	19.8	2.20	22.3	1.80	100	6.96	59.60	20.0	57.22
	2	166.8	20.1	2.08	20.8	1.73	200	4.2	108.75	24.6	104.94
	3	172.6	19.8	2.19	24.5	1.76	400	2.04	150.23	25.0	109.54
	4	173.7	19.7	2.21	23.7	1.79	600	4.29	301.78	25.0	231.47
disturbed	5	182.4	20.2	2.27	20.7	1.88	150	4.01	73.49	20.0	52.67
	6	175.3	19.8	2.22	25.2	1.78	300	4.86	152.98	20.0	112.28
	7	180.1	19.8	2.29	21.7	1.88	400	4.54	192.21	20.0	144.72
	8	168.6	20.0	2.12	24.2	1.70	500	3.48	203.21	20.0	137.27
	9	182.5	20.2	2.27	16.0	1.96	500	3.56	220.03	20.0	163.24
	10	173.0	20.1	2.16	17.8	1.84	700	4.34	308.45	20.0	227.10
	11	171.4	19.6	2.20	19.0	1.85	800	2.68	286.42	20.0	205.05
	12	181.5	20.0	2.28	16.7	1.95	800	3.33	328.13	20.0	238.24
	13	169.4	20.2	2.11	21.3	1.74	1000	4.02	451.43	20.0	288.37

m_w: mass of sample (wet)h₀: height of sampleρ_w: wet density of sample

w: water content of sample at installation (mean water content directly after sampling 25.8 %)

ρ_d: dry density of sampleσ_n: normal stressd_{s-tot.}: total shear displacementσ_{s-max.}: max. shear stress (peak)d_{s-max.}: shear displacement at σ_{s-max.}σ_{s-res.}: residual shear stress at 20 mm shear displacement

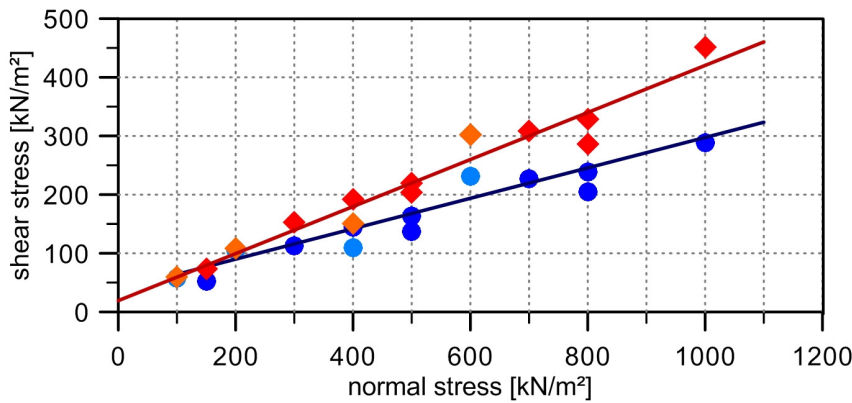
selected disturbed & undisturbed samples



Effective shear strength
 $\varphi' = 23.08^\circ$
 $c' = 11.98 \text{ kN/m}^2$
 correlation, $R^2 = 0.97$

Residual shear strength
 $\varphi_{\text{res}} = 14.54^\circ$
 $c_{\text{res}} = 38.13 \text{ kN/m}^2$
 correlation, $R^2 = 0.94$

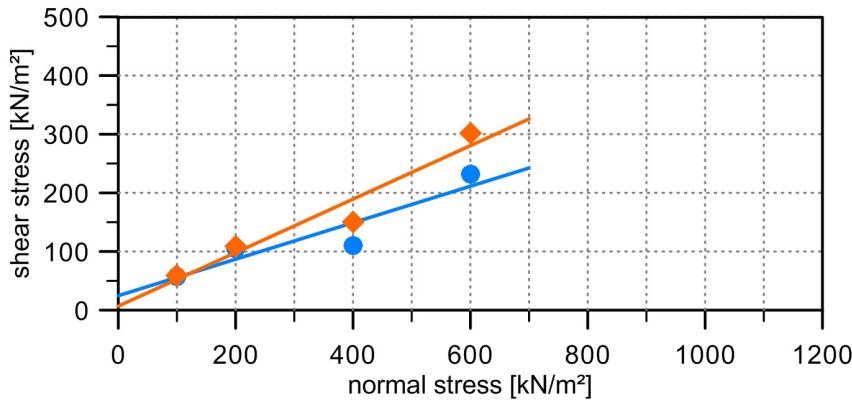
all disturbed & undisturbed samples



Effective shear strength
 $\varphi' = 21.85^\circ$
 $c' = 19.25 \text{ kN/m}^2$
 correlation, $R^2 = 0.95$

Residual shear strength
 $\varphi_{\text{res}} = 14.33^\circ$
 $c_{\text{res}} = 32.67 \text{ kN/m}^2$
 correlation, $R^2 = 0.92$

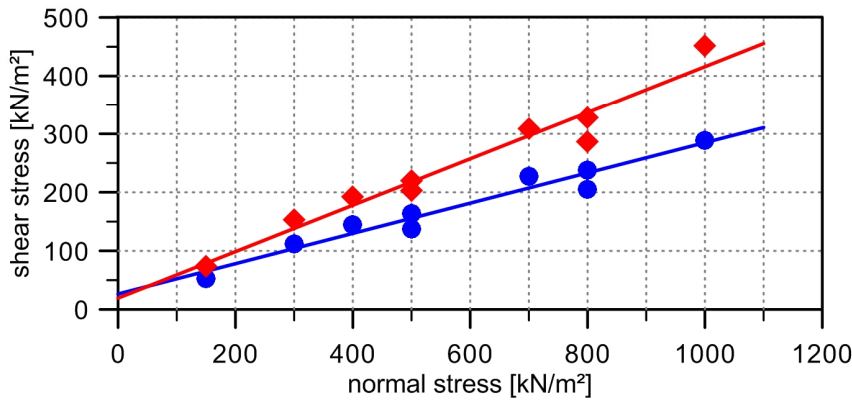
undisturbed samples



Effective shear strength
 $\varphi' = 24.51^\circ$
 $c' = 6.91 \text{ kN/m}^2$
 correlation, $R^2 = 0.93$

Residual shear strength
 $\varphi_{\text{res}} = 17.28^\circ$
 $c_{\text{res}} = 24.71 \text{ kN/m}^2$
 correlation, $R^2 = 0.86$

disturbed samples

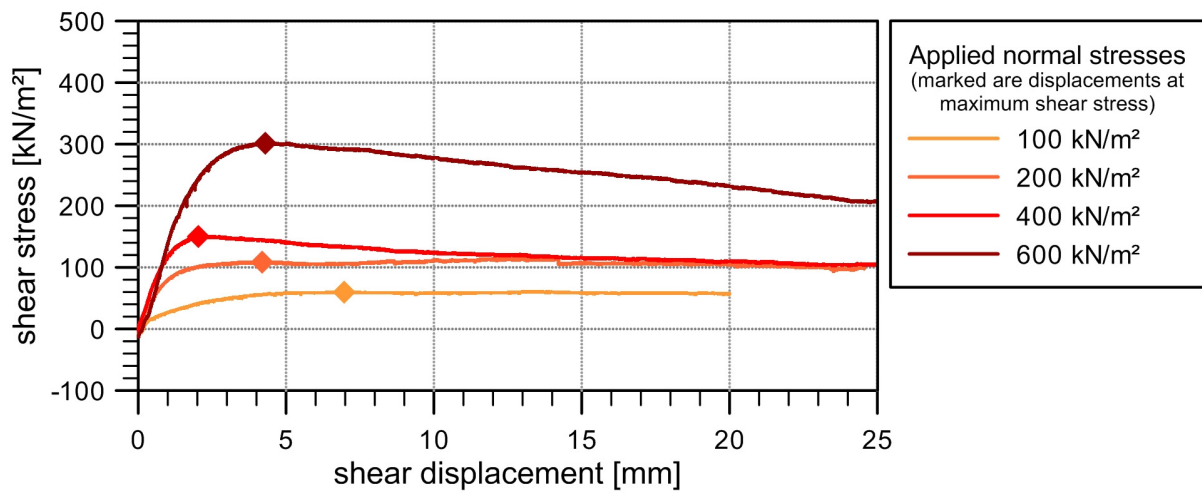


Effective shear strength
 $\varphi' = 21.63^\circ$
 $c' = 19.35 \text{ kN/m}^2$
 correlation, $R^2 = 0.95$

Residual shear strength
 $\varphi_{\text{res}} = 14.49^\circ$
 $c_{\text{res}} = 26.44 \text{ kN/m}^2$
 correlation, $R^2 = 0.95$

Figure X-1: σ_n - σ_s -diagrams of the direct shear test on the Kössen marls for the undisturbed and disturbed samples.

Displacement – shear stress diagram of undisturbed samples



Displacement – shear stress diagram of disturbed samples

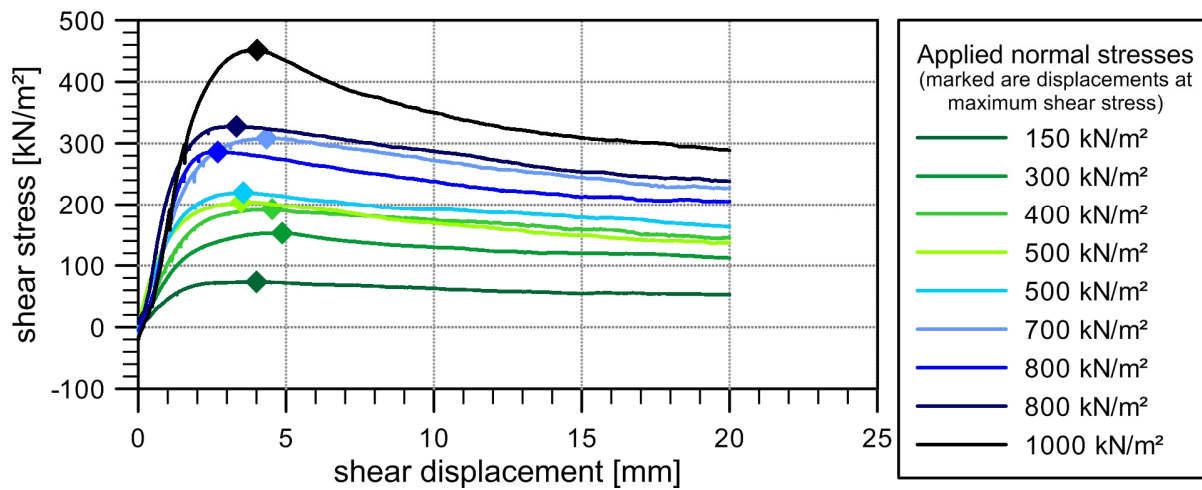


Figure X-2: Shear displacement plotted versus shear stress for the undisturbed and disturbed samples. The diamonds mark the point at which the maximum shear stress is reached. Readings of the shear stress for the residual shear strength calculation were taken at 20 mm displacement at each test for comparative reasons.